# Particle dynamics in turbulence : from the role of inhomogeneity and anisotropy to collective effects

Peter Dearborn Huck



Numéro National de Thèse : 2017LYSEN073

**THÈSE de DOCTORAT DE L'UNIVERSITÉ DE LYON**
opérée par
**l'École Normale Supérieure de Lyon**

**École Doctorale** N°52
**École Doctorale de Physique et Astrophysique de Lyon (PHAST)**

**Spécialité de doctorat : Physique**

Soutenance prévue le 6/12/2017, par :

**Peter Dearborn Huck**

# Particle dynamics in turbulence : from the role of inhomogeneity and anisotropy to collective effects

Devant le jury composé de :

| | | |
|---|---|---|
| Chibbaro, Sergio | Institut Jean Le Rond D'Alembert, UPMC | Rapporteur |
| Monchaux, Romain | ENSTA ParisTech | Rapporteur |
| Aliseda, Alberto | Dept. Mech. Engineering, University of Washington | Examinateur |
| Bourgoin, Mickael | Laboratoire de Physique, ENS de Lyon | Examinateur |
| Chilla, Francesca | Laboratoire de Physique, ENS de Lyon | Examinatrice |
| Mordant, Nicolas | LEGI, Université de Grenoble Alpes | Examinateur |
| Vinkovic, Ivana | LMFA, UCB Lyon 1 | Examinatrice |
| Volk, Romain | Laboratoire de Physique, ENS de Lyon | Directeur de thèse |

# Remerciements

I count myself as exceedingly fortunate to have had the opportunity to finish my studies as a doctoral student in the Physics laboratory of the École Normale Supérieure de Lyon. Many things stand out over the past three years, notably the general atmosphere of the lab, especially around 1 o'clock in the afternoon when most of the serious science seemed to get done.

I'd like to thank my advisor, Romain Volk who allowed me great freedom in the direction of this project, but who at the same time had the particular capacity of seeing the essential, and crucially seeing through the inessential in a way that kept my ideas focused. Working together was an immense pleasure. Thanks to Alberto Aliseda who welcomed me to his lab for 8 months and introduced me to multi-phase flows and helped shape one of the main thrusts of this manuscript. My return for the third year coincided with Mickael Bourgoin's full time presence at the lab and without whose help on the sedimentation problem I may have never gained the physical insight that I found, thank you. A general thanks to the administrative and technical staff for your professionalism, kindness, and skill.

Many thanks to Carol, Bruce, Rachel and Matthew Huck who have put of with me for 62 (in total) , 27, and 24 years, but mostly for supporting me during the last seven. Muito obrigado to all mes amis Marseillais who have been there since the beginning. Merci Jérémy, Victor, et Céleste pour votre amitié. Grazie Elisa for the moral support when everybody was on vacation, except for me and my thesis.

Je me tiens à remercier La France, qui m'a accueilli si chaleureusement pendant ces sept dernières années et m'a donné l'oportunité de réaliser cet travail. Merci.

*For Poppy...*

# Contents

# Chapitre 1

# Introduction

Interest in the characteristics of turbulent fluid flows may be traced back at least as early as the works of Leonardo da Vinci (1452-1519). Among other equally impressive feats, da Vinci is credited for the first recorded observations of a turbulent flow behind an obstacle placed in running water. The emphasis of his drawings was on the chaotic and vortical nature of the flow which led him to ask the simple question : *Dove la turbolenza dell'acqua si genera? Dove la turbolenza dell'acqua si riposa?*[1]. In these two questions, the essential themes of this dissertation are breached.

1. Where is the turbulence in water generated? Where does the turbulence come to rest? [1]

Underlying the second question is the notion of why turbulent transport, or how a turbulent flow moves a quantity of matter from one point to another. With wide ranging applications from industrial processes [2] to the dispersion of pollutants in the atmosphere [3] or the ocean [4], turbulence is characterized by its ability to *enhance* the mixing capacity of a given flow. Indeed, understanding the processes that may (or may not) lead to mass transport takes on particular significance when considering the recent nuclear meltdown at the Fukushima Daiichi power plant and the subsequent release of nuclear contaminants into the Pacific Ocean. A report by the California Coastal Commission underscores this point, "Because the Pacific Coast of North America is downwind and 'down-current' of Japan, the accident has led to widespread public concern about the prospect of radioactive contamination along the coast." [5]

The California Coastal Commission report underlines the importance of the underlying fluid flow in transporting the contaminant. In this case the convergence of the Kuroshio (from the south) and Oyashio (from the north) currents off the coast of Japan form the North Pacific Current which is generally qualified as a "jet" by geo-physicists [7]. Due to the strong shearing motion present in jets large patches of contaminant may be broken down into small patches which are broken down into even smaller structures and so on in a process one might qualify as "stirring". Eventually, the dominance of molecular diffusion at small scales leads to a state where the contaminant and the diluting fluid are indistinguishable; this is "mixing". These two states are observed experimentally in figure 1.1 where the concentration is proportional to the intensity of the (white) fluorescent dye illuminated by a laser sheet. The stirring process is dominant in figure 1.1(a) where a distinction between water (black) and the scalar (white) can be made. Mixing may be said to be dominant in

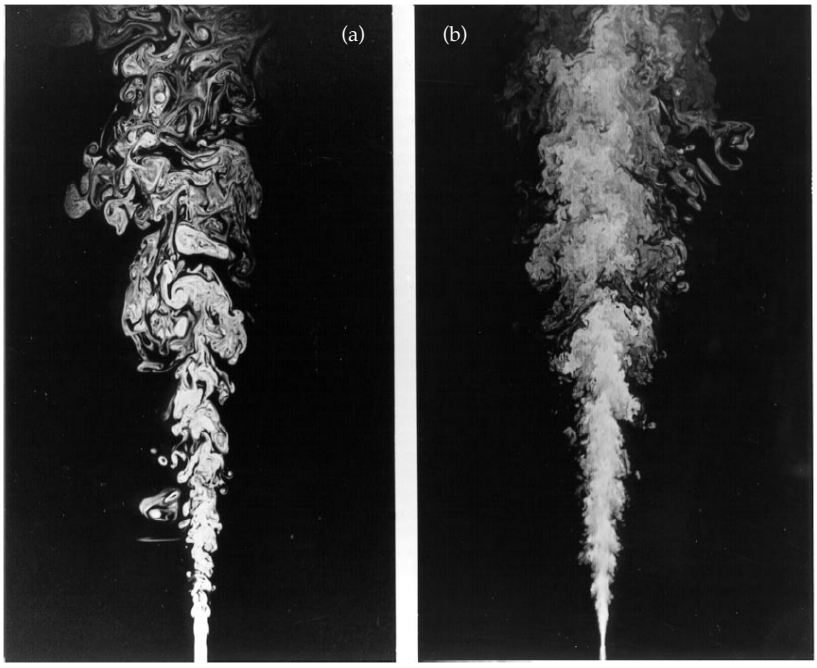


Figure 1.1: Liquid-phase turbulent jet [6] with a passive scalar field injected at the nozzle. When illuminated by a laser, the scalar emits light in proportion to its concentration. (a) $\mathrm{Re} \simeq 2.5 \times 10^3$ (b) $\mathrm{Re} \simeq 1.0 \times 10^4$.

figure 1.1(b) demonstrating the role of turbulence in enhancing the breakdown of a highly concentrated scalar.

While the underlying flow is of importance for turbulent transport, a second consideration that takes into account the properties of the transported material is consequential. Cesium-137 released into the ocean at Daiichi can generally be thought to passively follow the fluid flow, the defining property of what will be referred to as *tracers*. However, situations often arise where the size and/or density of a substance seeded into a flow is such that their dynamics differ greatly from tracers and are typically referred to as "inertial". The release of nearly 80,000 Nike sneakers (or "particles" to the indoctrinated PhD student) into the Pacific Ocean when a freighter encountered heavy weather [8] is an example of such a situation. The particularities of inertial particles in turbulent flows has inspired a good deal of experimental [9, 10] and Direct Numerical Simulation (DNS) [11] studies.

A third consideration enters into play when studying particle transport: the interaction between the carrier phase and the particle phase when the latter is present in large concentrations. Much phenomenology exists in this subject but a concrete example is that of a column of quiescent fluid into which small, heavy beads are released. After attaining terminal velocity the beads will create perturbations to the fluid by nature of their trailing wake [12] and may even render a still fluid slightly turbulent. Coherent structures may form (for a particular parameter range), entraining particles and fluid while permitting the particles to settle faster than they otherwise would in isolation. The coupling of the particle and carrier phase is a phenomenon that can significantly enhance transport, as is the case here, but may also impede it [13].

The present study is at the frontier of themes evoked above. A novel Shadow Particle Tracking Velocimetry (S-PTV) technique is implemented to obtain Lagrangian trajectories. The turbulent flow to be studied is a square cylinder forced by two count-rotating impellers, a configuration that is typically referred to as the von Kármán flow. The noisy nature of these measurements for higher order derivatives (*e.g.* for the acceleration) requires careful signal processing and a new technique is developed in order to obtain unbiased single and two-time statistics. These subjects are presented in chapter 2.

A first question concerning the origin of turbulence in the present flow is the point of depart for this work. The von Kármán flow presents a stagnation point that is intimately related to the mechanisms of turbulence production. A detailed study of the Turbulent Kinetic Energy (TKE) budget is presented in chapter 3. The mechanism driving production of turbulence in a stagnation point is inextricably linked to the anisotropy of the underlying flow and this dependency has quantifiable effects on the dispersion of particles near the stagnation point. These results are presented in chapter 4.

The von Kármán flow is not only anisotropic, but it is strongly non-homogeneous. Consequently, particles explore regions where statistical quantities (such as velocity fluctuations) vary which causes their dynamics to become non-stationary. Adding inertia to the particles adds complexity to their dynamics that is quantified with respect to a tracer benchmark. Consequences of non-homogeneity and anisotropy on inertial particle transport is discussed in chapter 5.

Due to experimental constraints, the PTV experiments performed at the Physics Laboratory at the École Normale Supérieure de Lyon were carried out in the dilute limit. To study the coupling between inertial particles and the carrier flow, experi-

ments were performed in the Mechanical Engineering Department at the University of Washington. A wind tunnel was seeded with micro-meter sized water droplets such that the ratio of volume occupied by the droplets to the total volume was $10^{-5}$. In this regime no coupling is expected in contrast with the sedimentation experiment described above, where the volume fraction was $10^{-3}$. However, due to the particularities of inertial particle dynamics in turbulence, local concentrations may increase by over an order of magnitude, enhancing the settling velocities. A model derived from first principles accounts for the enhanced settling velocities by introducing a coupling between the carrier and particle phases and is presented in chapter 6.

Finally, publications resulting from collaborations with other PhD students and post-docs from the Physics Laboratory as well as colleagues from Karlsruhe Institut für Technologie are presented in appendices A & B.

## 1.1 Turbulence

Turbulence is a formidable problem, but it is a well posed problem. Something that most, if not all, who study it will agree upon is that a Newtonian fluid flow with a density $\rho$ and kinematic viscosity $\nu$ that has a divergence free velocity field $\vec{v}(\vec{x},t)$ satisfies the Navier-Stokes equation:

$$\partial_t \vec{v} + (\vec{v}\cdot\vec{\nabla})\vec{v} = -\frac{1}{\rho}\vec{\nabla}p + \nu\Delta\vec{u} + \vec{f}, \tag{1.1}$$

$$\vec{\nabla}\cdot\vec{v} = 0, \tag{1.2}$$

with suitable boundary conditions where $\vec{f}$ represents body forces per unit mass that may intervene. A natural question then arises, *what is a turbulent flow*? Osborne Reynolds [14] established that the ratio of the non-linear to viscous terms in equation (1.1) was a determining factor in whether the motion of a fluid should laminar or sinuous. The parameter that bears his name compares these two terms:

$$\mathrm{Re} = \frac{\text{non-linear terms}}{\text{viscous terms}} = \frac{VL}{\nu} \tag{1.3}$$

where $V$ and $L$ are some characteristic velocity and length of the flow, for example the inlet diameter and velocity in figure 1.1. The Reynolds number compares the viscous terms, which tend to dampen motion, with the non-linear terms that tend to amplify it. A turbulent flow is one for which $\mathrm{Re} \gg 1$.

Figure 1.1 displays two turbulent jets with different Reynolds numbers (*left:* $\mathrm{Re}\simeq 2.5\times10^3$ *right:* $\mathrm{Re}\simeq 10^4$). While large scale structures the size of the jet's width are apparent for both Reynolds numbers, much finer structures are apparent for the higher Reynolds number. Thus, increasing the Reynolds number feeds the non-linear terms of equation (1.1) which in turn enhances the small scales. The existence of scales that grow increasingly small with respect to the large scales with increasing Reynolds number is a key feature of turbulence.

To the observation of the sinuosity of a turbulent flow by Reynolds can be added Lewis Fry Richardson's interpretation of turbulence as a multi-scale phenomenon [15]. In this vision of turbulence, energy is injected into a system filled with "eddies" of different sizes; the largest ones take in the injected energy while breaking down into successively smaller eddies until reaching a scale at which viscous dissipation dampens them as depicted in figure 1.2.

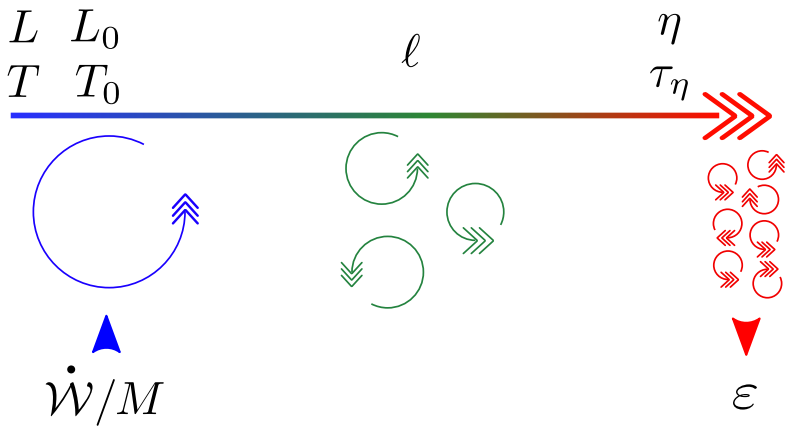


Figure 1.2: Turbulent cascade as envisioned by L. F. Richardson. A system with a characteristic length ($L$) and time ($T$) scales receives energy in eddies characterized by length (time) scales $L_0$ ($T_0$) corresponding to the forcing mechanism. Energy then passes through eddies of an intermediary size $\lambda$ before arriving at the dissipative length (time) scales $\eta$ ($\tau_\eta$) where energy is converted into heat by viscous dissipation.

What should the smallest scale be for a given Reynolds number? A.N. Kolmogorov's response to this question provided a rigorous framework in which to interpret Richardson's idea of a "cascade" of energy through eddies of different sizes [16]. In particular Kolmogorov posited that below scales linked to the turn-over time ($T_0$) and size ($L_0$) of the largest eddies in the flow (fig 1.2), small scale motions would be statistically isotropic for sufficiently high Reynolds numbers even if the largest scales were not [2]. Furthermore, the transfer of energy through the scales should be approximately equal to the rate at which it is eventually lost through viscous dissipation (given by the dissipation rate $\varepsilon$) due to small scale shearing. This constitutes a second hypothesis [3] which predicts a universal form of the small scales uniquely determined by $\varepsilon$ and $\nu$. With these two parameters the characteristic length, time and velocity of the dissipative range results from dimensional analysis:

$$\eta = \left(\nu^3/\varepsilon\right)^{1/4}, \tag{1.4}$$

$$\tau_\eta = \left(\nu/\varepsilon\right)^{1/2}, \tag{1.5}$$

$$v_\eta = \left(\varepsilon\nu\right)^{1/4}. \tag{1.6}$$

These relationships permit a schematic representation of the cascade process (fig. 1.2). For a system with a characteristic size $L$, time $T$, and velocity $L/T$ energy is injected at a size that corresponds to the largest eddies of the flow (respectively $L_0$, $T_0$, $V_0 = L_0/T_0$). In general this represents the power per unit mass ($\dot{\mathcal{W}}/M$) exerted on the flow to render it turbulent, *i.e.* a compressor accelerating the fluid or disks stirring the fluid exerts a certain amount of work per unit time on the flow. Energy then passes through a succession of eddies at a rate of $\varepsilon$ until it reaches the dissipative range where the viscosity plays a strong roll and the mechanical work is converted to heat. In this vision of a turbulent process the equilibrium condition $\dot{\mathcal{W}}/M = \varepsilon$ must hold. One should bear in mind that this *direct cascade* of energy

2. This is referred to as "Kolmogorov's hypothesis of local isotropy".
3. Known as the "First Similarity Hypothesis"

from large to small scales is valid in a statistical sense. Instantaneously, energy may be transferred either towards the large or small scales. Moreover, turbulent flow conditions may exist such that the direction of the cascade, in the statistical sense, reverses, sending energy from small to large scales such as in flows dominated by rotation [17].

Before reaching the dissipative range, eddies pass through an intermediate range called the "inertial range", where the statistics of motion are uniquely determined by $\varepsilon$, the scale $\ell$, and are independent of $\nu$ [4]. Because the dissipation rate is statistically steady, similarity implies that it is determined by the velocity $v_\ell$ at a particular scale $\ell$: $\varepsilon \sim v_\ell^3/\ell$. The ratio of the largest to smallest scales is related to the properties of the flow through the dimensionless relationship: $L_0/\eta = \mathrm{Re}_{L_0}^{3/4}$ where $\mathrm{Re}_{L_0} = V_0 L_0/\nu$. This relationship underlines the notion of *scale separation* that exists for large Reynolds number flows. In particular, increasing the Reynolds number by a factor of 10 in figure 1.1 where $L_0$ is fixed decreases the size of the smallest scales concomitantly [5]. As a result the inertial range extends over an increasing range of scales.

## 1.2 An experimental survey

In 1850 James Prescott Joule conducted an extraordinarily precise measurement of the "mechanical equivalent of heat", which provides an interesting illustration of the role fluid flows (and even turbulence) have in the transfer of energy [22]. Joule's hypothesis was that a given amount of work will produce an equivalent amount of heat provided that there are minimal loses in the transfer process. Using an insulated wooden tank 0.2 m in diameter (with an aspect ratio of nearly one) containing just over 6 kg of water, a network of paddles were driven by a 13.6 kg weight allowed to repeatedly fall a distance of 1.6 m (fig. 1.3 a) . With a precision of 3 mK, Joule was capable of measuring an increase in the temperature of water by 0.31 K corresponding to a consistent value of 778.24 foot pound force needed to raise the temperature of a pound of water by one degree Fahrenheit [6]. These measurements correspond startlingly well with the accepted value of the heat capacity of water, $c_p = 4.18\,\mathrm{kJ.kg^{-1}K^{-1}}$ at ambient temperature. His results were communicated to the Royal Society by none other than Michael Faraday [4].

A subtlety of Joule's experiment was that he placed baffles inside the cylinder to impede the creation of a mean circulation containing kinetic energy that would introduce supplementary terms into the energy budget he set out to calculate. The rotating paddles then drove fluid past the fixed baffles creating small-scale eddying, a characteristic of turbulence. Joule understood, at least intuitively, that the en-

4. This constitutes the Kolmogorov's second similarity hypothesis

5. This example is not to suggest an equivalency between a scalar ("contaminant") field and a velocity field. Indeed, the former is governed by the advection-diffusion equation while the latter by equation (1.1). In general the scales involved may be similar when the relationship between kinematic viscosity and molecular diffusivity is of order one, a ratio described by the Schmidt number: $Sc = \nu/D$, where $D$ is the scalar molecular diffusivity. The relationship between the smallest scales of the scalar in the jet (the Batchelor scale: $\ell_b$ [18]) and the Kolmogorov scale is $\ell_b/\eta = \mathrm{Sc}^{-1/2}$ indicating that for large Schmidt numbers ($Sc \sim 2000$ in fig. 1.1) the smallest scales of the turbulent mixture are much smaller than those of turbulence.

6. In SI units: $1.05{\times}10^3$ J of energy needed to raise the temperature of a 0.45 kg of water by 5/9 K.

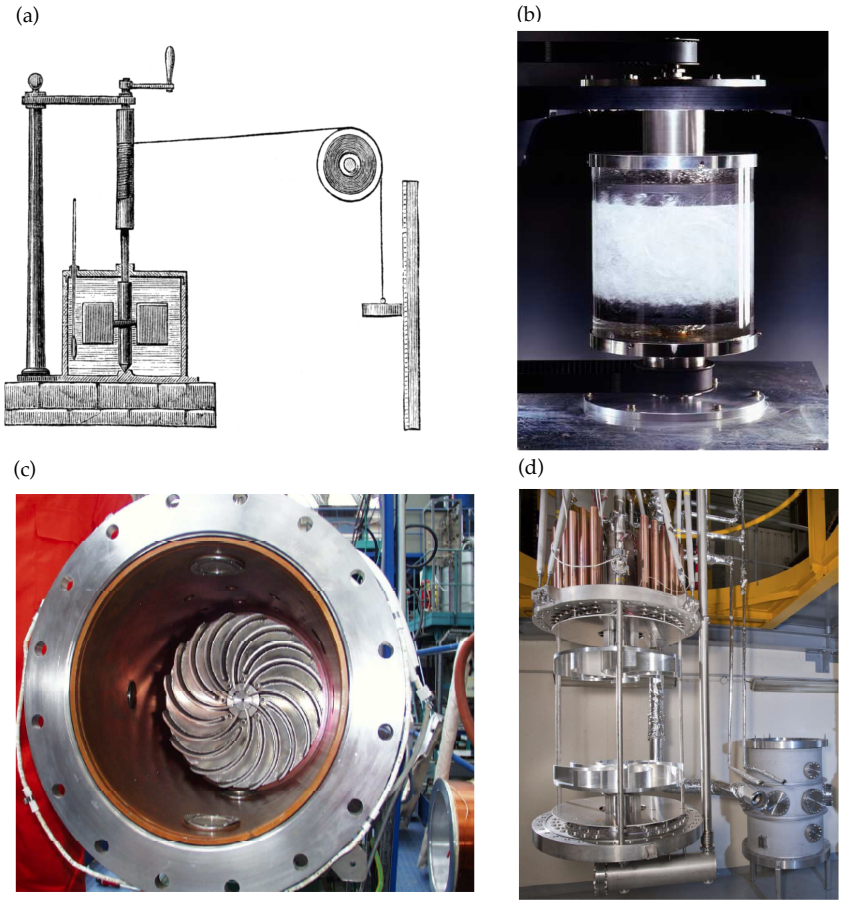


Figure 1.3: (a) Artist's rendering of Joule's experiment [19]. The baffles used to avoid solid body rotation are not pictured in this representation. (b) A water von Kármán flow seeded with air bubbles for visualization [20]. The impellers have curved blades and may to either "push" or "scoop" the fluid. (c) The von Kármán Sodium (VKS) device [20]. (d) The Superfluid High REynolds von Kármán (SHREK) experimental facility [21].

hanced shearing inherent in vortical motion greatly increased the rate at which the mechanical energy was transferred into heat. One might argue that Joule conducted one of the first recorded turbulence experiments, a full 33 years before the landmark experiments of Osborne Reynolds [14], with little more than a thermometer, a 13.6 kg weight, and an apparatus strongly resembling a rudimentary washing machine.

The role of turbulent dissipation in industrial mixing has long been known to engineers seeking a sufficiently homogeneous product for a minimum of energy paid into powering motors [2]. Indeed many industrial mixers resemble the apparatus used in Joule's experiment and many French laboratories have constructed similar devices, often with two spinning paddles (or impellers, propellers etc. [20]). In fact, so numerous have been studies interested in the turbulent aspects of liquid flows ranging from water (fig.1.3 b) to liquid sodium (fig.1.3 c), gallium and helium (He-I or He-II, fig.1.3 d), that these devices have collectively come to be called *French Washing Machines* in reference to the resemblance of Joule's apparatus to

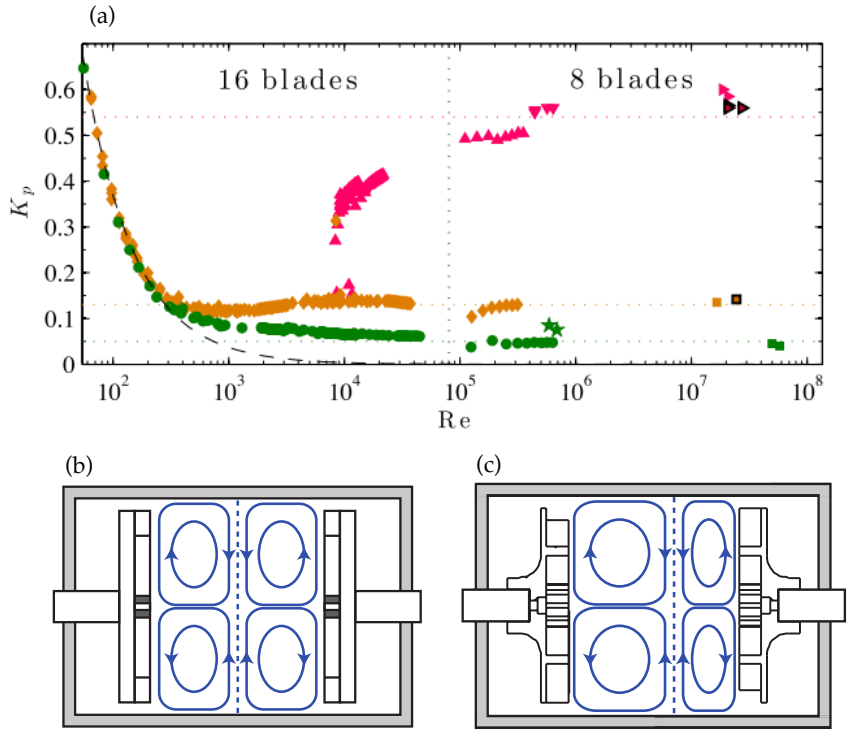


Figure 1.4: (a) Normalized power consumption in water, nitrogen, helium, and super-fluid helium von Kármán flows [26]. (b) Symmetrical state, (c) Symmetry breaking with respect to rotations of $\pi$ around any radial axis passing through the center of the device.

a *lessiveuse*[7], a device commonly used for laundry in the 19$^{\text{th}}$ century. More generally the flow produced by these are called *von Kármán flows* [23], in reference to the theoretical investigation of Theodore von Kármán into the solutions of equation (1.1) in the vicinity of a smooth disc with radius $R \to \infty$ rotating with an angular frequency $\Omega$ [24]. Later G. K. Batchelor would extend the study to a system of two counter-rotating disks creating two cells undergoing solid body rotation with a shear layer separating them [25]. The latter interpretation is generally the image most in the community have of the von Kármán flow between two counter-rotating disks.

Measurements of the normalized power consumption ($K_p = \Gamma(\rho R^5 \Omega^3)^{-1}$, where $\Gamma$ is the measured power) of two motors driving counter-rotating disks in the von Kármán flow respond to a question similar to that of Joule: how much power is required to establish a given rotation rate? Figure 1.4(a) is a compilation of water experiments conducted at CEA Saclay (fig. 1.3 b) and the SHREK experiment (fig. 1.3 d) at the NEEL institute in nitrogen, helium, and super-fluid helium. An essential difference in the experiments are the boundary conditions at the disks[8]. In the low Reynolds number limit, $K_p$ scales as $\mathrm{Re}^{-1}$ which corresponds to the laminar regime. The collapse of the curves in this regime indicates that despite varying the disk boundary condition, the power needed to put the fluid into motion is the same. Above $\mathrm{Re} \simeq 300$ the curves begin to deviate and attain measureably different satu-

7. It appears that the device most resembling that employed by Joule was made by the French company *Flandria*.

8. The disks have curved blades that may either bend with the direction of rotation ("scooping the fluid") or bend away from the direction of rotation ("pushing the fluid"), *cf.* figure 1.3(c)

ration regimes at large Reynolds number. This indicates that for the different disk boundary conditions investigated the price to pay to put the fluid into motion is the same. The disk boundaries conditions of the orange curve produce a much stronger bulk dissipation (due to the formation of Görtler vortices while "scooping" the fluid [27, 28]) with respect to the green curve, and more power is required to maintain the flow. The use of curved blades favoring the creation of vortices is analogous to the presence of baffles that create dissipative eddying behavior leading to the rapid arrest of the rotating flow in Joule's experiment. The pink curves result from the presence of multiple stable states in the von Kármán flow [29]. A symmetric state (fig.1.4b) where the two counter-rotating rolls are evenly spaced between the disks (the case of the orange and green curves), and a symmetry breaking state (fig.1.4c) where one of the rolls dominates the bulk while the other approaches its corresponding disk. The roll dominating the bulk imposes its motion on the flow while the counter-rotating partner struggles to rotate at the angular frequency required by the motor. Thus, more power is required, shifting the value of $K_p$ upwards.

These results indicate that the geometry of the flow is fundamental to understanding its dynamics. This is intuitively known to industrial engineers who have for years understood that certain configurations cost less, in terms of electricity, to operate than others. One aspect of this class of flows that is often mentioned in passing is its inhomogeneous and anisotropic nature, although these aspects are well known [30, 31]. The von Kármán flow has two striking characteristics in its central region: strong shearing between its counter-rotating cells and a stagnation point imposed by the pumping action of the disks. While the turbulence producing properties of these two topologies are well known [32] the former is often cited as the dominating feature of turbulence generation while the latter is often mentioned in passing. Further, in over 25 years since the 1990s when the von Kármán flow became the subject of much experimental work, only one publication [9] has given an estimation of the strain rate in the central zone [33]. This is an unfortunate oversight as a mean strain may correspond to favorable situation for the process of vortex streching [34, 35] which would enhance the dissipative nature of the flow. Indeed DNS have shown that vorticity tends to align with the extensional directions of a straining flow [36, 37] where it is also amplified [38].

## 1.3 Eulerian and Lagrangian turbulence

Many techniques developed in the past 20 years have permitted the measurement of particle trajectories in turbulent flows [39, 40, 41]. Eulerian measurements are made at a given point in space, $\vec{\gamma}$, while Lagrangian measurements follow the trajectory of a marked particle $\vec{X}(t)$. Consider the Eulerian measurement of a velocity at $\vec{\gamma}$ at a time $t^*$: $\vec{v}(\vec{\gamma}, t^*)$. If the position of the trajectory coincides with the Eulerian measurement location: $\vec{X}(t^*) = \vec{\gamma}$, then the Lagrangian velocity $\vec{V}(t) = d\vec{X}(t)/dt$ will be equal to its Eulerian counterpart :

$$\vec{V}(t^*) = \vec{v}(\vec{\gamma}, t^*). \tag{1.7}$$

Temporal derivatives in the Eulerian reference frame are given by the unsteady time derivative $(\partial/\partial t)$. The Lagrangian measurement of the temporal evolution of a

9. To my knowledge...

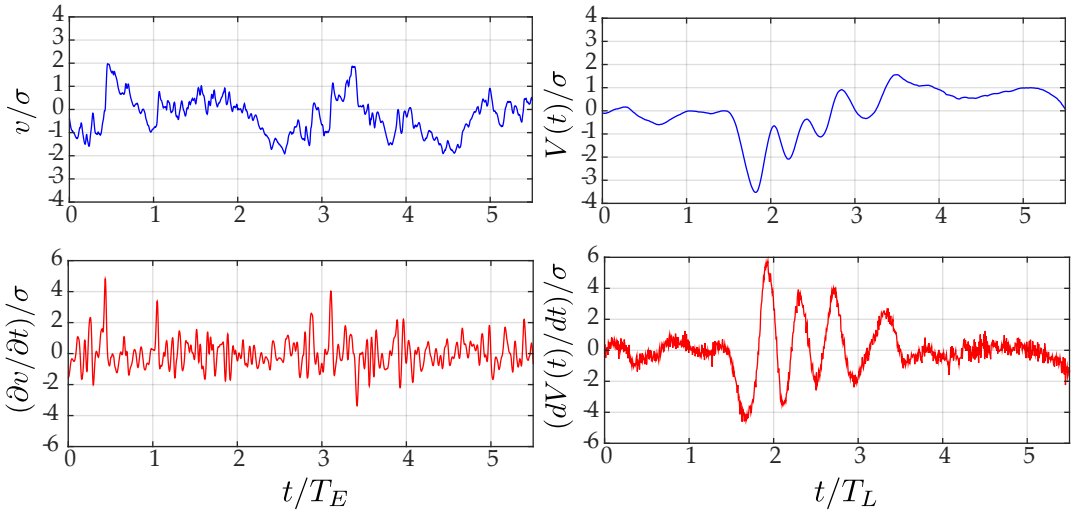


Figure 1.5: Comparison of Eulerian and Lagrangian signals normalized by respective rms values ($\sigma$) measured in the University of Washington Wind Tunnel and ENS de Lyon von Kármán respectively. The Lagrangian signal corresponds to a representative trajectory measured by PTV while the Eulerian signal corresponds to a HWA measurement in the central region of the WT. (a) Eulerian velocity. (b) Velocity along a trajectory. (c) Unsteady temporal derivative of the Eulerian velocity. (d) Acceleration along a trajectory. Lags are normalized by the Eulerian turn-over time ($T_E = \langle v'^2 \rangle / \varepsilon$) and Lagrangian integral time ($T_L$) calculated by integrating the velocity auto-correlation function.

given quantity along the trajectory of a fluid particle and is specified by the material derivative ($D/Dt$). These two are related by a advective term which is given by:

$$\frac{D}{Dt} = \frac{\partial}{\partial t} + \vec{v} \cdot \vec{\nabla}. \tag{1.8}$$

As long as $\vec{v}(\vec{X}, t)$ in the advective term is considered to follow the trajectory it can be said that $d\vec{V}(t)/dt = D\vec{v}(\vec{X}, t)/Dt$ which gives the acceleration along a trajectory.

The fundamental difference between an Eulerian and Lagrangian point of view may be understood considering a Hot Wire Anemometry (HWA) and Particle Tracking Velocitmetry (PTV) measurements. The former gives the Eulerian velocity $v$ and unsteady time derivative $\partial v/\partial t$ at position in space (fig. 1.5 a & c) while the latter gives the Lagrangian velocity $V(t)$ and acceleration $dV(t)/dt$ along a trajectory (fig. 1.5 b & d). These two velocity signals, measured at a fixed location in a wind tunnel, and obtained by PTV in a von Kármán flow are compared in figure 1.5. The Reynolds number is comparable for both experiments ($\mathrm{Re}_\lambda \simeq 225$).

The HWA and PTV results are given for the velocity where the mean value has been removed. The HWA signal displays a steady flow of turbulent structures that rapidly pass through the HWA probe. Fluctuations generally vary around the mean but rarely exceed more than one or two standard deviations. In contrast, the Lagrangian velcocity is relatively steady until the particle enters a vortex and experiences rapid velocity fluctuations. The difference between these two signals lies in the occurence of very strong and rare events [42], such as the vortical motion experienced by Lagrangian particles. Experimental and numerical work has shown

that when calculating spatial and temporal increments of a velocity signal the results become strongly non-gaussian, a phenomenon referred to as *intermittency* [43, 44]. Figures 1.5(c & d) display the evolution of $\partial v/\partial t$ and $dV(t)/dt$. Rare events are present in both signals which is indicative of non-gaussian statistics. However, the intermittency is more visible in the Lagrangian statistics.

## 1.4 A description of inertial particles in turbulence

The equation of motion for an inertial particle was first derived by Basset, Boussinesq, and Oseen ([45, 46, 46]) in the case of a sphere settling in a gravitational field where the fluid forces on the sphere were calculated from the results of an unsteady Stokes flow. Their result was later revisited independently by Maxey & Riley and by Gatignol [47, 48] which led to an equation of movement that is generally considered to be the reference for the motion a small inertial particle in a turbulent environment. The so called *Maxey-Riley-Gatignol equation* is written:

$$m_p \frac{d\vec{V}}{dt} = 3\pi\mu_f d_p(\vec{v} - \vec{V}) + \frac{1}{2}m_f \frac{d(\vec{v} - \vec{V})}{dt} + m_f \frac{D\vec{v}}{Dt} + \frac{3}{2}d_p^2\sqrt{\pi\rho_f\mu_f}\int_{-\infty}^{t} \frac{d(\vec{v} - \vec{V})}{dt}\frac{d\tau}{\sqrt{t-\tau}} + (m_p - m_f)\vec{g}, \tag{1.9}$$

where $\vec{V}$ is the particle velocity, $\mu_f$ is the dynamic fluid viscosity, $d_p$ is the particle diameter, $\rho_p$ and $\rho_f$ are the particle and fluid densities, $m_p$ is the particle mass and $m_f = \rho_f \pi d_p^3/6$ is the mass of fluid displaced by the particle. This equation corresponds to the point particle ($d_p \ll \eta$) limit where the particulate Reynolds number ($Re_p = d_p||\vec{v} - \vec{V}||/\nu_f$) is less than one. Second order corrections in $d_p$, known as Faxen corrections, that take into account the non-uniformity of the fluid flow around the particle may be introduced but are neglected here following numerical evidence against their use for small particles ($d_p \ll \eta$) [49, 50]. The terms on the right hand side are given below as they appear in equation (1.9):

• The Stokes drag force is due to the relative velocities existing between the particle and the fluid. This term is valid in the low particulate Reynolds number limit. The following viscous response time is used: $\tau_p = m_p/3\pi\mu_f d_p$.

• The added mass force is due to the displaced fluid caused by particle motion. It tends to oppose acceleration and deceleration by the particle.

• The pressure gradient term is equivalent to the fluid particle acceleration at the particle's center of mass.

• The history term takes into account the entirety of particle motion in the carrier fluid up to an instant $t$. This term mainly accounts for the interaction of a particle with its own wake.

• The Archimedes force accounts for the compensation of gravity by the particle's buoyancy.

A first approximation of equation (1.9) may be made in neglecting the history term which is valid in flows with a strong mean component. This term is potentially relevant in an isotropic flow where the particle may interact with regions previously perturbed by its own wake [51]. Under the hypothesis that inertial particle trajectories do not stray far from those of fluid particles, *i.e.* $(\vec{V}\cdot\vec{\nabla})\vec{v} \sim (\vec{v}\cdot\vec{\nabla})\vec{v}$, equation (1.9) is rewritten:

$$\frac{d\vec{V}}{dt} = \beta\frac{D\vec{v}}{Dt} + \frac{1}{\tau_p}(\vec{v}-\vec{V}) + \delta\vec{g}, \tag{1.10}$$

where $\beta = 3\rho_f/(\rho_f + 2\rho_p)$ is a density ratio that accounts for the added mass and pressure gradient forces, $\tau_p = d_p^2/12\beta\nu$ is the particle viscous response time, and $\delta = (\rho_p - \rho_f)/(\rho_p + \rho_f/2)$ is the buoyancy ratio. This equation is sometimes referred to as the *beta-Stokes model* and is in general parameterized by three non-dimensional numbers.

Comparing the fluid velocity contribution $\vec{v}/\tau_p$ with gravitational effects $\delta\vec{g}$ one obtains the Rouse number:

$$\mathrm{Rs} = \delta\frac{\tau_p g}{v}, \tag{1.11}$$

where $\tau_p g$ is often referred to as the settling velocity and the presence of $\delta$ accounts for buoyancy effects. The Rouse number compares the settling velocity with characteristic turbulent eddies and can describe the ability of a turbulent flow to either enhance and impede the settling of inertial particles [52, 53, 54].

Normalizing equation (1.10) by the Kolmogorov dissipative scales gives:

$$\frac{d\vec{V}}{dt} = \beta\frac{D\vec{v}}{Dt} + \frac{1}{St}(\vec{v}-\vec{V}) + \frac{1}{\mathrm{Fr}}\hat{\mathbf{e}}_z. \tag{1.12}$$

Two new non-dimensional parameters appear in equation (1.12). The Froude number is defined as:

$$\mathrm{Fr} = \frac{a_\eta}{\delta g}, \tag{1.13}$$

which takes into account gravity effects as well as particle buoyancy with respect to small scale turbulence[55]. The Stokes number is defined:

$$\mathrm{St} = \frac{\tau_p}{\tau_\eta}, \tag{1.14}$$

and describes the particle response with respect to the smallest temporal scales of turbulence.

In the small Rouse number approximation, gravity plays a negligible role and particle dynamics are determined by a combination of Stokes drag, fluid pressure gradients, and added mass forces. The latter two effects are understood by considering two limits of $\beta D\vec{v}/Dt$. First, $\beta = 3$ corresponds to light particles, such as bubbles, which have an added mass force but no inertia ($\rho_p d\vec{V}/dt \ll \rho_f d\vec{V}/dt$) [56, 57]. A particle trapped in a vortex, like the one giving rise to figures 1.5 (b) & (d) which correspond to intense pressure gradients [58], will have a strong contribution in this term. Experimental measurements shows that light particles display acceleration variances that are more than two times that of tracers is the central region of the von Kármán flow [59, 60] and may be even higher when the effects of gravity become strong with respect to the turbulence (small Froude number limit) [55].

Second, particles that are infinitely heavy ($\rho_p \gg \rho_f$), like a rain drop in the atmosphere where $\beta = 0$, reduces the *beta-Stokes* model to:

$$\frac{d\vec{V}}{dt} = \frac{1}{\tau_p}(\vec{v} - \vec{V}), \tag{1.15}$$

which is sometimes referred to as the *minimal model* due to the sole presence of the Stokes drag in the particle dynamics. This equation is often used in DNS studies [61, 11] although the gravitational force is often included [62, 63]. Assuming that the inertial particles evolve along tracer trajectories, which can only be valid in very limited cases, one may take the Fourier transform of equation (1.15) to obtain:

$$\widehat{V}(\omega) = \frac{1}{1 + i\omega\tau_p}\widehat{v}(\omega), \tag{1.16}$$

where $\widehat{v}(\omega)$ is the Fourier transform of the fluid velocity and $\widehat{V}(\omega)$ is that of the inertial particle evolving along a tracer trajectory. Equation (1.15) predicts that a heavy ($\rho_p \gg \rho_f$), point particle ($d_p/\eta \ll 1$) sees a filtered carrier phase velocity field through the transfer function $H = 1/(1 + i\omega\tau_p)$. The particle velocity spectrum $\phi_{_{Vp}}$ is then related to the fluid velocity spectrum $\phi_{_{vf}}$ by:

$$\phi_{_{Vp}} = \frac{1}{1 + (\tau_p\omega)^2}\phi_{_{vf}}. \tag{1.17}$$

Assuming an exponentially correlatd fluid phase velocity auto-correlation function Tchen derived an expression for the particle velocity variance as a function of the fluid velocity variance [64, 65]:

$$\langle\vec{V}^2\rangle = \frac{1}{1 + \tau_p/T_L}\langle\vec{v}^2\rangle, \tag{1.18}$$

where $T_L$ is the Lagrangian auto-correlation time. This relationship predicts that as the particle's inertia increases (increasing $\tau_p$) the velocity fluctuations seen along its trajectory decrease concomitantly, which is consistent with the filtering interpretation above.

The equation derived for the particle velocity spectra (eq. 1.17) indicates that only the high-frequency motion of the carrier phase is filtered out while the low frequency motion remains unchanged. The particle and the fluid tracer have approximately the same history with similar Lagrangian correlations which is equivalent to saying that inertial particles evolve along tracer trajectories. However, fluid line segments in a stationary turbulent fluid have a positive, constant logarithmic rate of lengthening [66, 67] and there is no reason to think that a particle should remain attached to its fluid neighbor indefinitely. In this case, equation (1.15) will take on a stochastic character and its spectrum is not as easily obtained as in equation (1.17). Furthermore, in the large Froude number limit gravitational settling forces heavy particles to rapidly change their fluid-particle neighborhood. Known as the *crossing trajectories* effect [68, 69, 3], this causes heavy inertial particles to have completely different histories than the fluid tracers in their immediate vicinity. In this light, while Tchen's approach provides some interesting insights, it also imposes strict assumptions on inertial particle dynamics which may be difficult to validate in reality.

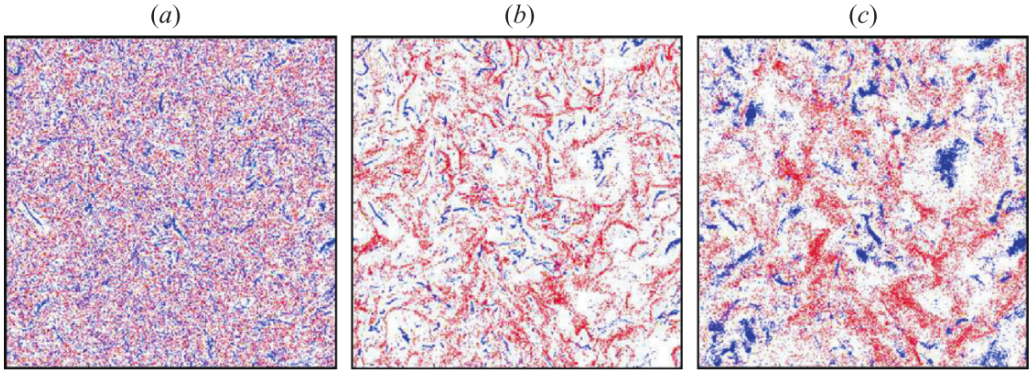


Figure 1.6: Projection of the inertial particles in a 3d DNS [70] onto a slice $19 \times 640 \times 640\eta^3$ at $\mathrm{Re}_\lambda = 180$. (a) St=0.1 (b) St=0.6 (c) St=4. Light particles ( $\beta = 3$) are shown in blue, heavy particles ($\beta = 0$) are shown in red.

### Preferential concentration

Whether using equation (1.10) or equation (1.15), numerical studies have consistently found that inertial particles tend to aggregate and form clusters. Figure 1.6 presents inertial particle data in a DNS of Homogeneous Isotropic Turbulence using equation (1.10) with no gravity for two different particle classes ($\beta = 0$, heavy; $\beta = 3$, light) at three different Stokes numbers ($\mathrm{St} = [0.1,\ 0.6,\ 4.0]$) [70]. At the smallest Stokes number small clusters of each particle class are visible. These clusters grow in size creating characteristic structures: heavy particles tend to form interconnected empty tunnels, whereas bubbles form isolated filamentary structures. As the Stokes number increases further, clustering is impeded when the strongly inertial particles become insensitive to small-scale turbulent fluctuations. Notice that the heavy and light particles, for all the Stokes numbers investigated, form clusters in particular zones of the flow that appear to be mutually exclusive.

This last point is an illustration of the phenomenon of *preferential sampling*. In general the heavy particles tend to be expelled (or centrifuged) from strongly vortical regions and light particles tend to be attracted to them. This behavior can be seen in the beta-Stokes model if one considers the limit where $\mathrm{St} \ll 1$ where inertial particles may be seen to approximately follow fluid trajectories. The particle acceleration is then: $\vec{a} = d\vec{V}/dt \simeq D\vec{v}/Dt$. Using this relationship in equation (1.12) gives:

$$\vec{V} = \vec{v} - \mathrm{St}(1-\beta)\vec{a}. \tag{1.19}$$

The divergence of $\vec{V}$ is written,

$$\vec{\nabla}\cdot\vec{V} = -\mathrm{St}(1-\beta)\left(||S||^2 - ||\Omega||^2\right), \tag{1.20}$$

where $||S||$ and $||\Omega||$ are the local strain and rotation-rate tensors, respectively [71]. Particles heavier than the fluid ($0 < \beta < 1$) tend to accumulate ($\vec{\nabla}\cdot\vec{V} < 0$) in regions where the strain-rate dominates the vorticity. Contrastingly, particles lighter than the fluid ($1 < \beta < 3$) tend to accumulate in regions of intense vorticity. Both behaviors are coherent with the phenomenon of preferential sampling described above. Equation (1.20) also predicts a monotonic evolution in the intensity of clustering

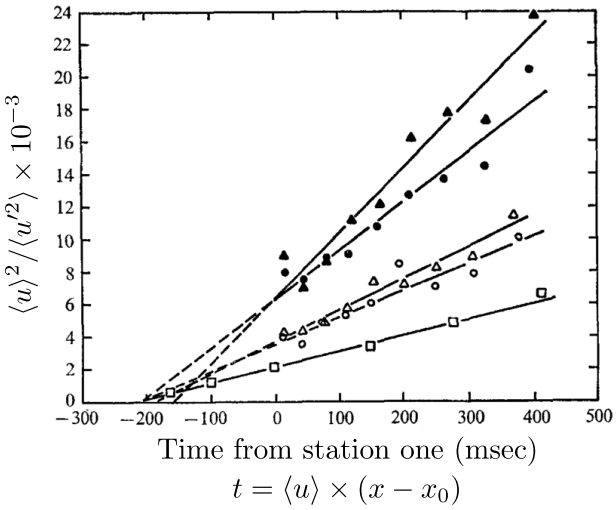


Figure 1.7: Turbulence and particle decay. □: turbulence ○: hollow glass (St=0.145) △: corn (St=1.72) ●: solid glass (St=3.85) ▲: copper (St=4.21). The Stokes number is calculated based on the Kolmogorov timescale at $t = 0$ [77].

with the Stokes number (compare figures 1.6a & b). However, the validity of equation (1.19) only holds for small Stokes numbers and this model cannot predict the subsequent decrease in clustering for large Stokes numbers. For large Stokes numbers, particles respond slowly to the flow and may only feel intermittent pulses from the turbulence. At intermediate Stokes numbers the particles are in resonance with the fluid flow and may reach a maximum in clustering near St $\sim$ 1, in agreement with a vast amount of literature. [72, 73, 74, 75, 76].

## 1.5 The particle dispersion problem in an inhomogeneous flow

The turbulence produced in a Wind Tunnel (WT) is often assumed to be homogeneous and isotropic. This may be true, but only locally. In reality, the grid-produced turbulence is advected through the WT where the absence of mean gradients preclude any further turbulence production. As a consequence, there is a region in the WT (the "initial period") where the turbulent energy follows the inverse linear decay law, $\langle u'^2\rangle \propto (x - x_0)^{-1}$ [78] where $x$ is the distance from the grid, and $x_0$ is the location of the virtual origin of decay, and $u' = u - \langle u\rangle$. The inhomogeneity of the WT flow is generally measured by the quantity $\langle u\rangle^2/\langle u'^2\rangle$, where $u$ is an Eulerian measurement of the velocity where the mean flow that does not depend on location and the variance does. Figure 1.7 plots this decay after the transformation $t = \langle u\rangle \times (x - x_0)$ [77]. The positive slope of the curves indicate that $\langle u'^2\rangle$ is indeed decaying. It is interesting to note that Snyder and Lumley seeded different inertial particles into the flow with Stokes numbers: St=$[0.15, 1.72, 3.85, 4.21]$ and the rate of decay increases with the Stokes number. The velocity fluctuations are much more inhomogeneous for the inertial particles than for the carrier flow.

How fast does a cloud of particles spread when released from an initial location given that the underlying flow is inhomogeneous? The question might resemble

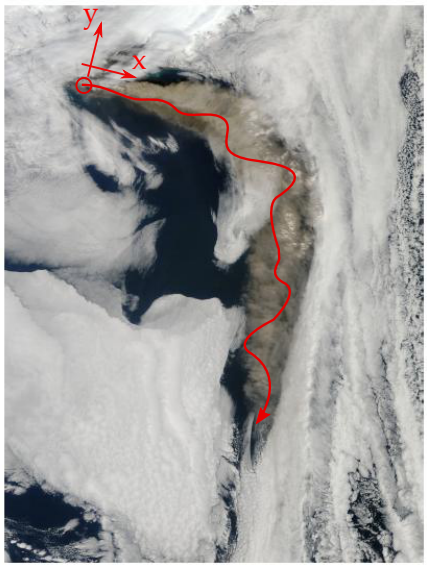


Figure 1.8: Eruption of the volcano Eyjafjallajökull in Iceland during May 2010.

the situation of the ashen emissions of a volcano (figure 1.8). One way to proceed would be to follow the steps taken by G.I. Taylor in 1921 with his seminal paper, "Diffusion by Continuous Movements" [79], where the limiting behavior of the mean square displacement of a fluid particle in turbulence is derived.

The position of a particle (which is considered to be be a passive tracer) is:

$$\vec{X}(t) = \big[x(t), y(t), z(t)\big], \tag{1.21}$$

while the Lagrangian velocity is given by:

$$\vec{V}(t) = \vec{v}(\vec{X}(t), t) = \big[u(\vec{X}(t), t), v(\vec{X}(t), t), w(\vec{X}(t), t)\big]. \tag{1.22}$$

The $x$ direction will be considered to be in the down stream direction, the $y$ direction will be the lateral direction, and $z$ will be aligned with gravity. Assuming that the gravity has no influence on dispersion (an admittedly simplistic hypothesis) and that the downstream location is simply advected downstream, only the lateral position is relevant to the question at hand and is calculated:

$$y(t) = y_0 + \int_0^t v(\vec{X}(t'), t')\mathrm{d}t'. \tag{1.23}$$

and its displacement has the notation: $\sigma(t) = y(t) - y_0$. At a given time $t$, $y(t)$ may be considered as a random variable with a mean, variance, and a probability density function. As the problem is statistically symmetric about the cloud's center line (until it is strongly deviated later on) the mean of $y(t)$ is zero. However the probability distribution function of the position $y(t) = \widetilde{y}$ in theory and experiments are often close gaussian:

$$\mathrm{PDF}(\widetilde{y}) = \frac{1}{\big(\langle\sigma(t)^2\rangle 2\pi\big)^{1/2}} \exp\Big(-\frac{\widetilde{y}^2}{2\langle\sigma(t)^2\rangle}\Big). \tag{1.24}$$

Thus to fully characterize the characteristic width of the growing cloud, its variance must be calculated.

Using the identity $2\sigma(t)v(\vec{X}(t),t) = d\sigma(t)^2/dt$, one may take an ensemble average $\langle\cdot\rangle$ over a collection of trajectories with the same initial position. Integrating the left hand side with respect to $t$ gives:

$$\langle\sigma(t)^2\rangle = 2\int_0^t \left\{ \int_0^{t'} \left\langle v'\left(\vec{X}(t''),t''\right)v'\left(\vec{X}(t'),t'\right)\right\rangle \mathrm{d}t''\right\}\mathrm{d}t'. \tag{1.25}$$

The above equation indicates that the dispersion $\langle\sigma(t)^2\rangle$ of a particle cloud is known in terms of its two-time Lagrangian velocity auto-covariance. Further deductions are most simply made in the case of homogeneous isotropic turbulence (as opposed to the decaying turbulence presented above). In this case, introducing the velocity autocorrelation function into equation (1.25) and integrating by parts gives:

$$\langle\sigma(t)^2\rangle = 2\langle v^2\rangle \int_0^t (t-\tau)R_L(\tau)\mathrm{d}\tau. \tag{1.26}$$

From this equation Taylor deduced that:

1. For times $\tau$ smaller than the Lagrangian velocity integral time scale ($\tau \ll T_L$), $R_L(\tau) \sim 1$ and the mean square displacement is written : $\langle\sigma(t)^2\rangle = \langle v^2\rangle t^2$.
2. For very large times ($t \gg T_L$): $\langle\sigma(t)^2\rangle = 2\langle v^2\rangle T_L t$.

For short times particles are spreading out ballistically ($\sim t^2$) and this dispersion is proportional to the velocity variance. At long times the behavior is diffusive and dependent on the large scale quantities of the flow ($T_L$). These results are particularly interesting from the perspective of the PDF in equation (1.24) which is approximately gaussian but whose width evolves in time due to the presence of $\langle\sigma(t)^2\rangle$. In the framework of dispersion by continuous movements, there is a direct relationship between a scalar field $\phi$ (smoke, fluorescein - fig. 1.1 - or even heat in certain cases) and the probability that the position $y(t)$ takes a value $\widetilde{y}$. The mean value of the scalar $\langle\phi(\vec{X}(t),t)\rangle$ is proportional to the probability density of the event $y(t) = \widetilde{y}$ given that both the particle and scalar originate from the source. As a consequence $\langle\phi(\vec{X}(t),t)\rangle$ should also take a transversally gaussian profile.

Similarly, experimental measurements of a thermal wake in a turbulent round jet [80] indicate ballistic growth of the temperature and perhaps the beginnings of a $\sqrt{\langle\sigma(t)^2\rangle} \propto t^{1/2}$ diffusive regime. However, the self-similarity of the jet may render the thermal plume less sensitive to the decay. A collection of thermal wake data in turbulent wind tunnels captures a short ballistic regime and a sub-diffusive ($\sqrt{\langle\sigma(t)^2\rangle} \propto t^{\alpha}$, $\alpha < 1/2$) regime [81, 82]. S. Pope demonstrated that the classic turbulent diffusion model, where molecular diffusivity is enhanced by a "turbulent diffusivity", is incapable of predicting the short time ballistic regime [83]. Along with M.S. Anand, he built a stochastic model for $v$ and with a relaxation rate in the drift term characterized by the kinetic energy and dissipation rate of the flow [84]. The subtlety of his model was that while the dissipation was constant the kinetic energy varied along the wind tunnel (as in fig. 1.7). In so doing he was able to reproduce the experimental results finding a sub-diffusive process with $\alpha = 0.34$, the power being small than 1/2 due the turbulent decay.

Figure 1.8 was purposefully selected for the topological peculiarity occuring towards the latter half of the highlighted trajectory. It appears as if the cloud of ash

emitted from Eyjafjallajökull encounters a barrier before being redirected onward. The von Kármán flow displays similar stagnation-point features (fig. 1.4 c & d). While an inhomogeneous Langevin equation lies outside the scope of this dissertation, substituting a model for the Lagrangian velocity autocovariance in a decaying, or growing, turbulence into equation (1.25) to study tracer and inertial particle dispersion in the von Kármán flow is a possibility.

# Chapter 2

# Experimental methods

## 2.1 Introduction

All experimental data of the following chapters have been obtained by performing Particle Tracking Velocimetry (PTV) in a large von Kárm an flow. The experimental device as well as the PTV algorithms are presented in section 6.1. Examples of the 3d3c (3 components given in 3 dimensions) maps for velocity and acceleration as well as the respective auto-correlation correlation curves are given in section 2.3. The denoising technique applied throughout the manuscript to acceleration statistics is then rigorously presented. Section 2.4 describes the method and its implementation which is assessed by the numerical benchmark in section 2.5. The method is then applied to both experimental measurements and the results are compared to what is obtained by filtering considerations in section 2.6. A general discussion and conclusion is then given (section 2.7).

## 2.2 Shadow Particle Tracking Velocimetry (S-PTV)

In order to study [1] particle dynamics in a large portion of a von Kármán flow, a new PTV technique was optimized following previous work on the experimental apparatus (fig. 2.1, [86]). Observant readers will notice that the von Kármán apparatus pictured is a larger version (20x20x20 $cm^3$ used in previous investigations ([87, 86]) of the one used in this manuscript (15x15x20 $cm^3$). A smaller device was chosen in order ensure the salient features of the mean structure where confined to an experimentally accessible region, in effect "miniaturizing" the flow. Additionally, a square cylinder geometry was chosen with the hope of disrupting the vortices that circumscribe the walls and avoiding the known bistable nature of the flow in the circular cylinder geometry ([88]). As will be seen in chapter 3, we were not successful in this endeavor; a failure which nevertheless lead to unforeseen successes.

### 2.2.1 Experimental setup

The experimental apparatus is a von Kármán flow that has been used previously [89] with a square cross-section of 15 cm on each side. Two bladed discs of radius $R = 7.1$ cm counter-rotate at constant frequency $\Omega$ (figure 3.1 (a)) and are 20

1. The following sections were the subject of an article [85] detailing the experimental method used here and has been reproduced here.

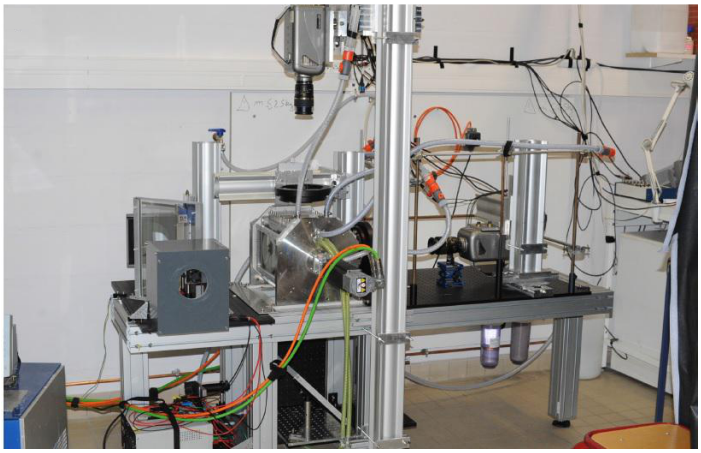

Figure 2.1: Photograph of the S-PTV setup used to study the von Kármán Flow.

cm apart. The flow has a strong mean spatial structure arising from the counter rotation of the disks. The azimuthal component resulting from this forcing is of order $2\pi R\Omega$ near the disks' edge and zero in the mid-plane ($z = 0$), creating a strong axial gradient (figure 3.1 (a)). The disks also act as centrifugal pumps ejecting the fluid radially in their vicinity, resulting in a large-scale poloidal recirculation with a stagnation point in the geometrical centre of the cylinder (figure 3.1 (b)). Using water to dilute an industrial lubricant, Ucon$^{\text{TM}}$, a mixture with a viscosity of 8.2 $\text{m}^2\text{s}^{-1}$ and a density of $\rho = 1000$ $\text{kg.m}^{-3}$ allows the production of an intense turbulence with a Taylor-based Reynolds number $R_\lambda = 200$ and a dissipative length $\eta = 130$ microns (see table 2.1 for more details on the flow parameters). Particle tracking of Lagrangian tracers (250 $\mu$m polystyrene particles with density $\rho_p = 1060\text{kg.m}^{-3}$) is performed in a large volume $6 \times 6 \times 5.5$ $\text{cm}^3$ centered around the geometrical centre ($(x, y, z) = (0, 0, 0)$) of the flow with 2 high-speed video cameras (Phantom V.12, Vision Research, 1Mpix@7kHz) with a resolution $800 \times 768$ pixels, and a frame rate up to $f_s = 12$ kHz. Such a sampling frequency is sufficient for resolving particle acceleration, calculated by taking the second derivative of the trajectories.

The camera setup is inspired from a previous work [89] and is depicted in figure 3.1 (c). It consists of 2 identical optical configurations with a small LED located at the focal point of a large parabolic mirror (15 cm diameter, 50 cm focal length) forming 2 collimated beams which are perpendicular to each other in the measurement volume. A converging lens and a diaphragm are used to make the LED a better point-like source of light. This large parallel ray of light then reflects on a beam splitter and intersects the flow volume before being collected by the camera sensor using a doublet consisting of a large lens (15 cm in diameter) and the camera objective. All optical elements are aligned using large (home made) reticules which also precisely measure the magnification in each arrangement. When placing an object in the field of view, it appears as a black shadow on a white background corresponding to the parallel projection of the object on the sensor. The particle size and shape do not depend on the object-to-camera distance, as opposed to classical lighting schemes where the apparent object size is a decreasing function of the object-to-camera distance. When particles are tracked, camera 1 will then provide their $(x_1, z_1)$ 2d positions while camera 2 will measure their $(y_2, z_2)$ positions. The $z$

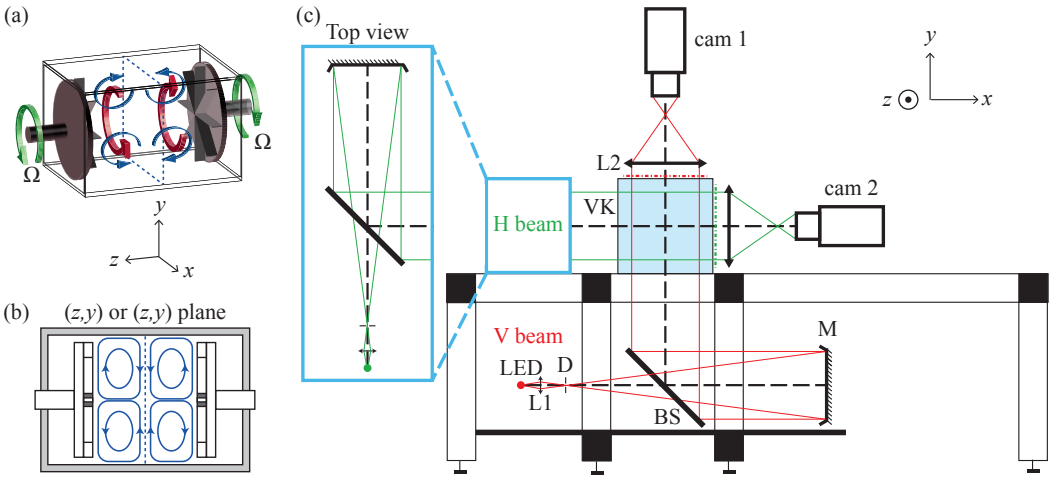


Figure 2.2: (a) Sketch of the counter-rotating von Kármán flow. Arrows indicate the topology of the mean flow, the dashed line indicates the mid-plane of the vessel. (b) Schematic cut of the vessel along the $(z, x)$ or $(z, y)$ plane. (c) Optical setup for S-PTV with 2 identical optical arrangements forming an angle $\theta = 90$ degrees (only the vertical arm is described). The 1W LED source is imaged in the focus of a parabolic mirror to form a large collimated beam. A converging lens and a diaphragm are used to make the LED a better point-like source of light. Light is propagating through the flow volume using a beam splitter (BS) before being collected using a 15 cm large lens whose function is to redirect the light into the camera objective of the camera. The optical system [$L_2$+objective] is focussed on the output face of the vessel marked with a dashed-dotted line.

coordinate is redundant and the equation $z_2 = az_1 + b$ where $a$ and $b$ accounts for slight differences in the magnification and centering between both arrangements, respectively.

### 2.2.2 Tracking algorithms

Given the magnification of the setup (1/4, 1px equals 90 $\mu$m), the depth of field of the optical arrangement is larger than the experiment. As both beams do not overlap on the entire flow volume, particles situated in one arm but outside the measurement volume can give a well contrasted image on one camera while not being seen by the other. Such a situation could lead to a wrong stereo-matching event when many particles are present. This is illustrated on figure 2.3 (a), where the shadows left by two particles situated at the exact same $z$ position but outside of the beams overlap (black dots) could be interpreted as one particle within the overlapping region (dashed circle). To mitigate these errors, 2d trajectories for each camera are constructed using the $(x_1, z_1)$ and $(y_2, z_2)$ coordinates separately. Once tracked in time, these trajectories may be stereo-matched instead of individual particle positions. One may note that while typical PTV algorithms perform stereo-matching on particle positions followed by trajectory construction, it is possible to proceed in the opposite order. The advantage of this method is that neither stereo-matching nor tracking errors are made, as will be detailed below. Due to the necessity of trajectory occurrence in the overlapping beam area, one must track many more 2d

| $\Omega$ | $v'_x$ | $v'_y$ | $v'_z$ | $v'$ | $\tau_\eta$ | $\eta$ | $\varepsilon_m$ | $\varepsilon$ | $R_\lambda$ | $Re$ |
|---|---|---|---|---|---|---|---|---|---|---|
| Hz | m.s$^{-1}$ | m.s$^{-1}$ | m.s$^{-1}$ | m.s$^{-1}$ | ms | $\mu$m | W.kg$^{-1}$ | W.kg$^{-1}$ | - | - |
| 4.2 | 0.39 | 0.37 | 0.24 | 0.34 | 2.9 | 162 | 4.2 | 1.0 | 175 | 16200 |
| 5.5 | 0.50 | 0.49 | 0.33 | 0.45 | 2.0 | 130 | 8.5 | 2.1 | 200 | 21200 |
| 6.9 | 0.62 | 0.62 | 0.41 | 0.56 | 1.5 | 111 | 15.5 | 3.6 | 225 | 26700 |

Table 2.1: Parameters of the flow. $\Omega$, rotation rate of the discs; the dissipative time-scale is estimated from the zero-crossing ($t_0 = (t_{0x} + t_{0y} + t_{0z})/3$) of each component in the acceleration auto-correlation function: $t_0 \simeq 2.2\tau_\eta$ [90, 33, 60], the dissipation rate is estimated $\varepsilon = \nu/\tau_\eta^2$ and dissipative length-scale is $\eta = (\nu^3/\varepsilon)^{1/4}$, $\varepsilon_m$, dissipation rate obtained from the power consumption of the motors. The root mean square ($rms$) velocities are obtained at the geometrical centre of the flow using data points situated in a ball with a 1 cm radius. The Taylor-based Reynolds number is estimated as $Re_\lambda = \sqrt{15v'^4/\nu\varepsilon}$ with $v' = \sqrt{({v'_x}^2 + {v'_y}^2 + {v'_z}^2)/3}$. The large scale Reynolds number is $Re = 2\pi R^2\Omega/\nu$. The kinematic viscosity of the water-Ucon$^{\text{TM}}$ mixture is $\nu = 8.2\ 10^{-6}$ m$^2$s$^{-1}$ with a density $\rho = 1000$kg m$^{-3}$.

trajectories than are stereo-matched. One last drawback is the projection of 3d positions into a plane, which strongly decreases the inter-particle distance making apparent particle overlap an issue when the particle diameter becomes large with respect to the effective measurement volume. However, the presence of a redundancy in the z coordinate may be used to overcome such indetermination when the apparent proximity results only from projection.

A 2d tracking scheme is implemented using using a 4 Frames Best Estimate method inspired from previous works. [40, 91, 92]. Stereo-matching is then performed by identifying trajectories with $z_1(t) \simeq z_2(t)$ using the relation $z_2 = az_1 + b$ as shown in figure 2.3 (b). This key relation is determined recursively using a dilute ensemble of particles for which an initial identification of a single pair of 2d trajectories allows a first estimate of the relationship between $z_2$ and $z_1$. As more trajectories are found, the affine relationship is refined until the maximum possible amount of trajectories for a single experiment is obtained. In this recursive manner, the tracking algorithm is self-calibrating. Here the parameters are $a = 0.98$, $b = 15.6$ px estimated from 1900 matched trajectories, corresponding to 6 $10^6$ data points as shown in figure 2.3 (c). Together with the pixel-to-mm conversion from one of the cameras, this method provides all relevant information about particle positions in laboratory coordinates. By taking only trajectories that are long enough to ensure a proper stereo-matching (typically 70 time-steps, approximately $2.5\tau_\eta$), the inclusion of any anomalous trajectories is prevented. Such an occurrence becomes increasingly unlikely as the trajectory duration threshold is increased. A false trajectory can only occur when the relationship $z_2 = az_1 + b$ leads to an indetermination when particles are close to colliding, an extraordinarily rare event in dilute situations. After tracking and stereo-matching each pair of movies gives an ensemble of trajectories as shown in figure 2.3 (d).

Once obtained, particle trajectories may be used to calculate velocity and acceleration statistics. Depending on the number of pixels constituting a particle's apparent diameter on the cameras, more or less noise may be introduced into the determination of its position in 3d space. This noise then propagates through the derivatives and is amplified by each successive one. The standard denoising tech-

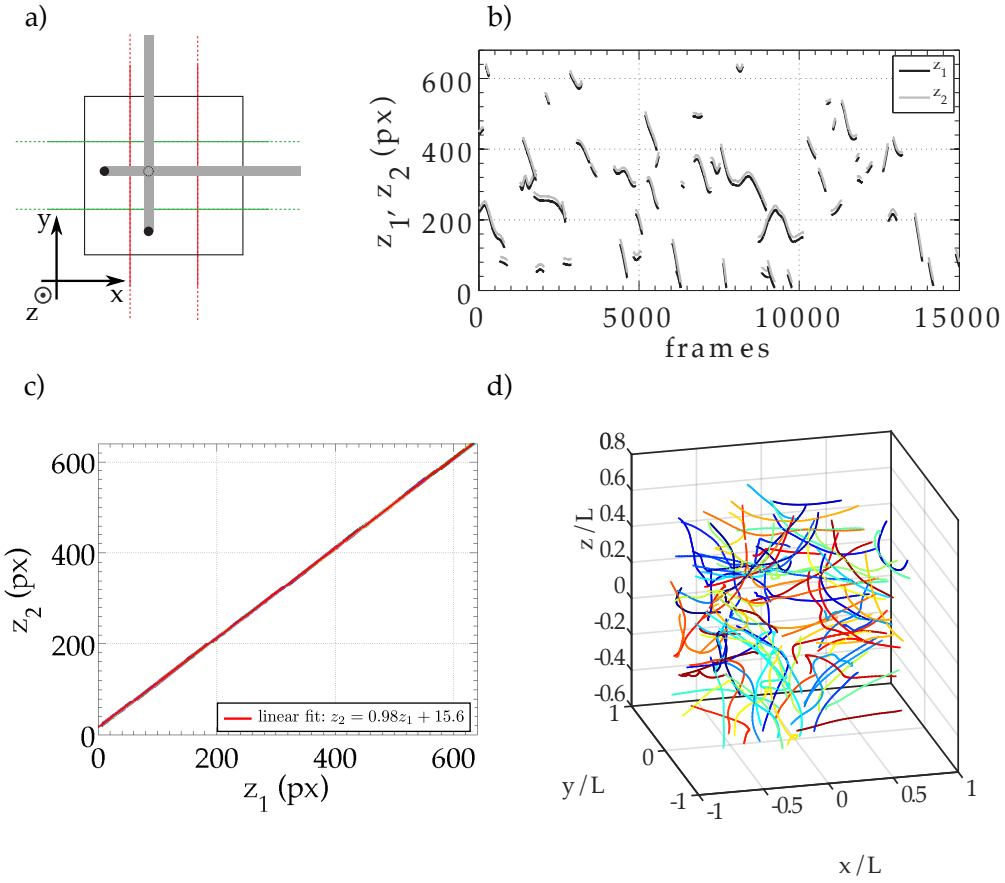


Figure 2.3: (a) Scheme of the intersecting parallel light beams showing individual particle stereo-matching is not reliable. The black dots are two particles at the same $z$ position outside of the beam overlapping region and the dashed circle is a particle at the same $z$ position within the region (both situations being measured identically by the cameras). (b) Time evolution of the raw $z$ (redundant) coordinate of the same particles as obtained with 2d tracking with cam1 and cam2. Only 38 matched trajectories are plotted. (c) Affine relation between $z_2 = az_2 + b$ ($a = 0.98$, $b = 15.6$ px) measured with 1900 trajectories corresponding to 6 $10^5$ data points. (d) Random sample of 150 trajectories in the vessel obtained from the same movie.

nique is to filter trajectories with a gaussian kernel [40] which invariably requires the choice of the filter's width. The effect of this choice on velocity (respectively acceleration) is plotted in figure 2.4(a) (resp. figure 2.4b). The velocity statistics are relatively resistant to the growing filter width indicating that the velocity carries relatively little noise. However, the acceleration displays a strong sensitivity to filter length, as seen by the strong peak at small filter widths (fig. 2.4 b). Filtering over only a few time steps leaves a massive amount of noise in the signal and unrealistic values are obtained. To estimate of the acceleration *rms*, a linear extrapolation from the linear portion of the filtered data ($w/\tau_\eta \gtrsim 0.4$) gives the *rms* value at $w/\tau_\eta = 0$. However, this technique has a drawback of being subjective; there is no criteria for where the linear region begins and it may change for different positions in the flow.

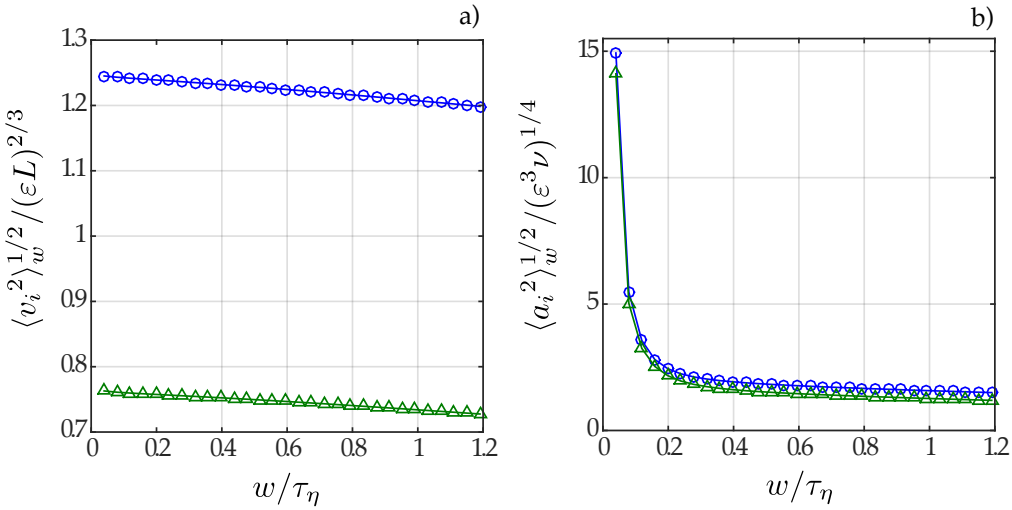


Figure 2.4: Effect of filter with ($w$) on calculating velocity (a) and acceleration (b) fluctuations for trajectories filtered with a Gaussian kernel $K = A_w \exp(-t^2/2w^2)$ where $A_w$ is a normalization factor. Velocity statistics are normalized using Taylor's dissipation rate estimate [34] and acceleration statistics is normalized using the Heisenberg Yaglom [93, 94] $x$ component: ○. $z$ component: △.

For these reasons, classical filtering methods are not practical for strongly inhomogeneous flows. Moreover, this technique provides little certainty as to how much of the actual signal is unwittingly removed when choosing a given filter length. An *objective* determination of acceleration variance is the object of section 2.4.

## 2.3 Flow measurements

The measurement volume ($6 \times 6 \times 5.5$ cm$^3$) covers more than an integral scale ($L_v = \mathrm{v}'^3\epsilon^{-1} \simeq 4.8$ cm) in all directions, and from this point of view it is expected to be inhomogeneous. A large number of trajectories are then need to converge spatially and temporally conditioned statistics . Over 200 pairs of movies with a duration of 1.3 seconds at 12kHz are recorded which gives access to nearly $\mathcal{O}(1000)$ tracer trajectories per film. A statistical ensemble of $\mathcal{O}(10^5)$ trajectories with mean durations $\langle t\rangle \sim 0.25/\Omega$ permits the spatial convergence of both Eulerian and Lagrangian statistics. The flow properties are obtained from the PTV data and are given in table 2.1. The fluctuating velocity of the flow is found to be proportional to the propeller frequency $\Omega$ (table 2.1) which is because the flow is produced by inertial steering using bladed discs and the turbulence becomes fully developed, provided $Re = \frac{2\pi R^2\Omega}{\nu} > 4000$ [88]. The turbulent energy dissipation rate is estimated in figure (2.5) with the formula: $\varepsilon_m = 2(P_{water} - P_{air})/M$ where $P$ is the power consumption of one motor and $M$ is the total mass of fluid [95]. This estimation takes into account mechanical friction but may slightly overestimate the global dissipation rate. Note that this estimation is made in water while the experiments are conducted with kinematic viscosities roughly 8.2 times larger than water. Previous work has shown that changing the viscosity by less than a factor a 10 has minimal effect on the power required for a given rotation frequency [86] . Injected power

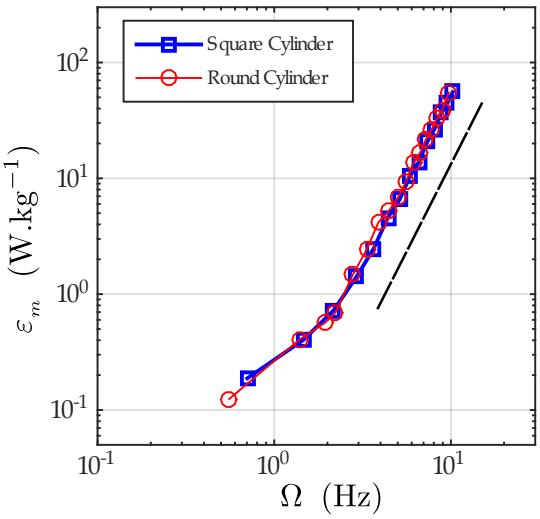


Figure 2.5: Estimation of injected power ($\varepsilon_m$) into the von Kármán flow ($\nu = 10^{-6}\mathrm{m}^2.\mathrm{s}^{-1}$) plotted against impeller rotation frequency ($\Omega$) for the present square cylinder set-up (□) and a von Kármán flow with a comparable volume with round cylinder geometry (○). The dashed line indicates an $\Omega^3$ power law and is indicative of the fully developed turbulence regime [96].

estimates are given for a von Kármán flow in circular cylinder with a similar aspect ratio: $w/\ell \sim 0.75$.

Interestingly, the global power injected by the motors ($\varepsilon_m$, fig. 2.5) is not a good prediction of the local dissipation at the center, $\varepsilon \neq \varepsilon_m$. Other experiments in slightly different geometry (a round cylinder) have shown the opposite: the global dissipation rate estimated by the power consumption of the motors gives a good prediction of the acceleration correlation time in the center of the flow [95]. Physically, a lower dissipation rate at the center of the square cylinder flow is likely due to the presence of walls that enhance dissipation in their corners. This enhancement is absent in a round cylinder geometry leading to larger dissipation rates at the center of the flow. The zero crossing of the acceleration auto-correlation function gives a classic estimation of the dissipative scales by $t_0 = 2.2\tau_\eta$ [90]. Measurements in a pure water flow at $\Omega = 6.9$ Hz in both geometries give $t_0 = 0.70$ ms in the a square section and $t_0 = 0.58$ ms in a round section. The differences in acceleration correlation time indicates that the dissipation rate ($\varepsilon = (\nu/\tau_\eta)^{1/2}$) is indeed smaller at the center of the square cylinder von Kármán flow than in the round cylinder.

### 2.3.1 3d Eulerian flow

The 3d particle tracking yields a set of trajectories, each containing the temporal evolution of Lagrangian velocity at the particle position. Based on this ensemble of trajectories, one may reconstruct the mean velocity field in 3d $\langle\vec{v}\rangle(x,y,z) = (\langle v_x\rangle, \langle v_y\rangle, \langle v_z\rangle)$ and the rms fluctuations of each velocity component $(v'_x, v'_y, v'_z)$.[2] The same approach is taken for the mean acceleration field $\langle\vec{a}\rangle(x,y,z) = (\langle a_x\rangle, \langle a_y\rangle, \langle a_z\rangle)$ and the rms fluctuations of each velocity component $(a'_x, a'_y, a'_z)$. This is achieved by an Eulerian conditioning of the Lagrangian dataset

2. In the chapters to come films will be separated into statistical ensembles. Here, all the films are used in one ensemble.

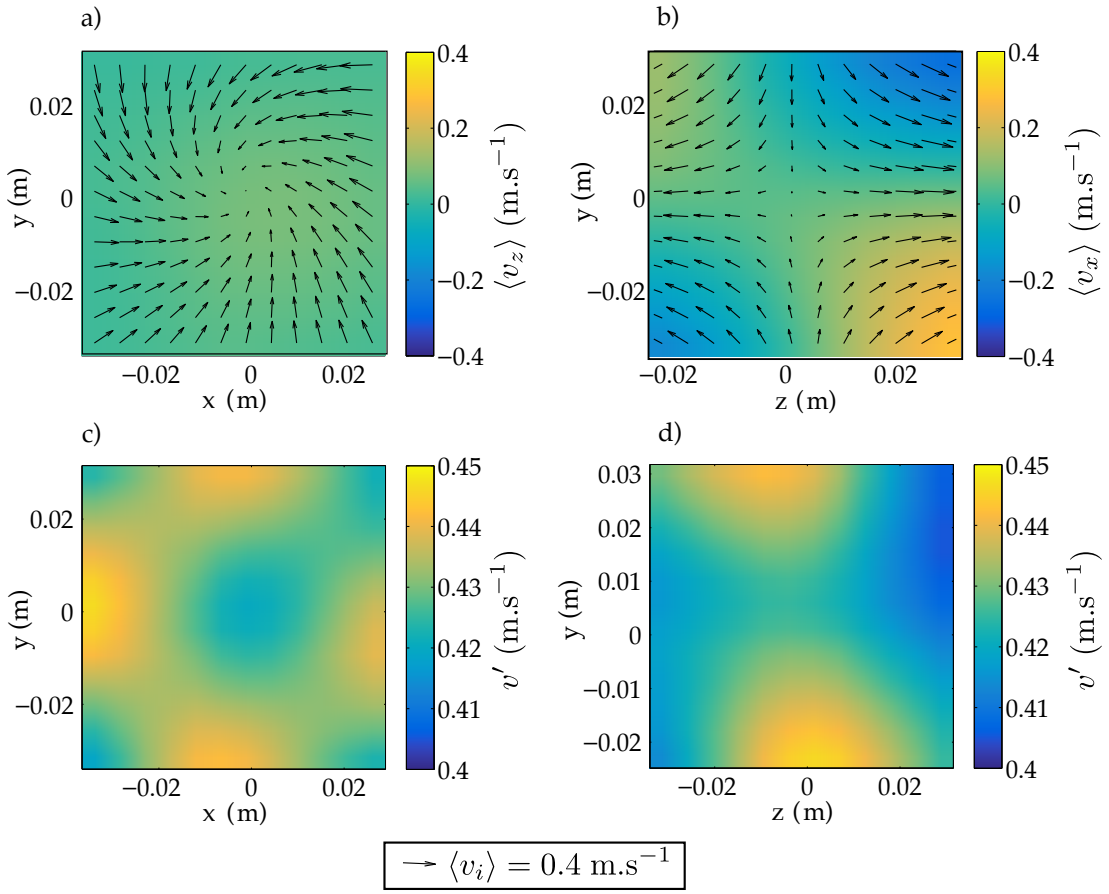


Figure 2.6: Cuts of the 3d reconstructed Eulerian mean velocity (a,b) field and rms velocity (c,d). The reconstruction is achieved by computing the mean $\langle\ \vec{v}\ \rangle$ and rms values $(v'_x, v'_y, v'_z)$ of the velocity in each bin of a $12^3$ cartesian grid. (a) $\Pi_{xy} = (x, y, z = 0)$ plane. Arrows are $(\langle v_x \rangle, \langle v_y \rangle)$, the color coding for the $\langle v_z \rangle$. (b) $\Pi_{yz} = (x = 0, y, z)$ plane. Arrows are $(\langle v_y \rangle, \langle v_z \rangle)$, the color coding for the $\langle v_x \rangle$. (c) rms value of velocity fluctuations $v' = \sqrt{({v'_x}^2 + {v'_y}^2 + {v'_z}^2)/3}$ in the $\Pi_{xy} = (x, y, z = 0)$ plane. (d) rms value of velocity fluctuations in the $\Pi_{yz} = (x = 0, y, z)$ plane.

on a $12^3$ cartesian grid, which corresponds to a spatial resolution of 5 mm in each direction. The choice of the grid size must satisfy several criteria: it must be small as compared to the typical scale of the mean flow properties (here $L_v \sim 4.8$ cm), but large enough so that statistical convergence is achieved. Here the grid size was chosen so that there are at least $\mathcal{O}(1000)$ trajectories across each bin which is enough to converge both the mean and rms values.

Figure 2.6(a,b) display two cross-sections of the reconstructed mean flow in two perpendicular planes, the mid plane $\Pi_{xy} = (x, y, z = 0)$ and $\Pi_{yz} = (x = 0, y, z)$, an horizontal plane containing the axis of rotation of the discs. A mean flow structure that is close to the schematic view of figure 3.1 (a) is observed. The flow is almost radial and convergent with $\langle v_z \rangle \sim 0$ in $\Pi_{xy}$, with a $z$ component which reverses under the transformation $z \to -z$ (figure 2.6(b)). A strong $y$-component of the velocity in $\Pi_{yz}$ is also observed and reverses under the transformation $y \to -y$ which corresponds to the differential rotation imposed by the discs. These cross-sections also reveal that the flow has the topology of a stagnation point at the

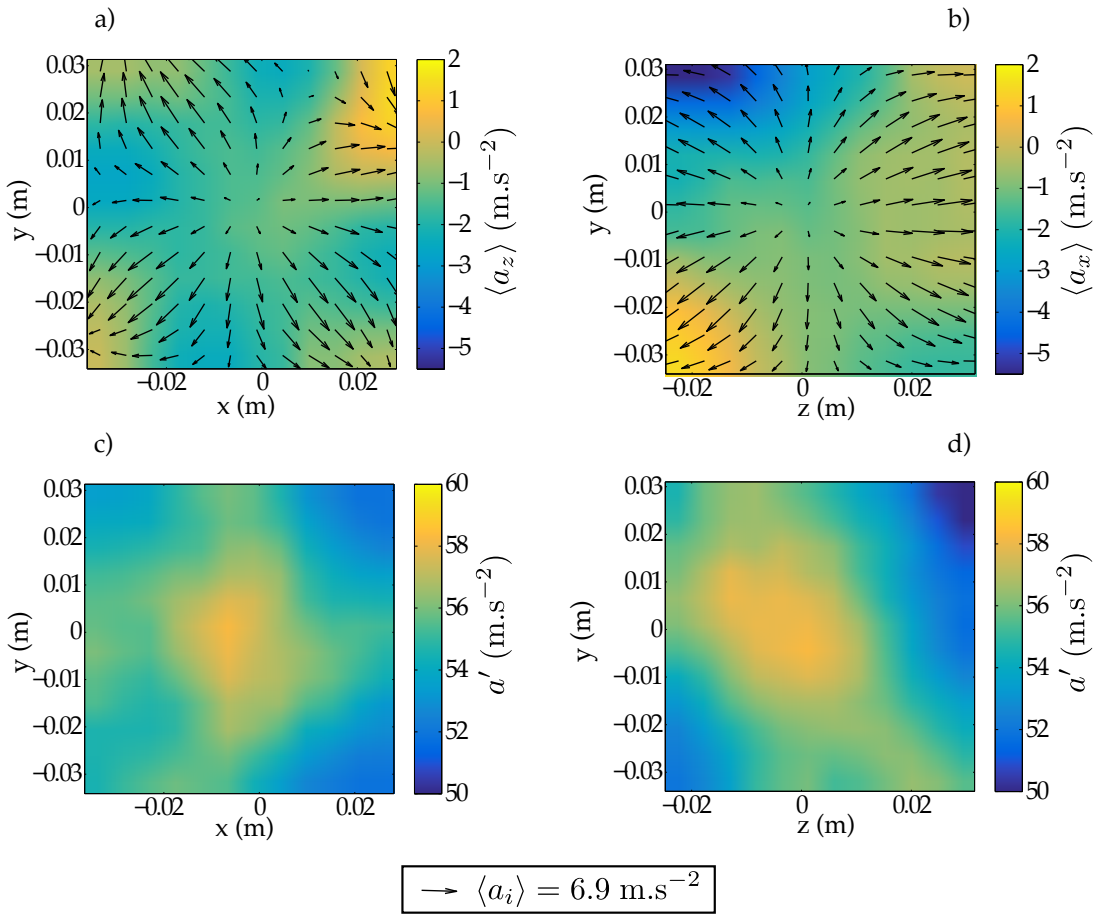


Figure 2.7: Cuts of the 3d reconstructed Eulerian mean acceleration (a,b) field and rms acceleration (c,d). The reconstruction is achieved by computing the mean $\langle\ \vec{a}\ \rangle$ and rms values $(a'_x, a'_y, a'_z)$ of the acceleration in each bin of a $12^3$ cartesian grid. (a) $\Pi_{xy} = (x, y, z = 0)$ plane. Arrows are $(\langle a_x \rangle, \langle a_y \rangle)$, the color coding for the $\langle a_z \rangle$. (b) $\Pi_{yz} = (x = 0, y, z)$ plane. Arrows are $(\langle a_y \rangle, \langle a_z \rangle)$, the color coding for the $\langle a_x \rangle$. (c) rms value of velocity fluctuations $a' = \sqrt{({a'_x}^2 + {a'_y}^2 + {a'_z}^2)/3}$ in the $\Pi_{xy} = (x, y, z = 0)$ plane. (d) rms value of acceleration fluctuations in the $\Pi_{yz} = (x = 0, y, z)$ plane.

geometric centre $(0, 0, 0)$ as was shown in another von Kármán flow with a circular section [97]. With a 3d measurement of the mean flow, it is possible to compute spatial derivatives along all directions. This leads to $\partial_x \langle v_x \rangle \sim \partial_y \langle v_y \rangle \simeq -1.5\ \Omega$ for the stable directions, and $\partial_z \langle v_z \rangle \sim 3.0\ \Omega$ for the unstable direction. Note that the sum of these terms must be zero because this quantity is the divergence of the mean flow. This condition is found to be well satisfied although the velocity components where computed independently without any constraint. Verifying that the flow is divergence free is then an *a posteriori* test that the reconstruction of the mean flow is physical.

The acceleration mean flow is plotted in figure 2.7(a,b). The stagnation point seen in the velocity meanfield $\Pi_{xy}$ plane can also be seen in figure 2.7(a) where particles arriving at the geometrical center (0,0,0) undergo net deceleration :$\langle a_x \rangle < 0$ when approaching from $x/L < 0$ and $\langle a_x \rangle > 0$ when approaching from

$x/L > 0$. Neglecting the viscous terms of the Navier Stokes equation, the mean acceleration is approximately the mean pressure gradient:

$$\langle \vec{a} \rangle \simeq -\frac{1}{\rho}\vec{\nabla}\langle p \rangle. \tag{2.1}$$

This is coherent with the eventual alignment of the acceleration with the axial $z$ component in figure 2.7(b) which reflects the centrifugal pumping occurring near the rotating discs. It is this pumping that eventually expels liquid towards the walls creating the poloidal recirculation depicted in figure 3.1(b).

Figure 2.6(c,d) display rms values of velocity fluctuations $v' = \sqrt{({v'_x}^2 + {v'_y}^2 + {v'_z}^2)/3}$ in $\Pi_{xy} = (x, y, z = 0)$ and $\Pi_{yz} = (x = 0, y, z)$. These maps reveal that the flow properties are non isotropic and non homogeneous at large scale, as already observed in similar setups (reference [98] for instance). The fluctuations increase with $r = \sqrt{x^2 + y^2}$ in the $\Pi_{xy}$ plane, the fluctuation map having the square symmetry of the vessel. However, this is not the case for the acceleration fluctuations $a' = \sqrt{({a'_x}^2 + {a'_y}^2 + {a'_z}^2)/3}$ in figure 2.7(c). Acceleration fluctuations in the $\Pi_{xy}$ are maximal in the geometrical center and decay as $r$ increases. An interesting result is that as opposed to what is observed in the $x$ and $y$ directions, the velocity fluctuations are only weakly varying in the $z$ direction as can be seen in the $\Pi_{yz}$ plane. On the contrary, the acceleration fluctuations decay just as strongly in the $\Pi_{yz}$ plane as in $\Pi_{xy}$. This indicates that there is a particularity of the stagnation point that appears in the acceleration fluctuations that is absent in the velocity fluctuations.

## 2.4 Signal processing

The mean and *rms* values above were estimated using the filtration method. The limitations of this technique reside primarily in the ambiguity of a trade off between filtering noise and filtering the true signal. This problem was enough to provoke the imagination of skeptics to search for a denoising method capable of avoiding this trap. The rudiments of such a method were proposed previously [86] and have since been fully developed [3]. The technique presented below will serve as the preferred method of signal processing when treating acceleration data in the rest of the manuscript.

### 2.4.1 Second order moments

The method presented below seeks to obtain unbiased one and two-point statistics of the derivatives of an experimental signal without introducing any filtering method. It is valid for any measured signal whose typical correlation scale is much larger than the noise correlation scale. While one aims at obtaining the real signal $\hat{x}$, the presence of noise $b$ implies that one measures $x(t) = \hat{x} + b$. For simplicity, the case of a temporal signal $x(t)$ that is centered, *i.e.* $\langle x \rangle = 0$ where $\langle . \rangle$ is an ensemble average, is considered. The method is based on the temporal increment $dx$ of the signal $x$ over a time $dt$, that is expressed as $dx = x(t+dt) - x(t) = d\hat{x} + db$. Assuming that the increments of position and noise are uncorrelated, the increment position variance writes $\langle (dx)^2 \rangle = \langle (d\hat{x})^2 \rangle + \langle (db)^2 \rangle$. Introducing the velocity $\hat{v}$ and acceleration

3. The signal processing chapter was the subject of a publication [99] and has been reproduced here.

$\hat{a}$ through a second order Taylor expansion $\hat{x}(t+dt) = \hat{x}(t) + \hat{v}\ dt + \hat{a}\ dt^2/2 + o(dt^2)$, one obtains:

$$\left\langle (dx)^2 \right\rangle = \left\langle (db)^2 \right\rangle + \langle \hat{v}^2 \rangle dt^2 + \langle \hat{a}.\hat{v} \rangle\, dt^3 + o(dt^3), \tag{2.2}$$

where $\langle (db)^2 \rangle = 2 \langle b^2 \rangle$ in the case of a white noise. In Eqn. (2.2) $\langle (dx)^2 \rangle$ is a function of $dt$ so that one can recover the value of the velocity variance $\langle \hat{v}^2 \rangle$ by calculating time increments of $\langle (dx)^2 \rangle (dt)$ over different values of $dt$ followed by a simple polynomial fit in the form of Eqn. (2.2). If the noise is colored, $\langle (db)^2 \rangle = 2 \langle b^2 \rangle - 2 \langle b(t) b(t+dt) \rangle$. The method hence requires the noise to be correlated only on short times compared to the signal correlation time, so that only the lowest values of $\langle (dx)^2 \rangle (dt)$ are biased by $\langle b(t) b(t+dt) \rangle$ and a fit still successfully allows for the evaluation of the root mean square (rms) velocity, $\hat{v}' = \sqrt{\langle \hat{v}^2 \rangle}$. For an experimentally measured signal $x$, equally spaced at an acquisition rate $f_s$, the minimal value of $dt$ is $1/f_s$; one may obtain the values of $dx$ for different values of $dt = n/f_s$. For this method, a value of the acquisition rate $f_s$ that is purposefully higher than usual is necessary. In so doing, access derivatives of the signal without aliasing error is possible.

It is possible to calculate higher order derivative statistics by considering higher order increments. The second order increment $d^2x = x(t+dt) + x(t-dt) - 2x(t)$, which is related to the acceleration variance $\langle \hat{a}^2 \rangle$ here, yields for instance:

$$\langle (d^2x)^2 \rangle \quad = \quad \langle (d^2b)^2 \rangle + \langle \hat{a}^2 \rangle dt^4 + \frac{1}{6} \left\langle \hat{a}.\frac{d^2\hat{a}}{dt^2} \right\rangle dt^6 + o(dt^6), \tag{2.3}$$

where $\langle d^2b^2 \rangle = 6 \langle b^2 \rangle$ in the case of a white noise, but otherwise introduces additional noise correlation terms which are functions of $dt$.

### 2.4.2 Auto-correlation functions

The approach developed above is not restricted to one time statistics of the signal derivatives but can be generalized to estimate the first and second order derivative auto-correlation functions of the noiseless signal $C_{\hat{v}\hat{v}} = \langle \hat{v}(t)\hat{v}(t+\tau) \rangle$ and $C_{\hat{a}\hat{a}} = \langle \hat{a}(t)\hat{a}(t+\tau) \rangle$. This is done by considering the correlations of first and second order increments $\langle dx(t).dx(t+\tau) \rangle$ and $\langle d^2x(t).d^2x(t+\tau) \rangle$ which are functions of $dt$ and $\tau$. As was done in the previous section for the variance, noiseless correlation functions are estimated, for each time-lag $\tau$, from a polynomial fit of the signal time increment $dt$ with the respective expressions:

$$\begin{cases} C_{dxdx}(\tau, dt) = C_{\hat{v}\hat{v}}(\tau) dt^2 + \dfrac{1}{2} \left( C_{\hat{v}\hat{a}}(\tau) + C_{\hat{a}\hat{v}}(\tau) \right) dt^3 + C_{dbdb}(\tau, dt) + o(dt^3) \\ \\ C_{d^2xd^2x}(\tau, dt) = C_{\hat{a}\hat{a}}(\tau) dt^4 + \dfrac{1}{12} \left( C_{\hat{a}(d^2\hat{a}/dt^2)}(\tau) + C_{(d^2\hat{a}/dt^2)\hat{a}}(\tau) \right) dt^6 \\ \\ \qquad\qquad + C_{d^2bd^2b}(\tau, dt) + o(dt^6), \end{cases} \tag{2.4}$$

where $C_{fg} = \langle f(t) g(t+\tau) \rangle$ is a cross-correlation function. It can be noted that the case of the rms values corresponds to $\tau = 0$ and that $\langle (dx)^2 \rangle$ and $\langle (d^2x)^2 \rangle$ are

functions of $dt$. In equations (2.4) it is possible to give an expression for the auto-correlation functions of the noise first and second order increments in the case of a white noise. The signal being sampled at a frequency $f_s$, one has $dt = n/f_s$ and $\tau = m/f_s$. The correlation functions of the digitized noise increments is written:

$$\begin{cases} C_{dbdb}(\tau = \dfrac{m}{f_s}, dt = \dfrac{n}{f_s}) &= \langle b^2 \rangle \, (2\delta_{m,0} - \delta_{m,n}), \\ C_{d^2bd^2b}(\tau = \dfrac{m}{f_s}, dt = \dfrac{n}{f_s}) &= \langle b^2 \rangle \, (6\delta_{m,0} - 4\delta_{m,n} + \delta_{m,2n}), \end{cases} \tag{2.5}$$

where $\delta_{m,n}$ is the Kroneker symbol. For both derivatives, the white noise magnitude in the first-order derivative auto-correlation functions is the highest for $\tau = 0$ and is an additive term. The noise then yields a negative term for $m = n$. In the case of second-order derivatives (for acceleration in the case of Lagrangian tracks), the noise magnitude has a bigger weight and the noise also contributes to a third time point of the function ($m = 2n$) with a positive term of smaller amplitude. Considering white noise terms up to $dt^6$, all other values of $\tau$ will directly yield the function without noise.

## 2.5 Numerical test

The numerical test uses tracer particles trajectories in homogeneous isotropic turbulence from [100, 59]. The particles are tracked in a periodic box of dimension $L = 2\pi$, with $512^3$ grid points, in a turbulent flow at a Taylor-based Reynolds number $Re_\lambda = 180$. The trajectories $(x_p(t))_{p\in[1,N]}$ are multi-scale temporal signals with a smallest time-scale $\tau_\eta$, and an integral time-scale $T \simeq \tau_\eta Re_\lambda$. In the present case $\tau_\eta = 0.047$ s and $T = 0.59$ s. Trajectories ($N = 2000$) of duration $170\tau_\eta \gg T$ which contain acceleration signals measured at the particle positions at a frequency $f_s^0 = 11.75/\tau_\eta$. These acceleration signals are therefore not obtained by derivation of particle positions, and can be considered to be noiseless. For the purpose of the present test, a higher sampling frequency is needed and the acceleration signals are interpolated so that the noiseless acceleration trajectories, $(\hat{a}_p(t))_{p\in[1,N]}$, have a sampling frequency $f_s = 10 f_s^0$. Each acceleration trajectory is integrated twice to obtain the noiseless position trajectories $(\hat{x}_p(t))_{p\in[1,N]}$ to which a Gaussian random noise, $\hat{b}$, is added at each time step.

The method is tested on these noisy position trajectories and the result can then be compared to quantities computed on the originating signal of (interpolated) acceleration trajectories. To quantify the weight of the noise on the raw acceleration signal the noise-to-signal ratio is calculated: $(\hat{b}' f_s^2)/\hat{a}' = 19.7$, where $\hat{b}' = \sqrt{\langle \hat{b}^2 \rangle} = 23$ $\mu$m and $\hat{a}' = \sqrt{\langle \hat{a}^2 \rangle} = 7.3$ m.s$^{-2}$ are respectively the true rms value of the noise and acceleration, emphasizing the need of a method to eliminate this noise. While corresponding to a poor signal-to-noise ratio, this value is of the order of what can be found in particles tracking experiments (see Section 2.6.1).

### 2.5.1 Moments and correlations

Figure 2.8 shows the evolution of $\langle (dx)^2 \rangle$ and $\langle (d^2x)^2 \rangle$ with $dt$, where $\langle \cdot \rangle$ averages both over time (within a trajectory) and over the number of trajectories. As the velocity is only a first-order derivative, a low level of noise is observed ( $(\hat{b}' f_s)/\hat{v}' = 0.05$) and a linear function of $dt^2$, without considering any higher order term, fits $\langle (dx)^2 \rangle$

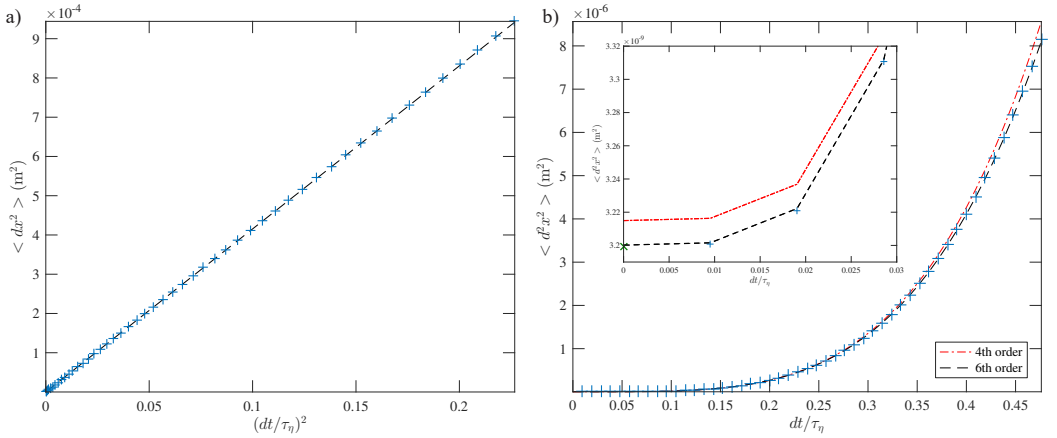


Figure 2.8: (colour online) a) Evolution of $\langle (dx)^2 \rangle$ with $(dt/\tau_\eta)^2$. The dashed line is a linear fit over the range $0 < dt/\tau_\eta \leq 0.07$. b) Evolution of $\langle (d^2x)^2 \rangle$ with $dt/\tau_\eta$. The dashed-dotted and dashed lines are respectively fourth and sixth order fits ($\alpha + \beta dt^4$ resp. $\alpha + \beta dt^4 + \gamma dt^6$) over the range $0 < dt/\tau_\eta \leq 0.14$. The inset is a zoom on low values of $dt/\tau_\eta$; the green cross ($\times$) at $dt = 0$ in the inset corresponds to $6\left\langle \hat{b}^2 \right\rangle$.

almost perfectly. For the acceleration, a sixth-order fit ($\alpha + \beta dt^4 + \gamma dt^6$, following Eqn. 2.3) is much better than considering a fourth-order regression, as is underlined in the inset of figure 2.8(b). This is expected because turbulent trajectories are known to exhibit two time-scales: one characteristic of velocity changes and a much shorter one associated with acceleration (note that this is not specific of turbulence but should hold for any multi-scale signals). The range $dt/\tau_\eta$ (i. e. the number of points used in the regression) considered by those fits is chosen to maximize the fits agreement with the data and corresponds to the values of the abscissa. The influence of this choice, while found not to be critical, is discussed in the following subsection. The fact that the behavior of $\langle (dx)^2 \rangle$ and $\langle (d^2x)^2 \rangle$ follows closely the one given in Eqn. 2.2 and 2.3 is expected as this numerical test respects the hypotheses of the method (considering a white noise uncorrelated with the signal).

By fitting $\langle dx(t).dx(t+\tau) \rangle$ and $\langle d^2x(t).d^2x(t+\tau) \rangle$ on each instant $\tau$ considered, as is done in figure 2.8 for $\tau = 0$, the correlation functions are estimated and compared in figure 2.9 with their true counterparts (computed directly with noise-free velocity and acceleration signals). An excellent agreement is obtained for this benchmark case, where only a slight difference (respectively 0.01% and 0.2% of maximal relative error) is observed for the auto-correlation functions of the first and second order derivatives.

### 2.5.2 Robustness of the method

This benchmark case allows for a quantitative comparison between what is estimated by the method and the real quantities. In order to do so the acceleration time-scale of the noiseless signal is defined: $\tau_{\hat{a}}$, is the integral of the positive part of the acceleration correlation function normalized by the acceleration variance. Table 2.2 presents the relative errors on the estimation of the acceleration, noise variance and acceleration time-scale evolution with the number of points used for the fits. While it is clear that an optimum value exists (around 15 in this case), one can

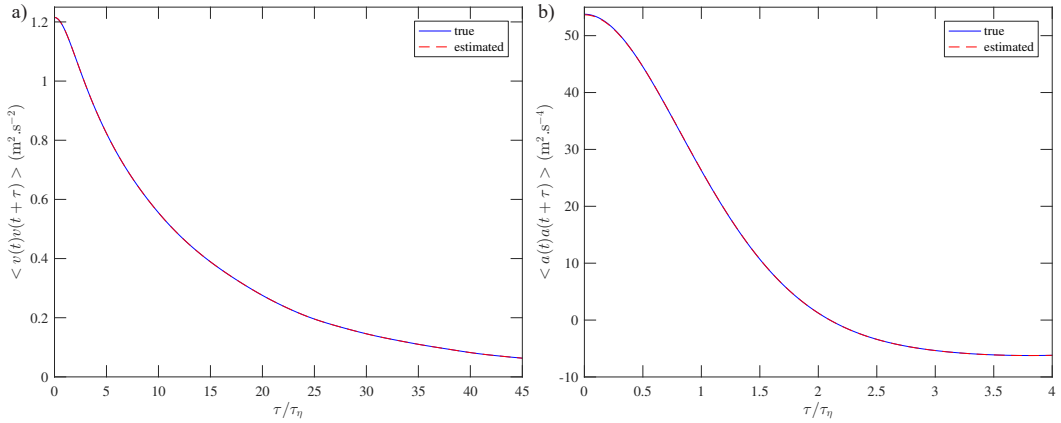


Figure 2.9: (colour online) Velocity (a) and acceleration (b) auto-correlation functions, from the numerical data prior to noise addition (continuous line) and estimated from the proposed method on the noisy data (dashed line). The noise-to-signal ratio is $\hat{b}' f_s^2/\hat{a}' = 19.7$. The fit ranges used to obtain the functions are the same than used in figure 2.8.

appreciate that even using only the bare minimum of points or exaggerating this number still yields very low errors (less than 0.4% for the acceleration variance). It means that the only criterion to choose this parameter should be the agreement between the fit and the data points, as long as the range considered remains physically relevant (in this example $(dt)_{max}/\tau_\eta$ should not be too close to 1, so that $\langle (d^2x)^2 \rangle$ is still relevant to an acceleration). Note that the high error of $\tau_a$ when considering 7 points only is linked to the fact that the noise for $\tau = dt$ and $\tau = 2dt$ still strongly biases the acceleration correlation function integral. The fact that the noise variance error is a decreasing function of the point number is easily understood considering the fact that $\langle (d^2x)^2 \rangle$ is a polynomially growing function of $dt$ and the more points considered, the less weight is given to the first points. This can be observed in the inset of figure 2.8(b) where the fit, by overestimation over the first few points because of their lesser weight, overestimates slightly the value of $\langle b^2 \rangle$.

| Fit ranges | | Relative errors | | |
|---|---|---|---|---|
| # of points | $(dt)_{\max}/\tau_\eta$ | $\frac{\langle a^2 \rangle - \langle \hat{a}^2 \rangle}{\langle \hat{a}^2 \rangle}$ | $\frac{\langle b^2 \rangle - \langle \hat{b}^2 \rangle}{\langle \hat{b}^2 \rangle}$ | $\frac{\tau_a - \tau_{\hat{a}}}{\tau_{\hat{a}}}$ |
| 7 | 0.07 | $4.2\times10^{-3}$ | $6.8\times10^{-5}$ | 0.94 |
| 15 | 0.14 | $3.4\times10^{-5}$ | $2.3\times10^{-4}$ | $2.8\times10^{-5}$ |
| 30 | 0.28 | $4.8\times10^{-4}$ | $2.3\times10^{-3}$ | $4.9\times10^{-4}$ |
| 50 | 0.47 | $3\times10^{-3}$ | $9.6\times10^{-2}$ | $3.1\times10^{-3}$ |

Table 2.2: Relatives errors on the estimation of the variance of the acceleration and noise and on the estimation of the acceleration time-scale for different (sixth order) fit ranges and a noise-to-signal ratio $\hat{b}' f_s^2/\hat{a}' = 19.7$. $\langle \hat{a}^2 \rangle$, $\tau_{\hat{a}}$, $\langle \hat{b}^2 \rangle$ are the true quantities, and $\langle a^2 \rangle$, $\tau_a$, $\langle b^2 \rangle$ are the quantities estimated with the method.

Lastly, the impact of the noise magnitude, estimated as $(\hat{b}' f_s^2)/\hat{a}'$, on the accuracy of the method is considered. Results are given in table 2.3. A first impact of this parameter is the need of more fit points to correctly estimate the acceleration time-scale $\tau_a$. To obtain a relative error on $\tau_a$ below 1%, one must consider at least 9, 12,

14, 16 (respectively) points for the noise magnitudes shown in table 2.3. Note that this is not the case for the error on the acceleration (or noise) variance that stays below 0.4% whatever the noise magnitude even when considering only 10 fit points. Hence, 16 points are used to compute the relative errors of this table. One can observe that even by multiplying the noise by about 4 compared to what has been considered in the previous sub-section, the relative errors barely change. This shows that as well as the noise is white and uncorrelated with the signal, the proposed method should work whatever the noise level. It should be emphasized that, with such low signal-to-noise ratios, it would probably be impossible to directly measure the statistics estimated here without a de-noising strategy.

| | Relative errors | | |
|---|---|---|---|
| $\hat{b}' f_s^2/\hat{a}'$ | $\frac{\langle a^2\rangle - \langle \hat{a}^2\rangle}{\langle \hat{a}^2\rangle}$ | $\frac{\langle b^2\rangle - \langle \hat{b}^2\rangle}{\langle \hat{b}^2\rangle}$ | $\frac{\tau_a - \tau_{\hat{a}}}{\tau_{\hat{a}}}$ |
| 19.7 | $2.5\times10^{-5}$ | $2.3\times10^{-4}$ | $4\times10^{-6}$ |
| 39.4 | $2.5\times10^{-4}$ | $2.6\times10^{-4}$ | $4.1\times10^{-6}$ |
| 59.1 | $3.5\times10^{-4}$ | $4.9\times10^{-4}$ | $1\times10^{-5}$ |
| 78.7 | $1.6\times10^{-4}$ | $1.3\times10^{-4}$ | $1\times10^{-5}$ |

Table 2.3: Relatives errors on the estimation of the variance of the acceleration and noise and on the estimation of the acceleration time-scale for different noise magnitudes, with a fixed fit range of $(dt)_{max}/\tau_\eta = 0.15$ (16 fit points). $\langle \hat{a}^2\rangle$, $\tau_{\hat{a}}$, $\langle \hat{b}^2\rangle$ are the true quantities, and $\langle a^2\rangle$, $\tau_a$, $\langle b^2\rangle$ are the quantities estimated with the method.

## 2.6 Experimental test

This section is devoted to the test of the method in two experimental configurations, where the noise is a priori either white (or correlated on much shorter times than the signal) or colored. Both cases consider Lagrangian tracks of particles in turbulent von Kármán flow produced by two counter-rotating discs in a vessel filled with water.

### 2.6.1 Shortly correlated noise

This first case uses the raw position trajectories of material particles from [101]. The method has been tested successfully for different particle diameters (from 6 to 24 mm), Reynolds numbers ($350 < Re_\lambda < 520$) and two density ratios (0.9 and 1.14), as well as for isodense particles from [102]. The case of particles 6 mm in diameter and of density ratio 1.14 at a Reynolds number $Re_\lambda = 520$ is considered in the following. The position trajectories are obtained by stereo-matching of successive image pairs obtained thanks to two cameras and global lighting. The particles appear as large, bright discs on an uniform dark background which yields sub-pixel noise for the trajectories (the apparent particle diameter is about 20 pixels) and is not correlated with the particle position as the background is uniform (nor with its velocity as the exposure time is short enough to fix the particles on the images). In practical situations, the presence of sub-pixel displacements can lead to a short-time correlation of the noise, typically on a few frames.

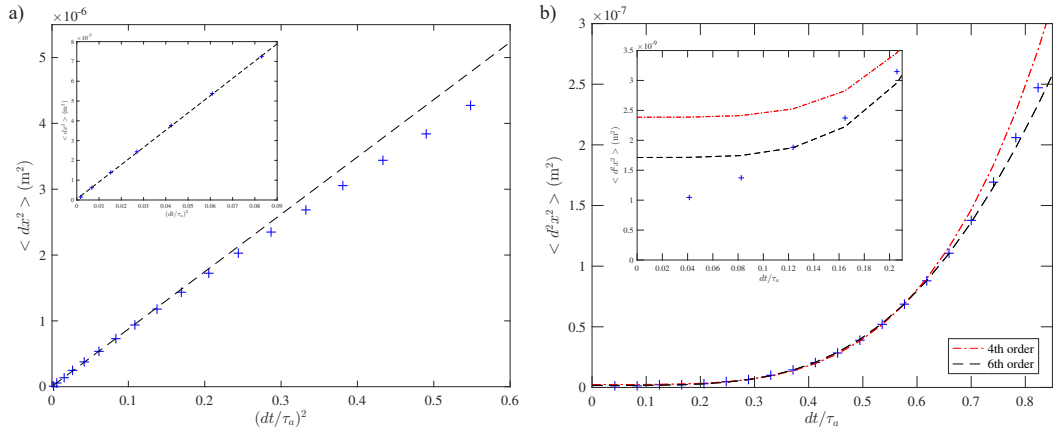


Figure 2.10: (colour online) a) Evolution of $\langle (dx)^2 \rangle$ with $(dt/\tau_a)^2$, where $\tau_a = 8.1$ ms is the particle acceleration time-scale (integral of the positive part of the particle acceleration auto-correlation function). The dashed line is a linear fit over the range $0 < dt/\tau_a \leq 0.25$. b) Evolution of $\langle (d^2x)^2 \rangle$ with $dt/\tau_a$. The dashed-dotted and dashed lines are respectively fourth and sixth order fits ($\alpha + \beta(dt/\tau_a)^4$ resp. $\alpha + \beta(dt/\tau_a)^4 + \gamma(dt/\tau_a)^6$) over the range $0 < dt/\tau_a \leq 0.62$. The insets are zooms on low values of $dt/\tau_a$.

Figure 2.10 shows the evolution of $\langle (dx)^2 \rangle$ and $\langle (d^2x)^2 \rangle$ with $dt$. As with the numerical test, a simple linear function of $dt^2$ is enough for $\langle (dx)^2 \rangle$ and a sixth-order one suits better $\langle (d^2x)^2 \rangle$. The first points of $\langle (d^2x)^2 \rangle$ do not follow Eqn. 2.3, which may be due to the fact that the noise may not be purely white as will be shown in figure 2.11(b). Using the estimated values of the rms acceleration, $a'$, and $\langle (d^2b)^2 \rangle$, noise-to-signal ratio may be defined as: $b' f_s^2 / a' = 11.9$, where $b' = \sqrt{\langle (d^2b)^2 \rangle / 6}$ was defined by analogy with the white noise case. When considering the noise weight on the velocity signals, a much smaller magnitude $b' f_s / v' = 0.14$ is found because it is a first order derivative ($v'$ being the rms of the velocity estimated with the method). Figure 2.11 shows the auto-correlation function of both the velocity and acceleration estimated with the proposed method, compared to the raw functions. With the low level of noise in this configuration, the velocity is almost unbiased and both functions are indistinguishable except for the first points of the raw function that are offset by the noise. Concerning the second-order derivative quantity, it can be observed in figure 2.11(b) that the raw acceleration auto-correlation function is not only biased on the three first points (see inset). This is because the noise is not white but has a short correlation time compared to the signal. Combined with the finite duration of the trajectories, the raw correlation function is noisy over the whole range of time-lags $\tau$. This curve is plotted together with the one estimated with the method, fitting the coefficient up to $dt = 5$ ms which corresponds to 30% correlation loss in acceleration signals (same range as in figure 2.10b, but the precise choice is not critical). Although the signal-to-noise ratio is poor, the estimated correlation function seems to be following the median line between the peaks caused by noise and crosses zero at the location that seemed indicated by the raw function. It is also close to the auto-correlation function from [101], estimated by filtering the data with a Gaussian kernel $K = A_w \exp(-t^2/2w^2)$ (with $w = 12$ points and a compact support of width $2w$) and $A_w$ is a normalization factor. It should be

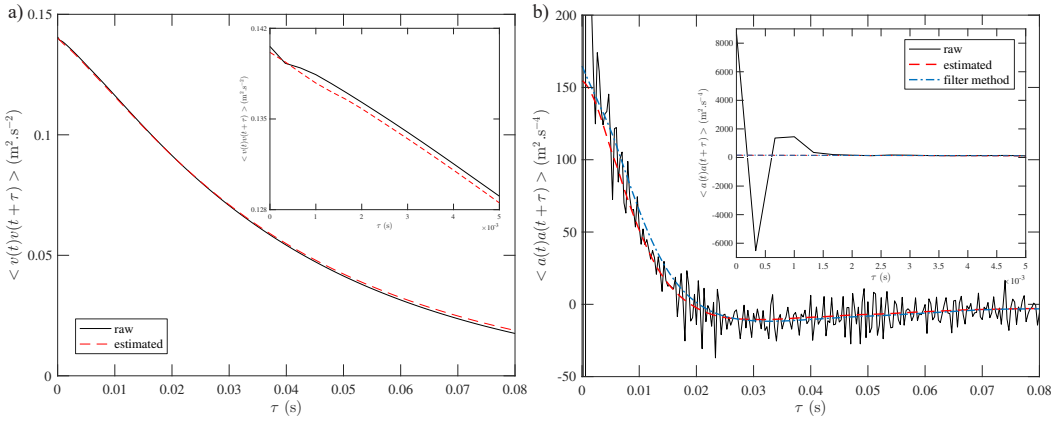


Figure 2.11: (colour online) (a) Auto-correlation functions of the velocity or acceleration (b) estimated from the proposed method (dashed line) and directly computed by differentiating the position signal obtained by PTV (continuous line). The insets are zooms on the low values of $\tau$. The fit ranges used to obtain the functions are the same than used in figure 2.10. The dashed-dotted line in figure (b) is the correlation estimated from filtered trajectories using a Gaussian kernel $K = A_w \exp(-t^2/2w^2)$, where $w = 12$ points and $A_w$ is a normalization factor.

stressed that the value $w = 12$ was chosen arbitrarily as a compromise between suppressing oscillations at small lags without altering too much the shape of the function at larger lags. With the new method, an acceleration time-scale of $\tau_a = 8.1$ ms and an acceleration magnitude $a' = 12.4$ m.s$^{-2}$ is calculated. The values are which to $\tau_a = 8.8$ ms and $a' = 12.9$ m.s$^{-2}$ found for the filtered data [101]. However, in the latter case, the value of $a'$ depends strongly of the choice of the filter width $w$, so that one usually estimates $a'$ by computing it for different filter widths which can then allow to extrapolate a best estimate value (as introduced in [33]).

### 2.6.2 Colored noise

The second case considers raw velocity trajectories from [60, 95], obtained by Extended Laser Doppler Velocimetry (ELDV) measurements of tracer particles. The velocity is directly obtained through a frequency demodulation by use of an approximate maximum likelihood method coupled to a Kalman filter [103]. Although the signal is sampled at very high frequency 1 MHz (the carrying frequency is 100 kHz), the instantaneous frequency is estimated over a short window (here 30 $\mu$s) and is influenced by its estimation at the previous time-step. Even assuming that the noise, noted $b_v$, is initially white, it is low-pass filtered and becomes colored in the process. Applying the Taylor expansion to the present case $\hat{v}(t+dt) = \hat{v}(t) + \hat{a}(t)dt + \frac{1}{2}\frac{d\hat{a}}{dt}dt^2 + o(dt^2)$, the correlation function of velocity increment is written:

$$\begin{aligned}\langle d\hat{v}(t)d\hat{v}(t+\tau)\rangle(\tau,dt) = \langle db_v(t)db_v(t+\tau)\rangle + C_{\hat{a}\hat{a}}(\tau)dt^2 \\ + \frac{1}{2}\left(C_{\hat{a}(d\hat{a}/dt)}(\tau) + C_{(d\hat{a}/dt)\hat{a}}(\tau)\right)dt^3 + o(dt^3).\end{aligned} \tag{2.6}$$

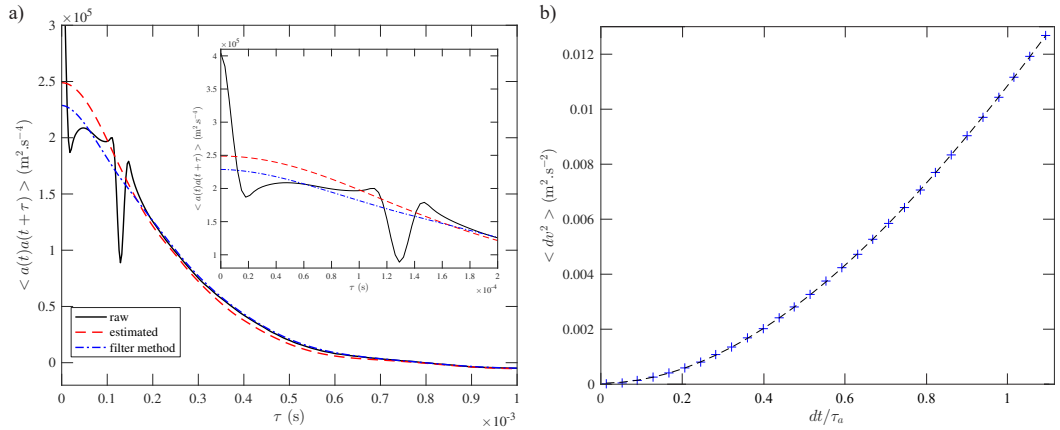


Figure 2.12: (colour online) a) Acceleration auto-correlation functions estimated from the proposed method (dashed line), or directly computed by differentiating the velocity signal obtained by ELDV (continuous line). The dashed-dotted line is the correlation estimated from filtered trajectories using a Gaussian kernel $K = A_w \exp(-t^2/2w^2)$, where $w = 20$ points and $A_w$ is a normalization factor. The inset is a zoom on the low values of $\tau$. b) (+): evolution of $\langle (dv)^2 \rangle$ with $dt$ (represented one point on three for clarity). The dashed line is a third order fit $(\alpha_v + \beta_v dt^2 + \gamma_v dt^3)$. In both figures, the increments where fitted over the range $0 < dt/\tau_a < 1$.

The acceleration is directly obtained from the first order derivative of the velocity here, so that $C_{\hat{a}\hat{a}}(\tau)$ is estimated using a fit of the form $\alpha_v + \beta_v dt^2 + \gamma_v dt^3$ for each time-lag $\tau$. Figure 2.12(a) displays the auto-correlation function of the acceleration, raw or estimated by the proposed method, for a very high Reynolds number $Re_\lambda = 950$. The raw acceleration correlation function clearly shows the correlated nature of the noise, being strongly biased over a large range of time-scales. The estimated function has been obtained by fitting over a wide range $0 < dt/\tau_a < 1$, so that a third order polynomial is required to properly fit the evolution of velocity increments with $dt$ (Figure 2.12(b)). Although such a range was chosen to be larger than the expected noise correlation time, its choice was not critical and fits over smaller ranges down to $(dt)_{max}/\tau_a = 0.6$ changed the values by less than 3%. This demonstrates that if the method framework was derived assuming an uncorrelated noise, it still can be used successfully in the case of a colored noise. Indeed, the estimated function presents a shape close to that which is expected in the absence of noise, and is found to be close to the auto-correlation function of filtered data from [95], which still exhibits some slight oscillations (around $\tau = 0.15$ ms) despite the large filter width $w = 20$ points. Increasing the filter width would suppress this oscillation at the cost of strongly decreasing the value at $\tau = 0$, altering more the shape of the function. The rms of the acceleration estimation for new method $a' = 498.9$ m.s$^{-2}$ is in good agreement to the value $a' = 496$ m.s$^{-2}$ which is found in [95] by extrapolation of this quantity using different filter widths. The acceleration time-scale is found to be $\tau_a = 0.232$ ms, changing less than 0.1% when changing the fitting range from $[0,\ 0.6\tau_a]$ to $[0,\ \tau_a]$, in very good agreement with the extrapolated value $\tau_a = 0.234$ ms from the variable filter width method [95]. Given the statistical convergence of the data, the different estimates of the time-scale should be considered the same, $\tau_a = 0.23$ ms. It is stressed here that the choice of the fitting range was not crucial

in the analysis, and did not require a bias study as is the case for the extrapolated results of filtered signals.

## 2.7 Discussion and conclusion

In this contribution a novel method was proposed for measuring the Lagrangian statistics of small particles or tracers in a highly turbulent flow known to be both inhomogeneous and anisotropic and which may be conditioned in space to reconstruct the Eulerian flow properties in 3d. The Shadow Particle Velocimetry setup, based on two large, perpendicular collimated rays of light requires two LEDs, instead of a high-power laser, and allows for the tracking of small objects in a large volume. The tracking algorithms implement an innovative one-component redundancy to overcome the difficulty of a large depth of field and prevents any wrong trajectory constructions. This setup yields long, clean trajectories necessary to study one-particle dispersion in turbulence and the properties of a flow that is anisotropic both at large and small scales. The technique is tested by computing the velocity and acceleration auto-correlation functions which present time scales in accord with those found in the literature. By using many trajectories, it is possible to reconstruct a 3d map of ensemble-averaged Eulerian quantities. This versatile setup may also be used with fewer particles to study flow statistics at long times [104] as is usually done with 1d (or 2d) measurements [105]. As the method measures two projections of the objects advected by the flow in two perpendicular planes, it is also suitable to study the translation and rotation dynamics of non-spherical objects, such as fibers or disks. A general method to estimate moments and auto-correlation functions of experimental signal derivatives ridden of measurement noise is also proposed. This method relies on two main assumptions:

1. The signal has to be correlated on a longer time-scale than the noise.
2. The sampling frequency, $f_s$, must be high enough so that the signal first and second order derivatives can be computed by taking increments over several ($N$) points.

Is was observed in the numerical tests that this adjustable parameter ($N$) has a small influence on the results and it is estimated that $f_s\tau_2 = 20$ is a good choice when one is interested in the signal second derivative, $\tau_2$ being the correlation time of the signal second derivative to be estimated. The method was tested in the context of Lagrangian particle tracks in turbulence, considering both first- and second-order derivatives of a time dependent signal. First, numerical data is used, artificially adding a white noise and successfully comparing quantities estimated through this method to those computed prior to noise addition. Second, tests were conducted on classical Particle Tracking Velocimetry and Extended Laser Doppler Velocimetry data. In the former the noise is correlated on times much shorter than the signal and in the latter the noise is made colored by a filtering operation inherent in the measurement. Whatever the case, the results are in good agreement to what is obtained by classical filtering processes, which require a long bias study specific to the data type [33, 95], and it is thought that they are more accurate. The method avoids subjective tuning of the filter width and choice of filter type while yielding unbiased quantities by requiring data fits in an appropriate range. While the fit range is still an adjustable parameter, its impact on the results is observed to be smaller than when filtering the data. The numerical test reveals that the

error remains very small even while varying the fit range by a factor 7. Another advantage of the method is an easy access to the noise magnitude. While building a new experimental setup, one can gather just enough statistics to converge second order moments to estimate the noise magnitude and try and improve the setup iteratively. With more statistics, having access to the noise correlation function ensures that the noise is not correlated (in cases where it is not expected to be so). The method is also tested in a more general context of a random position signal whose first and second-derivative auto-correlation functions are known (not shown here). The signal was generated using the 2-time Sawford model [106] which solves a coupled set of Langevin equations for both the velocity and acceleration. Once again, an almost perfect agreement was found between the analytical function and the one obtained by the proposed method. The method presents some drawbacks such as added computation time. The major drawback is the need to sample the signal at a larger rate than would usually be necessary. Indeed, this offers a larger range over which $d^2x$ still can be related to a second-order derivative. While this is easily achieved with ELDV measurements, as the sample rate is already very high and the data are not voluminous, this can cause a limitation on the trajectories duration for typical PTV setup or other measurements based on embarked-memory cameras, making the trade-off between temporal resolution and duration even harder.

# Chapter 3

# Production and dissipation of turbulent fluctuations close to a stagnation point[1]

## 3.1 Introduction

A large part of turbulence theory has been developed in the context of homogeneous and isotropic turbulence [96]. In such situations the mean flow is considered to be zero and flow properties are assumed to be invariant in space. However, common turbulent flows are often produced by mechanical forcing in the presence of boundaries, leading to non zero mean flows with complex topologies. Such is the case of a mechanically forced flow in a closed volume, which results in regions dominated by shear or recirculations with hyperbolic points. In this context, shear flows are well documented [108, 109], but the action of strain has received less attention and our knowledge relies either on measurements performed in quasi-homogeneous situations [110, 111], or in near wall regions [112].

We address the production and dissipation of turbulent fluctuations experimentally using a von Kármán flow with a square cross section (described in section 2). A mean flow is produced by counter-rotating impellers which impose inertial steering on the fluid and result in strong azimuthal velocity gradients and is generally considered to give rise to shear driven turbulence. However, the central region's stagnation point is typified by strong straining motion which is an often overlooked aspect of this configuration. We investigate the role of this topology in turbulence production, in particular we address the origin of the anisotropic velocity fluctuations observed in these type of flows [9, 113, 30].

The experiment is performed in a large volume in the central region where Lagrangian tracers are tracked and all scales of their motions are resolved. We show that the flow is bistable (section 3), where each of the two states resembles a pair of impinging jets with one stable and two unstable directions. This situation is not observed to be "free-shear flow" turbulence, but rather its main features point strongly to a stagnation-point topology whose study is lacking in the literature.
The local turbulent kinetic energy budget is presented (section 4) where the quantity $\langle \vec{a}' \cdot \vec{v}' \rangle = \langle \vec{a} \cdot \vec{v} \rangle - \langle \vec{a} \rangle \cdot \langle \vec{v} \rangle$ is shown to be an accurate local measurement of the dissipation in the vicinity of the stagnation point. We demonstrate a mechanism

1. A portion of this chapter was the subject of a publication [107].

by which energy is efficiently extracted from the mean flow such that production of turbulence is twice the value of energy dissipation. As a result, a significant amount of energy is transported by turbulent fluctuations in the vicinity of the stagnation point and renders the flow spatially inhomogeneous.

## 3.2 Experimental setup

**Description of the flow** The experimental apparatus is a von Kármán flow identical to the one used in [89]. A water-Ucon$^{TM}$ mixture with viscosity 8.2 that of water and equal density is used to fill a square cylinder where the flow is produced using two bladed discs of diameter $R = 7.1$ cm that counter rotate at constant frequency $\Omega$ (figure 3.1(a)) and are separated by 20 cm while the tank width is 15 cm. The angular velocity of the discs is adjusted so that they rotate at same velocity, but in opposite directions, imposing an inertial forcing which generates a fully turbulent flow ($Re_\lambda \sim 190$). As opposed to wind tunnel flows, the von Kármán flow has a mean tridimensional spatial structure and is sketched in figure 3.1(a). The discs rotate in opposite directions and generate a large azimuthal velocity component of order $2\pi R\Omega$ which goes zero in the mid plane ($z = 0$) of the square tank. The presence of blades improves stirring and creates an intense poloidal recirculation with a stagnation point in the geometrical center of the vessel. The dominant flow characteristics in the central region are strong shear and intense and anisotropic fluctuations close to the stagnation point [9, 113, 30] where most of the dissipation occurs [114, 115]. Table 3.1 gives a summary of the flow parameters measured at the stagnation point of the present setup.

**3d-particle tracking setup** We perform particle tracking of Lagrangian tracers (250 $\mu$m polystyrene particles, less than three times the Kolmogorov scale) in a large volume $6 \times 6 \times 5.5$ cm$^3$ centered around the geometrical center $(x, y, z) = (0, 0, 0)$ of the flow. Tracers are tracked with 2 high-speed video cameras (Phantom V.12, Vision Research, 1Mpix@7kHz) with a resolution of $800 \times 768$ pixels and a high frame rate $f_s = 12$ kHz, chosen to adequately resolve particle acceleration. The camera arrangement, inspired from previous work [89], is depicted in figure 3.1 b). It consists of 2 arms forming an angle $\theta = 90°$ with parallel lighting. This large parallel ray (15 cm in diameter) intersects the flow volume before being collected onto the camera using a doublet consisting of a large lens (15 cm in diameter, with a 50 cm focal length) and the camera objective. The doublet is focused on the face of the tank closest to the camera which was found to be the configuration best adapted to tracking small objects. As this arrangement requires precision mounting, all optical elements are aligned using large, homemade reticules also used to measure the magnification in each arm. When placing an object in the field of view, it appears as a black shadow on a white background corresponding to the parallel projection of the object on the sensor. As opposed to conventional PTV, particles are tracked independently on each view prior to stereo matching so that camera 1 provides the $(x_1, z_1)$ positions while camera 2 will measure their $(y_2, z_2)$ positions [85]. The $z$ coordinates are redundant and an affine relationship ($z_2 = az_1 + b$, figure 3.1 c)) permits the stereo-matching of trajectories satisfying $\max(|z_2(t) - az_1(t) - b|) < 3$ px, which is smaller than the particle's apparent radii on the image. This affine relation

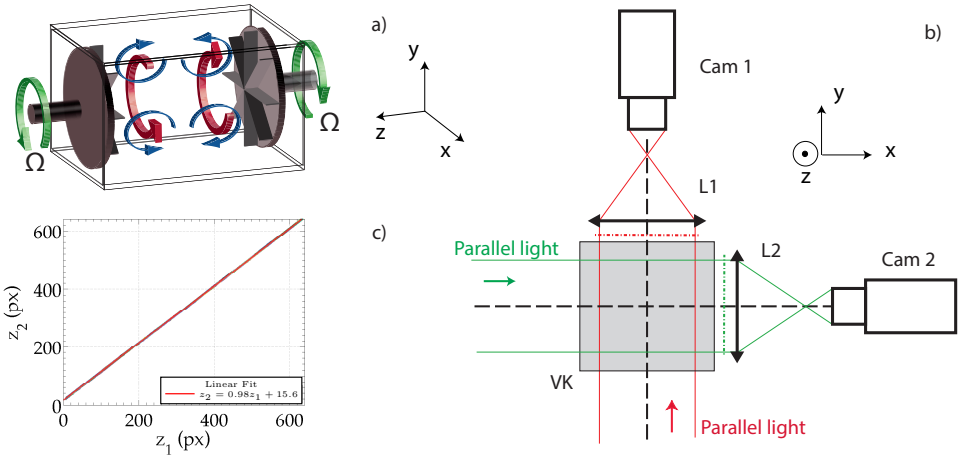


Figure 3.1: (color online) (a) Sketch of the counter-rotating von Kármán flow. Arrows indicate the topology of the mean flow when averaged over both states. (b) Optical setup for S-PTV with 2 identical optical arrangements forming an angle $\theta = 90°$: parallel light is propagating through the flow volume before being collected using a 15 cm-diameter lens whose function is to redirect the light into the camera objective of the camera. The optical system [$L_2$+objective] is focused on the output face of the vessel marked with a dashed-dotted line. (c) raw axial position of particles, $z_2$ (in pixels), as measured on cam 2 as a function of $z_1$ measured on cam 1. The line corresponds to a linear fit $z_2 = az_1 + b$ with $a = 0.98$, $b = 15.6$ pixels.

is first obtained with a dilute ensemble of particles that permits easy stereo-matching within a pair of movies and recursive estimations of the fit parameters ($a = 0.98$, $b = 15.6$ pixels is used here). Together with the magnification of camera 1 (90 $\mu$m per pixel), the calibration provides all requisite information concerning particle positions in laboratory coordinates. As the experiment was run at a low particle concentration, each pair of movies leads to an ensemble of trajectories from which single particle statistics can be computed. For each Reynolds number considered we record 500 pairs of movies lasting 1.3 seconds, each pair leading to $\mathcal{O}(1000)$ trajectories with a mean duration $\langle t \rangle \sim 0.25/\Omega$. A large ensemble of $\mathcal{O}(4 \times 10^5)$ trajectories allows Lagrangian single particle statistics to be conditioned in space in order to investigate the non homogeneity of the flow properties.

## 3.3 Bistability and mean flow properties

### 3.3.1 Mean flow topology

The counter-rotating von Kármán flow is known to exhibit long time dynamics [105]. To investigate the stationarity of the flow we conducted 8 hour measurement campaigns, obtaining 100 films separated by five minutes of data transfer. Figure 3.2 (a,b) display the time evolution of the rms values of the velocity components using all trajectories in each pair of movies for the intermediate Reynolds number and are computed directly from the trajectories by:

$$v_{rms,i}(t) = \sqrt{\frac{1}{N_p} \sum_{p \in movie}^{N_p} \left( \overline{(v_i^p)^2} - (\overline{v_i^p})^2 \right)}, \quad i = x, y, z \tag{3.1}$$

| $\Omega$ | state | $u'_x$ | $u'_y$ | $u'_z$ | $u'$ | $\tau_\eta$ | $\eta$ | $\epsilon$ | $R_\lambda$ | $Re$ |
|---|---|---|---|---|---|---|---|---|---|---|
| Hz | - | m.s$^{-1}$ | m.s$^{-1}$ | m.s$^{-1}$ | m.s$^{-1}$ | ms | $\mu$m | W.kg$^{-1}$ | - | - |
| 4.2 | $x$-dominant | 0.45 | 0.29 | 0.25 | 0.34 | 2.9 | 154 | 1.0 | 155 | 16200 |
| | averaged | 0.39 | 0.37 | 0.24 | 0.34 | 2.9 | 154 | 1.0 | 155 | 16200 |
| 5.5 | $x$-dominant | 0.58 | 0.39 | 0.33 | 0.45 | 2.0 | 128 | 2.1 | 190 | 21200 |
| | averaged | 0.50 | 0.49 | 0.33 | 0.45 | 2.0 | 128 | 2.1 | 190 | 21200 |
| 6.9 | $x$-dominant | 0.74 | 0.48 | 0.41 | 0.56 | 1.5 | 111 | 3.6 | 225 | 26700 |
| | averaged | 0.62 | 0.62 | 0.41 | 0.56 | 1.5 | 111 | 3.6 | 225 | 26700 |

Table 3.1: Parameters of the flow. $\Omega$, rotation rate of the discs. The rms velocities are obtained at the geometrical center of the flow using data points located in a sphere with a 1 cm radius. The kinematic viscosity of the water-Ucon$^{TM}$ mixture is $\nu = 8.2\ 10^{-6}$ m$^2$s$^{-1}$ with a density $\rho = 1000$ kg m$^{-3}$. The dissipative time-scale is estimated from the zero-crossing ($t_0 = (t_{0x} + t_{0y} + t_{0z})/3$) of each component in the acceleration auto-correlation function: $t_0 \simeq 2.2\tau_\eta$ [90, 9, 60], the dissipation rate is estimated $\varepsilon = \nu/\tau_\eta^2$ and dissipative length-scale is $\eta = (\nu^3/\varepsilon)^{1/4}$, the Taylor-based Reynolds number being estimated as $Re_\lambda = \sqrt{15u'^4/\nu\varepsilon}$ with $u' = \sqrt{({u'_x}^2 + {u'_y}^2 + {u'_z}^2)/3}$. The large scale Reynolds number is $Re = 2\pi R^2\Omega/\nu$.

where $N_p$ is the total number of particle trajectories $p$ in the $k^{\text{th}}$ pair of movies (leading to $t = 5\ k$, in minutes), and $\overline{v_i^p}$ is the velocity component $i = x, y, z$ averaged in time over its duration $T_p$. We observe that the axial component ($v_{rms,z}$) is always close to 0.35 m.s$^{-1}$ while the transverse components ($v_{rms,x}$ and $v_{rms,y}$) alternate between two values: 0.35 m.s$^{-1}$ and 0.55 m.s$^{-1}$. Moreover, $v_{rms,x}$ and $v_{rms,y}$ never have a large value at the same time, but instead exchange values. This behavior is observed regardless of the rotation frequency in the fully turbulent regime, indicating that the large scale flow is bistable with one transverse component dominating the other. The two states of the flow can be directly observed by introducing bubbles into the apparatus and using a back-light configuration with a webcam operating at 15 Hz oriented in the $x$ direction to observe a field lit by a LED panel. Upon visualization, coherent vortex structures trap the lighter bubble phase and stand out clearly in the images (figure 3.2(c,d)). These vortices occur in pairs attached to either set of horizontal (figure 3.2 c) or vertical walls (figure 3.2 d) and are situated at equal distance from the mid plane which is also the location of the shear layer. The vortices have their own dynamics. Their positions are observed to fluctuate, and may be found nearly one vortex core away from their typical wall-anchored positions. These vortices are thought to be central to the present bistability for which the persistency of either horizontal or vertical state is much longer (several minutes, confirmed by Laser Doppler Velocimetry measurements) than the large eddy turnover time $1/\Omega \simeq 0.2$ seconds. Reversals are preceded by a "dancing" motion whereby the vortex pairs become unstable and detach from their wall-anchored positions, eventually shifting 90° from a vertical set to a horizontal set or *vice versa*. Such a scenario is specific to the square-cylinder geometry, and differs from the typical bistability observed in circular-cylinders for which the two states correspond to a displacement of the shear layer, and mirror each other about the mid-plane [29, 105, 116].

In order to characterize the flow properties of each state separately the data

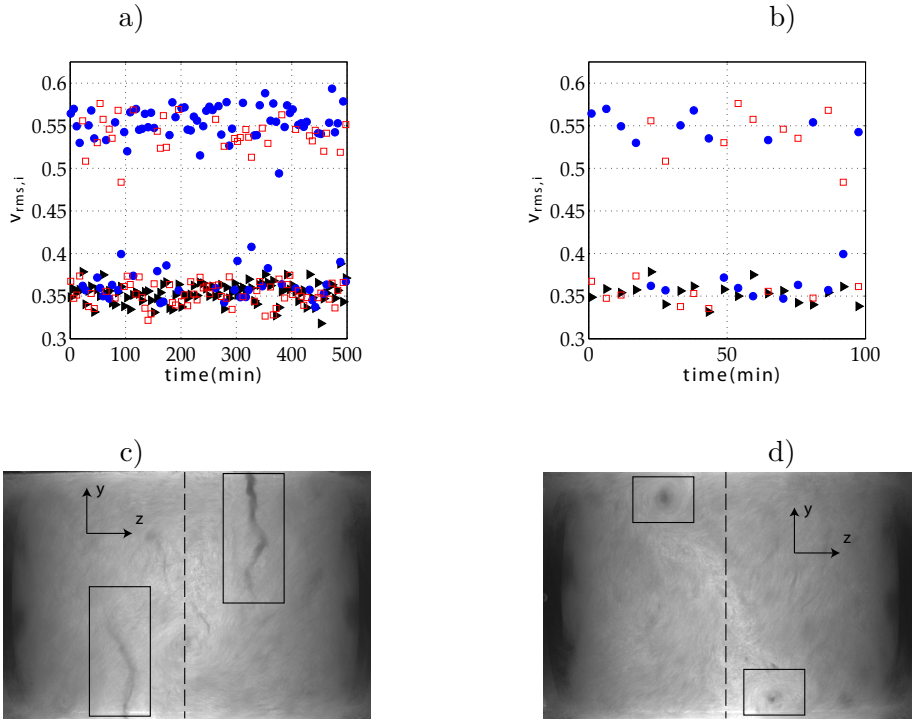


Figure 3.2: (color online).(a,b) Time evolution of the rms value of the velocity computed from each movie at $Re_\lambda = 190$. The time is defined as $t = kT$ where $k$ is the number of the movie and $T = 5$ minutes is the time between each successive recordings. • $x$-component, □ $y$-component, and ▶ $z$-component. (c,d): backlight visualization of bubbles injected in the flow, dark regions corresponding to bubbles concentrated in vortices are marked with a box. The webcam and the LED panel are placed apart the vessel in the $x$ direction, the discs being visible on the sides of each image. c) system of two vertical vortices aligned with $y$-direction. d) system of two horizontal vortices aligned with $x$-direction. In all cases the shear layer is located at the mid-plane (marked with a dashed line).

set is separated into two ensembles with the $x$-dominant (respectively $y$-dominant) state corresponding to movies with high values of $v_{rms,x}$ (resp. $v_{rms,y}$). Given these sets of trajectories, one may reconstruct the mean velocity field in 3d $\langle\vec{v}\rangle(x,y,z) = (\langle v_x\rangle, \langle v_y\rangle, \langle v_z\rangle)$ and the rms fluctuations of each velocity component. This is achieved by an Eulerian conditioning of the Lagrangian datasets on a $12^3$ cartesian grid, which corresponds to a spatial resolution of 5 mm in each direction. We found this grid size to be sufficiently small with respect to the typical scale ($R/2 = 3.5$ cm) of the flow, and sufficiently large to permit at least $\mathcal{O}(1000)$ trajectories to cross each bin which is enough to converge both the mean and rms values of the quantities considered.

Figure 3.3(a,c) (respectively figure 3.3(d,f)) display cross-sections of the reconstructed mean flow of the $x$-dominant (resp. $y$-dominant) state in two perpendicular planes: the $\Pi_{xz}$ plane containing transverse and axial components, and the axially orthogonal mid plane $\Pi_{xy}(x,y,z=0)$. These figures demonstrate that neither of the states presents a mean structure resembling that of the schematic view in figure 3.1(a) nor do they contain the double contracting axes $(x,y)$ and a single diverging direction $(z)$ near the geometrical center. Considering the $\Pi_{xz}$ plane in the

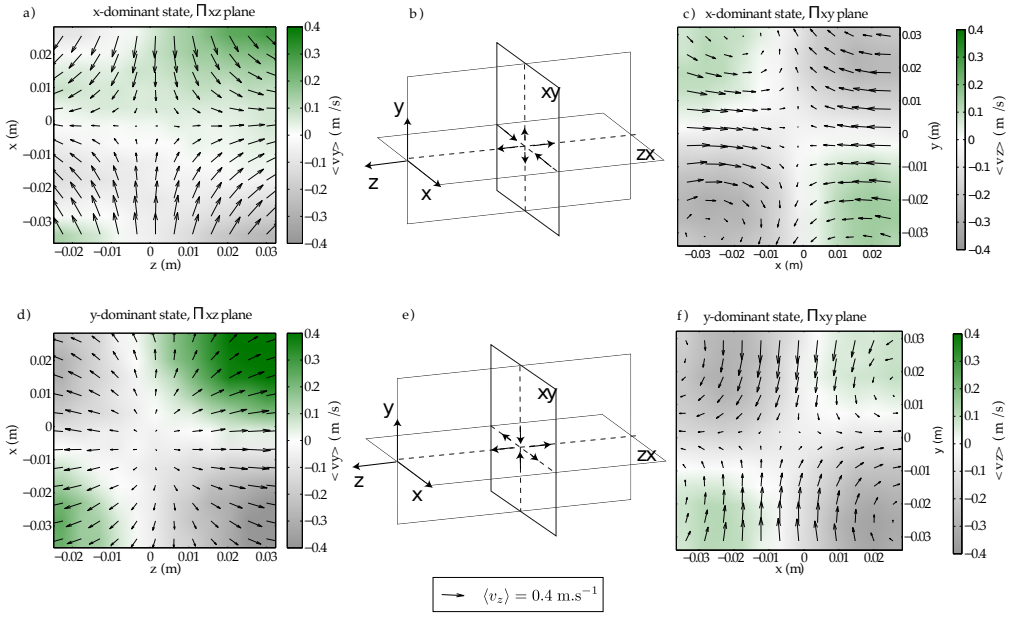


Figure 3.3: (a) $\Pi_{xz} = (x, y = 0, z)$ cut of the reconstructed Eulerian mean velocity field of the $x$-dominant state. Arrows are $(\langle v_x \rangle, \langle v_z \rangle)$, the color coding for the $\langle v_y \rangle$. (b) Topology of the $x$-dominant state at the geometric center. (c) $\Pi_{xy} = (x, y, z = 0)$ cut of the $x$-dominant state. Arrows are $(\langle v_x \rangle, \langle v_y \rangle)$, the color coding for the $\langle v_z \rangle$. (d,e,f) same figures as (a,b,c) for the $y$-dominant state.

$x$-dominant state, stagnation point topology is evident and indeed a single converging direction ($x$) is present (figure 3.3(a)). However, the same plane in the $y$-dominant state gives two diverging axes (figure 3.3(d)). In fact, these two figures would be exchanged when presenting cross-sections in the $\Pi_{yz}$ plane instead of $\Pi_{xz}$ to properly account for the dominant converging direction. This reversal is an important signature of the bistability in the mean flow and is apparent when observing cross-sections in the $\Pi_{xy}$ plane which illustrates dominant components coinciding invariably with a contracting direction, similar to the topology of two impinging jets (figure 3.3(b,e)).

The image of two jets creating the stagnation point is complicated by the presence of a network of vortices passing through the central region. The vortices are distinguishable in the velocity fields (fig. 3.3 c,f ). Centripetal acceleration field in $\Pi_{xy}$, but also felt in the other planes, established in their vicinity suggests a strong signature on the mean structure of the flow: particles are decelerated as they approach the stagnation point and accelerate as the pass through the central region, highlighting the role of a single converging and two diverging directions. The mean acceleration fields also display a distinct signature of the bistability (fig. 3.4) clearly changing orientation in lock-step with the diverging and converging directions.

The presence of two unstable directions and one stable direction is confirmed when computing the (normalized) gradient tensor of the mean flow components and the Reynolds stress tensor at the origin $(x, y, z) = (0, 0, 0)$ in the $x$-dominant state:

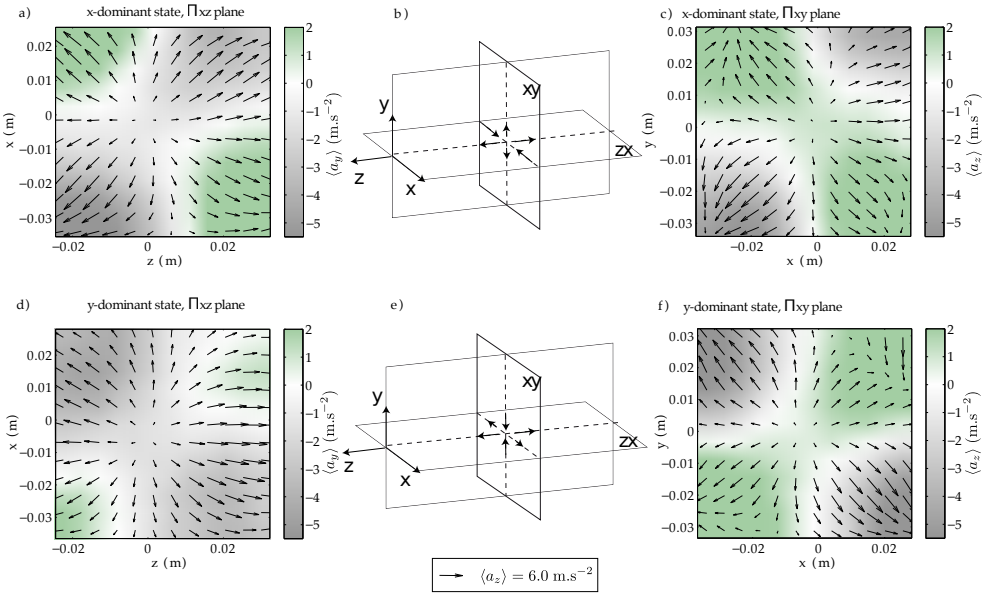


Figure 3.4: (a) $\Pi_{xz} = (x, y = 0, z)$ cut of the reconstructed Eulerian mean acceleration field of the $x$-dominant state. Arrows are $(\langle a_x \rangle, \langle a_z \rangle)$, the color coding for the $\langle a_y \rangle$. (b) Topology of the $x$-dominant state at the geometric center. (c) $\Pi_{xy} = (x, y, z = 0)$ cut of the $x$-dominant state. Arrows are $(\langle a_x \rangle, \langle a_y \rangle)$, the color coding for the $\langle a_z \rangle$. (d,e,f) same figures as (a,b,c) for the $y$-dominant state.

$$\frac{1}{2\pi\Omega}[\partial_i \langle v_j \rangle] = \begin{pmatrix} -0.90 & 0.18 & 0.00 \\ 0.00 & 0.31 & 0.00 \\ 0.08 & 0.00 & 0.60 \end{pmatrix} \qquad \frac{1}{2\langle k \rangle}[\langle v_i' v_j' \rangle] = \begin{pmatrix} 0.54 & 0.00 & 0.00 \\ 0.00 & 0.27 & 0.02 \\ 0.00 & 0.02 & 0.18 \end{pmatrix} \tag{3.2}$$

where $\langle k \rangle = (\langle {v_x'}^2 \rangle + \langle {v_y'}^2 \rangle + \langle {v_z'}^2 \rangle)/2$. The principle axes of both tensors are nearly aligned with $(x, y, z)$, indicating that strain and turbulent fluctuations are highest in the dominant contracting direction. Such a result is surprising because the flow is produced by the differential rotation of the discs and one may expect the turbulence to be of the free-shear flow type. We find that the Reynolds stress tensor is diagonal with fluctuation anisotropy coinciding with the contracting/dilating directions. The absence of cross-correlation between the velocity components indicates that the flow is not of the free-shear flow type [108], but is typical of stagnation-point-turbulence. All of the aforementioned results are valid for the $y$-dominant state (exchanging contraction along $x$ with $y$) and all of the Reynolds numbers investigated. In what follows we will consider the $x$-dominant state and the role of stagnation point topology in the production, dissipation, and transport of turbulent kinetic energy.

## 3.4 Turbulent Kinetic Energy budget (TKE)

### 3.4.1 Velocity fluctuations

Velocity fluctuations in the central region are strongly anisotropic and non homogeneous in space, as illustrated in figure 3.5(a) which displays the averaged kinetic

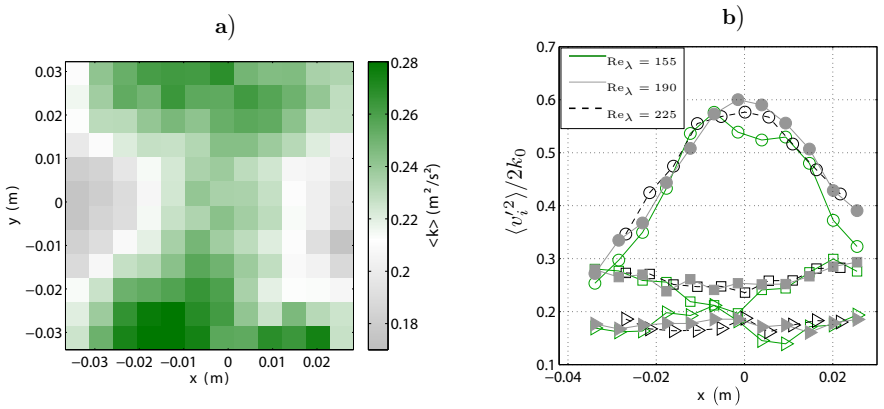


Figure 3.5: (color online). a) section of the mean turbulent kinetic energy $\langle k\rangle = (\langle {v'_x}^2\rangle + \langle {v'_y}^2\rangle + \langle {v'_z}^2\rangle)/2$ in the plane $\Pi_{xy} = (x, y, z = 0)$ measured for the $x$-dominant state at $Re_\lambda = 190$. b) $x$ profiles of the normalized velocity components $\langle {v'_i}^2\rangle(x, 0, 0)/2k_0$ where $k_0 = \langle k\rangle(0, 0, 0)$ as measured for the $x$-dominant state and the 3 Reynolds numbers. ($\circ$) $x$-component. ($\square$) $y$-component. ($\triangleright$) $z$-component. Statistical errors of each quantity, computed from the convergence toward the mean value, are smaller than 2% of the mean. This corresponds at most to the size of the symbols on the graph.

energy of the fluctuations, $\langle k\rangle = (\langle {v'_x}^2\rangle + \langle {v'_y}^2\rangle + \langle {v'_z}^2\rangle)/2$, in the $\Pi_{xy}$ plane. We find that the turbulent fluctuations present a local minimum at $(0, 0, 0)$ along the dilating direction $(x = 0, y, z = 0)$ and a local maximum along the contracting direction $(x, y = 0, z = 0)$. Velocity components along the stable direction displaying increasing anisotropy while approaching the geometric center in the $\Pi_{xy}$ plane (figure 3.5(b)), due primarily to the strong growth in dominant axis fluctuations ($\langle {v'_x}^2\rangle$) contrasting the weakly varying values in the other two components. Increasing anisotropy is understood by examining how velocity fluctuations are amplified or attenuated along a mean trajectory. Given the mean flow in the $x$-dominant state, particles starting at point $M_0 = (x < 0, 0, 0)$ travel directly toward the center and explore the corresponding velocity fluctuations of figure 3.5(b). In the spirit of an analysis using rapid distortion theory [117, 118] we use the Reynolds decomposition $(v_i = \langle v_i\rangle + v'_i)$ to write the equation the velocity fluctuation equation:

$$\partial_t v'_i + \langle v_j\rangle\partial_j v'_i + v'_k\partial_k\langle v_i\rangle = -\frac{1}{\rho}\partial_i p' + \nu\partial_j\partial_j v'_i + v'_k\partial_k v'_i - \langle v'_k\partial_k v'_i\rangle. \tag{3.3}$$

Neglecting the r.h.s. of the equation as a first approximation, this equation reads:

$$\frac{Dv'_i}{Dt} = \partial_t v'_i + \langle v_j\rangle\partial_j v'_i \simeq -v'_k\partial_k\langle v_i\rangle \tag{3.4}$$

and relates the amplification of $v'_x$ along a trajectory (from $x < 0$ to $x = 0$) to the velocity gradient ($\partial_x\langle v_x\rangle < 0$). Conversely, $v'_y$ must decrease as $\partial_y\langle v_y\rangle > 0$. Although our results are observed in a complex geometry, they are similar to findings in pioneering wind tunnel experiments [110]. It is worth mentioning that this first order theory does not explain why the axial fluctuations only vary weakly in space along $x$, which is also true along $y$ and $z$ in all the explored volume $|x, y, z| < 0.4\ R$. Fluctuations are not only distorted by the mean flow along particle trajectories, but are also strongly dissipated close to the center in order to maintain a statistically stationary state. We turn now to a discussion of the turbulent kinetic energy balance.

### 3.4.2 Production and dissipation of turbulence

As previously observed, the stagnation point topology of the mean flow is responsible for the strong anisotropy of velocity fluctuations close to the geometrical center. The anisotropy is larger than in any other canonical flow (wind tunnel, channel, boundary layer, jet or wake), and motivates the investigation of the local production, dissipation, and transport of turbulent fluctuations. A stationary, ensemble averaged Turbulent Kinetic Energy budget is written [109, 108]:

$$\underset{\underline{1}}{\langle v_j\rangle\partial_j\langle k\rangle} + \underset{\underline{2}}{\partial_j\langle v_j' k\rangle} = \underset{\underline{3}}{\mathcal{P}} - \underset{\underline{4}}{\frac{1}{\rho}\partial_j\langle p' v_j'\rangle} + \underset{\underline{5}}{\nu\partial_j\partial_j\langle k\rangle} - \underset{\underline{6}}{\varepsilon}. \tag{3.5}$$

This equation is established far from the propellers where no forcing term is present. Its six terms are: $\underline{1}$ advection of mean kinetic energy $\langle k\rangle = \langle v_i' v_i'\rangle/2$, $\underline{2}$ transport of kinetic energy by turbulent fluctuations, $\underline{3}$ production of turbulent fluctuations $\mathcal{P} = -\langle v_i' v_j'\rangle\partial_i\langle v_j\rangle$, $\underline{4}$ transport due to pressure velocity correlations, $\underline{5}$ diffusion of mean kinetic energy, $\underline{6}$ dissipation $\varepsilon = \nu\langle(\partial_i v_j')(\partial_i v_j')\rangle$. In this equation, if $\nu\partial_j\partial_j\langle k\rangle$ is negligible as compared to dissipation in fully turbulent flows, the pressure-velocity correlation term cannot be measured directly as it would require a measurement of pressure at the particle position. Although this correlation has been found to be much smaller than dissipation in nearly homogeneous turbulent flows [109], it is kept in the budget so that equation 4.6 is rewritten:

$$\langle a_j' v_j'\rangle = \langle v_j\rangle\partial_j\langle k\rangle + \partial_j\langle v_j' k\rangle - \mathcal{P} = -\varepsilon - \frac{1}{\rho}\partial_j\langle p' v_j'\rangle, \tag{3.6}$$

where we have introduced the fluctuating acceleration $a_j' = a_j - \langle a_j\rangle$. In equation (3.6), the first four terms can be computed separately by averaging the Lagrangian data in each bin using the fluctuating velocity $v_j' = v_j - \langle v_j\rangle$ and acceleration $a_j' = a_j - \langle a_j\rangle$, while the various mean fields are interpolated at the positions of the particles. Figures 3.6(a,b) display the $x$ and $y$ profiles (in the mid-plane, $\Pi_{xy}$) of the different terms appearing in equation (3.6) obtained for the $x$-dominant state at $Re_\lambda = 190$. These profiles have been computed on a coarser cartesian grid with $9^3$ bins in order to get better convergence of $\langle\vec{a}'\cdot\vec{v}'\rangle$ and $\langle\vec{v}' k\rangle$ and correspond to raw data without any spatial filtering. These statistics are subject to statistical errors (in the computation of the mean of a given quantity in each bin) inherent in the limited number trajectories ($\mathcal{O}(4000)$) passing through each bin. The error $\sigma$ is defined as the standard deviation of the cumulative mean in the range $N \in [3000, 4000]$ trajectories. The figures are analyzed term by term below.

• Dissipation: the averaged power per unit mass $\langle\vec{a}'\cdot\vec{v}'\rangle$ is found to increase when approaching the center and reaches up to $-2.6$ W/kg. Subtracting the mean flow contribution, $\langle\vec{a}\rangle\cdot\langle\vec{v}\rangle$, is important because $\langle\vec{a}\cdot\vec{v}\rangle$ is found to be proportional, though much larger than the nominal dissipation rate. Our calculation of local dissipation should be compared to other estimates obtained from the zero crossing of the acceleration auto-correlation function, $\tau_0 \simeq 2.2\ \tau_\eta$, [90, 9, 60] which gives $(\tau_{0,x}, \tau_{0,y}, \tau_{0,z}) = (4.7, 4.4, 3.9)$ ms leading to $\varepsilon \in [1.8, 2.6]$ W/kg . This result holds for all bins on the Cartesian grid at each Reynolds number investigated and we conclude that $\langle\vec{a}'\cdot\vec{v}'\rangle$ is a reasonable estimate of the dissipation as the pressure-velocity transport term is smaller than $0.2 - 0.3\varepsilon$. The latter quantity is estimated as the difference between the value of $\varepsilon$ calculated from the acceleration auto-correlation

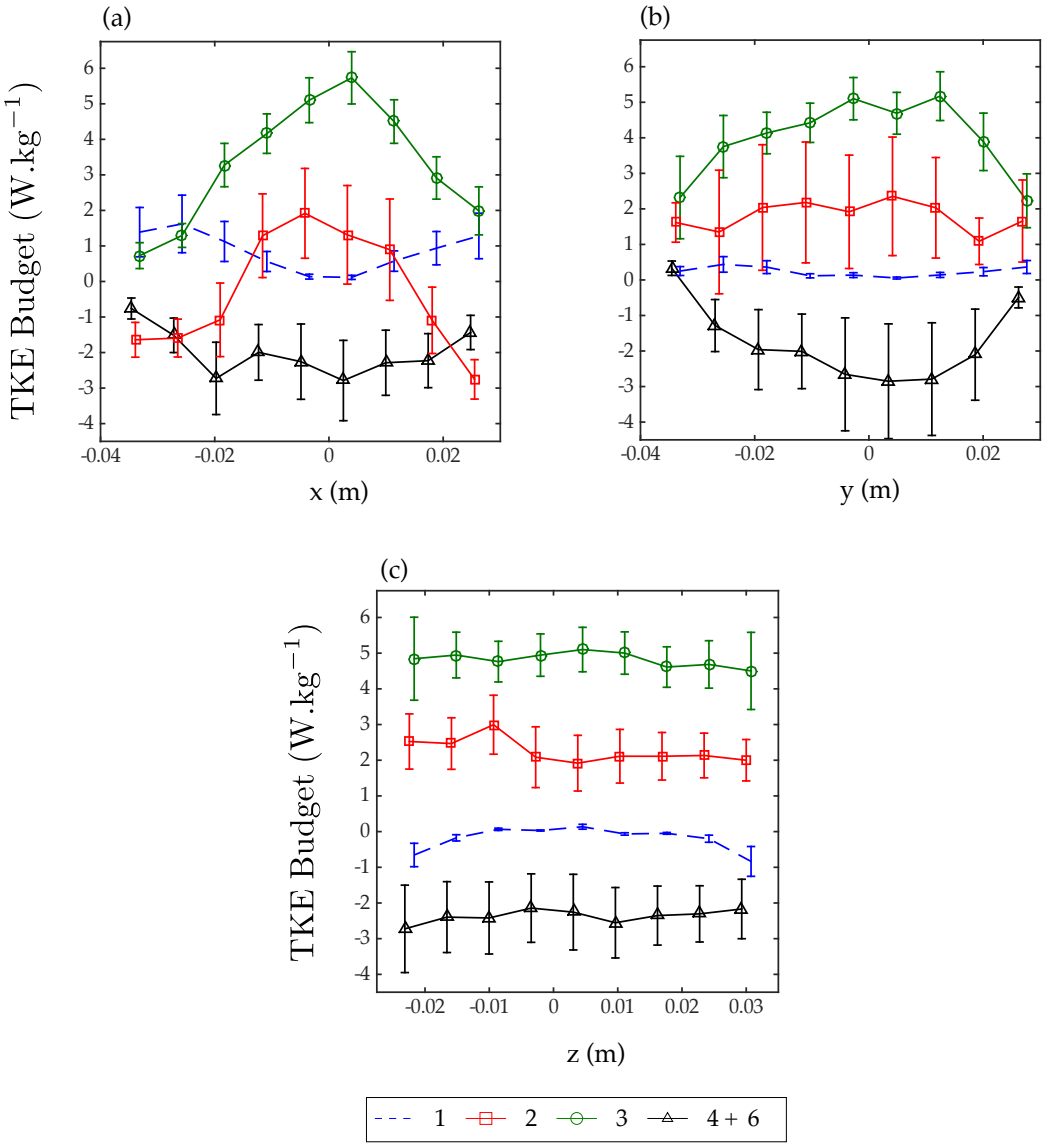


Figure 3.6: (color online) Figure a): $x$-profiles of the different terms of equation (4.6) plotted along the line $(x, y = 0, z = 0)$ for the $x$-dominant state at $Re_\lambda = 190$. $(--)$: advection of mean kinetic energy $\langle v_j \rangle \partial_j \langle k \rangle = \underline{1}$, $(\square)$: turbulent transport term $\partial_j \langle v'_j k \rangle = \underline{2}$. $(\circ)$: production of turbulence $\mathcal{P} = -\langle v'_i v'_j \rangle \partial_i \langle v_j \rangle = \underline{3}$. $(\triangle)$: averaged power per unit mass $\langle a'_j v'_j \rangle = \underline{4} + \underline{6}$. Figure b): $y$-profiles of the same quantities plotted along the line $(x = 0, y, z = 0)$ with the same legend. Figure c): $z$-profiles of the same quantities plotted along the line $(x = 0, y = 0, z)$ with the same legend. The error on the plots is given by $\pm 3\sigma$ where $\sigma$ is defined as the standard deviation of the cumulative mean of each quantity in the range $N \in [3000, 4000]$ trajectories.

function zero-crossing and local value of $\langle \vec{a}' \cdot \vec{v}' \rangle$.

• Production of turbulence: figures 3.6(a,b) demonstrate that the production term is positive and locally exceeds dissipation by nearly a factor 2 close to the stagnation point. Such large production in a turbulent flow is unusual, although it has been observed for instance in a non stationary mixing layer [119] and in the buffer layer of a channel flow [109], $\mathcal{P} \simeq \varepsilon$ is more typical in inhomogeneous flows. However, the mean flow serves to reinforce turbulent fluctuations in the $x$-direction where the strain is strongest, giving $\mathcal{P} \simeq -\langle {v'_x}^2 \rangle \partial_x \langle v_x \rangle - \langle {v'_y}^2 \rangle \partial_y \langle v_y \rangle - \langle {v'_z}^2 \rangle \partial_z \langle v_z \rangle \simeq 5$ W.kg$^{-1}$. This dissipation deficit translates an overly efficient extraction of kinetic energy from the mean flow in the central region and requires a compensatory mechanism.

• Transport of turbulent fluctuations: the transport of kinetic energy has two distinct contributions, advection of mean kinetic energy $\langle \vec{v} \rangle \cdot \vec{\nabla} \langle k \rangle$ and transport by fluctuations $\vec{\nabla} \cdot \langle \vec{v}' k \rangle$. The latter is found to be dominant near the geometrical center where both the mean flow and the gradient of mean kinetic energy vanish. It is found positive in a sphere of radius $r = \sqrt{x^2 + y^2 + z^2} \simeq 2$ cm so that an amount of energy nearly equivalent to the local value of $\varepsilon$ is transported outwards from the center of the flow. However the flux is very anisotropic, and depends strongly on the distance to the center as was demonstrated in a cylindrical vessel using an alternative approach [115]. Indeed, we observe advection of mean kinetic energy and turbulent transport in near equal proportions along the $x$-direction while the turbulent flux of energy always corresponds to a loss in the $y$-direction. Although the mean properties of the turbulence vary weakly near the geometrical center, our observations indicate that the counter rotating von Kármán flow should not be considered a quasi-homogeneous turbulent flow.

## 3.5 Variance transport equations

The TKE budget provides an overall view of Eulerian dynamics in the von Kármán flow, in particular the transport of kinetic energy by velocity fluctuations at the stagnation point renders the flow inhomogeneous. It is possible to gain further insight into the anisotropic nature of this transport and further consequences by calculating the transport equations of the velocity variances. The transport equation of the Reynolds stress tensor $\langle v'_i v'_j \rangle$ may be written:

$$\frac{\mathrm{D}\langle v'_i v'_j \rangle}{\mathrm{D}t} = \mathcal{P}_{ij} + \mathcal{R}_{ij} - \varepsilon_{ij} - \partial_k \mathcal{T}_{kij}, \tag{3.7}$$

where $\mathcal{T}_{kij}$ represents a Reynolds stress-flux term, $\varepsilon_{ij}$ is the viscous dissipation term, $\mathcal{R}_{ij}$ is the pressure redistribution term and $\mathcal{P}_{ij}$ is the production term. These terms are then defined by:

$$\mathcal{P}_{ij} = -\langle v'_i v'_k \rangle \partial_k \langle v_j \rangle - \langle v'_j v'_k \rangle \partial_k \langle v_i \rangle, \tag{3.8}$$

$$\mathcal{R}_{ij} = \langle p' (\partial_j v'_i + \partial_i v'_j)/\rho \rangle, \tag{3.9}$$

$$\varepsilon_{ij} = 2\nu \langle \partial_k v'_i \partial_k v'_j \rangle, \tag{3.10}$$

$$\mathcal{T}_{kij} = \mathcal{T}^v_{kij} + \mathcal{T}^p_{kij} + \mathcal{T}^\nu_{kij}, \tag{3.11}$$

where $\mathcal{T}^u_{kij} \equiv \langle v'_i v'_j v'_k \rangle$, $\mathcal{T}^p_{kij} \equiv \rho^{-1} \langle v'_i p' \rangle \delta_{jk} + \rho^{-1} \langle v'_j p' \rangle \delta_{ik}$, and $\mathcal{T}^\nu_{kij} \equiv -\nu \partial_k \langle v'_i v'_j \rangle$ [109]. Taking into account the symmetry in the central region of the von Kármán

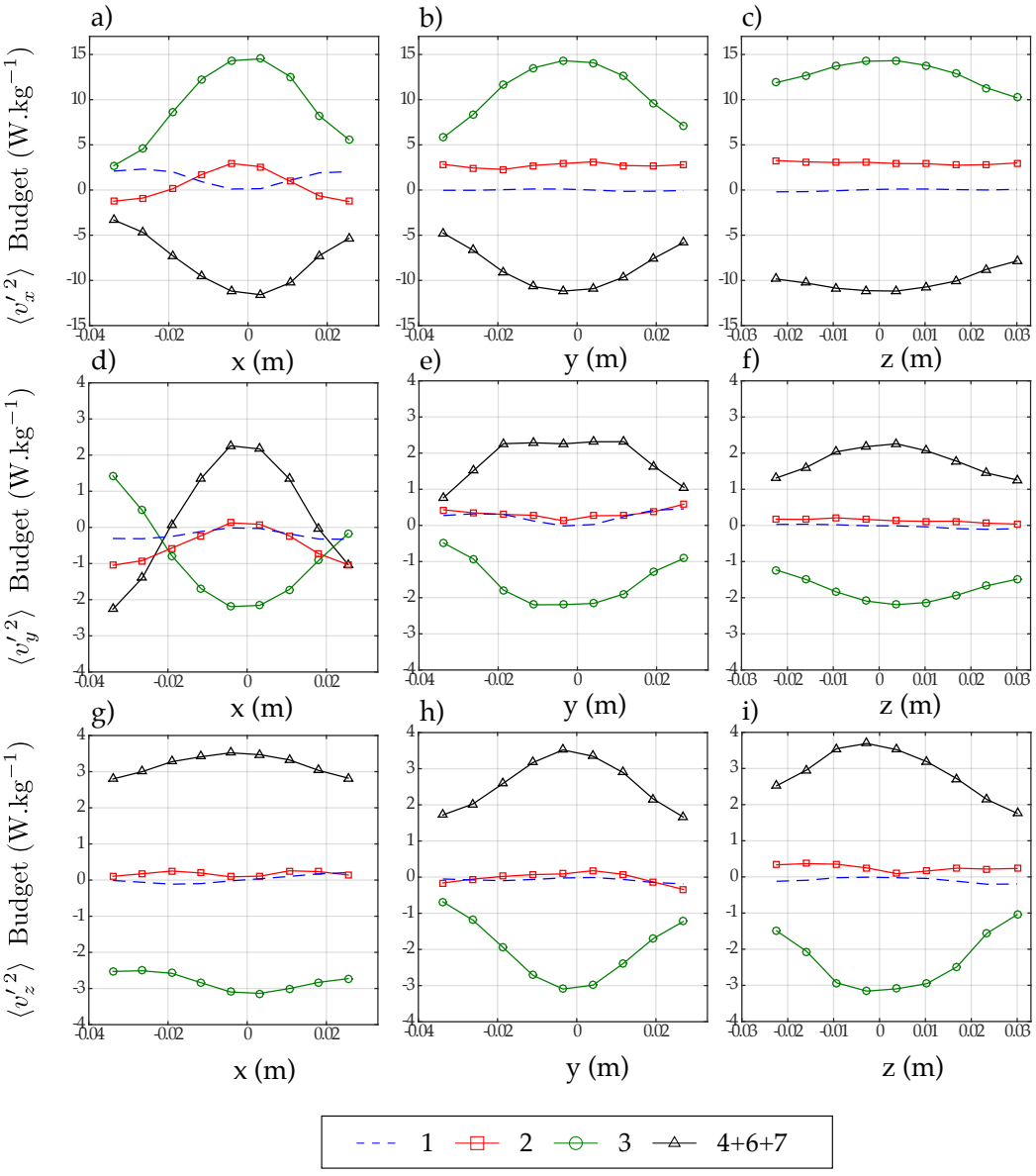


Figure 3.7: Variance transport terms for $\langle v_j'^2 \rangle$ (a-i) along the converging ($x$: a,d,g) and diverging ($y$: b,e,h, $z$: ,c,f,i) directions in the $x$-dominant state at $\mathrm{Re}_\lambda = 190$. $x$ profiles are traced along the line $(x, y = 0, z = 0)$, $y$ profiles are traced along the line $(x = 0, y, z = 0)$ and $z$ profiles are traced along the line $(x = 0, y = 0, z)$. **Figures (a-i):** Terms refer to equation 3.12 $(--)$: Advection of mean kinetic energy $\langle v_k \rangle \partial_k \langle v_j'^2 \rangle = \underline{1}$, $(\square)$: Turbulent transport $\partial_k \langle v_k' v_j'^2 \rangle = \underline{2}$. $(\circ)$: Production of turbulence $-2\langle v_j'^2 \rangle \partial_k \langle v_j \rangle = \underline{3}$. $(\triangle)$: Component wise contribution to averaged power per unit mass $2\langle a_j' v_j' \rangle = \underline{4} + \underline{6} + \underline{7}$. No summation is implied over $j$. The error on all plots are similar to figure 3.6.

flow, *i.e.* $\langle v_i' v_j' \rangle = 0$ for $i \neq j$, the Reynolds stress equations [2] result in equations for the velocity variances for the $j$ component:

$$\begin{array}{ccccccccc} \langle v_k \rangle \partial_k \langle v_j'^2 \rangle & + & \partial_k \langle v_k' v_j'^2 \rangle & = & - & 2\langle v_j'^2 \rangle \partial_k \langle v_j \rangle & - & 2\partial_j \langle u_j' p' \rangle / \rho. \\ \underline{1} & & \underline{2} & & & \underline{3} & & \underline{4} \\ & & & & + & \nu \partial_k \partial_k \langle v_j'^2 \rangle & - & 2\nu \langle (\partial_k u_j')(\partial_k u_j') \rangle \\ & & & & & \underline{5} & & \underline{6} \\ & & & & - & 2\langle p' (\partial_j u_j') \rangle / \rho, & & \\ & & & & & \underline{7} & & \end{array} \tag{3.12}$$

where no summation occurs over $j$. The terms are essentially the same as equation (4.6) which is obtained by taking the half sum of the three components. The supplementary term, $\underline{7} = 2\langle p'(\partial_j v_j') \rangle / \rho$, is the main source of energy transfer among the components and allows energy to be taken from the turbulent fluctuations and converted into a mean-flow exiting the stagnation point. This term is not found in equation (4.6) because it sums to zero due to the incompressible nature of the flow. The component-variance budgets are plotted in figure 3.7(a-i).

### 3.5.1 Negative Production of Turbulence

Turbulent flows must be constantly forced to produce a stationary state. Examples may include channel and boundary layer flows as well as the von Kármán flow investigated here. Conversely a turbulent flow with no production mechanism eventually undergoes decay, as is this case in wind tunnel flows where turbulence is produced at the grid but the transported downstream by the mean flow. The absence of production far from the grid creates a spatially inhomogeneous flow that eventually decays rapidly to a laminar flow far from the turbulence input. The difference between these two classes is the presence, or absence, of a production mechanism which renders equation (3.8) globally positive thus keeping turbulent fluctuations in the system. However, mechanisms exists by which the production term may be negative and will serve to break down turbulent fluctuations into energy used to sustain the mean-flow. In the von Kármán flow, this occurs in the diverging directions, while the converging directions assures the creation of turbulent fluctuations. This case is investigated below.

Considering $\langle v_x'^2 \rangle / 2$ along the converging (respectively diverging) direction in figure 3.7(a) (resp. b & c) the budget is qualitatively similar to the full TKE budget in figure 3.6(a) (resp. b & c). This observation underscores the predominance of the single converging direction in the turbulent kinetic energy budget of a stagnation point. From the TKE budget in figure 3.6(a,b,c) a turbulent transport is established such that $\partial_j \langle v_j' k \rangle \simeq \varepsilon$. However, the budgets for $\langle v_y'^2 \rangle$ and $\langle v_z'^2 \rangle$ (figure 3.7 (d-f) and (g-i)) indicate that the transport by turbulent fluctuations in these components is negligible. This implies that though a turbulent energy flux is directed outwards from the stagnation point; only the converging component's fluctuations are transported. Consequently, the stagnation point of the von Kármán flow is inhomogeneous, but the inhomogeneity is restricted the converging component while

2. Note that the definitions of the various Reynolds stress tensor transport equation terms are essentially the same as those that were found in the TKE budget. However, there will be a factor of two that routinely appears when considering the variance budget. This is due to the manner in which equation 3.7 is derived.

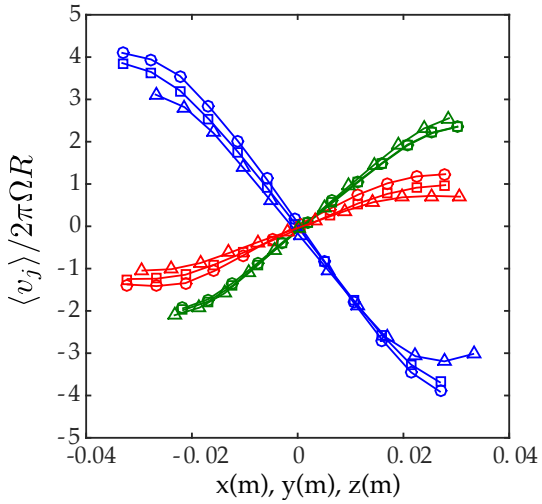


Figure 3.8: Normalized mean velocity. Various colors refer to the velocity components along the corresponding axis. Blue: x, red: y, green: z. Symbols refer to $\mathrm{Re}_\lambda$. ($\circ$) : $\mathrm{Re}_\lambda = 155$. ($\square$) : $\mathrm{Re}_\lambda = 190$. ($\triangle$) : $\mathrm{Re}_\lambda = 225$. Collapse of curves indicates similar meanfield will generate similar production and "negative production" of turbulent fluctuations.

the diverging components may be considered quasi-homogeneous with a turbulent flux nearly an order of magnitude smaller than in the converging component. This observation will have an effect on the Lagrangian transport of particles to be discussed in the following chapter.

The lack of turbulent transport in the diverging components implies that $\langle v'_y a'_y \rangle = -\mathcal{P}_{yy}$ (idem. for $z$), where the left hand side represents the pressure and dissipative terms. From figure 3.7(d-f), $\langle v'_y a'_y \rangle > 0$ indicating the presence of "negative production" of turbulence ($\mathcal{P}_{ii} < 0$). For a purely diagonal Reynolds tensor, the sign of production is determined uniquely by the sign of the velocity gradient. Thus, negative production occurs in the diverging direction where the velocity gradient is positive (figure 3.8). For the "negative production" (or destruction) of turbulence, the component balance (eq. 3.12) requires that $\langle p'(\partial_y v'_y)\rangle/\rho - \partial_y \langle v'_y p' \rangle/\rho - \nu \langle (\partial_y v'_j)(\partial_y v'_j)\rangle > 0$ and vice versa in the case of production. In the former case the combined effect of the pressure terms must be larger than the dissipation term, which is positive definite. In section 3.4, $-\partial_y \langle v'_y p' \rangle/\rho$ was estimated to be small ($\leq 0.3 \mathrm{W.kg}^{-1}$ per component). Thus the pressure rate of strain tensor has a key role in establishing negative production in the diverging components.

The physical interpretation of "negative production" of turbulence is evident when comparing the TKE budget (eq. 4.6) with the mean-flow kinetic energy budget:

$$\langle v_j \rangle \partial_j \langle E \rangle + \partial_j \langle v_j \rangle \langle v'_i v'_j \rangle = -\mathcal{P} - \frac{1}{\rho} \partial_j \langle p \rangle \langle v_j \rangle + \nu \partial_j \partial_j \langle E \rangle - \widehat{\varepsilon}, \tag{3.13}$$

where $\langle E \rangle = (\langle v_i \rangle \langle v_i \rangle)/2$ is the mean kinetic energy, and $\widehat{\varepsilon} = \nu (\partial_i \langle v_j \rangle)(\partial_i \langle v_j \rangle)$ the mean pseudo-dissipation. Comparing equation 3.13 with equation 4.6, the main difference is the sign in front of the production terms ($\mathcal{P}$) which indicates that production ($\mathcal{P} > 0$) adds to turbulent fluctuations to the detriment of the mean flow. Conversely, "negative production" ($\mathcal{P} < 0$) pumps energy from the turbulent

fluctuations and converts it to energy in the meanfield. This is an understandable situation for the diverging components at the stagnation point which must create a mean flow outward to preserve the divergence free nature of the flow. The following paragraph proposes a mechanism by which the negative production in the diverging components is fed by the over production of the converging components via inter-component energy transfer.

### 3.5.2 Intercomponent transfer of energy

One of the difficulties alluded to previously in calculating the TKE budget is that no measurement is available at the particle position for the pressure. As a result, there is very little experimental evidence for the role of pressure in turbulent flows. Existing measurements calculate equation (3.9) indirectly by measuring all other terms and taking the remaining balance equal to the pressure terms [120]. Consequently, the cumulative error of the measurement technique is mixed with these terms rendering them the most uncertain. The approach taken below to investigate the component-wise budgets is in this line of reasoning.

DNS have provided some insight into the role of the pressure terms with benchmark simulations in a boundary layer [121] and a channel flow [122] indicating that the pressure transport term reach a maximum in the buffer layer near $y^+ \simeq 10$ but account for less than 10% of the turbulence production in this region. The particularity of this region is that it is where the production is maximal, likening it to the stagnation point region in the von Kármán where strain is maximal. From the estimates in section 3.4, it was found that $\partial_j \langle v_j' p' \rangle / \rho \simeq 0.2 - 0.3 \mathrm{W.kg}^{-1}$, equivalent to approximately 10% of the estimated dissipation rate. The von Kármán, channel, and boundary layer flows both have $\mathcal{P}/\varepsilon \simeq 2$ and a ratio of $\frac{1}{\rho}\partial_j \langle v_j' p' \rangle / \varepsilon \simeq 0.1$. Pressure transport is always among the weakest of all the contributing terms, as is assumed to be the case in the von Kármán flow. The similarity of these aspects of the budget equations is all the more striking in that the former relationship is at the upper end of all of the well known canonical flows [109], even when the forcing mechanisms in the boundary layer and von Kármán flow are completely different.

The pressure rate of strain term in equation (3.7) contains a term that contributes uniquely to the component budget and has no contribution the TKE budget:

$$\langle p' \partial_j v_j' \rangle = 0, \tag{3.14}$$

where summation is implied over the repeated indices. When considering the component budget, these terms are sometimes referred to as the "Robin Hood" terms [123]. Numerical simulations [121] indicate that they may rival the production and dissipative terms in magnitude and serve to redistribute the energy among the components. Typically energy is extracted from the strongest component, $\langle {v_x'}^2 \rangle$ in the x-dominant stagnation point, and delivered to the weakest $\langle {v_y'}^2 \rangle$ and $\langle {v_z'}^2 \rangle$, implying:

$$\langle p' \partial_x v_x' \rangle = -(\langle p' \partial_y v_y' \rangle + \langle p' \partial_z v_z' \rangle) \tag{3.15}$$

where loss on the left hand side implies equal gain on the right hand side. Considering the similarity in the pressure transport terms in the von Kármán and numerical simulation, the redistributive behavior of the pressure rate of strain terms is expected to exist in the von Kármán flow (figure 3.7).

### 3.5.3 Evaluating the Pressure Rate of Strain Tensor : $\mathcal{R}_{ij}$

Similar to the observations of the TKE budget, the component-wise budget displays a large amount of production that is not accounted for alone by the dissipation. The role of the pressure rate of strain tensor will be to take an over-abundance of turbulent fluctuations and make them available for conversion into mean flow kinetic energy. To investigate this process the variance transport equations are written for each component at the center of the flow, taking into account observations from figure 3.7:

$$\partial_k\langle {v'_x}^2 v'_k\rangle + 2\langle {v'_x}^2\rangle\partial_x\langle v_x\rangle = -2\nu\langle\partial_k v'_x\partial_k v'_x\rangle - 2\partial_x\langle p'v'_x\rangle/\rho + 2\langle p'\partial_x v'_x\rangle/\rho, \quad (3.16)$$

$$+2\langle {v'_y}^2\rangle\partial_y\langle v_y\rangle = -2\nu\langle\partial_k v'_y\partial_k v'_y\rangle - 2\partial_y\langle p'v'_y\rangle/\rho + 2\langle p'\partial_y v'_y\rangle/\rho, \quad (3.17)$$

$$+2\langle {v'_z}^2\rangle\partial_z\langle v_z\rangle = -2\nu\langle\partial_k v'_z\partial_k v'_z\rangle - 2\partial_z\langle p'v'_z\rangle/\rho + 2\langle p'\partial_z v'_z\rangle/\rho, \quad (3.18)$$

where the diffusion of mean fluctuations term ($\nu\partial_k\partial_k\langle {v'_j}^2\rangle$) has been neglected. The kinematic consequence of equation (3.7) is that right hand sides of the above equations are equal to $2\langle v'_j a'_j\rangle$:

$$\begin{aligned} 2\langle v'_j a'_j\rangle &= -2\nu\langle\partial_k v'_j\partial_k v'_j\rangle - 2\partial_j\langle p'v'_j\rangle/\rho + 2\langle p'\partial_j v'_j\rangle/\rho. \\ &= \quad -\varepsilon_{jj} \quad - \partial_j\mathcal{T}^p_{jjj} \quad + \mathcal{R}_{jj} \end{aligned} \quad (3.19)$$

Using equations (3.16), (3.17), (3.18) & (3.19) calculation of the pressure rate of strain tensor in the framework of locally isotropic and axisymmetric dissipative scales is proposed.

• Locally isotropic turbulence: The small scale velocity gradients are not necessarily isotropic, however, local isotropy is a useful hypothesis which permits an easy estimation of the dissipation rate with prior knowledge of the longitudinal velocity gradient,

$$\widetilde{\varepsilon} = \frac{1}{2}\varepsilon_{jj} = \nu\langle\partial_k v'_j\partial_k v'_j\rangle = 15\nu\langle(\partial_1 v'_1)^2\rangle, \quad (3.20)$$

where the index "1" refers to an arbitrary chosen axis in a cartesian reference frame that is equal to any other by the assumption of isotropy. The typical length for these gradients is normally referred to as the Taylor scale $\lambda$ whose definition follows from equation (3.20). Assuming local isotropy at small scales, the dissipation tensor is isotropic, i.e. $\varepsilon_{ij} = \frac{2}{3}\widetilde{\varepsilon}\delta_{ij}$, meaning that its diagonal terms are nearly equal. DNS by [121] shows that in a boundary flow this hypothesis is nearly verified, though in the inner-layer region dissipation becomes highly anisotropic.

With this approximation, an estimation of the local dissipation rate from table 3.1 implies that $\varepsilon_{jj}/2 \simeq$ 0.7 W.kg$^{-1}$ per component. Further assumption of local isotropy for the pressure transport term which was assumed to have a magnitude of 0.3 W.kg$^{-1}$, gives $\partial_j\langle p'v'_j\rangle/2\rho \simeq 0.1$ W.kg$^{-1}$ (no summation implied) per component. With the these hypotheses and the above system of three equations with three unknowns, it is possible to estimate the contribution of the pressure rate of strain term to each component's budget. The results are given in table 3.2 for the central region of the von Kármán.

• Axisymmetric turbulence: Even though the most part of turbulence experiments use equation 3.20 as an estimate of dissipation in a given flow, evidence indicates that such a situation is idealized, if not nonexistent in practice [120]. Theoretical attempts have been made to formalize so-called axisymmetric turbulence while numerical and

| Budget | $\langle v'_j a'_j \rangle$ | $-\mathcal{R}_{jj}/2$ | $\partial_j \mathcal{T}^p_{jjj}/2$ | $-\varepsilon_{jj}/2$ | $\mathcal{P}_{jj}/2$ |
|---|---|---|---|---|---|
| - | W.kg$^{-1}$ | W.kg$^{-1}$ | W.kg$^{-1}$ | W.kg$^{-1}$ | W.kg$^{-1}$ |
| $\langle v'^2_x \rangle/2$ | -5.6 | 4.8 | 0.1 | -0.7 | 7.1 |
| $\langle v'^2_y \rangle/2$ | 1.1 | -2.0 | 0.1 | -0.7 | -1.1 |
| $\langle v'^2_z \rangle/2$ | 1.8 | -2.8 | 0.1 | -0.7 | -1.5 |

Table 3.2: Locally isotropic estimation of pressure rate of strain tensor ($\mathcal{R}_{ij}$) from component wise $\langle v'^2_j \rangle/2$ budgets. The values read such that $\langle v'_j a'_j \rangle - \mathcal{R}_{jj}/2 + \partial_j \mathcal{T}^p_{jjj}/2 = -\varepsilon_{jj}/2$. A check on the budget is $\langle v'_j a'_j \rangle \simeq -\mathcal{P}_{jj}/2$ except for the $\langle v'^2_x \rangle/2$ budget where there is a significant turbulent flux. A sum on the columns gives the terms as they would appear in the TKE budget. The discrepancy observed in the z component is within the estimated errors of $\langle v'_j a'_j \rangle$.

experimental efforts have been made to study it. Strain dominated flows are ideal in this endeavor [38, 124]. One may assume as a first approximation that the stagnation point studied is axisymmetric when investigating the mean strain (eq. 3.8) and Reynolds tensor (eq. 3.2). Generally, this will mean that,

$$\varepsilon = \varepsilon_{\parallel} + 2\varepsilon_{\perp}, \tag{3.21}$$

where $\varepsilon_{\parallel}$ is in the converging direction and $\varepsilon_{\perp}$ is in the diverging direction and each contains various terms belonging to the dissipation tensor $\varepsilon_{ij}$. However, the single particle statistics considered here do not permit the measurement of spatial gradients. Thus, the estimation of the relative amount of the total dissipation in $\varepsilon_{\perp}$ and $\varepsilon_{\parallel}$ will be made by comparing a DNS study at intermediate $\mathrm{Re}_\lambda = 100$ [38] with *axisymmetric contraction* with the von Kármán stagnation point which is typified by *axisymmetric expansion*.

In a flow undergoing constant strain, the time at which production of turbulence was maximum - corresponding to particles at the von Kármán stagnation point - the velocity gradients in the extensional directions became asymptotically small compared to the gradients in the compressive direction, i.e. $\varepsilon_{\perp} = \nu \langle \partial_k v'_{\perp} \partial_k v'_{\perp} \rangle \sim 0$. This corresponds to situation of vortex stretching where the enstrophy component in the expanding direction is nearly an order of magnitude larger than the orthogonal components. In the axisymmetric contraction DNS [38], this implies that the dissipation is determined by to the velocity gradients in the converging direction, i.e. $\varepsilon \sim \varepsilon_{\perp}$. If this result is extended to axisymmetric expansion, the dissipation at the von Kármán stagnation point is also set by the velocity gradients in the converging direction, which instead corresponds to $\varepsilon \sim \varepsilon_{\parallel}$. From table 3.2 the pressure rate of strain terms provide a satisfactory closure to the variance budget within statistical error.

The goal of estimating the pressure rate of strain correlation was to understand how energy is transferred among the components which permits an illustrative interpretation of the stagnation point. An enormous amount of turbulent fluctuations are produced by the stagnation point, so much so that only a fraction of it is dissipated while the rest is transported outwards. The incompressible nature of the flow permits a coupling between the velocity components by the pressure field via the pressure rate of strain tensor, $\mathcal{R}_{ij}$. This term is strongly negative in the converging direction, and positive in the diverging directions, indicating that energy is transferred from the former to the latter. In the idealized situation where $\varepsilon_{\perp} \sim 0$,

| Budget | $\langle v'_j a'_j \rangle$ | $-\mathcal{R}_{jj}/2$ | $\partial_j \mathcal{T}^p_{jjj}/2$ | $-\varepsilon_{jj}/2$ | $\mathcal{P}_{jj}/2$ |
|---|---|---|---|---|---|
| - | W.kg$^{-1}$ | W.kg$^{-1}$ | W.kg$^{-1}$ | W.kg$^{-1}$ | W.kg$^{-1}$ |
| $\langle v'^2_x \rangle/2$ | -5.6 | 3.4 | 0.1 | -2.1 | 7.1 |
| $\langle v'^2_y \rangle/2$ | 1.1 | -1.2 | 0.1 | -0 | -1.1 |
| $\langle v'^2_z \rangle/2$ | 1.8 | -2.2 | 0.1 | -0 | -1.5 |

Table 3.3: Axisymmetric estimation of pressure rate of strain tensor ($\mathcal{R}_{ij}$) from component wise $\langle v'^2_j \rangle/2$ budgets. The values read such that $\langle v'_j a'_j \rangle - \mathcal{R}_{jj}/2 + \partial_k \mathcal{T}^p_{jjj}/2 = -\varepsilon_{jj}/2$. A check on the budget is $\langle v'_j a'_j \rangle \simeq -\mathcal{P}_{jj}/2$ except for the $\langle v'^2_x \rangle$ budget where there is a significant turbulent flux. A sum on the columns gives the terms as they would appear in the TKE budget. The discrepancy observed in the z component is within the estimated errors of $\langle v'_j a'_j \rangle$.

negative production results directly from the pressure rate of strain transfer,

$$\frac{\mathcal{P}_{jj}}{2} = -\langle v'^2_j \rangle \partial_j \langle v_j \rangle \simeq \langle p' \partial_j v'_j \rangle. \qquad j = y, z \tag{3.22}$$

Thus, the negative production responsible for the creation of a mean flow that removes fluid from the stagnation point is fed by the pressure rate of strain term which removes energy from the velocity fluctuations in the converging direction. It should be noted that this prediction is a result of the strong anisotropy brought about by the stagnation point. As particles explore regions with smaller strain rates, isotropy is expected to be restored. A quick return to isotropy is a recurrent observation in experiments [124] and simulations [38] and is strengthened by increasing the Reynolds number.

## 3.6 Conclusion

A first and very general result of the present study concerns local energy dissipation, a quantity very difficult to estimate in fully turbulent flows due to the high spatial resolution needed to resolve small-scale velocity gradients. Here we demonstrated that $\langle \vec{a}' \cdot \vec{v}' \rangle = \langle \vec{a} \cdot \vec{v} \rangle - \langle \vec{a} \rangle \cdot \langle \vec{v} \rangle$ is a good proxy for the local dissipation $\varepsilon \simeq -\langle \vec{a}' \cdot \vec{v}' \rangle$ in the bulk of the flow, away from regions where energy is injected. By resolving the acceleration of the particles in a non homogeneous flow, it is possible to estimate the local dissipation using only one-particle statistics, without computing spatial velocity increments as is usually done when estimating dissipation from Eulerian structure functions [9]. Our approach complements the result $\langle \delta\vec{a} \cdot \delta\vec{v} \rangle = -2\varepsilon$, derived in the context of homogeneous turbulence [125], which requires a higher particle concentration as it involves the computation of spatial increments of acceleration and velocity between two particles [126] and makes particle tracking harder.

A second and original result, specific to the present von Kármán flow, concerns its temporal dynamics. By a careful inspection of trajectories obtained from each movie, we demonstrated that the flow is bistable due to the presence of coherent structures attached to the walls, a consequence of the square tank geometry. Conditioning the dataset on the two states we have reconstructed corresponding mean flows and demonstrated a rotation of $\pi/2$ around the axis of rotation. Consequently,

the present bistability is different from those observed in similar flows produced in a cylindrical vessel for which the different states mirror each other in a reflexion about the mid-plane $z = 0$ [29, 105, 116, 127]. Further work is needed to fully characterize the reversals and their temporal dynamics, and to test modeling approaches typically used in confined flows or more generally, techniques pertaining to turbulent multi-stability such as [105, 104, 128]. For a given state, one transverse component dominates the other resulting in an impinging jet topology oriented towards the center and parallel to the $x$ or $y$ axis, depending on the bistable state. In such configuration, the flow has a stagnation point near the center which is responsible for the large anisotropy which is most accentuated in the direction of largest strain.

By a careful investigation of the turbulent kinetic energy budget, we demonstrated the extent to which the stagnation point topology, with only one stable direction and two unstable directions, is efficient at extracting energy from the mean flow. This was confirmed by our finding that the production of turbulence is nearly twice the dissipation. Production to dissipation ratios ($\mathcal{P}/\varepsilon$) locally larger than unity are not uncommon in regions responsible for the generation of turbulence, such as the near wall region of boundary layer flows. However, the measurement of $\mathcal{P}/\varepsilon \simeq 2$ in the center of the vessel, several integral scales away from where the flow is forced, is unexpected.

As a consequence of such strong energy extraction, a significant part of turbulent kinetic energy, of the same order of magnitude as $\varepsilon$, is transported by turbulent fluctuations so that such a flow should be seen as strongly non homogeneous in space, even in the central region. Such a result is not specific to the square tank geometry, and should hold when a stagnation point is present with a high level of anisotropy. This is confirmed by the data reported in [9], measured in the stagnation point of von Kármán flow produced in a cylindrical vessel, for which an estimate of the production term is found larger than dissipation. Voth *et al.* performed Lagrangian measurements at the stagnation point of a von Kármán flow produced in a cylindrical container [9]. They found the flow anisotropy is $u'_x \simeq u'_y \simeq 1.54u'_z$, and reported the mean gradient tensor is almost diagonal with $\partial\langle v_z\rangle/\partial z \simeq u'/L_g$, $L_g = 0.0492$ m, and $u'^2 = (u'^2_x + u'^2_y + u'^2_z)/3 \simeq 1.9u'^2_z$. This leads to a production term $\mathcal{P} \simeq 1.37u'^2_z\partial\langle v_z\rangle/\partial z \simeq 0.72u'^3/L_g$ slightly larger than the local value of $\varepsilon = u'^3/L$, $L = 0.073$ cm, estimated using the second order velocity structure function.

A complementary study of the variance transport equations reveals that of the turbulent diffusive flux set up to counter balance the insufficient dissipation in the central region is comprised of mostly fluctuations belonging to the converging direction ($x$). This permits a qualified statement regarding the inhomogeneity in an axisymmetrically expanding stagnation point: strong inhomogeneity in the converging component creates a turbulent flux transporting the variance of this component ($\langle v'^2_x\rangle$) while the diverging components have relatively homogeneous fluctuations in the measurement volume and have negligible flux. This point will be of consequence while investigating the role of an inhomogeneous flow topology, and therefore non-stationarity, on relevant small scale statistics and Lagrangian transport of particles.

# Chapter 4

# Non-stationarity: from an Eulerian to a Lagrangian perspective.

The previous chapter investigated the mean-flow topology by an Eulerian approach to Lagrangian data. This approach proved adequate to calculate up to third order moments and the relevant fluxes. In general it may be said that an inhomogeneous Eulerian field begets non-stationary Lagrangian statistics as particles wander from one part of the flow to another. In this chapter the Lagrangian perspective is considered, in particular the consequences that an underlying Eulerian field will have on Lagrangian statistics are investigated.

Formally, a trajectory is defined by its natural variables: time $t$ and initial positions $\vec{\gamma}$ (defined to be at $t = t^*$). The position of a particle at time $t$ which initially was at $\vec{\gamma}$ is given:

$$\vec{X}_\gamma(t), \tag{4.1}$$

where $\vec{X}_\gamma(t^*) = \vec{\gamma}$. The Lagrangian velocity is then defined as:

$$\vec{V}(t) = \dot{\vec{X}}_\gamma(t). \tag{4.2}$$

The Eulerian velocity at a point $\vec{X}_\gamma(t)$ coincides with that of the fluid particle at the same place and time. The Eulerian velocity field is then related to the Lagrangian velocity by :

$$\vec{v}(\vec{X}_\gamma(t), t) = \vec{V}(t). \tag{4.3}$$

This is illustrated in figure 4.1 where an ensemble of particles is considered with the condition that at some point in time along each trajectory, occurring at $t^* = 0$, a point in space $\vec{X}_\gamma(t^*)/\eta = (0, 0, 0)$ is visited. For example, an ensemble average of the mean velocity at $\vec{X}_\gamma(t^*)/\eta = (0, 0, 0)$ is a velocity average over trajectories marked at $t^* = 0$ and is equal to the average value of the Eulerian velocity field at $\vec{\gamma}$ : $\langle \vec{V}(t^*) \rangle = \langle \vec{v}(\vec{X}_\gamma(t^*), t^*) \rangle$. This was the principle behind the Eulerian conditioning of the Lagrangian trajectories used in the previous chapter. The trajectories are selected to coincide with the x-dominant bistable state as described in section 3.3. Consequently, the Eulerian field is considered to be statistically stationary which permits trajectories captured in successive films, and different instants in time therein, to be included in statistical ensembles uniquely conditioned on their presence at the point of interest. In such a way, Eulerian stationarity implies that the origin of

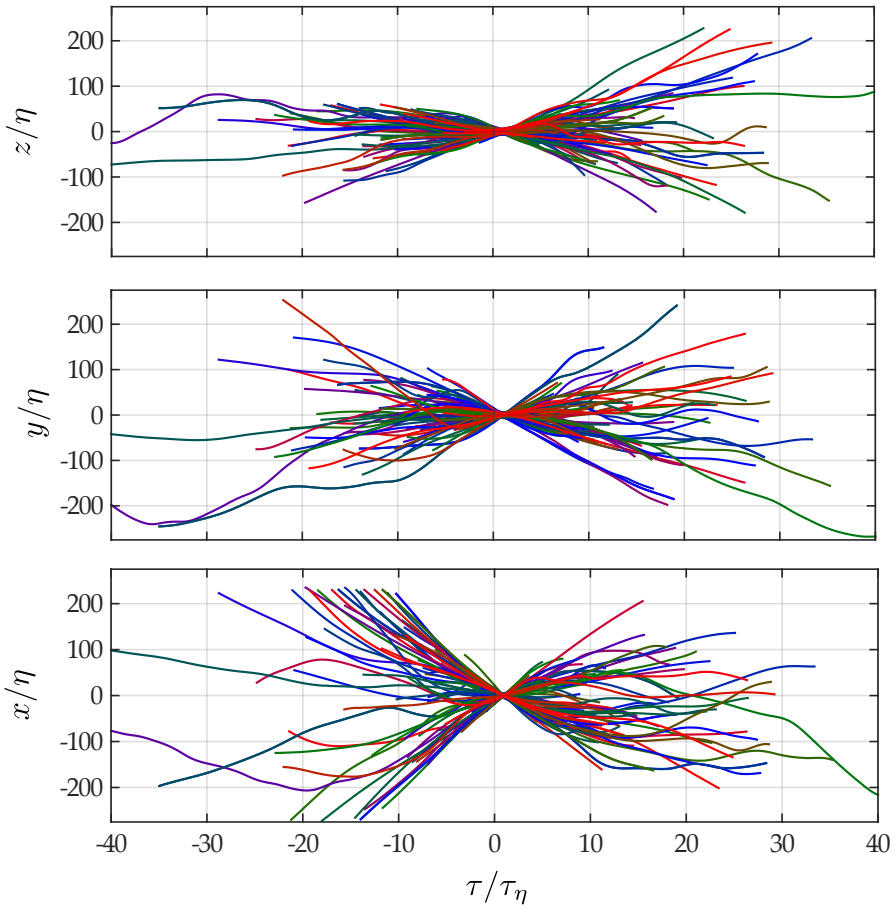


Figure 4.1: Visualization of an ensemble of trajectories conditioned based on their passage through the point (0,0,0) which coincides with the stagnation point's center. The point of closest approach to the origin is then defined as the initial time for each trajectory. The $x$-component is the most non-stationary, the $y$ and $z$ components display much more robust stationarity. Note that the "bow-tie" shape of each plot is a non-trivial consequence of the fact that particles may be thought to follow an "average" trajectory but in reality undergo dispersion about this path. This is essentially the problem of dispersion as envisioned by Taylor in 1922 [79].

time for each particle trajectory may be set to coincide with $t^*$ of the ensemble with time measured along each trajectory by $\tau = t - t^*$. From an experimental point of view, Eulerian stationarity greatly improves the statistics available by equating a trajectory passing through the stagnation point in the beginning of a film with another passage at the end of the film.

Considering the ensemble of trajectories in figure 4.1, the strict equivalence between the Eulerian and Lagrangian fields holds at $t^* = 0$ however there is clearly a difference for $\tau/\tau_\eta \gtrless 0$. This asymmetry is the most pronounced for the x-component which has the strongest transport by the meanfield and turbulent fluctuations while the $y$ and $z$ components are seemingly more symmetric and subject to weaker transport (*cf.* sect. 3.5). These contrasting behaviors foreshadow an effect related to the Eulerian field at $\vec{X}_\gamma(t^*)/\eta = (0,0,0)$ on statistics in negative and positive time, a

signature of non-stationary Lagrangian trajectories in an inhomogeneous flow. To be clear, non-stationarity in Lagrangian trajectories is a direct consequence of a particle's exploration of an inhomogeneous Eulerian flow and should be differentiated from the concept of Eulerian non-stationarity.

To clarify the nature of Lagrangian non-stationarity it will be necessary to study the evolution of various quantities along specific ensembles of trajectories, which necessitates a Lagrangian average. For a given quantity, *e.g.* the mean velocity, along an ensemble of trajectories passing through $\vec{\gamma}$ at $t^*$ one may calculate the Lagrangian average as:

$$\langle V_i(t^*+t)\rangle = \langle V_i\rangle_L(\tau) \qquad \tau = t - t^*, \tag{4.4}$$

where the subscript $L$ will be used to denote a Lagrangian average, when absent subscripts will be assumed to refer to Eulerian quantities. When $\tau = 0$, equation (4.4) reduces to an Eulerian average [1].

Trajectories near the stagnation point are chosen to coincide with the x-dominant bistable state and the role of Lagrangian non-stationarity is investigated as pertains to *rms* values and covariance of the velocity and acceleration as well as the relevant time scales. In addition a quantity heretofore without any experimental precedent, the hyperacceleration (or the derivative of the acceleration) is presented.

## 4.1 Velocity statistics

The asymmetry of figure 4.1 with respect to $\tau/\tau_\eta = 0$, especially for the x-component, indicates that if one is to properly analyze the evolution of a quantity along an ensemble of trajectories, the trajectories must be precisely conditioned. To wit, the origin of time ($t^*$) is defined to be the moment at which a particular trajectory passes its point of closest approach to the center of a region of interest. Trajectories are kept when crossing through a 1.5 cm radius sphere centered on the stagnation point, $\vec{X}_\gamma(t^*)/\eta = (0,0,0)$. It should be noted the dependency of the velocity variance on the gaussian filter width used is weak and the velocity statistics here are calculated over filtered trajectories. The fluctuating velocity along trajectories is calculated by removing the Eulerian mean velocity: $\vec{v}\,'(t) = \vec{v}(t) - \langle\vec{v}\rangle_E(\vec{X}_\gamma(t))$.

### 4.1.1 Velocity variance

With a proper ensemble of trajectories the evolution of fluctuating velocity variance along trajectories is a quantity of interest, $\langle v_i'^2\rangle_L(\tau)$ which is a time dependent quantity. Normalizing this quantity by the *rms* at $t^*$ permits the collapse of the three $\mathrm{Re}_\lambda$ experiments in figure 4.2(a). There is a clear asymmetry in time for $t \to -t$ with large increase in the *rms* value of particle velocity as it approaches $t^*$. Physically, the build up in velocity fluctuations for particles ($i = x$) approaching $t^*$ in negative time corresponds to particles approaching a region with stronger fluctuations than their starting point. A Taylor series expansion of the velocity variance about $t^*$

1. When $\tau = 0$ the equality between the Lagrangian and Eulerian averages gives the identity : $\langle\vec{V}\rangle(0) = \langle\vec{v}(\vec{X}_\gamma(t^*),t^*)\rangle$ implies that $\langle V_i'\rangle_E = \langle v_i'(\vec{X}_\gamma(t^*),t^*)\rangle$. For brevity, and coherence with previous chapters, the script $v$ will be used to refer Lagrangian quantities with the subscript $L$ to denote Lagrangian averages. When subscripts are absent $\langle\cdot\rangle$ will be taken to be the Eulerian average of the quantity in question. Eulerian quantities are understood to be evaluated at $t^*$ in this case and no indication of time is given in the interest of clarity.

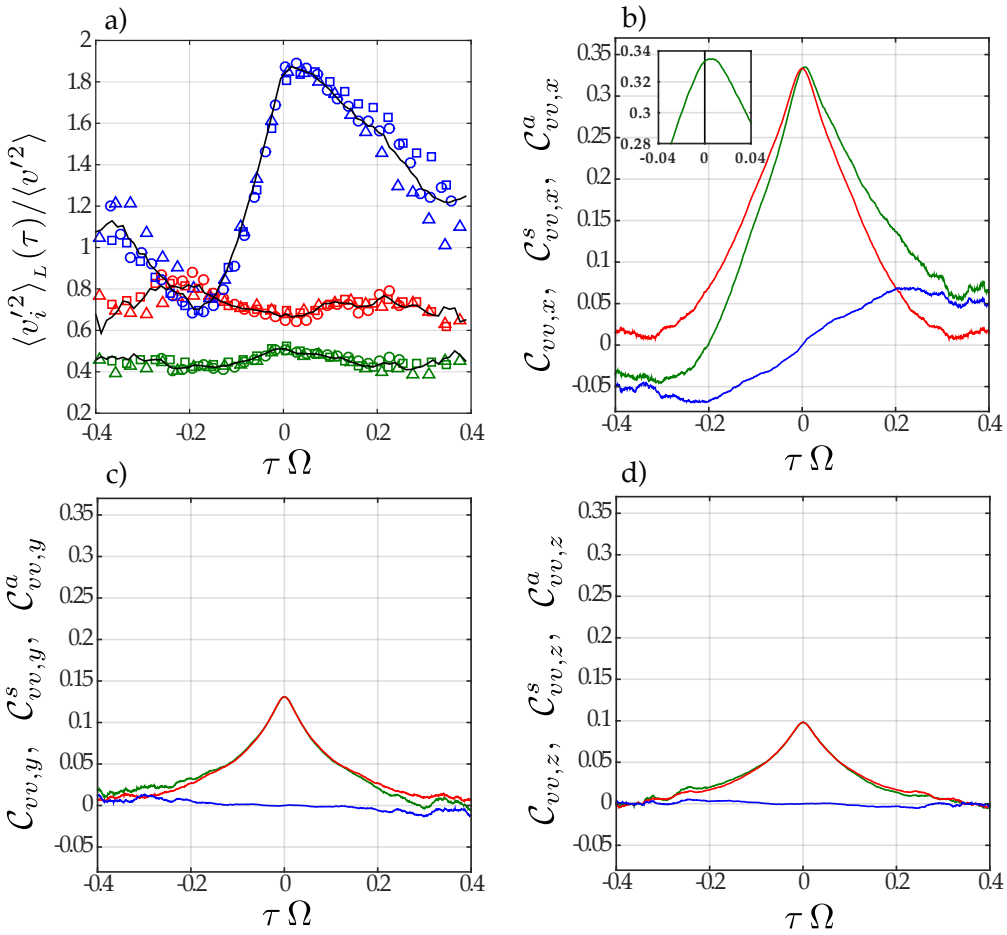


Figure 4.2: Investigation of the role of non-stationarity in the temporal evolution of fluctuating velocity statistics for conditioned trajectory ensembles. *(a)*: Normalized velocity variance. $\langle v'^2\rangle = \frac{1}{3}\sum_i \langle v_i'^2\rangle_E$. $\circ$: $\mathrm{Re}_\lambda = 155$. $\square$ : $\mathrm{Re}_\lambda = 190$. $\triangle$: $\mathrm{Re}_\lambda = 225$. Solid Line: Average of three $\mathrm{Re}_\lambda$ experiments as a reference. Blue symbols: $x-$component. Red symbols: $y-$component. Green symbols: $z-$component. *(b-d)*: Fluctuating velocity covariance for the $i-$component (x, y, z respectively) at $\mathrm{Re}_\lambda = 190$ and $\Omega = 5.5$ Hz. Green curve: $\mathcal{C}_{vv,i}$ non-normalized fluctuating velocity covariance (eq. 4.8). Red curve: Symmetric covariance function $\mathcal{C}^s_{vv,i}$ (eq. 4.10) . Blue curve: Anti-symmetric covariance function $\mathcal{C}^a_{vv,i}$ (eq. 4.11). (*b, inset*): Zoom of the fluctuating velocity covariance function at $\tau = 0$ reveals a strong asymmetry with respect to $\tau = 0$ that is much less apparent in the $y$ and $z$ components.

gives $\langle v_i'^2 \rangle_L(\tau) = \langle v_i'^2 \rangle + \langle Dv_i'^2/D\tau \rangle \times \tau$ permits the expression [2] of the increments of velocity variance which provide an accurate measure of the non-stationarity and may be calculated by:

$$\frac{\langle v_i'^2 \rangle_L(\tau) - \langle v_i'^2 \rangle_L(-\tau)}{2} = \left\langle \frac{D}{D\tau} v_i'^2 \right\rangle \tau, \tag{4.5}$$

where a centered difference in velocity variance along the trajectory is clearly related to the material derivative of the component-wise velocity variance at $\vec{X}_\gamma(t^*)$. Measurements of this quantity provide results that are similar to an analogous method of calculating nearly the same term using the velocity covariance (*cf.* sec. 4.1.2). Table 4.1 provides the values obtained from the latter calculation.

Interestingly, the sum over the three components is roughly $2\varepsilon$ (table 4.1), however this result is a fortuitous result of the geometry of the flow at $\tau = 0$ and results from the relationship between equation (4.5) and the velocity variance budget:

$$\left\langle \frac{D}{D\tau} v_i'^2 \right\rangle = \langle v_k \rangle \partial_k \langle v_i' v_i' \rangle + \partial_k \langle v_k' v_i' v_i' \rangle = 2\mathcal{P}_{ii} - \frac{2}{\rho} \partial_i \langle p' v_i' \rangle + \nu \partial_k \partial_k \langle v_i' v_i' \rangle - 2\varepsilon_{ii}, \tag{4.6}$$

where a component-wise investigation implies no summation over the repeated $i$ indices. Equivalently, this equation may be written:

$$\left\langle \frac{D}{D\tau} v_i'^2 \right\rangle = 2\mathcal{P}_{ii} + 2\langle v_i' a_i' \rangle, \tag{4.7}$$

as was used in the TKE budget. The rate of change of the velocity variance may be interpreted in one of two ways : when pressure and viscous transport are negligible it is the sum of production and dissipation (eq. 4.7), or it is the turbulent transport of velocity fluctuations (eq. 4.6). Considering the variance budgets of section 3.5 the latter interpretation is instructive. The major conclusion of the velocity variance budget was that only fluctuations in the converging component were subjected to turbulent transport. If $\partial_k \langle v_k' v_i' v_i' \rangle \sim 0$ for $i = y, z$ then the corresponding measurements in equation (4.5) should likewise be negligible, as is the case in table 4.1 [3]. This reinforces the claim that turbulent fluctuations only transport converging component ($x$) variances and that the total transport is approximately $2\varepsilon$.

### 4.1.2 Velocity correlation

An interesting conclusion drawn from the above analysis is the Eulerian field has a quantifiable effect on Lagrangian quantities. These observations indicate that either of advective or turbulent transport of fluctuations may result in non-stationarity which has a limited deterministic effect on particle trajectories. The following paragraph derives quantities that are independent of the non-stationary nature of the flow.

2. The reader is reminded that time derivatives are calculated along trajectories ($d/dt\,\cdot$). However, when $\tau = 0$ this derivative is replaced by $D/Dt\,\cdot$, the material derivative of an Eulerian field.

3. Traditionally the variance budget is calculated for $\langle \frac{dv_i'^2}{dt} \rangle$ and therefore $2\varepsilon_{ii}$ is the dissipative contribution. On the otherhand $\langle \frac{1}{2} \frac{d}{dt} v_i'^2 \rangle$ is relevant to the TKE budget and $\varepsilon$ results on the RHS of the budget equation. The latter is given in table 4.1 and explains the missing factor of 2 with respect to the prediction above.

| | $\langle \frac{1}{2}\frac{\mathrm{d}v_i'^2}{\mathrm{d}t} \rangle$ W.kg$^{-1}$ | | | $\sum_i \langle \frac{1}{2}\frac{\mathrm{d}v_i'^2}{\mathrm{d}t} \rangle \varepsilon^{-1}$ - |
|---|---|---|---|---|
| $\mathrm{Re}_\lambda$ | $i = x$ | $i = y$ | $i = z$ | - |
| 155 | 1.08 | -0.05 | -0.05 | 0.98 |
| 190 | 2.51 | -0.07 | -0.07 | 1.13 |
| 225 | 4.0 | -0.15 | -0.15 | 1.03 |

Table 4.1: Degree of non-stationarity in each component as measured by an $\mathcal{O}(\tau)$ fit of the small time approximation of the antisymmetric fluctuating velocity covariance (eq. 4.12) for each $\mathrm{Re}_\lambda$ investigated at the center of the stagnation point (middle column). Note that a multiplication by 2 of the middle column permits an estimation of the velocity variance difference calculated in equation 4.5. Positive values indicate transport of the relevant component's velocity variance away from the stagnation point. Transport is largely of the contracting component's variance. The third column indicates that in total rate of change of velocity variance is nearly $\varepsilon$, in agreement with the TKE budget.

| | $\langle v_i'^2 \rangle$ (m.s$^{-1}$)$^2$ | | | $\langle a_i'^2 \rangle$ (m.s$^{-2}$)$^2$ | | | $\tau_\lambda/\tau_\eta$ - | | |
|---|---|---|---|---|---|---|---|---|---|
| $\mathrm{Re}_\lambda$ | $i = x$ | $i = y$ | $i = z$ | $i = x$ | $i = y$ | $i = z$ | $i = x$ | $i = y$ | $i = z$ |
| 155 | 0.20 | 0.07 | 0.06 | 1744 | 752 | 848 | 6.5 | 4.2 | 4.2 |
| 190 | 0.33 | 0.13 | 0.09 | 4167 | 3015 | 2270 | 6.3 | 4.3 | 3.9 |
| 225 | 0.47 | 0.17 | 0.13 | 12500 | 7086 | 6462 | 6.5 | 4.3 | 4.1 |

Table 4.2: Velocity and acceleration of each component as measured by an $\mathcal{O}(\tau^2)$ fit of the small time approximation of the symmetric fluctuating velocity covariance function (eq.4.13) for each $\mathrm{Re}_\lambda$ investigated at the center of the stagnation point (red curves, fig. 4.2b-d). The Taylor time scale is defined $\tau_{\lambda,i} = 2\langle v_i'^2 \rangle / \langle a_i'^2 \rangle$ and is normalized by Kolmogorov time-scale. The acceleration variance used to calculate $\tau_{\lambda,i}$ comes from an analogous fitting procedure of the acceleration covariance function, these values are deemed to be more accurate due to the multi-step method used in their calculation as opposed to the gaussian filtering method used in the velocity statistics.

When following the same conditioning procedure as was described previously, the velocity covariance is written:

$$\mathcal{C}_{vv,i} = \langle v_i'(0)v_i'(\tau)\rangle_L \qquad \tau = t - t^*. \tag{4.8}$$

Initially G.I. Taylor proposed a normalized version as a method of measuring the velocity autocorrelation of particles released from a point source [79], much like a soot emitting chimney [4]. A small time development of the preceding equation is written:

$$\mathcal{C}_{vv,i} \simeq \langle v_i'^2\rangle + \Big\langle \frac{1}{2}\frac{Dv_i'^2}{D\tau}\Big\rangle\tau - \Big(\Big\langle\big(\frac{Dv_i'}{D\tau}\big)^2\Big\rangle - \Big\langle\frac{1}{2}\frac{D^2v_i'^2}{D\tau^2}\Big\rangle\Big)\frac{\tau^2}{2}. \tag{4.9}$$

It is always possible to deconstruct a function into a symmetric and antisymmetric part. Doing so to $\mathcal{C}_{vv,i}(\tau)$ gives:

$$\mathcal{C}^s_{vv}(\tau) = \frac{\mathcal{C}_{vv,i}(\tau) + \mathcal{C}_{vv,i}(-\tau)}{2} \tag{4.10}$$

$$\mathcal{C}^a_{vv}(\tau) = \frac{\mathcal{C}_{vv,i}(\tau) - \mathcal{C}_{vv,i}(-\tau)}{2}, \tag{4.11}$$

where $\mathcal{C}^s_{vv,i}$ (respectively $\mathcal{C}^a_{vv,i}$) is the symmetric (resp. antisymmetric) form of $\mathcal{C}_{vv,i}$.

As the small time approximations of the symmetric and antisymmetric covariances gives:

$$\mathcal{C}^a_{vv,i}(\tau) \simeq \Big\langle\frac{1}{2}\frac{Dv_i'^2}{D\tau}\Big\rangle\tau \tag{4.12}$$

$$\mathcal{C}^s_{vv,i}(\tau) \simeq \langle v_i'^2\rangle(1 - (\tau/\tau_\lambda)^2), \tag{4.13}$$

where $\tau_\lambda^2 = \langle a_i'^2\rangle/(2\langle v_i'^2\rangle)$ is commonly called the Taylor time scale, a Lagrangian alternative to its spatial equivalent, derived in much the same way [108]. Applying an $\mathcal{O}(\tau)$ fit to $\mathcal{C}^a_{vv,i}$ (figure 4.2b-d , blue) is sufficient to estimate $\langle Dv_i'^2/D\tau\rangle/2$ and the values obtained are noted in table 4.1. The same analysis applied above holds here and it suffices to say that $\langle Dv_i'^2/D\tau\rangle/2 = \partial_k\langle v_k'v_i'^2/2\rangle \sim \varepsilon$ when $i = x$ and is negligible otherwise. This non-stationarity is apparent in the highly asymmetric correlation curve (green) in figure 4.2(b) and its non-negligible slope at $\tau\Omega = 0$ (fig. 4.2 b,inset). In contrast, figures 4.2(c-d) indicate negligible non-stationarity in agreement with near zero values of the turbulent fluxes for these components (table 4.1).

The small time approximation of $\mathcal{C}^s_{vv,i}$ in equation 4.13 implies two assumptions. First, $\langle D^2v_i'^2/D\tau^2\rangle = 0$. This seems plausible in light of equation (4.5). Second, $\langle(Dv_i'/D\tau)^2\rangle = \langle a_i'^2\rangle$. This appears reasonable when considering the values of $\langle a_i'^2\rangle$ measured in table 4.2. These values are similar to those measured elsewhere (*cf.* chapter 5) although slightly larger which may imply that this approximation is largely accurate but may be neglecting some corrective terms [5]. Acceleration variances were inferred using the parabolic fits near the origin which permit an estimation of $\tau_\lambda$ in the red curves of figures 4.2(b-d). Interestingly, $\tau_\lambda \sim 6.3\tau_\eta$ for the strongly non-stationary component and is closer to $4.2\tau_\eta$ for the quasi-stationary

4. Another concrete example that members and visitors of the ENS de Lyon Physics Lab will have noticed are the emissions from the Gerland garbage incinerator, as seen from the *salle de café*.

5. Kinematically it is known that the material derivative $\frac{dv_i'}{d\tau} \sim (\langle v_k\rangle_E + v_k')\partial_{x_k}v_i'$ while $a_i' = \frac{dv_i}{d\tau} - \langle\frac{dv_i}{d\tau}\rangle_E = \frac{dv_i'}{d\tau} + v_k'\partial_{x_k}\langle v_i\rangle_E - \langle v_k'\partial_{x_k}v_i'\rangle_E$. The latter two terms in the expression of $a_i'$ are negative but likely negligible.

components.

Ultimately, correlation in Lagrangian statistics is determined by a stationary contribution (eq. 4.13) which is sensitive to the anisotropy of the flow, and a non-stationary contribution (eq. 4.12) which is related to the exploration of an inhomogeneous field. Discussion of the competition of these processes is given in section 4.3 where a modified Taylor time scale $\widetilde{\tau}_\lambda$, which is obtained from an $\mathcal{O}(\tau^2)$ approximation of the normalized velocity autocorrelation function, is discussed. This time scale is thought to have contributions from the non-stationarity in Lagrangian trajectories as well as flow anisotropy.

## 4.2 Acceleration statistics

Upon investigation of covariances and variances, Lagrangian velocity statistics were seen to demonstrate strong signatures of non-stationarity linked to underlying inhomogeneity of the flow. These effects where observed up to times on the order of $0.25\Omega$ which is essentially the time taken for velocity statistics to decorrelate and is on the order of the Lagrangian integral time $T_L$. The relationship between this time scale and the dissipative time scale ($\tau_\eta$) is a reflection of the Reynolds number via the relationship $T_L/\tau_\eta \sim \mathrm{Re}_\lambda$ [129]. For the Reynolds numbers considered here, which are not enormous but satisfactorily in the fully developed turbulence range ($\mathrm{Re} > 3300$ [88]), it is not clear if the non-stationarity apparent in a large scale quantity such as the velocity covariance (where $T_L$ is the characteristic time) will still hold for a small scale quantity such as the acceleration covariance (where $\tau_\eta$ is the characteristic time). This question is addressed in the following section.

The same trajectory ensembles used in section 4.1 are applied in the following paragraphs. However, where filtering operations have little effect on the velocity variance of a signal, acceleration statistics are strongly effected by these methods that have no objective constraint. To address this problem statistics are gathered using the multi-step method for estimating one and two-time acceleration statistics (*cf.* chapter 2).

### 4.2.1 Acceleration variance

As successive derivatives are taken of trajectories, more weight is cast up on higher frequency motion. An interesting point to address is the degree to which the signature of non-stationarity is found in the second-order derivative (acceleration) of the Lagrangian trajectories. As with the velocity variance, the evolution of the acceleration variance is examined by conditioning trajectories approaching the geometrical center of the stagnation point and defining the initial time $t^*$ to be the time of closest approach. Figure 4.3(a) illustrates non-stationarity in the acceleration variance, albeit to a lesser degree than was seen in the velocity variance (figure 4.2a). Most notably, there is a period of time roughly $2\tau_\eta$ to either side of $t^*$ that the trajectories adapt to the constraint of the Eulerian field at $\vec{X}_\gamma(t^*)$. This corresponds roughly to time over which the correlation functions evolve (figure 4.3, b-d). The difference in the plateau values of $\langle a_i'^2 \rangle$ at $t^* \pm 2\tau_\eta$ indicates global tendency of trajectories to regions with stronger fluctuations where the variance increases by about 20%.

Acceleration events that evolve over roughly $4\tau_\eta$ are interesting from a particle

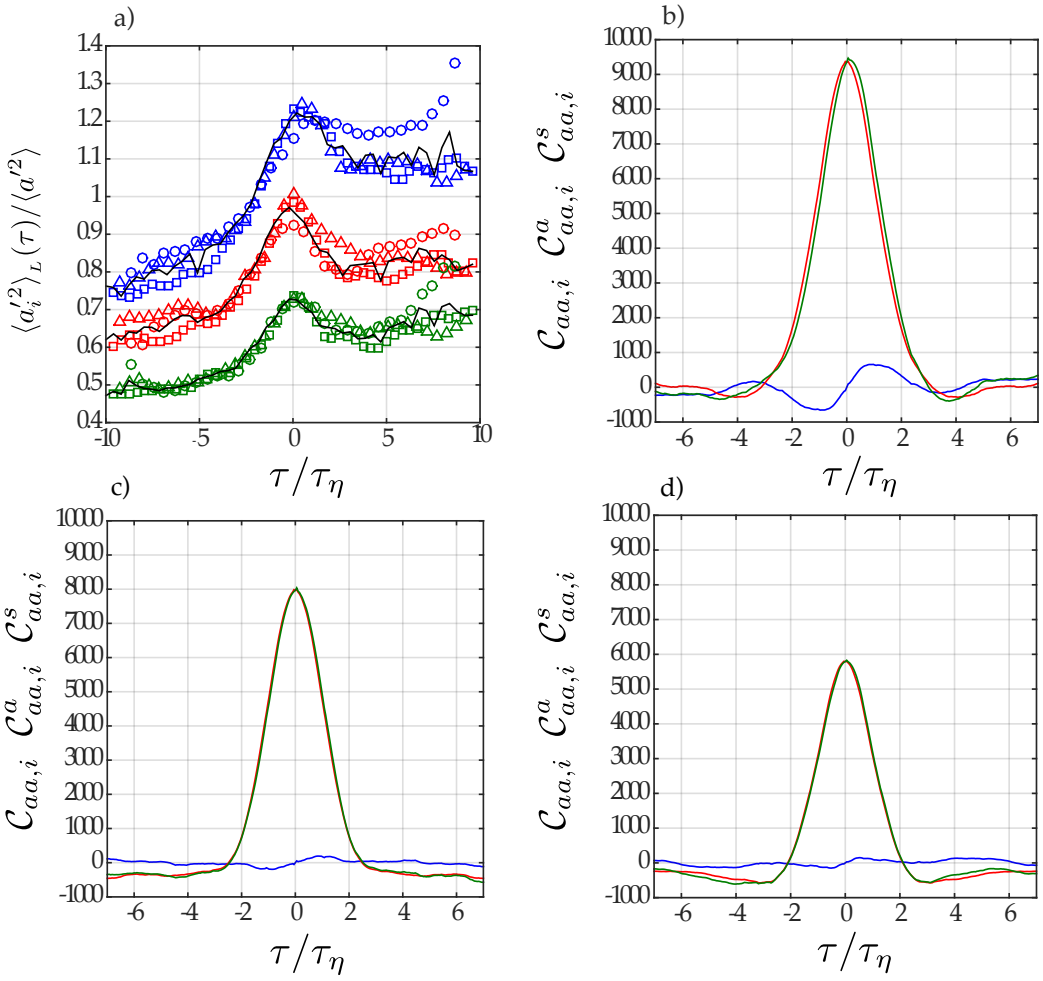


Figure 4.3: Investigation of the role of non-stationarity in the temporal evolution of acceleration statistics for conditioned trajectory ensembles. *(a)*: Normalized acceleration variance. $\langle a'^2\rangle = \sum_i \langle a_i'^2\rangle_E/3$. $\circ$: $\mathrm{Re}_\lambda = 155$. $\square$ : $\mathrm{Re}_\lambda = 190$. $\triangle$: $\mathrm{Re}_\lambda = 225$. Solid Line: Average of three $\mathrm{Re}_\lambda$ experiments as a reference. Blue symbols: $x-$component. Red symbols: $y-$component. Green symbols: $z-$component. *(b-d)*: Acceleration covariance for the $i-$component (x, y, z respectively) at $\mathrm{Re}_\lambda = 225$ and $\Omega = 6.9$ Hz. Green curve: $\mathcal{C}_{aa,i}$ non-normalized acceleration covariance (eq. 4.20). Red curve: Symmetric covariance function $\mathcal{C}^s_{aa,i}$ (eq. 4.21) . Blue curve: Anti-symmetric covariance function $\mathcal{C}^a_{aa,i}$ (eq. 4.22).

dispersion point of view, but are less directly related to the Eulerian field at $\vec{X}_\gamma(t^*)$. As with the velocity variance it is instructive to investigate the acceleration variance increments which are linked to the Eurlerian field in the small time limit. They are written as:

$$\frac{\langle a_i'^2\rangle_L(\tau) - \langle a_i'^2\rangle_L(-\tau)}{2} = \Big\langle \frac{D}{D\tau} a_i'^2 \Big\rangle \tau, \tag{4.14}$$

By analogy with the velocity variance equations (4.6) & (4.7):

$$\Big\langle \frac{Da_i'^2}{Dt} \Big\rangle = \langle v_k\rangle \partial_k \langle a_i' a_i'\rangle + \partial_k \langle v_k' a_i' a_i'\rangle, \tag{4.15}$$

$$\Big\langle \frac{Da_i'^2}{Dt} \Big\rangle = 2\mathcal{P}_{ii}^a + 2\langle a_i' \mathring{a}_i'\rangle, \tag{4.16}$$

where no summation is implied over $i$ and $\mathcal{P}_{ii}^a = \langle a_i' v_k'\rangle \partial_{x_k}\langle a_i\rangle$ is analogous to variance budget production term (ch. 3, eq. 3.8 [6]) and simplifies to $\langle a_i' v_i'\rangle \partial_{x_i}\langle a_i\rangle$ as the cross terms are negligible ($\langle a_i' v_k'\rangle = 0$ when $i \neq k$). The two terms on the right hand side of equation 4.15 are analogous to the advective and turbulent transport terms in the variance budget, however, the advective term is likely zero at the center of the flow ($\langle v_j\rangle \sim 0$). As opposed to the velocity field where the mean and fluctuating fields may be of the same order of magnitude, the mean acceleration fields may be up to an order of magnitude smaller than the fluctuating component (ch. 2, fig. 2.7) and it is therefore reasonable to assume that the production term is smaller than the turbulent transport, i.e. $\mathcal{P}_{ii}^a \ll \partial_k \langle v_k' a_i' a_i'\rangle$ [7], which permits the direct calculation of the acceleration-hyperacceleration cross-correlation via:

$$\langle \frac{Da_i'^2}{Dt} \rangle = 2\langle a_i' \mathring{a}_i'\rangle. \tag{4.17}$$

This term is related to the slope of the temporal acceleration autocorrelation. If an acceleration signal is stationary it follows that $\langle a_i'(t^*) a_i'(t^*+t)\rangle = \langle a_i'(t^*-t) a_i'(t^*)\rangle_L$. In the limit where $t \to 0$ stationarity holds if:

$$\langle a_i' \mathring{a}_i'\rangle = \langle a_i'(t^*)\mathring{a}_i'(t^*)\rangle = -\langle \mathring{a}_i'(t^*) a_i'(t^*)\rangle = 0, \tag{4.18}$$

which implies that $\langle a_i' \mathring{a}_i'\rangle = 0$ for a stationary acceleration signal. Measurement of this quantity using equation (4.14) gives similar values to an analogous measurement using the acceleration correlation (*cf.* section 4.2.2), the latter of which is presented in table 4.3. To estimate the role of non-stationarity in the signal it is necessary to calculate the acceleration-hyperacceleration correlation coefficient, a dimensionless parameter that is written:

$$\alpha_{a,i} = \frac{\langle a_i \mathring{a}_i\rangle}{\langle a_i^2\rangle^{1/2}\langle \mathring{a}_i^2\rangle^{1/2}}, \tag{4.19}$$

From the data in table 4.3, $\alpha_{a,i} \sim 0.06$ for the $i = x$ at $\mathrm{Re}_\lambda = 190$. Smaller values for the orthogonal components reflect the smaller slopes of the blue lines in figures 4.3(c-d). It is of note that a similar tendency occurs in the velocity auto-correlation although $\alpha = 0.17$ in that case ($x-$component at $\mathrm{Re}_\lambda = 190$) and again the orthogonal components are much smaller. However, the fact that $\alpha_a < \alpha$ reflects a diminished effect of the non-stationarity in the higher order derivative (acceleration

6. Note that the $i$ variance is calculated here while in chapter 3 the $j$ variance is calculated.

7. Indeed a quick calculation gives $\mathcal{P}_{xx}^a \sim 420\,\mathrm{m}^2.\mathrm{s}^{-5}$ which is much smaller than the values of $\langle a_x' \mathring{a}_x'\rangle$ in table 4.3 indicating that this assumption is valid.

| | $\langle a_i'^2 \rangle$ $(\mathrm{m.s}^{-2})^2$ | | | $\langle \mathring{a}_i'^2 \rangle$ $(\mathrm{m.s}^{-3})^2 \times 10^8$ | | |
|---|---|---|---|---|---|---|
| $\mathrm{Re}_\lambda$ | $i=x$ | $i=y$ | $i=z$ | $i=x$ | $i=y$ | $i=z$ |
| 155 | 1141 | 959.6 | 830 | 1.636 | 1.586 | 1.685 |
| 190 | 3816 | 3128 | 2710 | 10.742 | 9.240 | 9.268 |
| 225 | 9984 | 8237 | 7003 | 40.602 | 35.262 | 35.030 |
| | $\langle a' \mathring{a}_i' \rangle$ $(\mathrm{m}^2.\mathrm{s}^{-5}) \times 10^4$ | | | $\tau_{\lambda,a}/\tau_\eta$ - | | |
| $\mathrm{Re}_\lambda$ | $i=x$ | $i=y$ | $i=z$ | $i=x$ | $i=y$ | $i=z$ |
| 155 | 3.92 | 1.21 | 0.50 | 1.29 | 1.24 | 1.17 |
| 190 | 12.29 | 10.05 | 6.78 | 1.33 | 1.30 | 1.20 |
| 225 | 73.2 | 17.41 | 19.91 | 1.48 | 1.44 | 1.33 |

Table 4.3: Fit parameters from short time approximations to the symmetric and antisymmetric acceleration covariance functions. The acceleration-hyperacceleration cross correlation results from an $\mathcal{O}(\tau)$ fit of the antisymmetric function (eq. 4.22 while acceleration and hyperacceleration variances result from a $\mathcal{O}(\tau^2)$ fit of the symmetric function (eq. 4.21). Similar to the definition of the $\tau_\lambda$, a time scale results from the ratio of acceleration and hyperacceleration variance: $\tau_{\lambda,a} = 2\langle a_i^2 \rangle / \langle \mathring{a}_i^2 \rangle$.

versus velocity). This may be seen in the slope at $\tau = 0$ of figure 4.2(b) as opposed to an almost negligible, albeit present, slope in the corresponding acceleration plot (fig. 4.3 b). The near absence of asymmetry in the correlation curves in corresponding to the diverging directions (fig. 4.2c-d & fig. 4.3c-d) indicates that the strong strain corresponding to the contracting direction directs the "arrow of time" while the expanding directions display little distinction between past and future events. A distinguishable notion of "past" and "future" in the correlated motion of the acceleration and velocity points to the role of transport by mean and turbulent mechanisms in the non-stationarity of Lagrangian statistics.

The previous discussion foreshadows the importance of correlation coefficients. These quantities will be of interest when investigating the normalized correlation functions (*cf.* section 4.3). In the following paragraph, non-normalized temporal correlations are investigated to further elucidate the role of stationarity in the acceleration signal.

### 4.2.2 Acceleration correlation

From equation 4.19, the cross correlation of the acceleration and hyper-acceleration was found to be strongest for the converging direction, the component most affected by the inhomogeneity of the Eulerian field. In the following two paragraphs the evolution of the acceleration covariance is investigated in much the same manner as section 4.1.2, revealing the aspects of the acceleration signal that are independent of the underlying flow non-stationarity.

The acceleration covariance $\mathcal{C}_{aa,i}(\tau)$ is written:

$$\mathcal{C}_{aa,i}(\tau) = \langle a_i'(0) a_i'(\tau) \rangle_L \qquad \tau = t - t^*. \tag{4.20}$$

Decomposing $\mathcal{C}_{aa,i}(\tau)$ into a symmetric and antisymmetric function gives:

$$\mathcal{C}^s_{aa,i}(\tau) = \frac{\mathcal{C}_{aa,i}(\tau) + \mathcal{C}_{aa,i}(-\tau)}{2} \tag{4.21}$$

$$\mathcal{C}^a_{aa,i}(\tau) = \frac{\mathcal{C}_{aa,i}(\tau) - \mathcal{C}_{aa,i}(-\tau)}{2}, \tag{4.22}$$

where $\mathcal{C}^s_{aa,i}$ (respectively $\mathcal{C}^a_{aa,i}$) is the symmetric (resp. antisymmetric) form of $\mathcal{C}_{aa,i}$. As $\tau \to 0$ a similar development of equation 4.20 as equation (4.9) gives the following for the symmetric and antisymmetric functions:

$$\mathcal{C}^a_{aa,i}(\tau) = \langle a'_i \mathring{a}' \rangle \tau, \tag{4.23}$$

$$\mathcal{C}^s_{aa,i}(\tau) = \langle a'^2_i \rangle (1 - \frac{\langle \mathring{a}'^2_i \rangle}{2\langle a'^2_i \rangle} \tau^2), \tag{4.24}$$

where equation (4.23) results from the equivalence between the rate of change in the acceleration and the acceleration-hyperacceleration cross correlation, hypothesized in equation (4.17). Using the equations (4.23) & (4.24) to fit the curves of figure 4.3(b-d) as $\tau \to 0$, a second estimation of $\langle a'^2_i \rangle$ is obtained as well as an estimation of the hyper acceleration $\langle \mathring{a}'^2_i \rangle$. The latter quantity is seldom discussed but results from the finite curvature of the acceleration autocorrelation function at $\tau = 0$. Accurate measurement of $\langle \mathring{a}'_i \rangle$ has been experimentally inaccessible due to the use of filtering which primarily acts on the initial lags constituting the curvature of the autocorrelation as $\tau \to 0$. Such filtered measurements may provide an estimate of $\mathring{a}'_i$, but lead to an inevitable trade off between the amount of signal kept versus noise removed (*cf.* chapter 2). As a consequence, the measurement of the hyperacceleration has largely been confined to a few numeric works [130, 131]. On the contrary, the multi-step method discussed in chapter 2 provides a measurement of such events as long as the working hypotheses of the method are validated.

Provided the temporal resolution of the measurements is sufficient to estimate the hyperacceleration, equation 4.23 permits the definition of an analogous timescale, $\tau^2_{\lambda,a} = 2\langle a'^2_i \rangle / \langle \mathring{a}'^2_i \rangle$. Interestingly, this scale is close to the Kolmogorov time scale, and the ratio has a slight tendency to increase with $\mathrm{Re}_\lambda$. Furthermore, its anisotropy is much smaller, $\tau_{\lambda,a,x}/\tau_{\lambda,a,z} \sim 1.1$, with respect to the Taylor time scale, $\tau_{\lambda,x}/\tau_{\lambda,z} \sim 1.6$. As with the Taylor time scale, $\tau_{\lambda,a}$ is an $\mathcal{O}(\tau^2)$ term and therefore independent of the non-stationarity of the flow. The results pertaining to the hyper acceleration (and $\tau_{\lambda,a}$) are presented with a speculative caution as to the temporal resolution of these measurements. Indeed, for them to be resolved it is necessary that the correlation time of these events, $\tau_h$, be of the same order of magnitude as $\tau_\eta$. The implications of such correspondence and preliminary evidence is given in the following paragraph.

### 4.2.3 Hyperacceleration

It is of note a measurable value of $\tau_{\lambda,a}$ implies that the acceleration field is differentiable and indicates finite variance of the hyperacceleration. There is little research into this quantity and what does exist is based on a third-order Lagrangian stochastic model [130, 131] equivalent to a stochastic model for Lagrangian accelerations with incremental noise that is exponentially correlated in time. For statistically

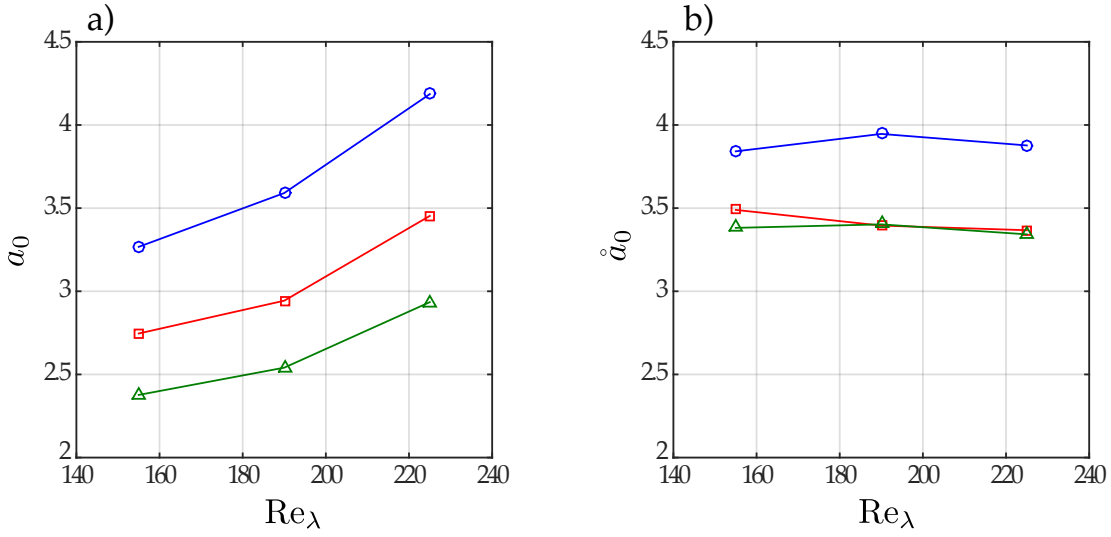


Figure 4.4: Normalized acceleration ($a$) and hyperacceleration ($b$) statistics for conditioned trajectories at the center of the stagnation point at each $\mathrm{Re}_\lambda$ investigated. $\circ$: $x$-component (blue). $\square$ : $y$-component (red). $\triangle$: $z-$component (green). The non-dimensional constants $a_0$ and $\mathring{a}_0$ are derived from Kolmogorov phenomenology and are given in equations 4.27 and 4.26.

stationary turbulence the noise correlation time ($\tau_h$) obeys the following :

$$\frac{\langle \mathring{a}_i'^2 \rangle}{2\langle a_i'^2 \rangle} = \tau_{\lambda,a}^{-2} = (T_L^{-1}\tau_\eta^{-1} + \tau_\eta^{-1}\tau_h^{-1} + T_L^{-1}\tau_h^{-1})/2, \tag{4.25}$$

which results from the kinematic relationships between velocity and acceleration autocorrelation functions, and between the acceleration and hyperacceleration autocorrelation functions [130, 131]. This equation may simplify to $\tau_h \sim \tau_{\lambda,a}$ for large enough $\mathrm{Re}_\lambda$ assuming that $\tau_h \ll T_L$ and when considering the experimental result $\tau_{\lambda,a} \sim \tau_\eta$ (*cf.* table 4.3). As a consequence, $\tau_h \sim \tau_\eta$. This result is unexpected as the interpretation of the timescale governing the incremental noise is that of the "molecular" scales of motion. However, channel-flow DNS experiments confirm the absence of such a separation of scale. In a region just outside of the viscous layer $\tau_h > T_L > \tau_\eta$ where as in the center of the channel $T_L > \tau_h > \tau_\eta$ [131]. These observations corroborate our indirect measurement of $\tau_h$ via the large Reynolds number approximation of equation (4.25): $\tau_h \simeq \tau_{\lambda,a}^2/\tau_\eta$.

The correspondence of the incremental noise correlation time ($\tau_h$) to $\tau_\eta$ may justify the application of Kolmogorov phenomenology to the hyperacceleration, which could then be written:

$$\langle \mathring{a}_i'^2 \rangle \sim \langle a_i'^2 \rangle / {\tau_\eta}^2 = \mathring{a}_0 (\varepsilon^5 \nu^{-3})^{1/2}, \tag{4.26}$$

where $\mathring{a}_0$ is related to the Heisenberg-Yaglom constant of the acceleration variance ($a_0$) by the same constant that permits the relationship: $\tau_{\lambda,a} \sim \tau_\eta$. The acceleration variance is given by the well-known formula:

$$\langle a'^2 \rangle = a_0 \varepsilon^{3/2} \nu^{-1/2}. \tag{4.27}$$

The Heisenberg-Yaglom constant $a_0$ is plotted (fig. 4.4 a) by component for the three Reynolds numbers investigated here. Figure 4.4 (b) indicates that the scaling

in equation (4.26) has a limited Reynolds number dependence for the range investigated. A contrario, the Heisenberg-Yaglom constant is an increasing function of $\mathrm{Re}_\lambda$ [129]. Evidence from DNS and experiments suggest that normalized acceleration statistics reach plateau values at smaller $Re_\lambda$ than for velocity statistics [132, 133]. By extension, the higher order derivative corresponding to hyperacceleration may have saturated by $Re_\lambda \sim 155$ [8].

## 4.3 Inhomogeneity and anisotropy

The necessity of conditioning an ensemble of trajectories based on an initial position and defining positive and negative time with respect to this point was introduced in the introduction to this chapter. Indeed, figure 4.1 indicates that the diverging directions (with respect to the stagnation point) are nearly symmetric by the transformation $t \to -t$ while the converging direction, $x$, displays a strong asymmetry. The preceding paragraphs demonstrate that the presence, or absence, of symmetry is linked to the value of $\langle Dv_i'^2/Dt \rangle/2$, which when non-zero indicates inhomogeneity in the underlying Eulerian field and induces non-stationary Lagrangian statistics.

In this section, the competition between flow inhomogeneity and anisotropy in the determination of time scales relevant to the velocity auto-correlation is discussed. Non-stationarity has a signature in the velocity and acceleration auto-correlation function. The Cauchy-Schwartz inequality, upon which the definition of a correlation function rests [134], is only satisfied with the normalization of the auto-correlation function by the variance at the initial point in time as well as at a given lag. This is in contrast to a single value which is equal for all lags of a stationary Lagrangian signal. For example, the velocity auto-correlation is written:

$$R_{vv}(\tau) = \frac{\langle v'(0)v'(\tau)\rangle_L}{\sqrt{\langle v'^2\rangle_L(0)\langle v_i'^2\rangle_L(\tau)}} \qquad \tau = t - t^*. \tag{4.28}$$

Figure 4.5 displays the contrasting methods of calculating the auto-correlation function. The solid lines indicate equation 4.28 (and its acceleration counter-part) while the dash-dotted lines indicate that normalization is by the *rms* value at $\tau = 0$, and is equal to the *rms* of the entire signal if the trajectories statistics are stationary. The latter function renders the signal effectively stationary by mixing correlations at the beginning and end of the signal. In other words, it is the correlation function obtained by applying the Wiener-Khintchin theorem [135, 136] to the velocity signal. This formulation will be referred to as the "stationary" auto-correlation function while equation 4.28 will be referred to as the "non-stationary" correlation function.

The largest differences between the two calculations is apparent in the $x$-component. Inhomogeneity was seen to beget non-stationarity in this direction which is translated by the "stationary" curve which is falls below the "non-stationary" curve for all time lags. This is a consequence of mixing statistics from a region with low fluctuations with statistics from a region with high fluctuations, this process artificially decorrelates the signal. Even the acceleration correlation function, which places emphasis on the high frequencies of a velocity signal, displays a similar shift over all lags investigated. Physically, the incongruous forms of the two calculations may be

8. Again, experimental and numerical verification of this claim are welcome as a lack of temporal resolution may under estimate the hyper acceleration in such a way that it appears to saturate.

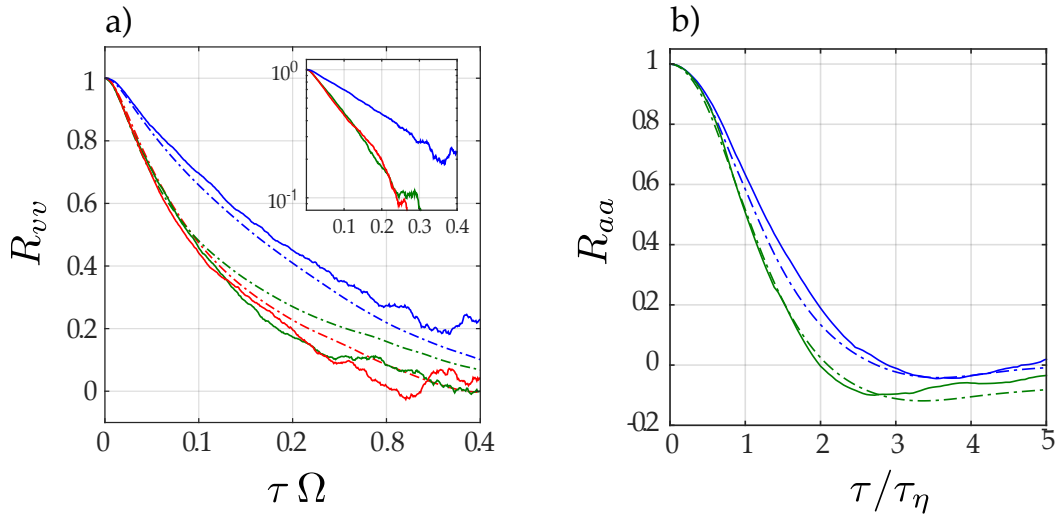


Figure 4.5: Velocity ($a$) and acceleration ($b$) autocorrelation functions. These auto-correlation functions are said to be "non-stationary" (solid lines) and "stationary" (dash-dotted lines). Velocity curves ($a$) correspond to $\mathrm{Re}_\lambda = 190$ and $\Omega = 5.5$ Hz while acceleration curves ($b$) correspond to $\mathrm{Re}_\lambda = 225$ and $\tau_\eta = 1.5$ms. *a, inset*: Semi-logarithmic scale indicates that to a large degree, the non-stationary velocity auto-correlation functions are exponential, regardless of the component.

| | $T = 1/\Omega$ (ms) | $T/T_{L,i}$ - | | | $\tau_{a,i}/\tau_\eta$ - | | |
|---|---|---|---|---|---|---|---|
| $\mathrm{Re}_\lambda$ | - | $i = x$ | $i = y$ | $i = z$ | $i = x$ | $i = y$ | $i = z$ |
| 155 | 238 | 6.3 | 13.1 | 12.5 | 1.42 | 1.30 | 1.11 |
| 190 | 181 | 6.1 | 12.8 | 12.2 | 1.37 | 1.25 | 1.13 |
| 225 | 145 | 6.1 | 13.0 | 11.2 | 1.35 | 1.22 | 1.15 |

Table 4.4: Integral scales measured using "non-stationary" velocity and acceleration auto-correlation functions in figures 4.5(a & b). The impeller rotation frequency is given by $\Omega$. The Lagrangian integral scale : $T_L = \int_0^{t_0} R_{vv}(\tau)d\tau$, and the acceleration integral time $\tau_a = \int_0^{t_0} R_{aa}(\tau)d\tau$, are normalized with flow quantities at large and small scale. In both cases $t_0$ is the zero-crossing of the auto-correlation function.

interpreted by the fact that the Eulerian field visited at the beginning of a trajectory is not the same as is visited at the end. This reflects non zero values of the transport terms in $\langle Dv_i'^2/Dt \rangle$ which are responsible for non-stationarity that appears across the relevant time scales: from nearly $\tau_\eta$ in figure 4.5(b) to the Lagrangian integral scale, $(T_L\Omega)^{-1} \sim 6$. Table 4.4 gives values for the integral time scales of the velocity and acceleration. Similar values for the Reynolds number range investigated here indicates that the non-stationarity measured here is truly a function of the flow topology and not likely to have a strong Reynolds number dependence.

Not all velocity and acceleration components feel the non-stationarity in the same way as was first apparent in the trajectories of figure 4.1 and then the autocorrelation functions of figure 4.2(b-d) and 4.3(b-d) where the slope of the blue curves indicated the contributions of advective and turbulent transport. The transport of velocity and acceleration variance in the diverging components (figure 4.2 and 4.3 c-d) were negligible in comparison to the converging components. This is reflected in the near perfect collapse of the "non-stationary" and "stationary" correlation functions in figure 4.5(a & b).

Quantification of the difference between non-stationary and stationary estimates of the correlation functions are of interest and are the subject of the following paragraph.

### 4.3.1 The Taylor time scale

As was seen in section 4.1.2 the Taylor scale results from a short time approximation of the symmetric form of the velocity co-variance (eq. 4.13) and seems to be driven by the anisotropy of the underlying flow:

$$\tau_{\lambda,i}^2 = 2\frac{\langle v_i'^2 \rangle}{\langle a_i'^2 \rangle}. \tag{4.29}$$

However, the velocity auto-correlation function (eq. 4.28) is often the tool used in Lagrangian studies, in particular to define the integral Lagrangian time $T_L$. This equation was shown to be sensitive to the inhomogeneity of the flow, and a similar intuition led to investigation into the effects of decaying turbulence in a wind tunnel (a spatially inhomogeneous flow) on the values of $\tau_\lambda$ [137]. Below is a calculation inspired by this work and takes into account the inhomogeneity of the present flow on a modified Taylor scale $\widetilde{\tau}_\lambda$.

Considering the non-stationary Lagrangian auto-correlation function in equation (4.28), the inhomogeneity of the flow translates the fact that $\langle v_i'^2 \rangle_L(0) \neq \langle v_i'^2 \rangle_L(-\tau)$. Expanding the numerator of equation (4.28) in a Taylor series gives:

$$\langle v_i'(0)v_i'(\tau)\rangle_L \simeq \langle v_i'^2 \rangle + \frac{\tau}{2}\Big\langle \frac{Dv_i'^2}{D\tau} \Big\rangle - \frac{\tau^2}{2}\Big(\Big\langle (\frac{Dv_i'}{D\tau})^2 \Big\rangle - \frac{1}{2}\Big\langle \frac{D^2v_i'^2}{D\tau^2} \Big\rangle\Big). \tag{4.30}$$

Similarly, expanding the square root into the numerator while keeping only $\mathcal{O}(\tau^2)$ terms gives an expression for the correlation function:

$$R_{vv}(\tau) \simeq 1 - \Big[\Big\langle (\frac{Dv_i'}{D\tau})^2 \Big\rangle - \frac{1}{4}\frac{1}{\langle v_i'^2 \rangle}\Big\langle \frac{Dv_i'^2}{D\tau} \Big\rangle^2\Big]\frac{\tau^2}{2\langle v_i'^2 \rangle}. \tag{4.31}$$

The form of equation (4.31) differs slightly from that given in the publication of Corrsin and Uberoi. In their publication, the authors assumed the ensemble average and temporal derivatives to be commutative, an assumption which does not hold

when turbulent fluxes given by $\partial_{x_k}\langle v_k' v_i'^2\rangle$ are present.

Kinematically, it is known that the Taylor time scale is given by:

$$\begin{aligned}\frac{1}{\widetilde{\tau}_\lambda^2} &= \lim_{\tau\to 0}\left(\frac{1-R_{vv}(\tau)}{\tau^2}\right)\\ &= -\frac{1}{2}\frac{d^2R_{vv}(\tau)}{d\tau^2}.\end{aligned} \tag{4.32}$$

It follows from the previous calculation that the Taylor time scale is given by:

$$\widetilde{\tau}_\lambda^2 = \tau_\lambda(1-\alpha^2)^{-1}, \tag{4.33}$$

where $\langle a_i'^2\rangle = \lim_{\tau\to 0}\langle(Dv_i'/D\tau)^2\rangle$, the classic Taylor time scale is $\tau_{\lambda,i} = 2\langle v_i'^2\rangle/\langle a_i'^2\rangle$ and $\alpha$ is related to the velocity variance budget at $\vec{X}_\gamma(t^*)$ and is written:

$$\alpha = \frac{1}{2}\frac{\langle Dv_i'^2/Dt\rangle}{\langle v_i'^2\rangle^{1/2}\langle a_i'^2\rangle^{1/2}}. \tag{4.34}$$

In equation 4.34 $\alpha$ may drastically increase the effective Taylor time scale ($\widetilde{\tau}_\lambda$) as its value approaches one. In the following paragraph we investigate the status of this correlation term and its relationship to the non-stationarity of Lagrangian statistics.

### 4.3.2 Anisotropic versus inhomogeneous contributions to $\widetilde{\tau}_\lambda$

Up until now Lagrangian non-stationarity has been referred to as the exploration of an inhomogeneous Eulerian field by a particle. The modified Taylor scale ($\widetilde{\tau}_\lambda$) relates this exploration to non-negligible values of $\alpha$ which is directly related to the quantity ($\langle Dv_i'^2/D\tau\rangle$) used to study non-stationarity in section 4.1. This time scale is of interest because it determines the form of the velocity autocorrelation curve up to a few Kolmogorov time scales.

The modified Taylor time scale depends on the the value of $\alpha$ which may be re-expressed taking into account the kinematic relationship for $\langle Dv_i'^2/D\tau\rangle$ (eq. 4.7). Rewriting $\alpha$ in equation (4.34) gives:

$$\alpha_i = \frac{1}{2}\frac{\langle Dv_i'^2/Dt\rangle}{\langle v_i'^2\rangle^{1/2}\langle a_i'^2\rangle^{1/2}} = \frac{\langle v_i' a_i'\rangle}{\langle v_i'^2\rangle^{1/2}\langle a_i'^2\rangle^{1/2}} + \frac{\mathcal{P}_{ii}}{\langle v_i'^2\rangle^{1/2}\langle a_i'^2\rangle^{1/2}}, \tag{4.35}$$

where summation is not implied over repeated indices. The first term on the right hand side of equation (4.35) is essentially a normalized Navier-Stokes equation multiplied by $v_i'$ and thus describes the particle dynamics as the stagnation point is approached. Figure 4.6(a) demonstrates that the correlation ($\langle v_i' a_i'\rangle$) is negative for $i = x$ which indicates that as the particle velocity undergoes positive fluctuations it has a tendency decelerate while the opposite is true in the $y$ and $z$ directions. This is coherent with a strongly converging direction ($x$) and two weaker ($y$ and $z$) directions. The largest values are attained at the stagnation point's center, $x/L = 0$, indicating that the underlying flow is soliciting a maximal response from the particles. While $\langle Dv_i'^2/D\tau\rangle$ is relevant to the general notion of inhomogeneity, the correlation term indicates *how* particles explore this inhomogeneous field.

The second term is directly related to the anisotropy of the flow. It was observed that the reynolds tensor was diagonal which imposes the existence of anisotropy if

production of turbulence is to occur in an incompressible flow. In other words, if $\langle v_x'^2\rangle = \langle v_y'^2\rangle = \langle v_z'^2\rangle = \langle v'^2\rangle$, then by writing the total production as it appears in the TKE budget:

$$\mathcal{P} = 3\langle v'^2\rangle(\partial_x\langle v_x\rangle + \partial_y\langle v_y\rangle + \partial_z\langle v_z\rangle) = 0. \tag{4.36}$$

Therefore, in the flow considered where total local production is nearly double the local dissipation rate, the constraint of a diagonal Reynolds tensor implies that $\mathcal{P}_{ii}$ reflects the anisotropy of the flow. Figure 4.6(b) indicates the hierarchy of this term's contribution follows that of the production investigated in chapter 3 and is coherent with maximal values at the stagnation point's center.

To fully understand the corrective term $\alpha_i$ in equation (4.33), one must add the contributions of figures 4.6(a) & 4.6(b), the result is plotted in figure (4.7). The largest correction to $\tau_\lambda$ is in the $x$-direction corresponding to the most inhomogeneous direction as well as the component producing the most turbulence. The values of $\alpha_i$ given in figure (4.7) ought to reflect measurements made of $\langle Dv_i'^2/D\tau\rangle/2$ using the antisymmetric form of the velocity covariance (table 4.1). Indeed, using the velocity and acceleration variance values estimated in table 4.2 to calculate the product, $\alpha_i(\langle v_i'^2\rangle\langle a_i'^2\rangle)^{1/2}$, the values of $\langle dv_i'^2/d\tau\rangle/2$ measured in section 4.1.2 are obtained. [9]

Coherence between Lagrangian and Eulerian estimates of $\langle Dv_i'^2/D\tau\rangle/2$ permit the calculation of the modified Taylor time scale $\widetilde{\tau}_\lambda$. From equation (4.33), $\widetilde{\tau}_{\lambda,i}/\tau_{\lambda,i} = (1-\alpha^2)^{-1/2}$. For $i = x$, the modifying term $\alpha_x^2 = 0.0025$ which is negligibly small in the and indicates that even for the most non-stationary component, $\widetilde{\tau}_\lambda = \tau_\lambda$ at the stagnation point's center. This is an essential result. In effect it says that at short times, any differences in the shape of the velocity auto-correlation curve among different components are due to anisotropy, and not the inhomogeneity of the flow.

However, zones exist where the fluctuating components of the velocity and acceleration conspire to elevate the role played by non-stationarity in the of the modified Taylor time scale. Perhaps counter-intuitively, these regions are roughly $0.5L$ away from the geometrical center (fig. 4.7) where the flow may be significantly "calmer" but result in increases of about 3% in $\widetilde{\tau}_\lambda$. Interestingly, in their derivation of equation 4.33, Corrsin and Uberoi posited that the correction to the Taylor scale might only be of consequence in the low Reynolds numbers range. Results in the following chapter will indicate that $\mathrm{Re}_\lambda$ is approximately constant in the within $0.5L$ of the stagnation point, however, elsewhere the $\widetilde{\tau}_\lambda$ may be more susceptible to the non-stationary aspects of the Lagrangian statistics.

Concerning the $\mathrm{Re}_\lambda$ dependence of $\alpha$, the use of $(\langle v_i'^2\rangle\langle a_i'^2\rangle)^{1/2}$ is the natural normalization of the cross correlation $\langle v_i'a_i'\rangle$ and should take into account any Reynolds number dependency of this quantity. On the other hand the same may not be true for the production term for which one may estimate the Reynolds number dependence by writing:

$$\frac{\mathcal{P}_{ii}}{\langle v_i'^2\rangle^{1/2}\langle a_i'^2\rangle^{1/2}} = -\frac{\langle v_i'^2\rangle\partial_{x_i}\langle v_i\rangle}{\langle v_i'^2\rangle^{1/2}\langle a_i'^2\rangle^{1/2}} = -\frac{\tau_{\lambda,i}\mathcal{S}_i}{\sqrt{2}}, \tag{4.37}$$

where $\mathcal{S}_i = \partial_{x_i}\langle v_i\rangle$ is a diagonal component of the mean velocity gradient. Note that $\mathcal{S}_i \sim \Omega \sim 1/T_L$ (ch. 2, table 4.4) and that $\tau_\lambda \sim (\tau_\eta T_L)^{1/2}$ [129]. Thus,

9. When $\alpha_x = .065$ and $\langle v_x'^2\rangle = 0.33$ and $\langle a_x'^2\rangle = 4100$, one may calculate $\alpha_x(\langle v_x'^2\rangle\langle a_x'^2\rangle)^{1/2} = 2.45$ which is close to the value of $\langle Dv_x'^2/D\tau\rangle/2$ given in table 4.1 for $\mathrm{Re}_\lambda = 190$.

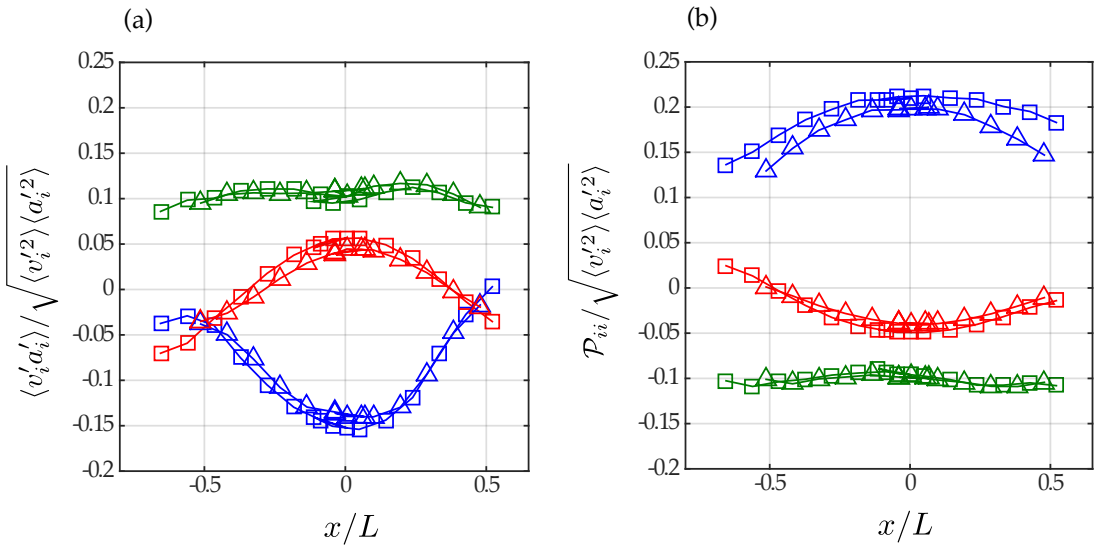


Figure 4.6: Contributing terms of equation (4.35). *(a) :* Normalized velocity-acceleration cross correlation. *(b) :* Normalized Production. □: $\mathrm{Re}_\lambda = 190$. △ : $\mathrm{Re}_\lambda = 225$. Blue symbols: $x-$component. Red symbols $y-$component. Green symbols: $z-$component. Spatial coordinates given as a function of the integral scale $L \equiv v'^3/\varepsilon = 4.8$ cm.

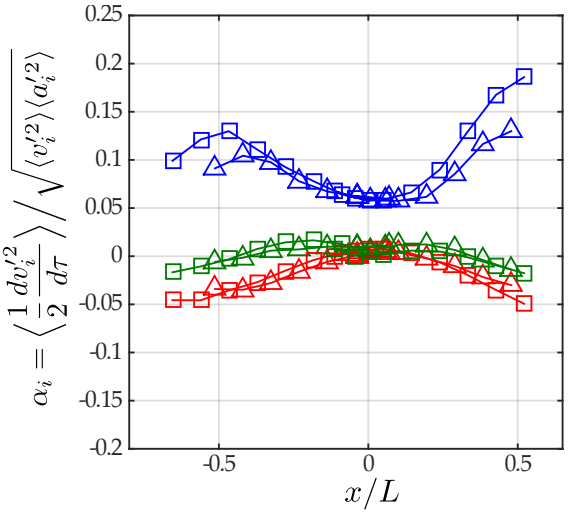


Figure 4.7: Sum of the contributing terms of equation (4.35) which give the term $\alpha$ used for the calculation of the modified Taylor time scale $\widetilde{\tau}_\lambda$. Symbols and abscissa normalization are the same as figure 4.6.

$\tau_{\lambda,i}\mathcal{S}_i \sim (T_L/\tau_\eta)^{-1/2} \sim \mathrm{Re}_\lambda{}^{-1/2}$ indicating that this term is negligible for large Reynolds numbers. Conversely, in the lower $\mathrm{Re}_\lambda$ range the production term may become dominant and increase the ratio $\widetilde{\tau}_{\lambda,i}/\tau_{\lambda,i}$ as postulated by Corrsin and Uberoi.

## 4.4 Conclusion

This chapter sought to quantify the initial observation from figure 4.1 that the behavior of trajectories before the conditioned origin of time ($t^*$) differed from that to come at some later time. Investigation of evolving velocity variance and the velocity auto-correlation was able to determine that such non-stationarity is directly linked to the underlying topology of the flow and the capacity of the Eulerian field to either advect velocity fluctuations or transport them via turbulent fluxes. The mean topology is dominated by a stagnation point and comparison of its principle axes indicated that velocity statistics along the strongly contracting direction are the most non-stationary, while the dilating directions are only marginally so. This analysis held for short times so as to explicitly, and quantitatively, link non-stationarity to the turbulent flux at the stagnation points center to the asymmetry in evolving velocity variances and autocorrelations along trajectories with respect to an origin $t^*$. These results are in agreement with the conclusions of the variance budget investigation (ch. 3).

A similar analysis was conducted on the acceleration signal of the conditioned Lagrangian trajectories. The non-stationarity was again seen to mostly effect the contracting component while minimally influencing the others. In general, the non-stationarity of the acceleration is less intense than that of the velocity. Non-stationarity in acceleration (and velocity) autocorrelation functions was quantified by a non zero cross-correlation coefficient $\alpha_a$ ($\alpha$).

A consequence of the finite curvature of the acceleration covariance curves as $\tau \to 0$ is finite variance of the hyperacceleration. No other experimental measurements of this quantity have been found in the literature. A few interesting properties were conjectured, perhaps the most interesting being its validity within Kolmogorov phenomenology. The measurements made seem to indicate that the correlation time of the hyperacceleration $\tau_h$ is of the same order of magnitude as the dissipative time $\tau_\eta$. However, these results require numerical and experimental confirmation.

The challenge of analyzing the present data is the proper calculation of an auto-correlation function when the quantity of interest has a non-stationary variance. To overcome this hurdle, fully "non-stationary" auto-correlation functions were proposed (eq. 4.28). Unsurprisingly, the non-stationarity of the flow strongly affects the converging direction autocorrelation functions while leaving the diverging directions virtually untouched, as witnessed by comparing "non-stationary" and "stationary" correlation functions. Following Uberoi and Corrsin, the modified Taylor time scale was investigated as a method of quantifying this non-stationarity. However, the measurements proved only marginally effected. This may be due to the fact that only short times have investigated for which the underlying anisotropy has a dominant effect while long time scales are characterized by Lagrangian integral time $T_L$ which is likely to take into account the inhomogeneity of the flow. In the next chapter the role of flow anisotropy, and more specifically the Taylor time scale $\tau_\lambda$, in understanding the difference between time scales in the dissipative range for tracer and inertial particles will be investigated.

# Chapter 5

# Small scale statistics of turbulent fluctuations close to a stagnation point.

## 5.1 Motivation

In the previous chapter the non-stationarity felt by Lagrangian trajectories was not seen to play a dominant role in the definition of time scales relevant to the velocity autocorrelation function. By extension, acceleration statistics are thought to be equally insensitive to the non-stationarity arising due to the inhomogeneity of the underlying flow. A question remains remains: *What mechanism drives the hierarchy of time scales in the acceleration statistics?* To respond to this question, attention is paid to the role of anisotropy, a flow property essential to the presence of turbulence in stagnation points. Using fluid tracers permits the connection between the Lagrangian time scales and the underlying flow characterized by an anisotropic Eulerian field. However, particles that have finite inertia present trajectories that deviate from those followed by fluid particles and a second question arises:*what role does inertia play in determining the characteristic time scales of particle acceleration?* The relevant parameters to so called "inertial particles" are the Stokes number, $\mathrm{St} = \tau_p/\tau_\eta$, the Kolmogorov time scale $\tau_\eta = (\nu/\varepsilon)^{1/2}$, the particle response time, $\tau_p = d^2/(12\beta\nu)$ given for a particle of diameter $d$ and $\beta = 3\rho_f/(1+2\rho_p)$ which compares a particle of density $\rho_p$ with a fluid of density $\rho_f$. Different classes of glass particles are seeded into the flow (*cf.* table 5.1) and used to investigate this question.

| Particle<br>- | $d$<br>$\mu$m | $d/\eta$<br>- | $\beta$<br>- | $\tau_p$<br>ms | $\tau_p/\tau_\eta$<br>- | $\mathrm{Re}_\lambda$<br>- |
|---|---|---|---|---|---|---|
| polysterene | 250 | 1.6 - 2.3 | 0.96 | - | - | 155-225 |
| glass | 290 | 1.9 - 2.6 | 0.52 | 1.7 | 0.5 - 1.0 | 155 |
| glass | 500 | 3.9 - 4.5 | 0.52 | 5.1 | 2.2 - 3.0 | 155-225 |
| glass | 900 | 7.0 - 8.1 | 0.52 | 16.5 | 7.6 - 9.9 | 155-225 |

Table 5.1: Characteristics of particles used in three different Reynolds number experiments. The range in $d/\eta$ as well as the $\tau_p/\tau_\eta$ reflect Reynolds number effects. $Re_\lambda$ column indicates Reynolds numbers at which each particle class was studied.

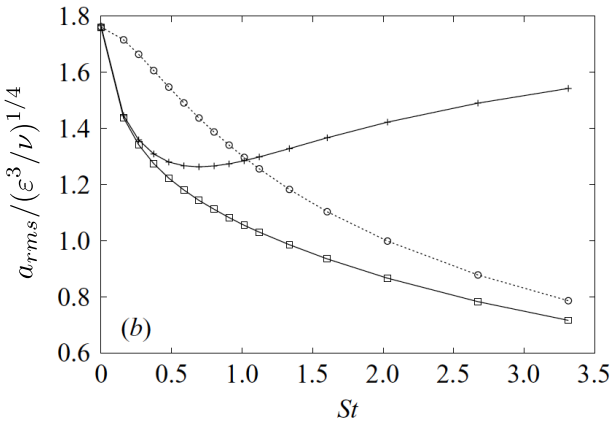


Figure 5.1: Reproduction of inertial particle statistics from the DNS study of [11] for homogeneous isotropic turbulence at $\mathrm{Re}_\lambda = 185$. The acceleration variance, $a_{rms}$ ($\square$) as a function of the Stokes number is compared with tracer acceleration measured at the particle position ($+$). The curve ($\bigcirc$) approaching Stokes dependent acceleration rms curve represents filtered tracer trajectories.

A brief comment on the phenomenology surrounding inertial particles is in order. There are several mechanisms that effect inertial particle dynamics in turbulent flows. First, particles with finite inertia cannot faithfully follow the vortical motion omnipresent in turbulent flows. The *centrifugation effect* causes heavy particles to be expelled from vortices where light particles are entrapped. Particles therefore tend to accumulate in particular regions. A direct numerical simulation of heavy particles in homogeneous isotropic turbulence highlights this effect [11]. Figure 5.1 plots the normalized inertial particle acceleration against the evolving Stoke number. At low Stokes number ($\mathrm{St} \lesssim 0.5$) the inertial particle acceleration is faithfully reproduced by calculating the fluid acceleration at the position of the particle. The implication is that heavy particles preferentially sample low vorticity regions of the flow leading to an attenuation in their acceleration fluctuations. Indeed, the monicker *preferential sampling* is often used to describe this effect.

At larger Stokes ($\mathrm{St} \gtrsim 1$ numbers a second effect becomes dominant: particle inertia may be seen as a low pass filter with a cut-off frequency $1/\tau_p$ acting on the underlying turbulence. This causes an attenuation of high frequency motion present in a given flow. In figure 5.1 the curve representing the the acceleration *rms* of trajectories filtered over a timescale $\tau_p$ converges upon the particle acceleration curve. There appear to be separate Stokes number regimes where each of these mechanisms is predominant. However, at intermediate Stokes numbers, $\mathrm{St} \sim [0.5 - 1.0]$ there may be a complex trade off between filtering and preferential sampling rendering modeling of these phenomenon particularly difficult. These two effects are sufficient to explain the behavior of particles much heavier than the fluid ($\beta \ll 1$).

When the particle density is comparable with that of the fluid ($\beta \sim 1$) "added mass" effects may become important and describe the effort exerted to displace the fluid so that the particle may move. Traditionally the added mass is grouped with the the contributions of the fluid pressure gradient and have been shown to play a non negligible role in the preferential concentration of inertial particles [70]. However, in the case of infinitely heavy particles with $\beta = 0$, such as a rain drop in

the atmosphere, these terms become negligible. Nevertheless, in the experiments considered, $\beta = 0.52$ and the effects of added mass and the fluid pressure gradient are likely substantial.

A fourth effect is ascribed to the size of particles. By varying $\mathrm{Re}_\lambda$ from 155 to 225 a range of Stokes numbers is attained: St=[0.5-9.9]. For the most part the particles are only a few Kolmogorov lengths in diameter and do not yet feel finite size effects which are related to the non-uniformity of the fluid flow at the particle scale. The so-called "Faxen" corrections become relevant for $d/\eta \simeq \sqrt{\mathrm{Re}_\lambda}$ [49] which amount to a filtering of acceleration statistics over the spatial extent of finite sized particles. The large particles used here ($d = 900\mu$m) are at the lower end of this bound and as a first approximation finite size effects are neglected.

Finally, the presence of gravity may introduce a fifth contribution to particle dynamics. The intensity of this contribution is generally measured by the Rouse number, $\mathrm{Rs} = \tau_p g/v'_z$, where $g$ is gravity and $v'_z$ are vertical fluid velocity fluctuations. For the Reynolds number experiments considered, $\mathrm{Re}_\lambda = [155, 190, 225]$ the Rouse numbers for the largest particles are: $\mathrm{Rs} = [0.65, 0.49, 0.35]$. The large value at $\mathrm{Re}_\lambda = 155$ indicates that for low Reynolds numbers gravitational effects may become predominant. Experimental trials at this Reynolds number revealed that the turbulence was not sufficiently strong to suspend 500-900 $\mu$m particles and are not included in the following analyses.

In this following chapter when the notion of an inertial particle is evoked, it may be understood with respect to these five mechanisms.

## 5.2 Anisotropy in the acceleration variance

The focus of this section is anisotropy in the variance of acceleration statistics which is deemed to be relevant to the small scale motion of the flow. The anisotropy that exists in the large scales inevitably propagates to the small scales [30] and the analysis of chapter 3 suggests that a signature of the turbulence production which occurs at the stagnation point should be found in the small scale motion of the flow. The following section presents measurements to clarify the role of anisotropy in the vicinity of the stagnation point from both Lagrangian and Eulerian perspectives. All variance and auto-correlation measurements are made using the multi-step method detailed in chapter 2.

### 5.2.1 Tracers

Acceleration statistics are investigated along trajectories confined to spherical regions with 1.5 cm radii. The various regions follow the mean flow from $\vec{x} = (\pm 3, 0, 0)$cm to $\vec{x} = (0, 0, 0)$cm, ending at the stagnation point. Figure 5.2(a) depicts the acceleration component magnitude compensated by $q_a = ({a'_x}^2 + {a'_y}^2 + {a'_z}^2)$, evaluated at the geometrical center. This normalization takes into account the acceleration magnitude's dependence on the Reynolds number, and emphasizes the inhomogeneity of the acceleration field. As opposed to the increasing velocity anisotropy (ch. 3, fig. 3.5b), the three components of the fluctuating acceleration increase in equal proportions and anisotropy is constant over the entire region of figure 5.2(a). Interestingly, the anisotropy $a_{0,x}/a_{0,z} \simeq 1.68$ is slightly larger than was measured in the Cornell University experiment [9] , though variations are well accounted for if

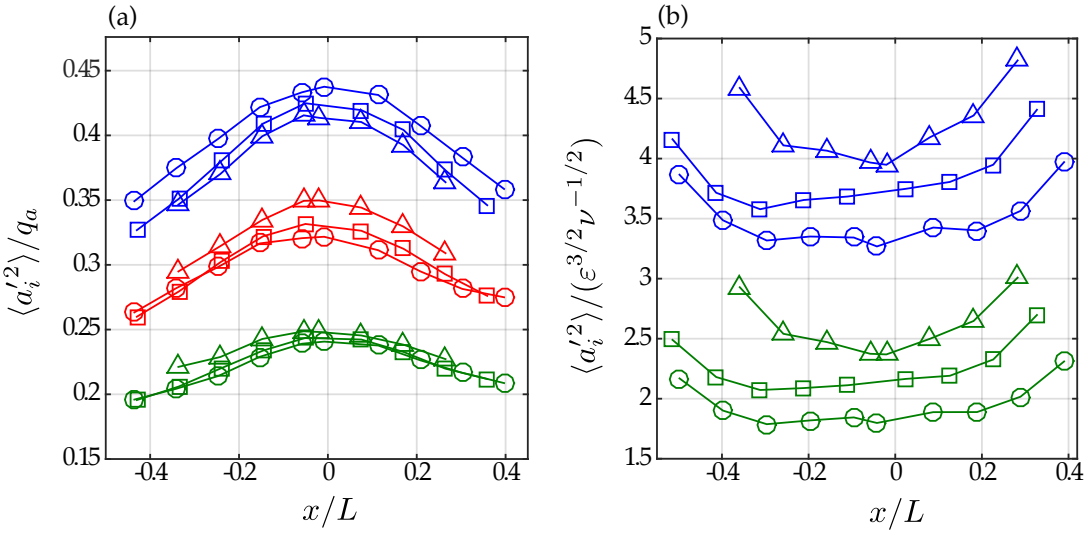


Figure 5.2: Acceleration variance near the stagnation point. ○ : $Re_\lambda = 155$, □ : $Re_\lambda = 190$, △ : $Re_\lambda = 225$. Colors indicate acceleration components: $x$: blue. $y$: red. $z$: green. *(a)* Normalized acceleration variance where $q_a = (a_x'^2 + a_y'^2 + a_z'^2)$ is evaluated at (0,0,0). *(b)* Heisenberg-Yaglom prediction of fluid particle acceleration as a function of $x/L$ using local dissipation values: $a_{0,i} = \langle a_i'^2\rangle/(\varepsilon(\vec{x})^{3/2}\nu^{-1/2})$.

the $x$ and $y$ directions are averaged as would be the case for a statistical mixture of the $x$ and $y$ dominant states.

The spatial profile of acceleration fluctuations attains a maximum value at the stagnation point which is coherent with the dissipation dependence of the Heisenberg-Yaglom prediction:

$$\langle a_i'^2\rangle = a_0\varepsilon^{3/2}\nu^{-1/2}, \tag{5.1}$$

where $a_0$ is an increasing function of the Reynolds number [9, 129]. Using this prediction we demonstrate the monotonic Reynolds number dependency of these small scales by evaluating $a_0$ in equation (5.1) using local values of the dissipation, $\langle\vec{v}'\cdot\vec{a}'\rangle(\vec{x}) \sim -\varepsilon(\vec{x})$. Figure 5.2(b) indicates the same hierarchy in fluctuating acceleration as figure 5.2(a) such that $a_{0,x} > a_{0,y} > a_{0,z}$. Following the increase in plateaus for a given acceleration component, the $Re_\lambda$ dependence of $a_0$ is observed. The values obtained may be slightly underestimated due to the the pressure-velocity correlation term contributing to the experimental determination of the dissipation rate by $\langle\vec{v}'\cdot\vec{a}'\rangle \sim -\varepsilon$. No experimental techniques have been able to measure the pressure term and it is estimated to be about 10-15% of the total measured by $\langle\vec{v}'\cdot\vec{a}'\rangle$ (ch. 3). Nevertheless, within the estimated error, the values $a_0$ measured here are consistent with similar Reynolds number measurements in the Cornell experiment [129].

An analytical expression of the fluctuating acceleration, inspired by [37], is derived as follows. The fluctuating acceleration may be written: $a_i' = a_i - \langle Dv_i/Dt\rangle$, where the material derivative is $D/Dt = (\langle v_j\rangle + v_j')\partial_{x_j}$. Therefore the variance of

the fluctuating acceleration may be written:

$$\langle a_i'^2\rangle = \left\langle \left( v_j' \frac{\partial v_i'}{\partial x_j} + \langle v_j\rangle \frac{\partial v_i'}{\partial x_j} + v_j' \frac{\partial \langle v_i\rangle}{\partial x_j} - \langle v_j' \frac{\partial v_i'}{\partial x_j}\rangle \right)^2 \right\rangle,$$
$$= \left\langle \left( \frac{Dv_i'}{Dt} + v_j' \frac{\partial \langle v_i\rangle}{\partial x_j} - \langle v_j' \frac{\partial v_i'}{\partial x_j}\rangle \right)^2 \right\rangle. \tag{5.2}$$

The above equation may be simplified in the case of a stagnation point where the off diagonal reynolds and velocity gradient tensor terms are negligible. Setting $i = j$ one obtains:

$$\langle a_i'^2\rangle \simeq \langle (\frac{Dv_i'}{Dt})^2\rangle + 2\langle \frac{Dv_i'^2}{Dt}\rangle \mathcal{S}_i + \langle v_i'^2\rangle {\mathcal{S}_i}^2, \tag{5.3}$$

where $\mathcal{S}_i$ are the diagonal components of the velocity gradient tensor. Considering an initially homogeneous and isotropic turbulence for which $\langle a_i'^2\rangle = \langle (Dv_i'/Dt)^2\rangle$, the second and third terms of equation (5.3) are contributions uniquely due to the presence of strain. For a homogeneous straining field (such as in [37]) the second term is zero, though the discussion of chapter4 implies that this term is non-zero for the stagnation point considered. More important however is the third term on the right, typically whose contribution most exaggerates the role of the straining field due to the presence of ${\mathcal{S}_i}^2$. These two mechanisms provide insight into the general observation that the contracting direction serves to amplify acceleration fluctuations more than the contracting directions. A rapid calculation using $\mathcal{S}_x \sim 33\,\mathrm{s}^{-1}$, $\langle {Dv_x'}^2/Dt\rangle \sim 2.5\,\mathrm{W.kg}^{-1}$, and $\langle v_i'^2\rangle \sim 0.33\,\mathrm{m}^2.\mathrm{s}^{-2}$ reveals that the anisotropic contributions are roughly 13% of the contracting components variance, $\langle a_i'^2\rangle = 4100\,\mathrm{m}^2.\mathrm{s}^{-4}$. This indicates that $\langle (Dv_i'/Dt)^2\rangle$ is a good approximation of fluctuating acceleration variance and provides insight into why estimations of the Heisenberg-Yaglom constant ($a_0$) in inhomogeneous turbulence are often larger than in HIT turbulence with similar Reynolds numbers [129].

Interestingly, the normalized curves are approximately constant over nearly an integral length scale $L$. This is consistent with the spatially invariant $Re_\lambda$ deduced from hot-wire measurements in low-temperature helium gas experiments using a similar counter rotating disk device [114]. Furthermore, constant $a_0$ in the central region indicates that the Heisenberg-Yaglom scaling is accurate in this region and that the dissipation $\varepsilon$ is the determining term in the acceleration magnitude. The upward turning tails of figure 5.2(b) may indicate that competing terms, pressure-velocity transport for instance, become important further from the stagnation point. The observed scalings for the acceleration variance indicate that K41 arguments may be valid in regions that are not necessarily homogeneous or isotropic but undergo strong turbulence production.

### 5.2.2 Inertial particles

Using three different classes of glass particles (*cf.* table 5.1), the role of particle inertia is studied on velocity, acceleration and hyperacceleration statistics. Except when explicitly stated otherwise trajectories are collected in a spherical region 1.5cm in radius located at the center of the stagnation point.

• Velocity variance The velocity statistics are calculated at $x/L = 0$ and maintain the hierarchy $\langle {v_x'}^2\rangle > \langle {v_y'}^2\rangle > \langle {v_z'}^2\rangle$ although the anisotropy increases with particle

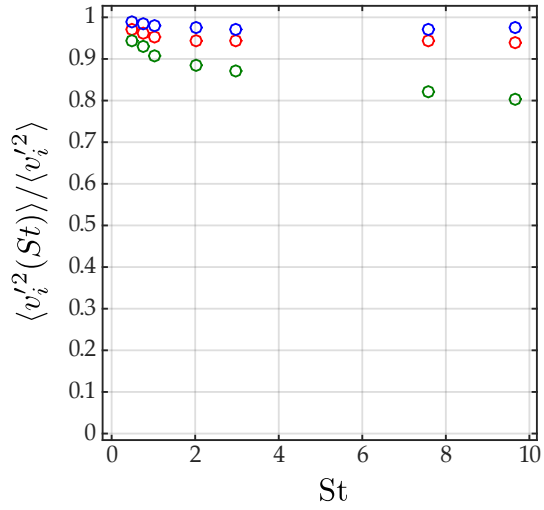


Figure 5.3: Inertial particle velocity variance ($\langle v_i'^2(\mathrm{St})\rangle$) normalized by the tracer velocity variance ($\langle v_i'^2\rangle$) for ensembles of trajectories taken at the stagnation point's center ($x/L = 0$). Blue: $x$, red: $y$, green: $z$.

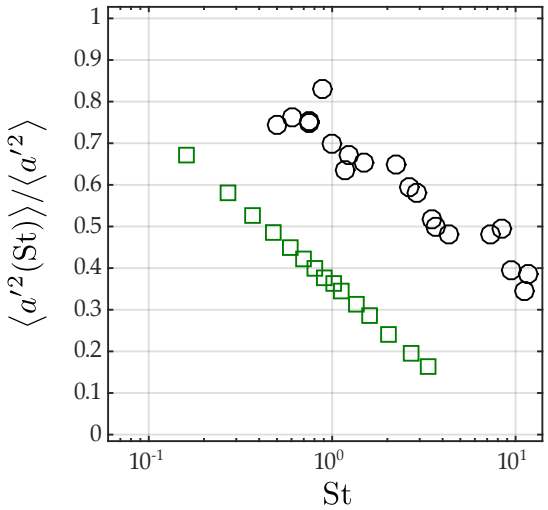


Figure 5.4: Comparison of decay in acceleration variance as a function of Stokes number in DNS (□, $\mathrm{Re}_\lambda = 185$, [139] ) and the experiments (○, $\mathrm{Re}_\lambda = [155 - 225]$). Inertial particle acceleration root means square $\langle a'^2(\mathrm{St})\rangle = (\langle a_x'^2(\mathrm{St})\rangle + \langle a_y'^2(\mathrm{St})\rangle + \langle a_z'^2(\mathrm{St})\rangle)/3$ normalized by the tracer acceleration root mean square $\langle a'^2\rangle$ for ensembles of trajectories taken at three locations: $x/L = [-0.3, 0, 0.3]$.

inertia (figure 5.3). This effect is primarily due to the evolution of the z-component variance which falls to about 80% that of the tracers for the largest Stokes and is the most spatially homogeneous component. This result may be compared with HIT simulations [138] where the same quantity falls to about 50% of the fluid velocity variance at a similar Stokes number. In contrast the $x$ and $y$ components evolve by less than 7% of the tracer value. The juxtaposition of the Stokes dependence in these directions suggests that strong inhomogeneity impedes the filtering effect on velocity statistics. This may explain a stronger decay in the $z$ component even though its evolution is weaker than is observed in homogeneous and isotropic turbulence.

• Acceleration variance: Acceleration statistics display increased sensitivity to particle inertia in figure 5.4. The square of the *rms* acceleration, $\langle a'^2 \rangle = (\langle a_x'^2 \rangle + \langle a_y'^2 \rangle + \langle a_z'^2 \rangle)/3$ is judged to be an adequate measure of acceleration statistics as no distinction can be made between the $x$, $y$, and $z$ component evolution with the Stokes number. The trajectories used to calculate $\langle a_i'^2 \rangle(\mathrm{St})/\langle a_i'^2 \rangle$ are sampled at $|x/L| = 0.3$ and $x/L = 0$. The collapse of these points onto a single curve suggests that the acceleration field seen by a particle is a weighted version of that which would be seen by a tracer and follows a relationship of the form:

$$\langle a_i'^2 \rangle_p(x, y, z, \mathrm{St}_\ell) = \langle a_i'^2 \rangle_t(x, y, z) f(\mathrm{St}_\ell), \tag{5.4}$$

where the subscripts refer to the inertial particle ($p$) and tracer ($t$) variance. The functional form of equation (5.4) may be a consequence of the local Reynolds number that is approximately constant (fig. 5.2). A local Kolmogorov time scale that evolves in space, $\tau_{\eta,\ell} = \tau_\eta(\vec{X}_\gamma(t))$, may be calculated using the local dissipation rate $\varepsilon(\vec{X}_\gamma(t))$. The local Stokes number may then be defined: $\mathrm{St}_\ell = \tau_p/\tau_{\eta,\ell}$ and governs the function $f(\mathrm{St}_\ell)$ which has the empirical form: $f(\mathrm{St}_\ell) = \zeta - \delta \log(\mathrm{St}_\ell)$. The constant $\zeta$ gives the ratio of inertial particle to tracer variances at $\mathrm{St}_\ell = 1$ and $\delta$ sets the rate of change in variance with respect to the local Stokes number.

Figure 5.4 compares experiments with DNS results for similar Reynolds numbers [11]. In the DNS experiments three Reynolds numbers were tested, $\mathrm{Re}_\lambda = [65,\ 105,\ 185]$, and the highest is presented here. Over this range the parameter $\delta$ increased slightly with $\mathrm{Re}_\lambda$, indicating that any intermittency corrections are largely taken into account when normalizing by the fluid acceleration. However, the value of $\zeta$ in the experiments is roughly double the value in the DNS and may be due to the added mass and fluid pressure gradient contributions to inertial particle dynamics. These terms are accounted for in a simplified version of the particle equation of motion [47] known as the *beta-Stokes* model [70]:

$$\vec{a}_p = \frac{d\vec{V}}{dt} = \beta \frac{D}{Dt}\vec{v}(\vec{x}(t), t) - \frac{1}{\tau_p}\left(\vec{V} - \vec{v}(\vec{x}(t), t)\right) \tag{5.5}$$

where $\vec{a}_p$ is the particle acceleration, $\vec{V}$ is the particle velocity, $\vec{v}$ is the fluid velocity, and $D/Dt(\,\cdot\,)$ is the material derivative. In the experiments $\beta = 0.5$ and the first term on the right hand side, accounting for added mass effects and the fluid pressure gradient contributions, may not be negligible. In contrast, the DNS results take $\beta = 0$ indicating that the particle is infinitely heavy (like a raindrop in air) and at large Stokes numbers (St>0.5) filtering of the fluid acceleration dominates the particle dynamics. If the experimental particle acceleration variance ($\langle \vec{a}^2 \rangle_p$) is considered to have two contributions, the fluid acceleration variance ($\langle \vec{a}^2 \rangle_t$) and the square of the

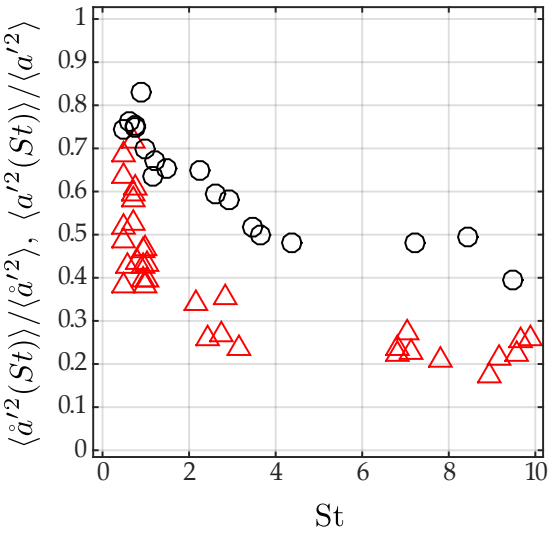


Figure 5.5: Comparison of the hyperacceleration (△) and acceleration (○) decay as a function of Stokes number for $\mathrm{Re}_\lambda = [155 - 225]$. Ensembles of trajectories are chosen at $x/L = [-0.3, 0, 0.3]$. As with the acceleration, hyperacceleration decay does not display a component wise dependence and the rms value is investigated: $\langle \mathring{a}'^2\rangle = (\langle \mathring{a}_x'^2\rangle + \langle \mathring{a}_y'^2\rangle + \langle \mathring{a}_z'^2\rangle)/3$.

Stokes drag ($\langle \vec{a}^2\rangle_s$) while ignoring the cross correlations, one may then write particle to tracer ratio as:

$$\frac{\langle \vec{a}^2\rangle_p}{\langle \vec{a}^2\rangle_t} = \beta^2 + \frac{\langle \vec{a}^2\rangle_s}{\langle \vec{a}^2\rangle_t}. \tag{5.6}$$

Assuming that the DNS result is a benchmark for the Stokesian contributions to acceleration variance decay ($\langle \vec{a}_s{}^2\rangle/\langle \vec{a}^2\rangle_t$) then the difference between the experimental decay and numerical decay is given by $\beta^2 = 0.27$ for the particles studied here. This factor adequately accounts for the offset between the DNS and experiments (fig. 5.4), indicating that the added mass and role of the fluid pressure gradients have non-negligible contributions to particle dynamics for density ratios ($\beta \simeq 0.5$) that are not too elevated.

• Hyperacceleration variance: The evolution of hyperacceleration statistics with particle inertia are plotted in figure 5.5. As with the acceleration statistics, no evident component wise evolution of the hyperacceleration variance was detected. Thus, the $\langle \mathring{a}'^2\rangle = (\langle \mathring{a}_x'^2\rangle + \langle \mathring{a}_y'^2\rangle + \langle \mathring{a}_z'^2\rangle)/3$ is sufficient to characterize the evolution of the hyperacceleration with particle inertia. A double derivative of the acceleration variance results in the hyperacceleration: $\langle \mathring{a}'^2\rangle = -\langle a'^2\rangle d^2 R_{aa}(0)/d\tau^2$, where $R_{aa}(0)$ is the acceleration autocorrelation function evaluated at zero lag. The increased weight put on the higher frequencies in the hyperacceleration accentuate the role of filtering due to particle inertia and explain the sensitivity of these statistics to the Stokes number.

## 5.3 Anisotropy in the dissipative time scales

To investigate the relevant time scales in the dissipative range, the acceleration autocorrelation function is typically employed whose integral is known to provide roughly equivalent to the Kolmogorov time [140, 59, 90]. In situations with strong anisotropy, such as the von Kármán flow, it is not immediately obvious how, if any, hierarchy of acceleration timescales should apply to the hierarchy of acceleration variances demonstrated in section 5.2.

### 5.3.1 Relevant time scales

Auto-correlation functions are calculated such that trajectories are selected based on the condition $\vec{X}_\gamma(t^*) = \vec{\gamma}$, where the point of departure of the trajectories (and origin of time) is the center of the stagnation point $\vec{\gamma}/\eta = (0, 0, 0)$. Acceleration of such trajectories $a(t) = \ddot{\vec{X}}_\gamma(t)$ is used to calculate the non-stationary acceleration autocorrelation function as in chapter 4:

$$R_{aa,i}(\tau) = \frac{\langle a_i'(0)a_i'(\tau)\rangle_L}{\sqrt{\langle a_i'^2\rangle_L(0)\langle a_i'^2\rangle_L(\tau)}} \qquad \tau = t - t^*. \tag{5.7}$$

The correlation function may be used to define a time scale $t_0$, such that $R_{aa,i}(t_0) = 0$. This time scale, aptly named the "zero-crossing" time, refers to the point at which the acceleration auto-correlation is zero. Experimental evidence has shown that the integral of equation (5.7) defines a timescale,

$$\tau_a = \int_0^{t_0} R_{aa}(\tau)\mathrm{d}\tau, \tag{5.8}$$

that is linked to the dissipative scale of turbulence $\tau_a \sim 1.1\tau_\eta$ [140]. Early simulations [90] calculated acceleration autocorrelation functions for a restricted range of small $Re_\lambda$ and found $t_0 \simeq 2.2\tau_\eta$. It is of note that the tracer correlation curves in figure 5.6(a) are taken at the two significantly different Reynolds numbers and display a component-wise collapse when normalized by $\tau_\eta$. Thus, for tracer particles either $t_0$ or $\tau_a$ is sufficient to characterize the acceleration correlation as they are both directly linked to the relevant time scale in the dissipative range, $\tau_\eta$. However, anisotropy among the components is maintained approximately constant despite the evolution in Reynolds number.

The hierarchy of the timescales from figure 5.6(a) is such that $t_{0,x} > t_{0,z}$ and may be contrasted with the hierarchy of acceleration variances $\langle a_x'^2\rangle > \langle a_z'^2\rangle$. This observation is somewhat counter-intuitive when considering the results of K41 phenomenology where $\tau_\eta = (\nu/\varepsilon)^{1/2}$ and that $\langle a_i'^2\rangle \propto \varepsilon^{3/2}$ (eq. 5.1). The combination of these results would suggest smaller dissipative time scale, and consequently a smaller zero-crossing for the most active components. However, the opposite is observed; the strongest fluctuations ($x$ component) has the largest zero-crossing whereas the weakest component ($z$ component) has the shortest.

To reconcile this apparent contradiction it is useful to investigate other time scales that are relevant to the problem. One that is recurring is the Lagrangian velocity integral time scale, $T_L$ which typifies the velocity auto-correlation function

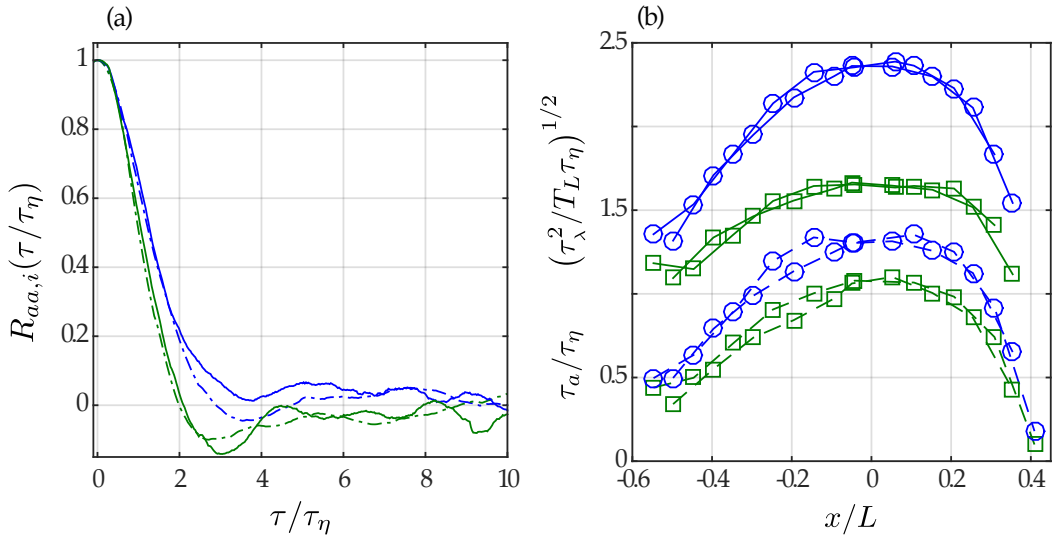


Figure 5.6: Acceleration correlation statistics for tracers. (a) Acceleration autocorrelation function at $\mathrm{Re}_\lambda = 155$ (solid line) and $\mathrm{Re}_\lambda = 225$ (dash-dotted line). Green lines: $z$ component. Blue lines: $x$ component. The $y$ component has removed for clarity. (b) Comparison of evolution in normalized acceleration integral time: $\tau_a/\tau_\eta$ (dashed lines), and normalized Taylor scale: $(\tau_\lambda^2/T_L\tau_\eta)^{1/2}$ (solid lines). $x$ component: ○, $y$ component □. Two Reynolds numbers experiments are given for each component, $\mathrm{Re}_\lambda = [190 - 225]$. The dissipative scale is calculated locally, $\tau_\eta = (\nu/\varepsilon(\vec{x}))^{1/2}$ where $\varepsilon(\vec{x}) = -\langle\vec{v}'\cdot\vec{a}'\rangle(\vec{x})$. The velocity integral time $T_{L,i}$ is nearly constant for each component near the stagnation point. An average value is calculated for each Reynolds number, $T_L = (T_{L,x} + T_{L,y} + T_{L,z})/3$.

that is an exponential at large times (ch. 4 fig. 4.5 a). An estimation of this integral time gives: $T_L \sim \tau_\eta \mathrm{Re}_\lambda$, indicating that $T_L$ may be too large to be of interest for characterization of tracer dissipative dynamics. Still, another time scale is available using the velocity autocorrelation function: the Taylor time scale where $\tau_\lambda^2 = 2\langle v'^2\rangle/\langle a'^2\rangle$. Stochastic modelling relates the Taylor time scale to the large and small scales via: $\tau_\lambda \simeq (\tau_\eta T_L)^{1/2} \sim \tau_\eta\,\mathrm{Re}_\lambda{}^{1/2}$ [129]. Measurements in chapter 4 indicate that $\tau_{\lambda,x} \sim 6.5\tau_\eta$ with weak Reynolds number dependence. For moderate Reynolds numbers, the Taylor time scales may provide insight into the hierarchy of the dissipative range temporal dynamics.

To compare evolving time scales at different locations along the contracting direction approaching the stagnation point (fig. 5.6 b), the acceleration integral time scale and Taylor time are normalized by the local dissipative time scale, $\tau_\eta(\vec{x}) = (\nu/\varepsilon(\vec{x}))^{1/2}$, where $\varepsilon(\vec{x}) \sim -\langle\vec{v}'\cdot\vec{a}'\rangle(\vec{x})$ (as in figure 5.2). Interestingly, both the Taylor time and the acceleration integral time demonstrate an increased anisotropy at $x/L = 0$ where the strain is the highest. However, anisotropy in the the Taylor time scales is roughly 20% larger than in the dissipative range which may be due to the fact the smaller scales are more isotropic.

Nevertheless, the anisotropy in the Taylor time scale strongly resembles the evolution of the small scale anisotropy as the stagnation point is approached. This is a direct consequence of the ratio $\langle v_i'^2\rangle/\langle a_i'^2\rangle$ appearing in the definition of $\tau_{\lambda,i}$. The results of chapter 3 in figure 3.5(b) indicate that $\langle v_x'^2\rangle/\langle v_z'^2\rangle$ nearly doubles from

1.75 at $|x/L| = 0.5$ (respectively $x = |0.04|$ cm in fig. 3.5b) to 3.0 at the stagnation point whereas $\langle {a'_x}^2 \rangle / \langle {a'_z}^2 \rangle \sim 1.7$ and remains roughly constant. These observations predict that the small scale dynamics evolve from a isotropic state to an anisotropic one as the stagnation point is approached. Figure 5.6(b) affirms this prediction when $|x/L| > 0.4$ and suggests that Lagrangian dynamics tends towards anisotropy near the stagnation point as a result of the mean strain.

The Taylor time scale contains information on high frequency motions, as implied by the presence of $\langle a_i'^2 \rangle$, while at the same time containing information on larger scales, evident from the role of $\langle v_i'^2 \rangle$. In the Cornell experiment [33] velocity anisotropy was shown to decay slowly to just below $\langle {v'_x}^2 \rangle / \langle v'_z \rangle^2 \simeq 2.2$ at $\mathrm{Re}_\lambda \simeq 1000$ while normalized acceleration amplitude decays to $a_{0x}/a_{0z} \lesssim 1.1$ and may even eventually reach near isotropy. However, as shown above, time scales imply interaction of both large (velocity) and small (acceleration) scales. Consequently, the persistent anisotropy in the large scales resulting from the presence of the stagnation point inhibit isotropization of time scales at large Reynolds numbers. Indeed, Lagrangian measurements spanning $\mathrm{Re}_\lambda = [450 - 810]$ indicate very little evolution in $\tau_{ax}/\tau_{az}$ [141]. Despite an increasing separation between the dissipative time scales and the Taylor time ($\tau_\lambda/\tau_\eta \sim {\mathrm{Re}_\lambda}^{1/2}$), a common mechanism appears to exist for the creation of anisotropy at the Taylor and dissipative time scales for the Reynolds numbers studied here ($\mathrm{Re}_\lambda = [155-225]$) and is consistent with persistent anisotropy in measurements up to $\mathrm{Re}_\lambda = 810$.

### 5.3.2 Two time statistics of inertial particle acceleration

In the following paragraphs the dynamics of inertial particle acceleration will be investigated. Much of the phenomenology surrounding this class of particles as well as the results of section 5.2.2 suggests their dynamics will decouple from the underlying flow. The role of particle inertia on the statistics presented previously are considered.

#### Evolution in the shape of the acceleration of correlation curves

The acceleration auto correlation curves are presented in figure 5.7(a-b) at $\mathrm{Re}_\lambda = 225$ for the four classes of particles studied. The role of the particle inertia is to cause particles to decorrelate over progressively longer time scales as is witnessed by increasing zero-crossing times [60, 140]. However, the effect of inertia is not felt in the same way for both components: $t_{0,x} \sim 10\tau_\eta$ while $t_{0,z} \sim 3\tau_\eta$ at $St = 9.7$. The asymmetric response of the particles to increasing inertia is evident when trying to determine a characteristic time scale. The zero-crossing estimate of the correlation time is adequate to renormalize the correlation curves when their shapes are similar. Such is the case for the $z-$component in figure 5.7(b,inset) which suggests that these small scale dynamics are a function of a single parameter, the Stokes number. In contrast, the shape of the $x$ component changes as the inertia of the particles increases ($\mathrm{St} = [1.0, 2.9, 9.7]$) and such a renormalization is not possible (figure 5.7 a,inset). For the largest Stokes numbers, the acceleration curve has not completely decorrelated until around $\tau/\tau_\eta \sim 5 - 10$ which is close to the Lagrangian velocity integral time $T_L$, indicating that large scales may play a role in strongly inertial particle dynamics.

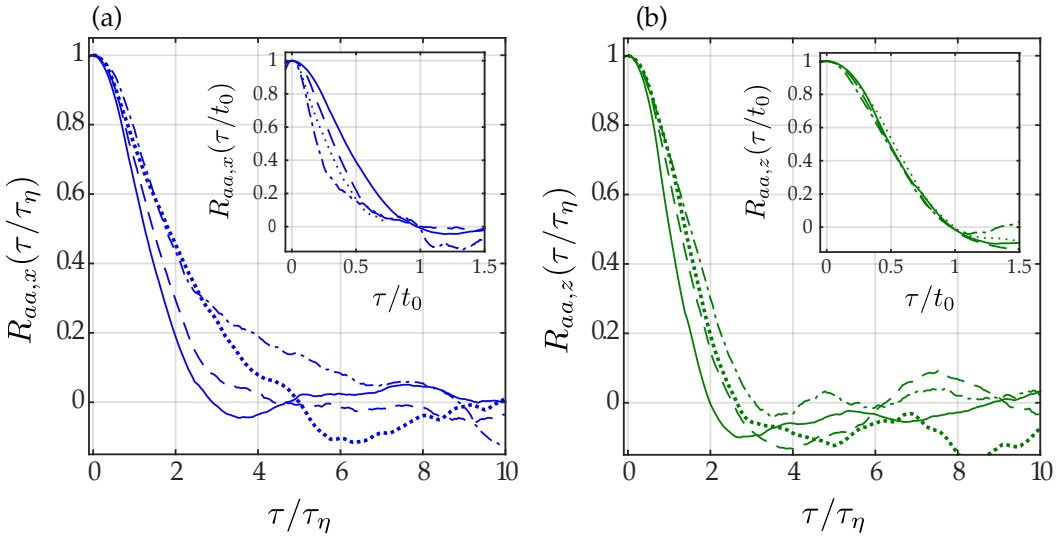


Figure 5.7: Acceleration auto-correlation functions calculated for the four classes of particles at $\mathrm{Re}_\lambda = 225$. Solid, dashed, dotted, and dash-dotted lines correspond to $\mathrm{St} = [0, 1, 2.9, 9.7]$, respectively. Trajectory ensembles are collected at $x/L = 0$. (a) $x$ component. (b) $z$ component. Normalization by the "zero-crossing" time, $t_0$ (inset), indicates that this time scale is adequate to describe the shape of the $z$ component but does not take into account the evolving shape of the $x$ component.

The appearance of time scales of order $\mathcal{O}(T_L)$ for the $x$ component that are absent in the $z$ component indicate that each component is distinct and their curves are not easily compared. In order to respond to this difficulty one may look at shorter times that may be less sensitive to an underlying process that deforms the $x$ component while leaving the $z$ components form relatively well conserved. Another standard estimate utilizes a time scale $t_{0.5}$ such that $R_{aa}(t_{0.5}) = 0.5$ leading to a new integral time scale defined as:

$$\widetilde{\tau}_a = \int_0^{t_{0.5}} R_{aa,i}(\tau)\mathrm{d}\tau, \tag{5.9}$$

where the positive part of the acceleration autocorrelation is integrated up to the time corresponding to the mid-height of the curve, $t_{0.5}$. Although not shown here, normalizing the correlation curves by $t_{0.5}$ permits a satisfactory collapse for short lags in the auto-correlation function while long times diverge. This behavior can be intuited by the evolution of the auto-correlation at small times as opposed to the brutal imposition of time scales of order $\mathcal{O}(T_L)$ for large Stokes numbers in the $x$ direction. This metric has been used elsewhere to compare different classes of particles [140] and is well adapted to understand the evolution of the dissipative timescales of the inertial particles.

The mid-height time is chosen instead of the zero-crossing because the latter displays increasing influence of large scale motion in the acceleration statistics of inertial particles. One of the main conclusions of chapter 4 was that strong inhomogeneity in a flow irrevocably condemns Lagrangian trajectories to non-stationary statistics. A conclusion to be drawn from the shape of the auto-correlation curves in figure

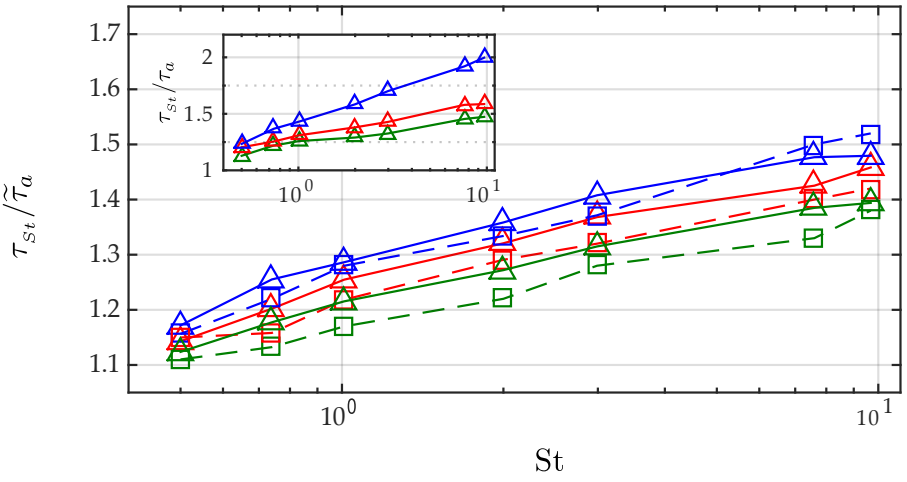


Figure 5.8: Evolution of the integral time of inertial particles ($\tau_{St}$) with respect to tracers (solid lines, △) as defined by integrating $R_{aa}$ up to $t_{0.5}$ (see $\widetilde{\tau}_a$, eq. 5.9). Dashed lines (□) indicate the estimation $\tau_\lambda/\widetilde{\tau}_a$ where $\tau_\lambda$ is calculated for each class of the inertial particles. (inset) The ratio of inertial particle to tracer acceleration integral times is evaluated using zero crossing time ($t_0$) definition of the integral in equation (5.9).

5.7 is that the progressive introduction of particle inertia enhances the effect of flow inhomogeneity as it is felt by the particles. This effect results in the appearance of time-scales of order $\mathcal{O}(T_L)$ which becomes difficult to characterize without a model for this behavior. The conclusion of chapter 4 was that anisotropy in small time statistics may be predicted by local properties of the flow. Thus, the anisotropic nature of the deformation seen in figure 5.7 may be a separate phenomenon from anisotropic dissipative dynamics of the particles. We investigate the latter in the following paragraph.

**Evolution in anisotropy among the acceleration auto-correlation curves**

The dissipative dynamics in the acceleration auto-correlation curves of tracer particles were shown to be adequately represented by a single time which in practice may be described by the "zero-crossing" of the curves, *i.e.* $t_0 \sim 2.2\tau_\eta$ . However, increasing particle inertia tends to deform the shape of acceleration auto-correlation function differently for each component. The integral time $\widetilde{\tau}_a$ was proposed as a substitute time-scale to measure the dissipative dynamics of these particles. While the Taylor time scale was adequate to describe tracer particle anisotropy at the dissipative scale it is not obvious that the same remains true for inertial particles.

Figure 5.8 plots the ratio of acceleration integral times for inertial particles ($\tau_{St}$) to tracers ($\widetilde{\tau}_a$). This figure indicate that increasing inertia causes particles to decorrelate slower which is coherent with figures 5.7(a & b). The evolution of the ratio is approximately logarithmic over more than a decade of Stokes numbers with a maximum increase in correlation times that is roughly 25% longer than tracer values. The anisotropy among the components remains constant when the integral

is evaluated up to $t_{0.5} \sim \tau_\eta$. The role of particle inertia on anisotropy in these small scale temporal dynamics is presumably insensitive to the inhomogeneities of the flow. However, upon taking the integral in equation (5.9) out to $t_0$ the anisotropy immediately increases between $x$ and the $z$ component by about 20% for the largest Stokes number as seen in figure 5.8(inset). Interestingly, the change in integral limits only marginally effects the $y$ and $z$ components by introducing a slight vertical shift. A change in integration limits for the $x$ component vertically shifts the $\tau_{St}/\tau_a$ and increases the slope. The latter observation seems to indicate that the large scale motion incorporated in $t_{0x}$ introduces correlated dynamics into the dissipative motion of inertial particles that are absent on time scales of the order $t_{0.5,x}$.

It is not obvious how to take into account the emergence of a second time scale in the acceleration dynamics. However, it is possible to account for the anisotropy present in the acceleration correlation at small times. When measuring the small time behavior present in $\widetilde{\tau}_a$, the Taylor time presents a similar time scale evolution with increasing Stokes numbers (fig. 5.8). While one should not confound the Taylor time scale with the dissipative scales, the preservation of the level of anisotropy in each metric points to a similar process that governs the determination of these time scales.

This emergence of acceleration dynamics on time scales of the order $\mathcal{O}(T_L)$ implicate the role of the strong inhomogeneity in the stagnation point topology in acceleration dynamics for inertial particles. The preferential exploration of certain regions of the flow may explain the preponderance of these time scales on the converging direction while having a smaller impact on the orthogonal directions. In the following section a somewhat speculative interpretation of the particular role the von Kármán flow's stagnation point plays in the dynamics of inertial particle acceleration.

### A phenomenological interpretation of accelerative dynamics

A phenomenological interpretation of particle motion near the stagnation point is possible. Heavy inertial particles tend to experience increasingly rectilinear accelerative motion as their inertia increases. This generality is consistent with the $x$ component losing the negative lobe of its correlation curve (fig. 5.7 a). This lobe is typically associated with eddying movement particles undergo when trapped in vortices and its disappearance is associated with the vortical structures of the flow.

The inhomogeneity of the fluid flow may be responsible for the contrasting shapes of the correlation curves in the $x$ and $z$ directions. DNS has shown that the vorticity tends to amplify [38] and align [36, 37] with the extensional direction. These observations are coherent with the mean-field maps in chapter 3 reproduced in figure 5.9(a) that indicate vortical structures aligned with the extensional $z$ direction and seem to implicate a large scale "vortex stretching " [34, 35] scenario at the stagnation point. Indeed, the presence of the vortices anchored to the walls presented in chapter 3 (fig. 3.2) may explain the vortical motion at the center of the experiment.

Figure 5.9(b) presents a trajectory seemingly trapped in the counter-clockwise rotating vortex in the upper left of figure 5.9(a) for a duration of roughly $12\tau_\eta$. The fluctuating acceleration in figure 5.9(c) demonstrates a signature of circular motion in the $\Pi(xy)$ plane with minimum acceleration aligned along the $z$ direction. A first approximation of an inertial particle response to the fluid flow may be obtained by filtering a tracer trajectory over a time scale relevant to the particle dynamics [142]. By applying exponential filters taking into account the previous history along the

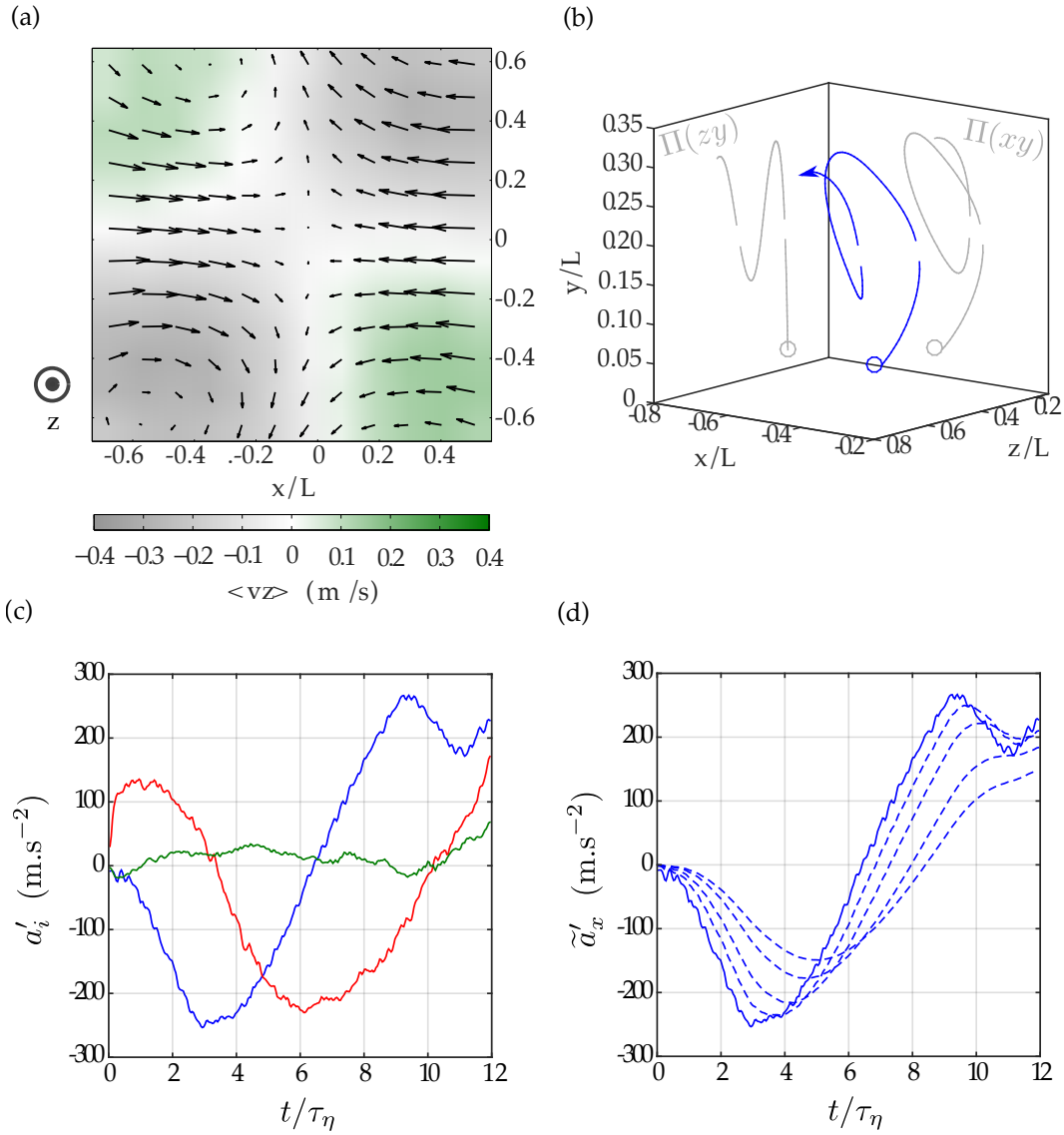


Figure 5.9: Study of a particle trapped in a vortex close to the von Kármán flow stagnation point. (a) Mean flow in the meridional, $\Pi(xy)$, plane. (b) A 3d trajectory projected onto the $\Pi(zy)$ and $\Pi(xy)$ planes. The circles indicate the trajectories initial position. (c) A portion of the fluctuating acceleration signal for the three components. Blue: $x$. Red: $y$. Green: $z$. (d) Raw and low pass filtered time evolution of $a_x'$. using exponential filters with characteristic times $t_s = [0.2 - 6]\tau_\eta$.

trajectory up to times $t_s = [0.2 - 6]\tau_\eta$ on the $x$ component, the particle clearly becomes less sensitive to the instantaneous acceleration caused by the vortex (fig. 5.9d). In particular, the possibility for the particle acceleration to have a negative covariance is diminished, corresponding to the progressive loss of the negative lobe in figure 5.7(a).

As an example, take an initial time $t^* = 3/\tau_\eta$ and a lag of $t = 4/\tau_\eta$. For the unfiltered acceleration $a'_x(t^*)a'_x(t^* + t) \simeq -12500$ m$^2$.s$^{-4}$ while for the most filtered acceleration the covariance is positive: $a'_x(t^*)a'_x(t^* + t) \simeq 12500$ m$^2$.s$^{-4}$. This is a direct effect of the tendency of strongly inertial particles to lag behind the flow. Considering the $z$ component in figure 5.9(c), the acceleration is too steady for filtering to have much of an effect. The evolution of the $z$ correlation curve (fig. 5.7b) is then attributable to particles' tendency to preferentially sampling low vorticity regions. These zones are relatively calm and Kolmogorovian phenomenology will predict lower local dissipation rates and thus larger correlation times.

This phenomenological picture, which is particular to the geometry of the present von Kármán flow, should demonstrate the difficulty in the modeling of inertial particle behavior in an inhomogeneous flow. The response of different components to the various mechanisms thought to govern inertial particle dynamics renders this zeroth order cartoon of the flow rather useful.

## 5.4 Scale by scale analysis: spectra

In the previous sections emphasis has been placed on describing the role of anisotropy in small scale statistics. The acceleration variance and integral times were investigated and the role of particle inertia emerged as a critical factor in the amplification of anisotropy in these statistics. However, these two statistics involve the integration of multi-scale functions (the spectrum and auto-correlation function) which necessarily confounds the contributions of a range of scales. In particular, this renders slightly ambiguous the notion of "small scale" when referring to the acceleration integral time or variance. The investigation of spectra is useful as it provides a scale by scale analysis and is investigated in the following section. This study will respond to two questions. First: *How do the contributions of different scales shape the acceleration spectra?* This question gives rise to a second: *Given the hierarchy of scales and their relative contributions to the acceleration signal, how is the anisotropy among the components accounted for?*

### 5.4.1 A brief overview of Sawford's Two-Time Model

Few analytical results exist for the acceleration of particles in turbulence. Sawford's 1991 stochastic modeling provides an estimation of the acceleration auto-correlation function, and therefore the spectra, and is of use as a base of comparison with the experimental results. The so called "two-time" model is presented summarily below.

Paul Langevin first introduced a stochastic equation for the velocity of a Brownian particle in 1908 [143] which has served as the building block of stochastic modeling for over a century since. A major result of Langevin's result is the exponential velocity auto correlation function that results from the existence of a single relevant time scale, the viscous relaxation time of the Brownian particle. However

the use of non-derivable, white noise as a forcing term proscribes the existence of the acceleration. Sawford's model [106] is in effect a second order Langevin equation for the fluctuating velocity and acceleration with two time scales: $T_L$ and $\tau_a$.

In this model the fluctuating velocity is given by a Langevin type model with an exponentially correlated noise ($f_i$) with a characteristic time scale $\tau_a$:

$$a = \frac{dv}{dt} = -\frac{v}{T_L} + f, \tag{5.10}$$

where the prime has been removed from the acceleration and velocity for clarity. Due to the correlation of the forcing term, the fluctuating velocity is differentiable and therefore the acceleration exists. However, the acceleration's derivative is proscribed as was the velocity's in the order 1 model. The forcing equation may be written:

$$df = -\frac{dt}{\tau_a} f + \sqrt{\frac{2\langle f^2 \rangle}{\tau_a}} dW, \tag{5.11}$$

where $dW$ is a gaussian white noise. Sawford's publication gives the following relationship between the forcing variance and the velocity variance: $\langle f^2 \rangle = {T_L}^{-1}({T_L}^{-1} + {\tau_a}^{-1})\langle v^2 \rangle$. Using this relation and equation 5.10 in the large Reynolds number limit ($\tau_a \ll T_L$) the variance of acceleration is given by : $\langle a^2 \rangle \simeq \langle v^2 \rangle / (T_L \tau_a)$. The Taylor time scale is then give by: $\tau_\lambda^2 = 2\langle v^2 \rangle / \langle a^2 \rangle = 2 T_L \tau_a$.

From this model, the following velocity auto-correlation function is derived:

$$R_{vv}(\tau) = \frac{T_L \exp(-\tau/T_L) - \tau_a \exp(-\tau/\tau_a)}{T_L - \tau_a}. \tag{5.12}$$

This double exponential auto-correlation function has been shown to fit Lagrangian experimental data quite well [10] and has been used as a diagnostic tool for determining $T_L$ when long time lags are not attainable for technical reasons [144]. Assuming a stationary signal, [1] the auto-correlation function is related to the spectrum by the cosine transform [109]:

$$\phi_v(\omega) = \frac{2}{\pi} \int_0^\infty \mathrm{R}_{vv}(\tau) \cos(\omega\tau) d\tau, \tag{5.13}$$

which is kinematically related the acceleration spectrum by :

$$\begin{aligned} \phi_a(\omega) &= \frac{2}{\pi} \int_0^\infty \mathrm{R}_{aa}(\tau) \cos(\omega\tau) d\tau, \\ &= \frac{2}{\pi} \int_0^\infty \omega^2 \mathrm{R}_{vv}(\tau) \cos(\omega\tau) d\tau, \end{aligned} \tag{5.14}$$

where $R_{aa}(\tau)$ is the acceleration auto-correlation function. Applying the cosine transform to equation (5.12) gives an analytic expression of the velocity spectrum:

$$\phi_v(\omega) = \frac{(1 + T_L/\tau_a) T_L^2/\tau_a}{(T_L/\tau_a - \omega^2 T_L^2)^2 + (1 + T_L/\tau_a)^2 \omega^2 T_L^2}. \tag{5.15}$$

1. All though text books and publications reference the cosine transform for the calculation of spectra, in practice this is very difficult due to the rapid propagation of noise in the auto correlation functions. Instead, it is much more practical to calculate the spectra (*e.g.* using the MATLAB® function "pwelch" ) directly from an ensemble of trajectory acceleration signals and then take the arithmetic mean. This is how the experimental spectra ($\phi_v(\omega)$ and $\phi_a(\omega)$) were calculated.

Note[2] that $\tau_a$ is essentially the dissipative timescale $\tau_\eta = (\nu/\varepsilon)^{1/2}$ and $T_L/\tau_a \simeq T_L/\tau_\eta \sim \mathrm{Re}_\lambda$. For infinite Reynolds number, equation 5.15 reduces to a Lorentzian, the spectrum obtained by Langevin's equation. Equation (5.15) indicates that $\phi_v(\omega) \propto \omega^{-2}$ in the inertial range and $\phi_v(\omega) \propto \omega^{-4}$ in the dissipative range. The implication for the acceleration spectrum is then a plateau in the inertial range and $\phi_a(\omega) \sim \omega^2\phi_v(\omega) \propto \omega^{-2}$ in the dissipative range. A third order stochastic equation for which the derivative of the acceleration exists thanks to a third time scale characterizing the correlation of its noise (*cf.* chapter 4 section 4.2.3) presents an acceleration spectrum of the form: $\phi_a(\omega) \propto \omega^{-4}$. This is the Reynolds model for the dissipative range [130]. These models are only likely to apply in a restricted frequency range since the true form of the spectra is likely to eventually experience an exponential decay as in the Eulerian spectrum [140]. The Lagrangian spectra are investigated in the next paragraph.

### 5.4.2 The shape of acceleration spectra

The specificity of spectra are that they are inherently *stationary*. As opposed to the auto-correlation functions calculated in chapter 4 that were conditioned on an initial time to account for the non-stationary nature of a given quantity, the spectra confound the initial moments of a trajectory with its final moments by nature of the projection of the signal onto a Fourier series of periodic functions. Accounting for the Shannon criteria and conditioning statistics with respect to a single bistable state, the number of trajectories available is reduced and the spectra calculated just barely reach the inertial range of turbulence. As will be seen below this is adequate to differentiate the acceleration dynamics of tracer and inertial particles. The Sawford model predicts two regimes for the acceleration spectra: one corresponds to uncorrelated motion in the inertial range while the dissipative range ought to be characterized by an algebraic decay. These two regimes are investigated in the following paragraph for the spectra of the *raw* acceleration, with neither filtering nor the removal of $\langle a_i \rangle(x, y, z)$.

Figure 5.10(a & b) give the normalized acceleration spectra for the four classes of particles at the same $\mathrm{Re}_\lambda$ such that the plateau value of the tracer curve gives a value of the Kolmogorov constant $C_0$ typically obtained from the second order Lagrangian structure function (*cf.* annex C). The average value of the $x$ and $y$ components ($y$ not shown here) gives $C_0 = 5.5$ which is in good agreement with measurements previous von Kármán flow measurements at $\mathrm{Re}_\lambda = 740$ [10] and is coherent with atmospheric [145] and oceanic boundary layer measurements [146]v. The decreasing values of $C_0$ is likely to be an effect of the propensity of inertial particles to sample regions of low vorticity. This may explain why the uncorrelated motion represented in a spectral plateau displays monotonic decrease with increasing particle inertia and is coherent with the acceleration variance results of section 5.2.2.

In perfectly stationary Lagrangian data the relationship in equation 5.14 should hold and $\phi_a(\omega)/(\omega^2\phi_v(\omega)) \sim 1$. Figure 5.10(a,inset) indicates that this is the case for the large frequencies regardless of the Stokes number, however, at low frequencies there is an monotonic amplification of the ratio $\phi_a(\omega)/(\omega^2\phi_v(\omega))$ with increasing Stokes number. In figure 5.7 the increasing prominence of correlation at time scales of order $\mathcal{O}(T_L)$ was attributed to the tendency of inertial particles to preferentially

2. Using Sawford's model, it can be shown that $\tau_a = \int_0^{t_0} R_{aa}(\tau)d\tau = \frac{C_0}{2a_0}\tau_\eta$. The ratio of the Kolmogorov constants is of order $\mathcal{O}(1)$. This permits the simplification $\tau_a \sim \tau_\eta$ and is coherent with experimental measurements [140].

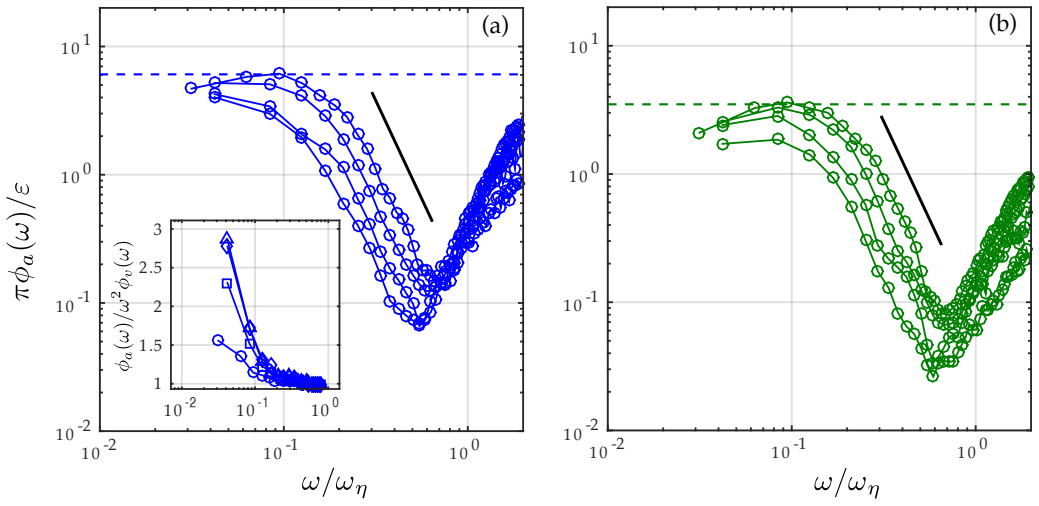


Figure 5.10: Component-wise comparison of acceleration spectra (normalized by $\omega_\eta = 2\pi/\tau_\eta$) for tracers and inertial particles (St $= [0, 0.7, 2.2, 7.6]$) for $\mathrm{Re}_\lambda = 190$. (a) $x$ component. (b) $z$ component, the $y$ component has a similar form and an intermediate magnitude and is left off for clarity. Black bars indicate a $\omega^{-3}$ power law present for each particle class. Horizontal dashed lines indicate the value of the Kolmogorov constant $C_0$ as estimated from the acceleration spectra for tracers; $C_{0x} = 6.1$, $C_{0y} = 4.8$, $C_{0z} = 3.6$ (see annex C for details). (inset) Estimation of non-stationarity in spectra (if stationary, the ratio is unity) for the x-component of particle classes. Tracer: ○, St $= 0.7$: □, St $= 2.2$: △, St $= 7.6$: ◇. The $y$ and $z$ components give similar results.

sample the inhomogeneous flow. The unique relationship between the spectrum and the auto-correlation function (eq. 5.14) indicate that this mechanism is likely the cause of the non-stationarity of figure 5.10(a,inset).

The shape of the $x$ (respectively $y$) spectra in figure 5.10(b) (resp. figure 5.10 b) display a relatively short plateau and then a transition to an algebraic fall-off; the black bar represents $\phi_{_A}(\omega) \propto \omega^\alpha$ with $\alpha = -3$. This behavior occurs near the dissipative range ($\omega\tau_\eta/2\pi > 0.1$) where a standard Kolmogorov argument would still predict a flat spectrum for the acceleration. The measured power law is not consistent with either of the stochastic models discussed earlier. The Sawford two-time model under predicts ($\alpha = -2$) the fall-off while the Reynolds model over predicts it ($\alpha = -4$). The Sawford model misses some of the small scale correlated motion while the Reynolds model assumes a separation of scale between a third time scale and $\tau_\eta$ that appears to be insignificant. The algebraic decay of the spectrum may only be a transitory regime in the the experiments and an artifact of the two (or three) relevant timescales in the models. It is more likely that decay eventually becomes exponential as is the case in the spatial, Eulerian spectrum [109].

Interestingly, figures 5.10(a & b) indicate that $\alpha = -3$ for both tracers and inertial particles. The similarity of these spectra is in agreement with other studies [101] where large particles (with respect to the integral scale $d/L \sim 0.2$), both slightly heavier and lighter than the carrier fluid, were seen to have $\alpha = -3$. That work suggested that the pressure gradient acts to trap particles in specific regions that dominate their small scale dynamics. Such observations may be explained as

an effect of added mass. Using equation (5.5) in the spirit of the Tchen-Hinze theory [65] one obtains the following relationship between the particle ($\phi_{V,p}$ and tracer ($\phi_{v,t}$) velocity spectra:

$$\phi_{V,p} = \frac{1 + (\beta\omega\tau_p)^2}{1 + (\omega\tau_p)^2}\,\phi_{v,t}. \tag{5.16}$$

This relation predicts that the velocity spectra should evolve similarly at high frequencies. As a consequence of the stationarity of these high frequencies (fig 5.10 a,inset) the same should hold for the acceleration spectra.

### 5.4.3 Isotropization of the small scales

In the Kolmogorovian vision of turbulence the large scales are anisotropic, reflecting the forcing mechanism, and the small scales become progressively more isotropic as energy is transferred to smaller and smaller eddies. Recent Lagrangian investigations have measured persistent anisotropy in the inertial range as measured by the second order structure function as well as the acceleration spectra [30]. However, those experiments relied on trajectory filtering to obtain exploitable data, an operation that unfortunately polluted the small scales where isotropy may have been expected. The following paragraph presents similar measurements made with particles sufficiently large to have incorporated minimal noise in the particle tracking step of the PTV algorithm, yet still small with regard to the Kolmogorov scale. As a result the measurements are more resistant to noise, though are not exempt.

Figure 5.11(a) shows the acceleration spectra for tracers. Clearly at $\omega \sim 10^{-1}\omega_\eta$, a significant amount of anisotropy is present and is due to the turbulence producing mechanisms investigated in chapter 3. However, as the dissipative range is approached the curves collapse onto a single curve which decreases as a power law $\phi_a(\omega) \propto \omega^{-3}$. Figure 5.11(a,inset) presents the same normalization as in [30] as a basis of comparison, $\phi_a(\omega)/\varepsilon$ is plotted and gives a related Kolmogorov constant at the plateau values: $B_0 = C_0/\pi$ (*cf.* annex C). The collapse of the curves was absent in that work but is present here, even in a semi-logarithmic scale.

As the inertia of the particles is increased (St = [0.7, 2.2, 7.6]) in figures 5.11(b-d) the isotropization of the small scales becomes increasingly visible. While isotropy was attained near $\omega = \omega_\eta/2$ for tracers, it occurs at much lower frequencies for the inertial particles, in some as low as $\omega = \omega_\eta/10$ which corresponds to the inertial range. Figures 5.11(b-d,inset) confirm that this isotropy is not an illusion of the log-log scaling.

The role of particle inertia is to progressively push the beginning of the isotropic range to lower and lower frequencies as observed by comparing figures 5.11(a & d). Inspection of figure 5.10(a & b) indicate that the cut off frequency of the acceleration spectra is close to $\omega_\eta/6$, a frequency roughly corresponding to the Taylor scale. Increasing these timescales may correspond to decreasing the cut-off frequency concomitantly. This behavior is apparent in figures 5.10(a & b) where the $x$ and $z$ component display a similar shift to lower frequencies. Consequently, there is an isotropization of the spectra at progressively lower frequencies as demonstrated in figure 5.11.

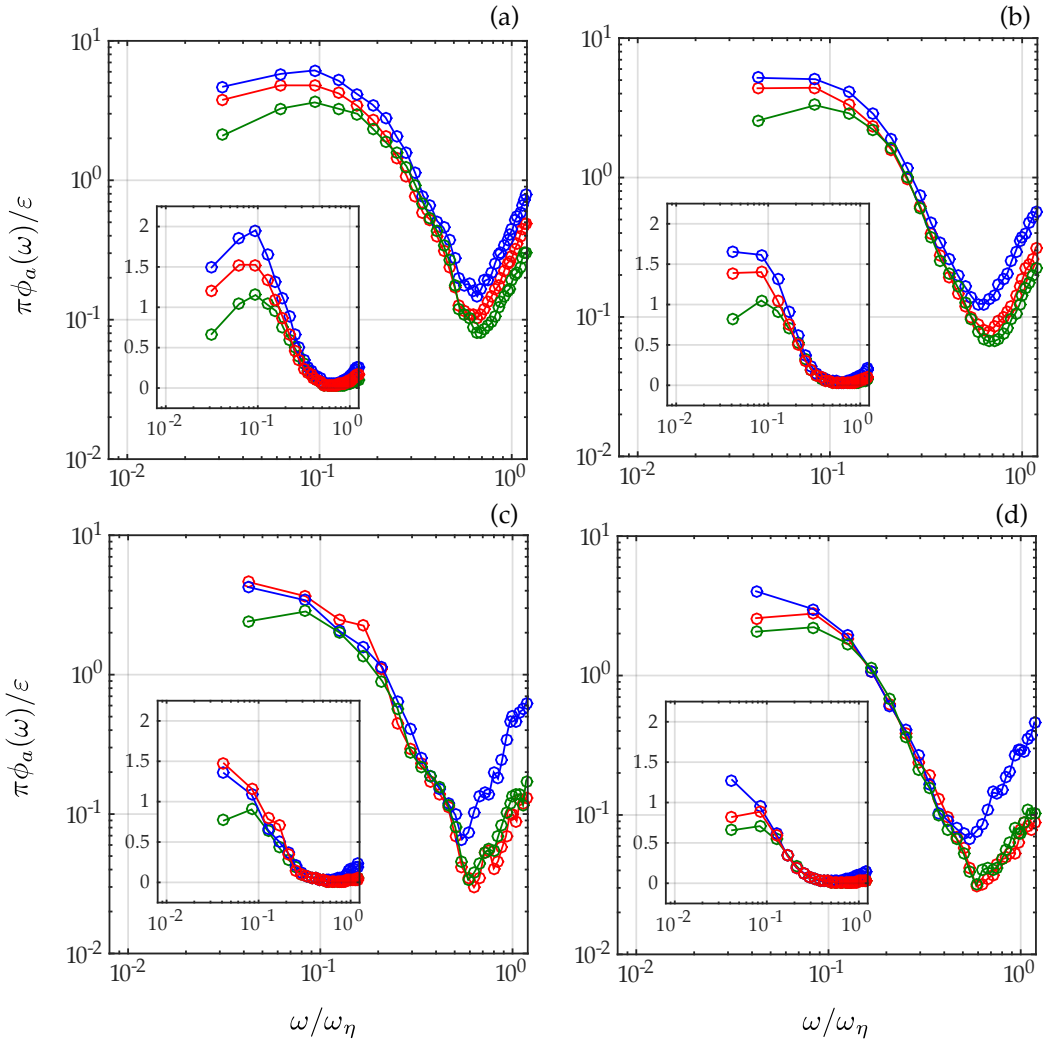


Figure 5.11: Acceleration spectra undergoing isotropization of the small scales for the four particle classes at $\mathrm{Re}_\lambda = 190$. Plateaus give the Kolmogorov constant $C_0$. (a) Tracer (b) $\mathrm{St} = 0.7$ (c)$\mathrm{St} = 2.2$ (d) $\mathrm{St} = 7.6$. (insets) Renormalization of spectra in semi-log scale for comparison with [30]. Spectra plotted: $\phi_a(\omega)/\varepsilon \simeq C_0/\pi$ at the plateau. The constant $B_0 = C_0/\pi$ is another Kolmogorov constant often cited in the literature (*cf.* annex C).

## 5.5 Conclusion

This chapter focused on the anisotropy present in acceleration statistics for tracer particles as well as inertial particles. A series of conclusions is given for each particle class.

• Fluid Tracers: Anisotropic fluctuations in the acceleration where measured and are understood qualitatively by two anisotropic contributions to the acceleration variance (eq. 5.3). First, $\langle Dv_i'^2/Dt\rangle\mathcal{S}_i$ contains the contributions of the advective and turbulent transport of velocity fluctuations. These are generally small with regards to the second, $\langle v_i'^2\rangle{\mathcal{S}_i}^2$ where strong anisotropy in the velocity components is exaggerated by differences in the strain rates ($\mathcal{S}_i$). Together these terms account 13% of the total variance and may explain why anisotropic and inhomogeneous turbulence produces stronger acceleration fluctuations than for comparable Reynolds number homogeneous isotropic turbulence [129].

Integral acceleration time scales also presented a strong anisotropy in the central region of the von Kármán flow. However, the diverging directions' correlation times were shorter than the converging direction's. This result indicates that strength of acceleration fluctuations is not sufficient to determine the correlation time as suggested by Kolmogorov phenomenology for HIT. The Taylor time scale was shown to display similar spatial evolution in anisotropy as the acceleration integral scale in the vicinity of the stagnation point. The Taylor time scale attains a level of anisotropy 20% larger than the integral acceleration statistics, in large part due to the isotropic nature of the small scales contributing to the auto-correlation function.

The notion of small scale was refined when referring to acceleration statistics. A scale-by-scale analysis of the acceleration spectra indicate that anisotropy is mostly contained in frequencies smaller than $1/\tau_\lambda$. At "small scales", frequencies larger than $1/\tau_\lambda$, the spectra become isotropic. The contributions of the "large scales" of the acceleration are thus dominant in the calculation of integral quantities such as the variance (integrating the spectrum) and the acceleration correlation time (integrating the correlation function) which are strongly anisotropic.

• Inertial Particles: Due to the incapacity of inertial particles to faithfully follow the fluid flow several surprising results were obtained. When calculating acceleration variance, a logarithmic decay was observed and is coherent with several numerical studies [61, 63, 11]. The experimental data compared with the DNS results of [11] was particularly interesting. The overall evolution is the same in both the experiments and DNS with the exception of an off-setting factor of $\beta^2$. This factor may be related to the presence of "added mass" effects in the experiments that were numerically neglected in the DNS. However, the exact origin of the logarithmic decay is unknown.

Increasing particle inertia plays an important role in the shape of the acceleration auto-correlation functions. In the expanding ($z$) direction the curves are well renormalized by the zero-crossing time, or equivalently the Kolmogorov time. However, with increasing inertia the contracting ($x$) decorrelates on time scales reaching the Lagrangian integral time ($T_L$). Restricting evaluation of the correlation curves to times of order $\mathcal{O}(\tau_\eta)$, timescales for particles with increasing inertia were shown to display the same evolution with respect to tracers as the Taylor time.

As with the tracer particles, inertial particles undergo isotropization at small

scale, however, this process occurs for progressively lower frequencies as the Stokes number increases. However, the Taylor scale was shown to have a weak, monotonically increasing, dependency on the Stokes number and may account for the transition to isotropy for progressively lower frequency. This is a proposition, the exact mechanism for the transition is unknown.

The anisotropy in acceleration statistics at small times and large frequencies bears an undeniable similarity with to the anisotropy in the Taylor time scale. These time scales have a non-negligible separation of scale ($\tau_\lambda \sim \tau_\eta \mathrm{Re}_\lambda{}^{1/2}$) which renders this observation all the more striking. The exact relationship between these timescales is unknown. Long time and large frequency behavior that emerges with increasing particle inertia raises some questions. Notably: *What is the role of the inhomogeneity of the underlying flow on inertial particles*? While chapter 4 concluded that the non-stationarity arising from a non-homogeneous flow was not at the heart of acceleration timescale anisotropy, it is not clear if this assertion should hold when particle inertia permits exploration of the fluid flow in ways forbidden to tracers.

# Chapter 6

# The role of collective effects on the enhancement of the settling velocity of inertial particles in turbulence

In the previous chapters, single particle statistics have been studied. The S-PTV setup (ch. 2) was particularly well adapted to a dilute particle regime but became much less robust at large particle concentrations. As a trade off, all aspects concerning the collective effects particles exert when in close proximity were all but impossible. The work presented in this chapter was carried out during an eight month collaboration at the University of Washington under the supervision of Professor Alberto Aliseda where the role of collective effects on the enhancement of the settling velocity of inertial particles in turbulence was studied. The experimental set-up was put into place by the Prof. Aliseda's PhD student Colin Bateson who has since successfully defended his thesis. My contribution to the experimental effort was to build a new data set of high-speed images and tracking water droplets in a wind tunnel over a large imaging area, nearly an integral length per side. Unexpectedly, this collaboration led to a new model predicting the settling velocity of inertial droplets as a function of their local concentration and is the main result of this section. A condensed version of this chapter is under review for publication in *Journal of Fluid Mechanics Rapids*.

---

The dynamics of inertial particles in turbulence represents a fundamental problem in multiphase flows, with both major gaps in physical understanding and multiple applications where it represents the key obstacle to improved technological and geophysical process modeling and optimization. As a relevant example, modeling processes leading to warm rain formation requires understanding and quantification of inertial droplet collisions induced by turbulence to close the size gap where diffusional growth and gravitational collision is ineffective in growing droplets, a dominant hypothesis that has seen significant research and growing evidence in its support in recent years (see [147] for a recent review). Homogeneous isotropic turbulence generated by active grids inside wind tunnels seeded with micron-sized water droplets represent a canonical flow that contains all the key physical ingredients to study the turbulence-induced collision problem [73, 148, 124]. Although the

Reynolds numbers attainable in wind-tunnel-generated turbulence ($\mathrm{Re}_\lambda \approx 300$) differs from those in cumulus clouds ($\mathrm{Re}_\lambda \approx 10,000$), and thus separation between scales can not be matched in the laboratory, similarity in small scale physics and dissipation rate inertial dynamics can be achieved [149]. Similarly, the liquid volume fraction in lab experiments is typically one to two orders of magnitude higher than in cumulus clouds, increasing the statistical convergence of the particle data necessary to study “rare" collision or close interaction events, without altering the dilute interaction between the bulk carrier and disperse phase [150].

Collisions between inertial particles are made more likely by modified particle settling in turbulent environments, a phenomenon attributed to two distinct mechanisms: preferential sweeping and loitering. Finite inertia, measured by the particle response time to small scale turbulence time ratio (the Stokes number: $\mathrm{St} = \tau_p/\tau_\eta$), particles are susceptible to these two mechanisms. When fluid velocity fluctuations $u'$ dominate over the terminal velocity $v_t = \tau_p|g|$, *i.e.* Rouse numbers $\mathrm{R} = v_t/u'$ less than one, an “inertial bias" leads particles to preferentially sample high strain regions [151]. Only in the presence of gravity does this inertial bias lead to preferential sweeping on the downward side of eddies and enhance settling velocities [152]. When the Rouse number is larger than one, particles traverse the turbulent eddies in a random fashion, spending more time “loitering" on the upward sweeping side than on the downward side. The result is that the vertical velocity is slowed down, resulting in hindered settling. Experimental and numerical evidence exists for this so-called loitering mechanism [54, 53, 63]). Increased local concentration , abetted by any of the mechanisms described above, may lead to aerodynamic interactions which may enhance settling further [73, 153].

The aim of this paper is to quantify the role of turbulence in controlling the instantaneous, local concentration of inertial particles in the flow, and subsequently their settling velocity. Various techniques have been developed to quantify inertial particle clustering in turbulence [154, 155, 156]. Voronöi tesselations, in particular, provide insights into the concentration field at the particle scale, without spatial or temporal averaging [157, 12, 158, 159]. Dense regions, referred to as “clusters" are identified and the settling velocity of these regions measured experimentally, as a function of turbulent dissipation rate and the time scale of particles interacting with the turbulence. The settling velocity is observed to increase dramatically with cluster size. Increasing cluster concentration is also associated with the settling velocity enhancement. These two signatures of collective effects on the settling velocity underlie the development of a novel model, that reinterpret the phenomenological model in [73]. This new model rigorously derive the settling velocity statistics based on volume averaging techniques [160] and the Voronoi local concentration of each particle, quantitatively describes the relationship between particle-particle interactions and the settling velocity enhancement.

## 6.1 Experimental Set-up

Inertial particles in a homogeneous and isotropic, slowly decaying, turbulence gas phase are studied experimentally by injecting a polydisperse liquid droplet population in a wind tunnel (WT) that has been characterized previously [161]. A network of 54 liquid atomizing jets are mounted on the bar intersections of a 9 x 9 grid, figure 6.1(a), and serve the dual purpose of generating an initially uniform distribution of water droplets and inducing high Reynolds number turbulence. To

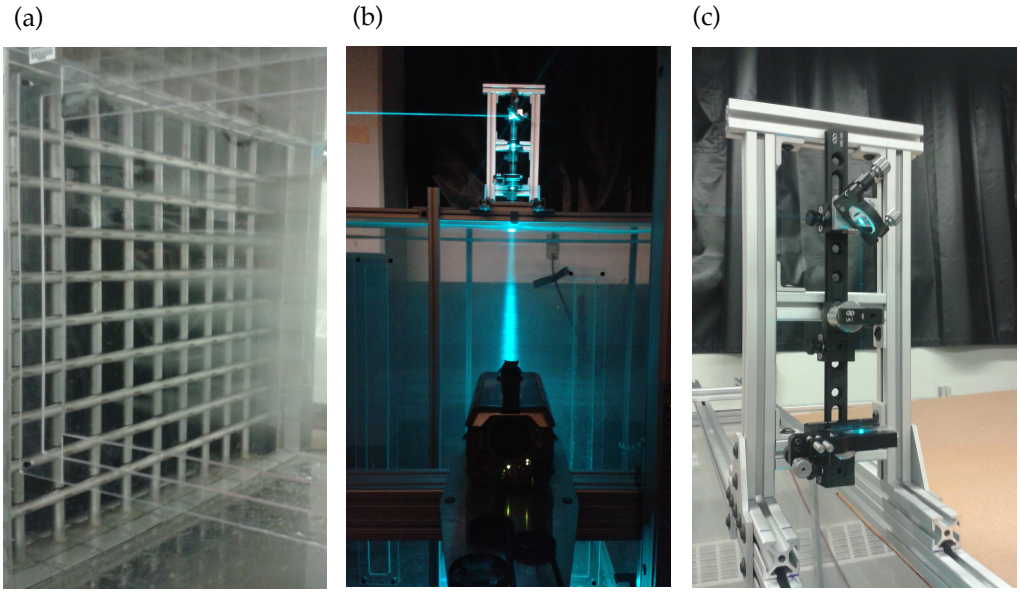


Figure 6.1: Experimental set-up. (a) Turbulence generated at grid and network of atomizing jets also serving to seed the flow with subKolmogorov particles at a volume fraction of $\phi_o = 4.5\ 10^{-5}$. (b) Typical experimental run. Images are taken at the mid-height of the WT over a region roughly $5 \times 9$ cm$^2$. (c) Optical doublet consisting of a spherical and cylindrical lens used to create a laser sheet with a thickness of 3-5$\eta$.

| $x/M$ - | $U_0$ ( m s$^{-1}$) | $u'$ ( m s$^{-1}$) | $\varepsilon$ ( m$^2$ s$^{-3}$) | $\lambda$ ( mm) | $\eta$ ( µm) | $\tau_\eta$ ( ms) | $u_\eta$ (cm s$^{-1}$ ) | Re$_\lambda$ - | St - | R - |
|---|---|---|---|---|---|---|---|---|---|---|
| 20 | 3.09 | 0.33 | 0.26 | 9.9 | 340 | 7.7 | 4.40 | 215 | 0.60 | 0.14 |
| 30 | 3.04 | 0.26 | 0.11 | 11.8 | 420 | 11.7 | 3.58 | 205 | 0.40 | 0.17 |
| 40 | 3.00 | 0.24 | 0.06 | 14.7 | 490 | 15.8 | 3.08 | 235 | 0.29 | 0.19 |

Table 6.1: Turbulence characteristics at the center of the wind tunnel where the particle trajectories are analyzed. Average carrier phase velocity and fluctuations are $U_0$ and $u'$. The dissipation rate $\varepsilon$ was obtained from the longitudinal velocity spectra. The Taylor scale is computed as $\lambda = \sqrt{15v'^2\nu/\varepsilon}$, where the gas kinematic viscosity is $\nu = 1.5\ 10^{-5}$ with $Re_\lambda = v'\lambda/\nu$, St $= \tau_p/\tau_\eta$, and R $= \tau_p g/u'$. The Kolmogorov length and time scales are $\eta = (\nu^3/\varepsilon)^{1/4}$ and $\tau_\eta = (\nu/\varepsilon)^{1/2}$.

avoid coalescence of the individual jets into a single recirculating structure, a supplementary source of momentum along the four walls of the tunnel establishes a nearly uniform velocity profile in the central region of the WT, with very thin (less than 5% of the tunnel width) boundary layers at the walls. The test section, where the inertial particle interaction with turbulence is studied, is 1 m$^2$ in cross section and 5 m in length.

Hot-wire anemometry was used to measure the carrier-flow velocity across the test section. Specifically, a region located at the mid-height, 40 cm from the wall was chosen for all inertial particle measurements, based on velocity statistics showing the

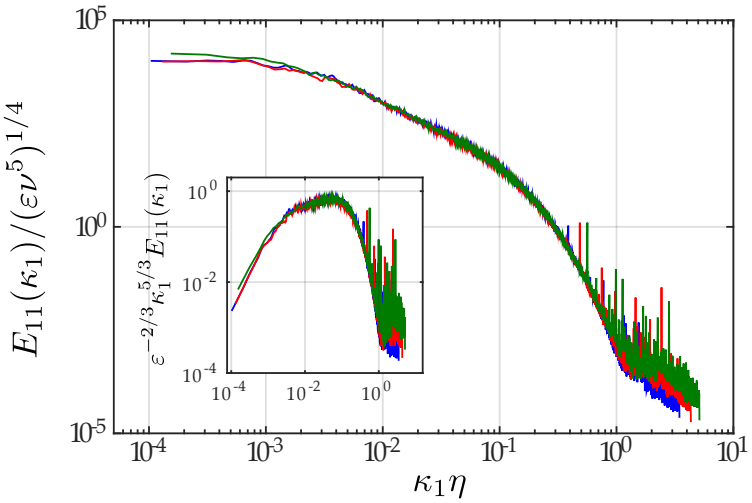


Figure 6.2: Normalized longitudinal turbulent spectra calculated at $x/M = 20$: blue, $x/M = 30$: red, $x/M = 40$: green. (Inset) Compensated spectra indicate a restricted inertial range with a $-5/3$ scaling for each location.

single-phase turbulence to be very approximately homogeneous and isotropic. The longitudinal velocity spectra (fig. 6.2) are used to calculate the turbulence parameters (table 6.1). The Taylor-scale Reynolds number $Re_\lambda = 220$ is approximately constant, in agreement with equilibrium similarity theory [108] of wind-tunnel turbulence in its initial period of decay [78] and experimental measurements in the literature [162]. Collapse of the spectra and the beginnings of a $-5/3$ power law (fig. 6.2 inset) indicate that equivalent inertial subranges exist for each down stream location.

A constant water flux of 7.5 L min$^{-1}$ is injected through the atomizing jets at a free stream velocity of $U_0 \approx 2.8$ m s$^{-1}$ resulting in a global volume fraction $\widetilde{\phi}_o = 4.5 \times 10^{-5}$ in the experiments. Phase Doppler Particle Analyzer (PDPA) data permits the calculation of the particle response time distribution (figure 6.3) and gives a typical value of $\tau_p = \frac{1}{18}\frac{\rho_p}{\rho_f}\frac{\langle d^2\rangle}{\nu} = 4.6$ ms and St=[0.60, 0.40, 0.29]. Of note is the associated particle diameter distribution (figure 6.3, inset) which when normalized by the mean diameter ($\langle d\rangle = 32$ µm) corresponds to a single parameter Gamma distribution. The particle size distributions are similar to those studied in [155] and are assumed to be stationary throughout the WT.

Flow visualization of the particle trajectories was performed via high-speed imaging, collecting the light scattered at 90$^\circ$ by the particles illuminated with a high power CW laser plane aligned with the streamwise and vertical directions (figure 6.1b). The field of view had dimensions approximately equal to the integral turbulence length scale (with a 3:2 vertical to horizontal aspect ratio) and a thickness of $\ell = 1$mm obtained by pairing a spherical and cylindrical lens (figure 6.1c), with each image containing $\mathcal{O}(1000)$ particles. In order to compute fully-converged velocity statistics, 5000 independent sequences with 10 images each, were collected and standard particle tracking velocimetry algorithms, based on [163] and upgraded in [161], were applied to compute the particles' position, velocity and acceleration.

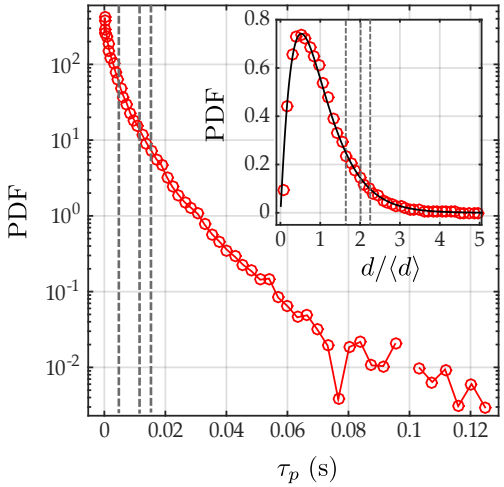


Figure 6.3: Particle response time ($\tau_p$) PDF at $x/M = 20$ is assumed to remain constant throughout the wind tunnel. Vertical dashed lines correspond to St = 1 particles at $x/M = [20, 30, 40]$ where $\tau_\eta = [7.7, 11.7, 15.8]$ ms. Inset: Particle diameter PDF at the same location. The black solid line corresponds to a Gamma distribution with a single parameter , $n = 2.1$. Vertical dashed lines correspond to the diameter of a St=1 particle.

## 6.2 Experimental Characterization of Clustering

Given a two-dimensional spatial distribution of particle locations, a network of vertices is drawn around each particle such that any point within the resulting cell is closer to the assigned particle than any other in the ensemble. The result is a Voronoï tesselation that fills the entire domain. Each particle is associated to a cell of area $\mathcal{A}_v$, and the local concentration at each particle location can be defined as $\mathcal{C} = 1/\mathcal{A}_v$. Small (large) Voronoï cells with area $\mathcal{A}_v$ that are statistically more probable than a random Poisson process (RPP) are considered to be part of clusters (voids) [157] in figure 6.4(a). Contiguous cells are assembled into clusters, as shown in figure 6.4(c).

Considering the normalized area of these cells, $\mathcal{V} = \mathcal{A}_v/\langle \mathcal{A}_v \rangle$, the standard deviation $\sigma_\mathcal{V}$ is used to define the level of clustering with respect to a 2D RPP distribution of particles where $\sigma_\mathcal{V}{}^{RPP} = 0.53$. Measurements at successive downstream locations, where the turbulence dissipation rate decays, yielded values of $\sigma_\mathcal{V} = [1.03,\ 0.96, 1.02] \pm 0.08$ showing strong clustering ($\sigma_\mathcal{V} \gg \sigma_\mathcal{V}^{RPP}$). The average concentration inside a cluster (the total number of particles divided by the total cluster area, normalized by the background concentration, $\widetilde{\mathcal{C}} = \langle \mathcal{C} \rangle / \mathcal{C}_o$) is approximately log-normally distributed with no clear dependency on the turbulent dissipation rate or residence time in the wind tunnel. The value of $\langle \log(\widetilde{\mathcal{C}}) \rangle$ takes approximately the same value throughout the test section ($\langle \log(\widetilde{\mathcal{C}}) \rangle = [1.43,\ 1.40,\ 1.39] \pm .01$) with constant standard deviation for the three measurement stations ($\sigma_{\log \tilde{\mathcal{C}}} = [0.37,\ 0.41,\ 0.44] \pm .02$). In this regime the average cluster concentration is $4.5\,\mathcal{C}_0$ and figure 6.4(b) indicates that average concentrations in clusters may reach values as high as $\mathcal{O}(10\,\mathcal{C}_o)$. The collapse of the Voronoï area distributions (figure 6.4a) and average cluster concentrations (fig. 6.4b) for the three downstream locations indicates that the mechanism governing clustering is stationary.

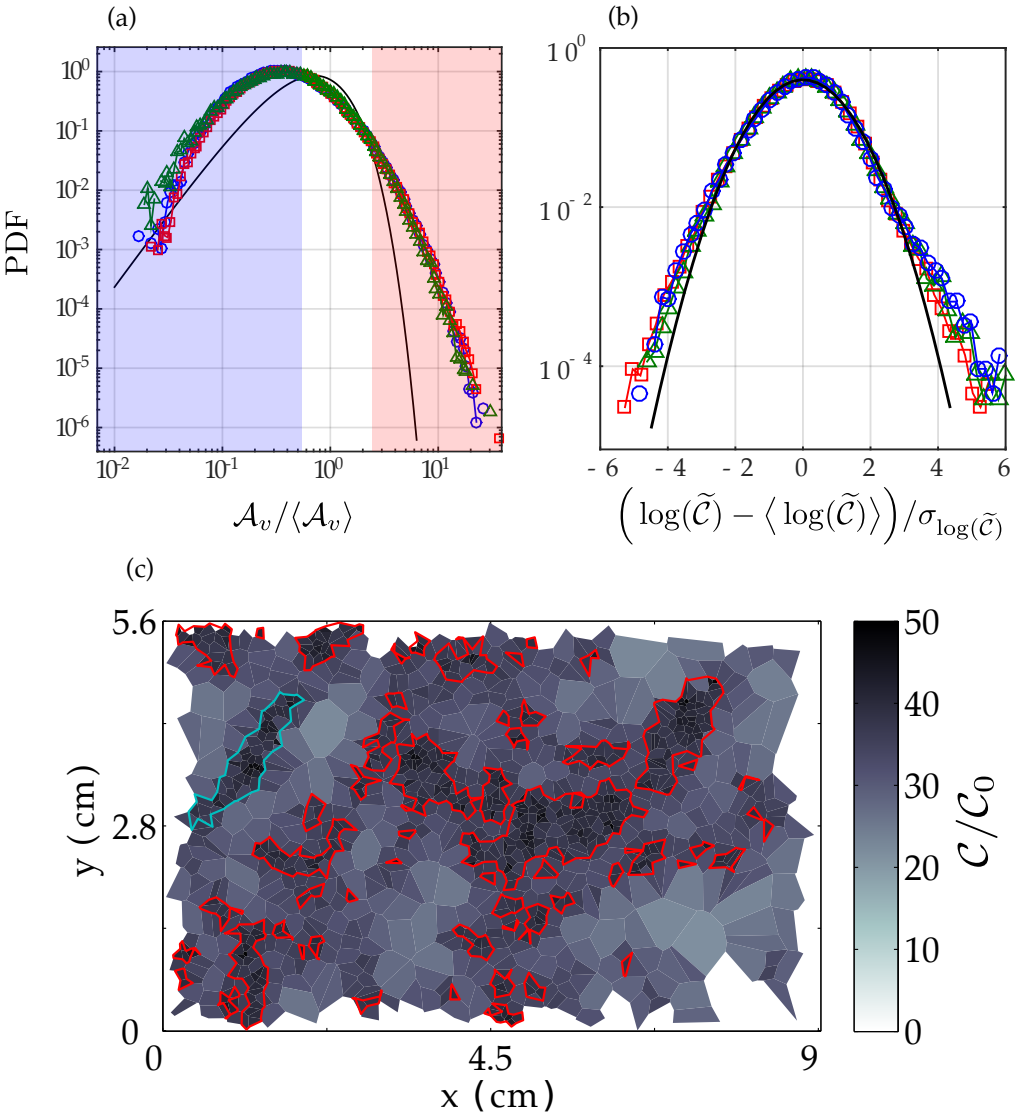


Figure 6.4: Clustering statistics. Wind tunnel locations $x/M = [20,\ 30,\ 40]$ corresponding to the dissipation rates $u' = [33,\ 26,\ 24]\,\mathrm{cm.s}^{-1}$ at $Re_\lambda \approx 220$ and $\mathrm{St} = 0.1$ given by the symbols [○,□,△]. (a) PDFs of normalized Voronoï areas. The black line is an approximation of a Random Poisson Process (RPP) [167] . Clustered (void) regions correspond to small (large) areas statistically more probable than a RPP are are shown in blue shade (red shade). (b) PDFs of normalized cluster concentrations ($\widetilde{\mathcal{C}} = \langle\mathcal{C}\rangle/\mathcal{C}_o$) plotted as with zero mean and unit variance signal are compared to a Gaussian distribution (black solid line). (c) Typical image where a Voronöi area $\mathcal{A}_v$ is assigned to each particle. Concentration is given by $\mathcal{C} = 1/\mathcal{A}_v$, normalized by the background concentration $\mathcal{C}_0 = \langle\mathcal{N}\rangle/A_{img}$, where $\langle\mathcal{N}\rangle$ is the average number of particles per image and $A_{img}$ is the image area. Dark colors are dense regions. Contiguous $\mathcal{A}_v$ identify clusters (red and cyan outlines). The cyan cluster is interpreted to be the accumulation of particles on the outer edge of a vortex stretched by alignment of the fluid volume with the settling droplets.

The near log-normality of average cluster concentrations is a new result concerning the structure of inertial particle aggregative behavior in turbulence. Previous study has revealed the log-normality of Voronoï areas (figure 6.4a), however when considering the interiors of clusters the area distributions becomes gaussian, centered on the mean concentration. Interestingly, these mean values ($\widetilde{\mathcal{C}} = \langle \mathcal{C} \rangle / \mathcal{C}_o$) decrease monotonically with particle loading [157]. Additionally, applying the Voronoï analysis to the center of mass of clusters (such as the red outlines in figure 6.4 c) permits the construction of larger "superclusters" which are themselves governed by a log-normal area distribution [164]. It is of note that the coarsened field of superclusters fluctuates less (the standard deviation of the Voronoï areas is closer to that of a RPP) than the constitutive particle field of Voronoï areas. The recurrence of log-normal statistics in various characterizations of clustering may suggest a multiplicative process involved in the construction of intertial particle clusters. Indeed models accounting for such processes have been successful in describing scalar mixing in porous media ([165]) and turbulence ([166]).

## 6.3 Enhanced Settling

The settling velocity measured for each particle is conditioned on the local concentration, $\mathcal{C} = 1/\mathcal{A}_v$ with respect to the background concentration $\mathcal{C}_o$ in figure 6.5(a). The reference concentration is experimentally accessible ($\mathcal{C}_o = 2 \times 10^5\,\mathrm{m}^{-2}$) and is useful when estimating the associated volume fraction $\phi_o = \mathcal{C}_o \pi \langle d^3 \rangle / (6\ell) \sim 1.0 \times 10^{-5}$ where $\ell = 1\mathrm{mm}$ is the laser sheet thickness. This value is reasonably close to the nominal volume fraction $\widetilde{\phi}_o = 4.5 \times 10^{-5}$ considering that some particles are too small to be properly visualized.

Enhanced settling is generally attributed to events where particle velocity exceeds the Stokes velocity $v_t$. Considering the settling velocity averaged over all particles $\langle v \rangle$, one may estimate the enhancement $(\langle v \rangle - v_t)/v_t = [1.4,\ 1.2,\ 0.9]$ for increasing down stream locations. These values are large when compared to those found in the literature (see [168] for a summary) and may be understood in terms of a non-zero background velocity found at the measurement location. Figure 6.5(a) depicts the settling velocity of particles conditioned on their local relative concentration. At the lowest concentrations an offset velocity ($w_v$, *cf.* table 6.2) occurs and likely results from large-scale advective motions due to confinement discussed in §6.5. In the reference frame of these advective motions more reasonable values are obtained: $(\langle v \rangle - w_v)/v_t = 0.70 \pm 0.01$ which indicates that settling velocity enhancement occurs at low concentration.

Settling velocities at low ($w_v$) to mid level ($\langle v \rangle$) concentration levels display a dependency on turbulence quantities. However due to the constant Reynolds number of these experiments no difference can be made between $u'$ and $u_\eta$ as both are related by the Reynolds number ($u' \sim u_\eta \mathrm{Re}_\lambda^{1/2}$). In the particular case of decaying turbulence with constant $\mathrm{Re}_\lambda$, the dissipation rate and velocity fluctuations may give a near equivalent characterization of these dependencies, *i.e.* $u' \propto \varepsilon^{1/4}$ at constant $\mathrm{Re}_\lambda$.

Particles being advected by $w_v$ are in low concentration regions where *a priori* preferential sweeping does not occur and a dependence on the fluid fluctuations appears reasonable. As for regions near the reference concentration where $\langle v \rangle$ characterizes vertical velocities that are larger than $w_v$, preferential sweeping is likely to play an important role. Decay in $\langle v \rangle$ with downstream location (decreasing $u'$)

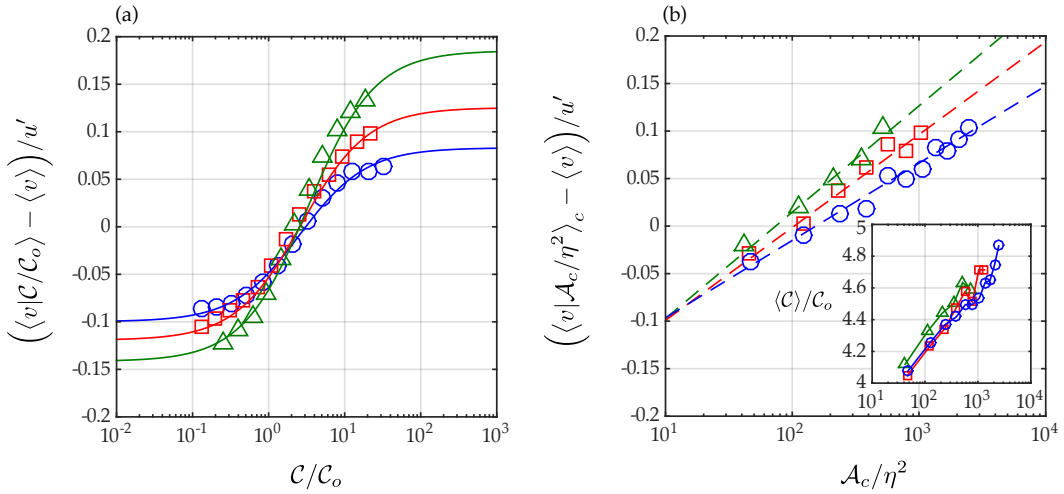


Figure 6.5: (color online) Enhanced settling statistics. Wind tunnel locations $x/M = [20,\ 30,\ 40]$ corresponding to the dissipation rates $u' = [33,\ 26,\ 24]\,\mathrm{cm.s}^{-1}$ at $Re_\lambda \approx 220$ and $\mathrm{St} = [0.60,\ 0.40,\ 0.29]$ given by the symbols [○,□,△]. (a) Settling velocity enhancement with respect to the global average settling velocity $\langle v\rangle$ conditioned on relative particle concentration and normalized by the fluid velocity fluctuations, $u'$. Solid lines correspond to fitting of equation (6.15). (b) Cluster settling velocity enhancement with respect to $\langle v\rangle$, conditioned on normalized cluster area and normalized the fluid velocity fluctuations. Dashed lines correspond to model fitting of (6.18). Inset : Normalized cluster concentration conditioned on cluster size.

reinforces this interpretation. However, the gap between settling velocities at weak ($\mathcal{O}(10^{-1}\mathcal{C}_o)$) and strong ($\mathcal{O}(10\mathcal{C}_o)$) concentrations in figure 6.5(a) increases for the furthest downstream locations (and decreasing $u'$). This implies that a mechanism for this increase lies beyond preferential sweeping. In §6.5 this enhancement as is interpreted a result the generation of increasing body forces on locally dense regions. The general term of "collective effects" will refer to enhanced settling velocities due to this mechanism. Maximum enhancement occurs for concentrations on the order of $\mathcal{O}(30\mathcal{C}_o)$ and correspond to volume fractions $\phi = 10^{-4} - 10^{-3}$, a regime in which two-way coupling may strongly effect both the fluid and particle phases. In this regime, particles are settling quickly, likely entraining others which may generate a perturbation in the local fluid pressure gradient. In §6.4 a locally modified pressure gradient provides the main coupling term between the fluid and particle phases which generates a buoyant drag responsible for the saturation in settling velocity enhancement by collective effects.

Clusters are identified by assembling all contiguous Voronoï cells with values smaller than a statistically determined value (see §6.2) as shown by the red outlines in figure 6.4(c). The average settling velocities conditioned on cluster size ($\langle v|\mathcal{A}_c/\eta^2\rangle_c$) increase logarithmically with cluster area in figure 6.5(b). Although the smallest clusters settle slower than the global settling velocity $\langle v\rangle$, clusters larger than $\mathcal{O}(100\eta^2)$ settle faster. Incidentally, this size roughly corresponds to the average cluster size though physical significance of this threshold is unknown. Indeed, for a cluster of a given size $\mathcal{A}_c/\eta^2$ the settling velocity enhancement is strongest for the furthest downstream locations. This reinforces the interpretation of collective

effects as the dominant mechanism leading to the strongest settling velocities.

From the inset in figure 6.5(b), the average concentration in clusters is 4-5 $\mathcal{C}_o$ over a wide range of sizes ($\mathcal{A}_c = 10^2 - 10^3\ \eta^2$). The average concentration depends logarithmically on cluster size. This dual dependency of the cluster settling velocity and the cluster concentration on cluster size is the key to developing the model of settling enhancement by collective effects described in the following section, shown by the fitted dashed lines in figure 6.5(b).

The results presented here are the first to establish that the average concentration and cluster area are equivalent measures of particle accumulation with larger clusters corresponding to more concentrated regions (fig. 6.5b, inset) . However, the logarithmic dependency require a large range in $\langle\mathcal{C}\rangle/\mathcal{C}_o$ and $\langle\mathcal{A}_c\rangle/\eta^2$ for accurate measurements of this phenomenon.

## 6.4 Settling Enhancement by Collective Effects Model based on Two-Fluid Averaging

Numerous theoretical formulations have sought to address sedimentation of heavy spheres in an otherwise quiescent suspension [169]. Notably, [170] proposed a scaling for particle aggregates subjected to statistical fluctuations in local density commensurate with cluster size leading to increasingly large velocity fluctuations. Similarly, [73] proposed a model in the context of a turbulent dispersion of heavy particles to estimate terminal velocity as a function of local concentration. The proposed model closely follows the volume averaging approach of [171] whereby the equations of motion are derived for a continuous particle and fluid phase which permit the calculation of a gravitationally induced flux of particles.

The averaged momentum equations for the particle, liquid, and mixture phases are constructed based on [160]:

$$\frac{\partial}{\partial t}(\rho_p\phi\mathbf{v}) + \nabla\cdot(\rho_p\phi\mathbf{v}\mathbf{v}) = \nabla\cdot\mathbf{\Pi}_p + \mathbf{f} + \phi\rho_p\mathbf{g}, \tag{6.1}$$

$$\frac{\partial}{\partial t}(\rho_f(1-\phi)\mathbf{u}) + \nabla\cdot(\rho_f(1-\phi)\mathbf{u}\mathbf{u}) = \nabla\cdot\mathbf{\Pi}_f - \mathbf{f} + (1-\phi)\rho_f\mathbf{g}, \tag{6.2}$$

$$\frac{\partial}{\partial t}(\rho\mathbf{w}) + \nabla\cdot(\rho\mathbf{w}\mathbf{w}) = \nabla\cdot\mathbf{\Pi} + \rho\,\mathbf{g}. \tag{6.3}$$

We note that $\phi$ is the local volume fraction and the momentum equation for the mixture (6.3) is simply constructed by adding the particle phase contribution (6.1) to that of the fluid phase (6.2). The barycentric velocity of the mixture phase $\mathbf{w} = (\rho_p\phi\mathbf{v}+\rho_f(1-\phi)\mathbf{u})/\rho$ is determined by the locally-averaged carrier and disperse phase velocities, $\mathbf{u}$ and $\mathbf{v}$, using a local mixture density $\rho = \phi\rho_p + (1-\phi)\rho_f$. The right-hand-side terms are the effective particle (gas and mixture) stress tensors, $\mathbf{\Pi}_p$ ($\mathbf{\Pi}_f$ and $\mathbf{\Pi} = \mathbf{\Pi}_p + \mathbf{\Pi}_f$), the fluid-particle interaction force ($\mathbf{f}$), and the specific gravity force.

The effective particle stress tensor contains hydrodynamic, inter-particle, and Brownian contributions, and all of them are considered negligible under the dilute, finite particle Stokes number assumptions here, *i.e.* $\mathbf{\Pi}_p \sim 0$. Carrier phase stress is purely hydrodynamic, with negligible deviatoric contributions [172],

$$\mathbf{\Pi}_f = -(1-\phi)p\mathbf{I}. \tag{6.4}$$

The contribution of this term is essential for the fluid-particle interaction, $\mathbf{f}$, and is partitioned, per [160]:

$$\mathbf{f} = \phi \nabla \cdot \mathbf{\Pi}_f + n\mathbf{f}_d. \tag{6.5}$$

The first term is a particle contribution to the local average pressure gradient, which provides a buoyant resistance of order $\mathcal{O}(\phi)$ by Newton's third law [160]. The second term, weighted by the local particle number density $n$, may contain drag, added-mass, and lift contributions, although most often only the drag contribution is considered [160, 172]. However, the effects of local particle accumulation on drag may be considered to be different from the contributions of overall number density ($n_o$), variations of which enhance drag on the particle phase [168]. Because the fluctuations of the Voronoï areas (and thus local concentration $\mathcal{C}$) are on the order of the reference values $\mathcal{C}_o$, the leading order contribution to the inter-phase interaction term is hypothesized to result from the reference number density weighted Stokes drag in the single particle limit:

$$n\,\mathbf{f}_d \simeq n_o\,\mathbf{f}_d = n_o\,3\pi d\mu(\mathbf{u}-\mathbf{v}) = \phi_o \frac{18\mu}{d^2}(\mathbf{u}-\mathbf{v}). \tag{6.6}$$

It is clear that (6.1) and (6.2) are not independent of (6.3), and it suffices to consider the momentum equation for the particle and mixture phase. Defining the volume-averaged mixture velocity as $\mathbf{w}_v = \phi\mathbf{v} + (1-\phi)\mathbf{u}$, the conservation equations for the mixture and particle phase respectively, are [172]:

$$\nabla \cdot \mathbf{w}_v = 0, \tag{6.7}$$

$$\frac{\partial \phi}{\partial t} + \nabla \cdot (\phi \mathbf{v}) = 0. \tag{6.8}$$

Note that the volume-averaged mixture velocity $\mathbf{w}_v$ is different from the barycentric velocity $\mathbf{w}$ of (6.3). By rewriting (6.8) one may obtain:

$$\frac{\partial \phi}{\partial t} + \mathbf{w}_v \cdot \nabla \phi = -\nabla \cdot \left[\phi(\mathbf{v} - \mathbf{w}_v)\right]. \tag{6.9}$$

The evolution of the material derivative of $\phi$ is driven by the ability of particles to *fall out* of the mixture as droplet-laden clusters when a sufficient relative velocity is generated. It is this fall-out flux, $\mathbf{j}_f = \phi(\mathbf{v} - \mathbf{w}_v)$, that represents enhanced settling by collective effects in this model.

In order to simplify (6.1) and (6.3), statistical stationarity is assumed and inertial terms are neglected. Consequently, the momentum equations for the particle phase and the mixture become:

$$0 = 18\frac{\mu}{d^2}\phi_o(\mathbf{u}-\mathbf{v}) + \phi(\rho_p - \rho)\mathbf{g}, \tag{6.10}$$

$$0 = -\nabla p - \rho \mathbf{g}. \tag{6.11}$$

Notice that the lowest order (in $\phi$) contribution from buoyancy to (6.10) is simply the hydrostatic pressure needed to support the weight of the mixture, $\phi\nabla\cdot\Pi_f \sim \phi\partial p/\partial z = \phi\rho g$. This simple mechanism provides a hydrodynamic coupling between the mixture and the particle phase by the substitution of $\mathbf{f} = \phi\rho\mathbf{g} + n_o\mathbf{f}_d$ into (6.1). Multiplying both sides of (6.10) by (1-$\phi$), the relative velocity in the Stokes drag

term can be rewritten to give an explicit expression for lowest order contribution to the fall-out flux that is purely gravitational:

$$\mathbf{j}_{fo} = \phi_o(\mathbf{v} - \mathbf{w}_v) = \phi(1-\phi)\tau\mathbf{g}, \tag{6.12}$$

which highlights the role of local volume fraction (local concentration) and the particle inertia ($\tau = (\rho_p - \rho)\frac{1}{18}\frac{d^2}{\mu}$) in the enhancement of the settling as the local concentration increases in dense regions. Like results using the suspension balance model [173, 172] the volume averaging technique employed here derives an expression for the flux characterizing particle migration.

DNS studies suggest that two-way coupling may reduce the slip velocity between particles and the carrier phase [150], indicating that the particle response time of an isolated particle may not be the appropriate time scale in very dense mixtures. Indeed, considering the left hand side of the second equality in (6.12) at order $\mathcal{O}(\phi)$ in a dense mixture (*i.e.* $\phi \to 1$ and $\rho \to \rho_p$) the particle response time $\tau \to 0$ indicating a relaxation of the fluid phase to the particle phase and not the inverse, in agreement with two way coupling simulations [168, 174]. When $\phi \ll 1$ it is illustrative to rewrite $\tau$ as:

$$\tau \approx \tau_p\Big(1 + \phi_{mo}\frac{\phi}{\phi_o}\Big)^{-1} + \mathcal{O}(\phi_m), \tag{6.13}$$

where $\phi_{mo} = \phi_o\rho_p/\rho_f$ is the reference mass loading. The $\mathcal{O}(\phi_m)$ term is in general negligible and the right hand side may be thought of as a modified particle response time. This term bears resemblance to the time scaling arising in the *short relaxation time* approximation discussed in [160] which neglects the contributions of added mass with respect to drag forces in (6.6) and is valid when $\tau \ll \tau_\eta$. Note that the Stokes time, $\tau_p$, refers to the value for an isolated particle ($\phi \ll \phi_o$), whereas in highly concentrated regions ($\phi \gg \phi_o$), the particle response time is some fraction of the Stokes time determined solely by the overall mass loading ($\phi_{mo}$).

From (6.12) the slip velocity between the particle phase and mixture is proportional to $\phi/\phi_o$ and thus a conditional average based on local relative concentration gives an equation for the particle phase:

$$\langle \mathbf{v}|\phi/\phi_o\rangle = \langle \mathbf{w}_v|\phi/\phi_o\rangle + \tau\mathbf{g}\phi/\phi_o + \mathcal{O}(\phi_m, \phi^2). \tag{6.14}$$

This model equation for the particle phase velocity is compared with the experimental data in the following section. In what follows vector notation is dropped. All velocities and fluxes are projected onto the vertical axis with which gravity is aligned, $\mathbf{g} = |g|\vec{e}_z$.

## 6.5 Discussion

In order to apply (6.14) to the experimental data it is important to be able to compare the relative volume fraction $\phi/\phi_o$ with the relative number concentration $\mathcal{C}/\mathcal{C}_o$, the former being relevant theoretically and the latter being available experimentally. The laser sheet width is $\ell \sim 2-3\eta$ and is assumed to be sufficiently thin to consider the illuminated particle aggregates to be elementary slices of a larger cluster which are characterized by linear scale of roughly $10\eta$ [175, 73]. The quantitative measure of clustering, the standard deviation of Voronoï areas $\sigma_\mathcal{V}$, is not strongly

| $x/M$ - | $u'$ cm s$^{-1}$ | $w_v$ cm s$^{-1}$ | $\widetilde{v}_{tp}$ cm s$^{-1}$ | $w^*_{vc}$ cm s$^{-1}$ | $\widetilde{v}_{tc}$ cm s$^{-1}$ | $\beta$ - | $\tau_p$ ms | $\tau$ ms | $\phi_o\rho_p/\rho_f$ - | $\alpha$ - |
|---|---|---|---|---|---|---|---|---|---|---|
| 20 | 33 | 7.7 | 6.3 | 5.1 | 1.2 | 0.3 | 2.4 | 1.6 | 0.37 | 2.5 |
| 30 | 26 | 6.9 | 6.5 | 4.7 | 1.2 | 0.3 | 2.4 | 1.6 | 0.36 | 2.5 |
| 40 | 24 | 5.6 | 8.7 | 4.0 | 1.2 | 0.3 | 2.4 | 1.6 | 0.27 | 2.5 |

Table 6.2: Fitting parameters corresponding to locally enhanced settling (6.15) and cluster settling (6.19) velocities for measurements made at $x/M = [20,\ 30,\ 40]$ at $\mathrm{Re}_\lambda \approx 220$ where the fluid velocity fluctuations are $u'$ and $\mathrm{St} = [0.60,\ 0.40,\ 0.29]$. For (6.15) the parameters include the background flow $w_v$ as seen by individual particles, particle response time $\tau_p$ (held fixed), mass fraction $\phi_{mo} = \phi_o\rho_p/\rho_f$, and the collective effects velocity $\widetilde{v}_{tp} = \tau_p g/\phi_{mo}$. For (6.19) the parameters include the background flow as seen by clusters $w^*_{vc} = w_{vc} + \alpha\tau g$ and the cluster collective effects velocity $\widetilde{v}_{tc} = \alpha\beta\tau g$. The particle number-Voronoï area correlation term $\beta$ evaluated at $\langle \mathcal{A}_c \rangle \simeq 150\eta^2$, the geometrical constant $\alpha$ setting initial velocity enhancement, and a modified particle response time $\tau$ (held constant) based on the most probable cluster's concentration are used to evaluate these parameters.

effected by changing the thickness of the visualization plane from $2\eta < \ell < 6\eta$ [176]. Additionally, Voronoï analysis on DNS data indicates quantitative similarity between 2D and 3D post-processing, suggesting that 2D slices are a legitimate approximation of the 3D clustering phenomenon [176]. With these points in mind, the relative relative number concentration per area is thought to be a good approximation of the relative volume fraction, $\phi/\phi_o \simeq (\mathcal{C}v_p/\ell)/(\mathcal{C}_o v_p/\ell) = {\mathcal{A}_v}^{-1}/\mathcal{C}_o$, where $\mathcal{A}_v^{-1}$ is the experimentally accessible number concentration taken from Voronoï areas and $v_p$ is the characteristic particle volume. Under this assumption the measures of local volume fraction or number concentration are used interchangeably.

### 6.5.1 Locally enhanced settling

In (6.14) the mixture velocity ($\langle w_v|\phi/\phi_o\rangle$) has an a priori dependence on local volume fraction, however, it is not clear how to incorporate this dependency into (6.14). As a first approximation the mixture velocity is taken to be independent of the local relative volume fraction, an admittedly simplistic hypothesis which is discussed below. The resulting model equation is:

$$\langle v|\,\phi/\phi_o\rangle = w_v + \frac{\phi}{\phi_o} v_t \Big(1 + \phi_{mo}\frac{\phi}{\phi_o}\Big)^{-1}, \tag{6.15}$$

and is fit as a function of $\phi/\phi_o$ to the data in figure 6.5(a). Three fitting parameters are present in (6.15): $w_v$, $v_t = \tau_p g$, and $\phi_{mo} = \phi_o\rho_p/\rho_f$ which are tabulated in table 6.2. The latter two parameters are measurable while the former is experimentally inaccessible. Note that $v_t$ is forced to remain constant throughout the wind-tunnel to respect the stationarity of the particle size distributions.

In the dilute limit when $\phi/\phi_o \to 0$, (6.15) simplifies to $\langle v|\phi/\phi_o\rangle \simeq w_v$ and settling is governed solely by the volume averaged mixture velocity. From (6.7), the mixture velocity is incompressible which implies that regions of strong downward volume flux must be compensated by a back-flow elsewhere. Such fluxes may be

induced by confinement effects or by entrainment due to sedimentation. In the case of confinement effects, the variation of the mixture velocity likely occurs over scales comparable to the experimental apparatus which are much larger than the observation volume suggesting that $w_v$ operates as an offset which may either enhance or hinder settling. An analogous interpretation of the background flow is given for PDPA measurements ($V_{physical}$ in chapter 6 of [53]) in a similar experiment. In that study, the offset velocity was measured to be independent of $\phi/\phi_o$, reinforcing the previous hypothesis concerning $w_v$. As a result, $w_v$ is interpreted to be the local contribution of a background flow that is applied uniformly over the observation region to enhance the particle settling velocity and is independent of local concentration. We note that average mixture velocity scales with the fluid velocity fluctuations, $w_v/u' = 0.24 \pm 0.02$ and the role of small scale turbulence (Stokes number) or gravitational effects (Rouse number) may play important roles.

In highly concentrated regions, $\phi \gg \phi_o$, (6.15) takes the asymptotic form:

$$\langle v|\phi/\phi_o\rangle = w_v + \widetilde{v}_{tp}. \tag{6.16}$$

The first term on the right hand side is the background flow described above while the second term represents the contribution of what we call the collective effects velocity $\widetilde{v}_{tp} = v_t/\phi_{mo}$ which is strictly determined by the composition of the mixture: overall mass fraction ($\phi_{mo} = \phi_o\rho_p/\rho_f$) and the Stokes velocity $v_t = \tau_p g$. Because $\tau_p$ is constant, increases in $\widetilde{v}_{tp}$ result from a decrease in the overall mass fraction. Although this tendency may seem paradoxical, it may be understood by the delay in the mechanism which decreases the effective particle response time $\tau$ with respect to its nominal value $\tau_p$ in (6.13). Initial settling velocity increases are linear in $\phi/\phi_o$ which corresponds to the Stokes drag (proportional to $\phi_o$) compensating the excess body force due to particle accumulation (proportional to $\phi$) as given by (6.10). If the reference mass loading is large then $\phi_{mo}\phi/\phi_o \sim \mathcal{O}(1)$ for smaller relative volume fractions in (6.13), precipitating a decrease in $\tau$ and ultimately smaller values of $\widetilde{v}_{tp}$. This is a manifestation of the modified pressure gradient contributing to a buoyant drag on settling particles in dense regions.

Subtracting $\langle w_v\rangle$ from (6.15) and normalizing by $\widetilde{v}_{tp}$ gives the solid black curve in figure 6.6(a), applying the same procedure to the data indicates that the model equation describes the data well. Figure 6.6(a) depicts the normalized enhanced settling velocity at the particle level due to collective effects. The value $\phi_{mo}$ used as a fitting parameter (*cf.* table 6.2) is at the lower bound of the fit's 99% confidence interval which corresponds to a volume fraction roughly 7-9 times the reference value, $\widetilde{\phi}_o = 4.5 \times 10^{-5}$. This fit parameter is considered a reasonable approximation of the reference value considering that the densest regions correspond to local volume fractions on the order of $30\,\widetilde{\phi}_o$. Interestingly, the monotonically decreasing values of $\phi_o$ resulting from the fit roughly correspond with the difference in the number of particles (nearly 30%) counted between $x/M = 20$ and 40. A decrease in the overall volume fraction with downstream location is inferred and is coherent with the increasing gap between low high density settling velocities due to late onset saturation in $\tau$ as described above. We believe this to be evidence of the dominant role of collective effects in enhancing settling velocities with respect to mechanisms such as preferential sweeping which would predict this gap to decrease rather than increase with decreasing $\varepsilon$ (increasing downstream location).

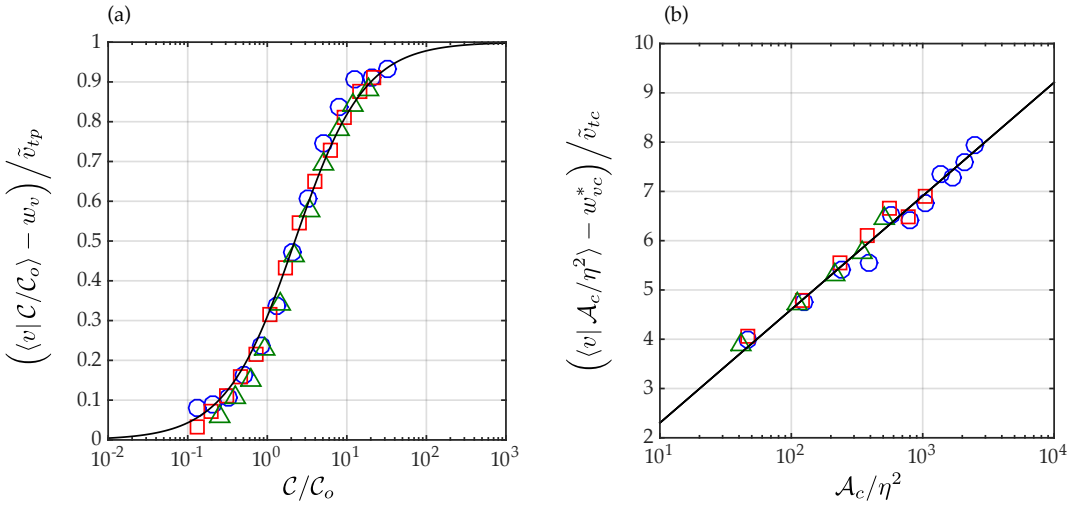


Figure 6.6: (color online) Normalized settling velocity enhancement due to collective effects. Parameters are as given in figure 6.5. (a) Local settling enhancement with respect to the volume average mixture velocity $w_v$ and the collective effects velocity $\widetilde{v}_{tp} = \tau_p g/\phi_{mo}$. The solid black line is a fit of (6.15) (b) Cluster settling enhancement with respect to the modified volume averaged mixture velocity $w^*_{vc} = w_{vc} + \alpha V_t$ and cluster collective effects velocity $\widetilde{v}_{tc} = \alpha\beta V_t$ (see §6.5.2). The solid line corresponds to a fit of (6.19).

### 6.5.2 Enhanced settling in clusters

Clusters are identified as described in §6.2 and in general correspond to structures with average concentrations higher than, but on the order of $\mathcal{C}_o$: $\langle\mathcal{C}\rangle/\mathcal{C}_o \gtrsim 1$. The average concentration in a cluster of area $\mathcal{A}_c$ containing $\mathcal{N}$ particles can be expressed by:

$$\langle\mathcal{C}(\mathcal{A}_c)\rangle \simeq \mathcal{C}_o + \frac{\langle\mathcal{N}\rangle}{\mathcal{A}_c}\Big(1 - \frac{\langle\mathcal{N}'\,\mathcal{A}'_v\rangle}{\langle\mathcal{N}\rangle\langle\mathcal{A}_v\rangle}\Big), \tag{6.17}$$

where the subscript $c$ ($v$) refers to clusters (Voronoï areas). A Reynolds decomposition has been applied to $\mathcal{C}(\mathcal{A}_c) = \mathcal{N}/\sum_1^N \mathcal{A}_v$ and $\mathcal{A}_c \approx \sum_1^N \langle\mathcal{A}_v\rangle$. The term in parenthesis $\beta(\mathcal{A}_c) = (1 - \frac{\langle\mathcal{N}'\,\mathcal{A}'_v\rangle}{\langle\mathcal{N}\rangle\langle\mathcal{A}_v\rangle})$ is evaluated experimentally (not shown) and is an increasing function of cluster size . Its correlation term is near unity for the smallest clusters and saturates to a positive, non-zero value for the largest. Large correlations are indicative of growing inter-particle distances within clusters (measured by positive $\mathcal{A}'_v$), and therefore the growth of the cluster, corresponding to a rapid accumulation of particles (measured by positive $\mathcal{N}'$). Indeed, in figure 6.5(b,inset) cluster growth occurs in such a way as to increase particle concentration with respect to the background value.

It can be seen in the inset of figure 6.5(b) that the average concentration in clusters $\langle\mathcal{C}\rangle/\mathcal{C}_o$ depends logarithmically on the normalized cluster area $\mathcal{A}_c/\eta^2$. Based on this experimental observation, the second term on the right hand side of (6.17) can be written as $\beta\log(\mathcal{A}_c/\eta^2)$ where $\beta$ is evaluated for the average cluster size, $\langle\mathcal{A}_c\rangle \simeq 150\eta^2$, for each down-stream location. When taking $\langle\mathcal{C}\rangle/\mathcal{C}_o$ from (6.17) and substituting it into (6.14) one obtains:

$$\langle v|\mathcal{A}/\eta^2\rangle_c = w_{vc} + \alpha V_t(1 + \beta\log(\mathcal{A}_c/\eta^2)), \tag{6.18}$$

where the subscript $\langle\cdot\rangle_c$ indicates that the average pertains to clusters and $V_t = \tau g$ is the incipient cluster settling velocity with $\tau$, the effective particle response time in (6.13). The geometrical constant, $\alpha$, which is of the order $\mathcal{O}(1)$ and sets the initial increase of $\langle v|\mathcal{A}_c/\eta^2\rangle_c$ is estimated by extrapolating the data in figure 6.5(b,inset) to $\mathcal{A}_c/\eta^2 \sim 1$. The interpretation of $w_{vc}$ is similar to that of $w_c$, it is the contribution of a background flow to the settling velocity of clusters. For simplicity we consider as single offsetting velocity $w^*_{vc} = w_{vc} + \alpha V_t$. Thus, (6.18) presents two fitting parameters, $w^*_{vc}$ and a velocity we refer to as the cluster collective effects velocity $\widetilde{v}_{tc} = \alpha\beta V_t$ which gives the following simplified fit equation:

$$\langle v|\mathcal{A}/\eta^2\rangle_c = w^*_{vc} + \widetilde{v}_{tc}\log(\mathcal{A}_c/\eta^2), \tag{6.19}$$

In the limit where $\mathcal{A}_c \sim \eta^2$ particles are distributed such that the local concentration is approximately $\mathcal{C}_o$. Collective effects do not play a role and particles are swept downward by a background flow in much the same manner as discussed in the individual particle case. Indeed the background flow velocity $w^*_{vc}$ measured in the clustering case is close to that for the individual particle case $w_v$ and have a similar dependence on the fluid velocity fluctuations: $w^*_{vc} = 0.17u'$ (as compared with $w_c = 0.24u'$). We note that $w_v$ was measured based on the limit $\mathcal{C} \ll \mathcal{C}_o$ while $w^*_{vc}$ is measured where $\mathcal{C} \sim \mathcal{C}_o$. It is not obvious if the difference between $w_v$ and $w^*_{vc}$ is significant, though it is smaller than the terminal velocity magnitude $\tau_p g$. From discussion in §6.5.1, the background flow is thought to apply equally to dense and sparsely populated zones which indicates that $w^*_{vc}$ and $w_v$ may be substantially the same.

In the limit $\mathcal{A}_c \gg \eta^2$ collective effects generate increased settling velocities for larger and larger clusters. Figure 6.6(b) plots a the enhancement due to collective effects as a function of cluster size. Thus, the rate at which collective effects generate increased settling velocities is set by the cluster collective effects velocity $\widetilde{v}_{tc} = \alpha\beta V_t$ which is in turn governed by the particle number-Voronoï area correlation $\beta$ for a given distribution of particle sizes (holding $\tau$ fixed). This term reflects the capacity of a growing cluster to incorporate new particles. When calculated experimentally, $\beta$ was not seen to evolve with down-stream location, and consequently was insensitive to the varying Stokes number at each location. It is possible that the Reynolds number is an important parameter in determining $\beta$ though investigation of this dependency is not accessible in the current experimental configuration.

The logarithmic increase in cluster settling velocity is unlikely to continue indefinitely. Within the context of the model, a similar saturation in settling velocity as was seen in figure 6.5(a) may occur in the clusters due to decreases in $\tau$ which in (6.13) occur when $\phi_{mo}\phi/\phi_o \gg 1$. When clusters have grown large enough to double their average concentration from $\langle\mathcal{C}\rangle = 5\,\mathcal{C}_o$ to $10\,\mathcal{C}_o$ the effective particle response time will have fallen to 20% of its original value. Assuming that the logarithmic growth of cluster concentration with size continues, clusters will only reach these concentrations when they have grown to the size of the experimental device which is clearly unrealistic. It may be that divergence from a logarithmic growth in average cluster concentration occurs when a limiting size is reached. Future work will need to investigate the role of a saturation mechanism for cluster settling.

## 6.6 Conclusion

A polydisperse distribution of inertial particles in a turbulent wind tunnel with decaying turbulence (dissipation rate decreasing slowly with distance downstream) at constant Reynolds has been studied. Experimental measurements of particle size, concentration and vertical velocity have been collected to investigate inertial particle settling and clustering. Voronoï area analysis provides evidence of local accumulation of particles showing that their average concentrations are approximately log-normally distributed with fluctuations reaching an order of magnitude increase with respect to the background volume fraction.

Settling of particles influenced by turbulence can be split for study in three regimes conditioned on the local volume fraction. First, for the smallest local volume fractions ($\phi \leq 10^{-6}$), particles are isolated and responsive to a general background flow which is likely the result of confinement effects. Second, at intermediate concentrations near the reference value $\mathcal{C}_o$, particles display settling velocity enhancement coherent with the preferential sweeping mechanism. As particles begin to cluster, a third regime is attained where rapid settling velocity increases saturate when the local volume fraction nears $\phi = 10^{-3}$. This is a novel observation from experimental evidence, and presents a limit to the settling velocity enhancement at approximately 60-100% of the initial value. The gap between settling velocities in low density regions and high density regions increases with decreasing turbulent kinetic energy dissipation rates. Were these increases due to a mechanism such as preferential sweeping, one would expect a concomitant decrease in enhancement with decaying turbulence dissipation rates. The opposite is observed both at the particle and cluster level which represents our strongest evidence for the role of collective effects - the generation of excess body forces on locally dense regions - on the enhancement of settling velocities.

A new model is derived from first principles to capture the interaction of turbulence with inertial particle settling. The salient features of the model include terms describing isolated particle settling, coupling between the carrier and the particle phase to account for collective effects, and a mechanism to account for saturation. The contribution determining isolated particle settling is a general background flow which is sensitive to the experimental or numerical conditions employed. The particle phase is coupled to the carrier phase by the pressure gradient (hydrostatic to first approximation). Local accumulation such that $\phi > \phi_o$ leads to enhanced settling. Saturation is accounted for by the introduction of a effective particle response time ($\tau$) which is parameterized solely by mass loading $\phi_{mo}$. It may be seen that $\tau \ll \tau_p$ when $\phi \gg \phi_o$, indicating that the carrier phase relaxes to the particle phase, further highlighting the coupling between the particle and carrier phases via the pressure gradient. This term, along with the cluster size-concentration correlation $\beta$ serves to determine the settling enhancement dependency due to clustering. Extension of this model in the cluster regime is needed to account for eventual settling velocity saturation for large, integral scale sized, clusters

This study has significant implications for the mechanisms governing the coalescence of inertial particles or droplets due to turbulence-induced collisions. Clusters act as a large collector particle (for which the collision efficiency is nearly 1 [177]), trapping smaller particles due to their larger settling velocity. Trapped particles then find themselves in environments where the volume fraction is up to 10 times that of the surrounding fluid, leading to increased collisions [154]. This process

may decrease the time for cloud particles to close the size gap and attain runaway growth and the millimetric size of raindrops observed in warm rain events [178, 177].

# Chapter 7

# Conclusion

A Lagrangian study of the dynamics of particles in turbulence was carried out in order to determine the role of an inhomogeneous and anisotropic flow as well as collective effects. Due to technical limitations the experiments were carried out in two devices: a counter-rotating von Kármán flow at the École Normale Supérieure de Lyon and a Wind Tunnel in the Mechanical Engineering Department at the University of Washington.

The von Kármán experiment was performed with an innovative Shadow Particle Tracking Velocimetry (S-PTV) setup permitting the tracking of $\mathcal{O}(100\mu\text{m})$ particles in a large region of the flow with two high speed cameras. To overcome the noise inherent in experimental Lagrangian data, an unbiased method of calculating one and two-time statistics was developed.

The Lagrangian data was then conditioned onto an Eulerian grid where mean and fluctuating components of the velocity and acceleration were obtained. This conditioning permitted the full characterization of the two bistable states of the flow. The spatial resolution of the Eulerian grid was sufficient to calculate the turbulent kinetic energy budget which exposed the role of the mean strain in establishing a strongly anisotropic velocity field in the central region of the von Kármán flow. This is one of the principle results in this dissertation.

The turbulent kinetic energy budget was found to play a fundamental role in the velocity dynamics of particles travelling through the central region of the flow. In particular, the presence of a flux of turbulent energy was sufficient to quantify the degree to which the inhomogeneity of the flow prolonged the ballistic regime of particle dispersion about a fixed point in space. The inhomogeneity of the flow had minimal impact on acceleration statistics due to their rapid decorrelation with respect to the scales governing the turbulent flux.

The Taylor time scale was found to describe the anisotropy found in the velocity and acceleration correlation functions. While predicting anisotropy in the long time behavior in the velocity statistics was not possible, the Taylor scale was found to be relevant to short time statistics and in particular mirror the spatial evolution of anisotropy in the acceleration correlation function.

Adding inertia to the particle dynamics exacerbated the anisotropy in the acceleration statistics. This could only be accounted for in part by the Taylor scale because long time correlations occur as a result of a complex exploration of the inhomogeneous flow. Acceleration spectra revealed that the anisotropy resides in the inertial range frequencies while dissipative regions are isotropic. Increasing particle inertia broadens the range of isotropic frequencies. The tendency of small scales to

isotropy is an important result of this study.

To study the role of collective effects, 2d image sequences were taken in a turbulent Wind Tunnel seeded with micrometer sized water droplets. The Voronoï analysis was used to detect regions with locally intense concentrations of particles. Settling velocities were conditioned based on local concentration and were found to increase by 60-100% for the densest regions with respect to an isolated particle. A model derived from first principles faithfully reproduced this effect and notably reinforced the image of local aggregates of particles settling collectively as "pseudo-particles". This is another principle result of this dissertation.

**Perspectives for future work**

Several subjects remain to be investigated:

• In section 3.5.3 speculation was made as to the degree of anisotropy in the pseudo-dissipation tensor. Our measurements are only capable of giving $\langle v' \cdot a' \rangle \simeq -\varepsilon$ but nothing can be said component wise because $\langle v_i' a_i' \rangle$ contains contributions from the pressure-rate of strain term. In the data acquisition process S-PTV films of thin rods were taken but have not yet been analyzed. Rods are known to align with the intermediate eigen-vectors of the strain rate tensor [179] and may provide some insight into the anisotropy in the pseudo-dissipation.

• The initial goal of the present study was to understand the role of the mean-flow on particle dynamics with an eye on Taylor's results which give predictions for short and long term dispersion [79]. The role of the meanfield on small time dispersion up to times of $\mathcal{O}(\tau_\lambda)$ has been accounted for. However, the long-time dynamics, both of tracers and inertial particles is as of now poorly understood. This will be a subject of future work.

• The model derived for describing the enhanced settling of particles in strongly concentrated regions only describes a steady state solution for a particle at a given concentration. As a consequence it gives no information of the transient process of cluster formation which may prove useful in understanding the mechanisms leading to rain droplet formation. Care must be taken when assessing a non-Galilean reference frame in the volume averaging formalism but this is probably not insurmountable. In addition, these type of models are often used for linear stability analysis [160], this might offer a path to determining a typical time scale of cluster formation.

# Appendix A

# Collaboration 1

N.G Huisman, T. Barois, M. Bourgoin, A. Chouippe, T. Doychev, P. Huck, C.E. Morales, M. Uhlmann and R. Volk. Columnar structure formation of a dilute suspension of settling spherical particles in quiescent fluid Phys. Rev. Fluids, **1**, 074204, (2016).

# Columnar structure formation of a dilute suspension of settling spherical particles in a quiescent fluid

Sander G. Huisman,[1] Thomas Barois,[1] Mickaël Bourgoin,[1] Agathe Chouippe,[2] Todor Doychev,[2] Peter Huck,[1] Carla E. Bello Morales,[1,3] Markus Uhlmann,[2] and Romain Volk[1]

[1]*Université Lyon, Ens de Lyon, Université Claude Bernard, CNRS, Laboratoire de Physique, F-69342 Lyon, France*

[2]*Institute for Hydromechanics, Karlsruhe Institute of Technology, 76131 Karlsruhe, Germany*

[3]*CICATA-Qro, Instituto Politécnico Nacional, 76090 Querétaro, Mexico*

(Received 22 June 2016; published 11 November 2016)

The settling of heavy spherical particles in a column of quiescent fluid is investigated. The performed experiments cover a range of Galileo numbers ($110 \leqslant \mathrm{Ga} \leqslant 310$) for a fixed density ratio of $\Gamma = \rho_p/\rho_f = 2.5$. In this regime the particles are known to show a variety of motions [Jenny, Dušek, and Bouchet, Instabilities and transition of a sphere falling or ascending freely in a Newtonian fluid, J. Fluid Mech. **508**, 201 (2004)]. It is known that the wake undergoes several transitions for increasing Ga resulting in particle motions that are successively vertical, oblique, oblique oscillating, and finally chaotic. Not only does this change the trajectory of single, isolated, settling particles, but it also changes the dynamics of a swarm of particles as collective effects become important even for dilute suspensions with volume fraction up to $\Phi_V = O(10^{-3})$, which are investigated in this work. Multicamera recordings of settling particles are recorded and tracked over time in three dimensions. A variety of analyses are performed and show a strong clustering behavior. The distribution of the cell areas of the Voronoï tessellation in the horizontal plane is compared to that of a random distribution of particles and shows clear clustering. Moreover, a negative correlation was found between the Voronoï area and the particle velocity; clustered particles fall faster. In addition, the angle between adjacent particles and the vertical is calculated and compared to a homogeneous distribution of particles, clear evidence of vertical alignment of particles is found. The experimental findings are compared to simulations.

DOI: 10.1103/PhysRevFluids.1.074204

## I. INTRODUCTION

The settling of a sphere in a quiescent viscous fluid is a long-standing problem, already explored by Newton [1] in the 17th century. The problem is simple only in appearance. The usual picture of a straight settling trajectory with a constant terminal velocity resulting from the balance between buoyancy and viscous drag is an important but only marginal situation in a much richer landscape of possible settling regimes.

A sufficiently small or slowly settling sphere (i.e., in a low Reynolds number approximation, so that the flow around the particle can be approximated as a Stokes flow) with diameter $d$ and density ratio $\Gamma = \rho_p/\rho_f$ (where $\rho_p$ is the particle density and $\rho_f$ the density of the fluid) surrounded by a fluid with viscosity $\nu$ will indeed settle along a straight vertical path, reaching a steady terminal vertical velocity $V$, where the linear viscous drag (due to the Stokes flow around the particle) $F_D = \frac{1}{8} C_D(\mathrm{Re}_p)\rho_f \pi d^2 v_s^2$ [with $\mathrm{Re}_p = dV/\nu$ the particulate Reynolds number and $C_D(\mathrm{Re}_p)$ the drag coefficient, which is simply $24/\mathrm{Re}_p$ for a sphere in the limit $\mathrm{Re}_p \ll 1$] is balanced by the buoyancy force, so that $V = (\Gamma - 1)gd^2/(18\nu)$. Several successive scenarios arise as the size or density of the particle increases and the particulate Reynolds number increases.

### A. Finite size effects

At finite particulate Reynolds number, the flow around a sphere departs from a simple Stokes flow and eventually develops wake instabilities. Such instabilities have been extensively studied

 

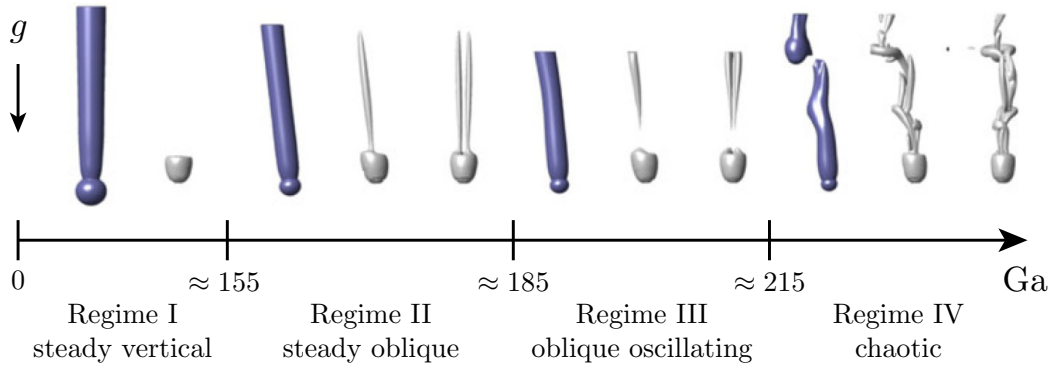


FIG. 1. Four regimes of single particle settling in ambient fluid as a function of Ga for $\Gamma = 1.5$. The snapshots are for (from left to right) Ga = 144, 178, 190, and 250. The visualizations are taken from Ref. [9] and show (in purple) the isocontour for which the velocity is $1.2V_g$ and show (in gray) from multiple angles the isocontour of a $\lambda_2$ criterion.

(numerically and experimentally) in the past 15 years for the case of fixed spheres in a flow [2–5]. The global picture is now clear, with several successive instabilities taking place as $\mathrm{Re}_p$ increases: from a steady axisymmetric wake at low $\mathrm{Re}_p$ to, first, a wake with steady planar double-threaded vortices (above $\mathrm{Re}_p \simeq 210$), then an unsteady time-periodic vortex shedding wake (above $\mathrm{Re}_p \simeq 275$), and finally a transition towards a fully three dimensional chaotic wake (above $\mathrm{Re}_p \simeq 360$). These successive modifications of the wake have two main implications. First, the value of the drag coefficient $C_D$ departs from the simple $24/\mathrm{Re}_p$ law as $\mathrm{Re}_p$ increases, reaching eventually a full nonlinear drag regime (with an almost constant value of $C_D$ at very high values of $\mathrm{Re}_p$ when the wake becomes fully turbulent).

Second, in the case of a free-falling sphere (with additional degrees of freedom compared to the case of a fixed sphere) these wake instabilities induce particle path instabilities, marking a departure from a simple vertical trajectory. The settling regime of a free-falling sphere is controlled by two dimensionless parameters: the density ratio $\Gamma = \rho_p/\rho_f$ and the Galileo number $\mathrm{Ga} = V_g d/\nu$, which can be thought of as a Reynolds number based on the gravitational velocity $V_g = [(\Gamma - 1)gd]^{1/2}$. A sphere settling in finite Ga regimes (hence beyond the Stokes approximation) is referred to as a "finite size sphere" (by definition the settling problem concerns the case $\Gamma > 1$). The settling Reynolds number $\mathrm{Re}_p = Vd/\nu$ is then an output parameter of the problem. The path instabilities at finite values of Ga are now well characterized and have been deeply investigated numerically [6] and experimentally [7,8] in the past decade for single finite size free-falling spheres; cf. the visualizations in Fig. 1 (see also the review by Ern *et al.* [10]).

### B. Collective effects

The case of many particles settling simultaneously raises further complexity, as long-range multiparticle hydrodynamic interactions emerge. In the limit of point particles (or equivalently in the limit $\mathrm{Ga} \ll 1$), the collective settling of such an ensemble of spheres and the underlying hydrodynamic interactions can be efficiently studied using Stokesian dynamics methods [11,12]. This approach yields a satisfactory quantitative comparison with experiments [13], although several questions remain, in particular, regarding the induced fluctuations and the correlation lengths of particles and flow motion. Much less is known, however, for the case of a settling ensemble of finite size particles. Systematic experimental studies remain scarce. Parthasarathy and Faeth [14] and Mizukami *et al.* [15] performed a series of experiments in dilute conditions (volume fraction of particles $\Phi_v < 1 \times 10^{-4}$) in a range of Ga from 40 to 340. Their experiments focused on measuring the fluctuations of the flow induced by the interacting wakes of the particles and showed that in dilute regimes a linear superposition of wakes gives a good approximation. It is only recently that accurate numerical simulations of a large number of fully resolved finite size particles settling collectively

and fully coupled with the fluid have become possible [16,17], mainly thanks to immersed boundary methods combined with direct numerical simulations of the Navier-Stokes equation. These methods permit a description of the coupling between the particle and the surrounding flow at the interface level. Uhlmann and Doychev [9,18] reported recently using this method that, depending on the value of Ga, particles may tend (or not) to align in columnar clusters along their wakes, resulting in an enhancement of their settling velocity (the average settling velocity was found up to 12% faster than for individual particles). Such a clustering and settling enhancement was observed for Ga = 178 (hence in a regime of steady oblique motion for individual settling particles; see Fig. 1), but was not observed for Ga = 121 (when individual particles settle along a steady vertical path). This study shows that the interplay of individual wake instabilities and collective interactions is crucial to understand the settling of an ensemble of finite size spheres, even in relatively dilute conditions (in their study $\Phi_v = 5 \times 10^{-3}$). However, the computational cost of these simulations does not yet allow a systematic exploration of the parameter space (density ratio, Galileo number, and volume fraction). At the moment these studies [9,18] only comprise three parameter points at a single value of the density ratio and for two different solid volume fractions and Galileo numbers. We propose here to explore the collective settling of finite size spheres experimentally, with the goal to broaden the range of parameters, in particular regarding the role of the Galileo number around the first wake instabilities. In the present article we therefore address the experimental counterpart of the aforementioned simulations, by exploring the settling behavior of a swarm of dense finite size particles. We look more particularly at the eventual emergence of clustering and columnar alignment, and its impact on local and global settling velocity, for increasing values of the Galileo number in the range Ga $\in$ [110,310] and comparable seeding densities of the order of $\Phi_V \approx 5 \times 10^{-4}$. We compare our experimental data with an existing numerical simulation [18] with Ga = 178, in the steady oblique regime when considering an isolated particle, and at a solid volume fraction $\Phi_V = 4.8 \times 10^{-4}$ of the same order in the experiments. The numerical method, the grid resolution, and the configuration are identical to case M178 of Uhlmann and Doychev [9]. The solid volume fraction, however, was reduced by a factor of 10: it employs the immersed boundary method of Uhlmann [16] on a triply periodic box elongated in the direction of gravity with a treatment of collisions with a repulsive force [19]. The simulation domain has an extension of 85 particle diameters in the horizontal directions and 171 diameters in the vertical direction with a uniform grid resolution $\Delta x$ such that $d/\Delta x = 24$. This simulation covers 1756 gravitational time units.

## II. EXPERIMENTAL DETAILS

In the current work we look at the collective effects of heavy spherical particles settling in a column of quiescent liquid; see Figs. 2(c) and 2(d). The 2 m high column has a square cross section with sides of 0.3 m. In order to vary Ga two sizes of glass particles ($d = 2$ mm and $d = 3$ mm) with density $\rho_p = 2.5 \times 10^3$ kg/m$^3$ and two fluid viscosities ($\nu = 2.05 \times 10^{-6}$ m$^2$/s and $\nu = 3.15 \times 10^{-6}$ m$^2$/s created using a mixture of water and Ucon$^{\text{TM}}$ oil) are used, resulting in Ga $\in$ [110,310]. Constant seeding of heavy particles is accomplished by gradually pouring particles on a stack of six perforated meshes, which has become the de facto standard; see, e.g., Ref. [14]. The particles that leave the last mesh were checked to have a Voronoï area distribution closely resembling a random set of Poisson points (RPP) distribution (and very far from the Voronoï distribution farther downstream) by injecting particles in a very shallow tank and then taking photographs of the injected particles. The columns are therefore not introduced because of the mesh but are formed during descent. The particles travel roughly 1 m before entering the field of view of the cameras, attaining their terminal velocity far before entering the view. For our largest particles this distance of 1 m corresponds to roughly $330d$. Numerical simulations [9] suggest that at least a distance of $250d$ is needed in order to observe clusters and columns [9]. The falling particles are recorded by a set of three Flare 2M360-CL cameras from IO Industries at up to 240 frames per second at a resolution of 2048 $\times$ 1088 using an 8 mm focal length lens covering a height of roughly 0.6 m. The particles are coated black and backlight illumination is employed for enhanced contrast. The cameras are calibrated using an

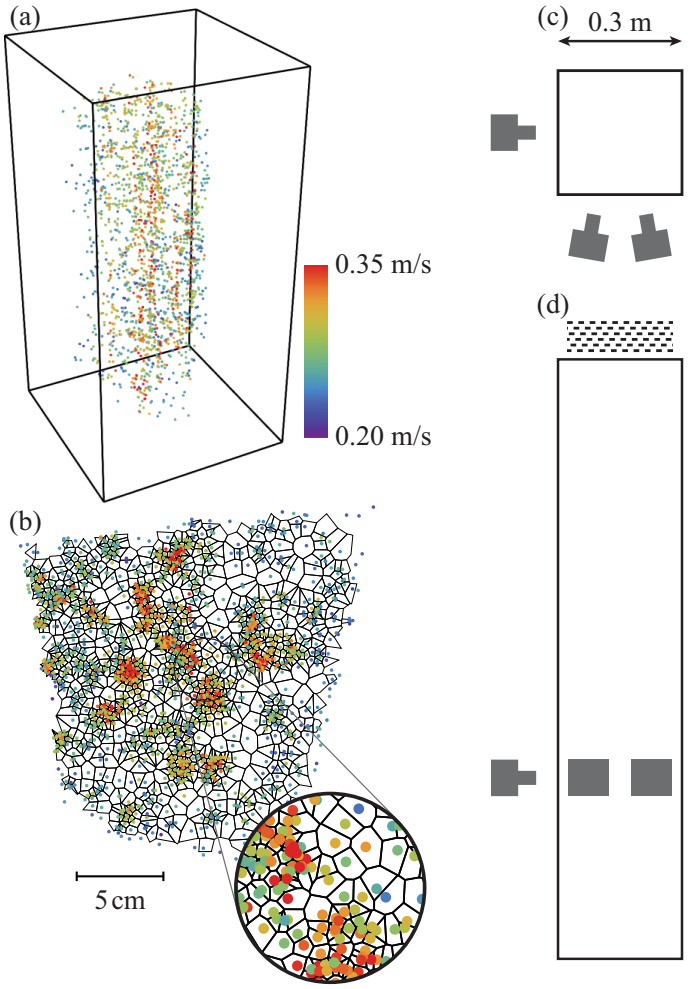


FIG. 2. (a) Three-dimensional reconstructing of settling particles with Ga = 170 colored by their velocities. Short sides of the box are 0.3 m. (b) Top view of (a) including scale bar and the corresponding Voronoï tessellation; see also the detailed (3×) zoom. (c) Top view with the camera arrangement. (d) Side view with the injector visible at the top. The injector comprises stacked perforated metal meshes in order to randomly inject the particles.

*in situ* calibration method [20] achieving a subradius resolution of roughly 300 $\mu$m. Picked from a set of experiments are those for which the volume fractions $\Phi_V$ are constant and comparable to one another (see Table I). Note that the injection is done manually and the volume concentration is only known *a posteriori*. Injections that are too short do not form columns and only show transient behavior and are therefore rejected. Furthermore, we look for experiments where the number of particles in the field of view remains roughly constant. The selected experiments all have a constant volume fraction in the range $1 \times 10^{-4}$–$1 \times 10^{-3}$ and have sufficiently long duration of injection such that columns can potentially be formed. In particular, we make sure to omit the transient part of each experiment, at the beginning when particles start entering the measurement volume and at the end when they leave it. These experiments have the following Galileo numbers: Ga = 110(2), Ga = 170(2), Ga = 200(2), and Ga = 310(3) where the values in parentheses are the number of experiments; see also Table I. Note that the values for Ga are rounded to the nearest 10 to reflect the errors in $\rho_f$, $d$, and $\nu$, which leads to an estimated error of 10 for the Galileo number. In the recorded imagery, particles are detected and using standard particle tracking velocimetry (PTV) the locations of the particles are tracked over time and three-dimensional space. A snapshot of the reconstructed particle positions can be seen in Fig. 2(a) for the case Ga = 170. Visual inspection reveals already clear vertical trails of particles.

TABLE I. Overview of the experimental parameters. $\mathrm{Re}_\infty$ is defined as $\mathrm{Re}_\infty = V_\infty d/\nu$ and $V_g = [(\Gamma - 1)gd]^{1/2}$.

| Ga | $\Gamma$ | $d$ (mm) | $\nu$ ($10^{-6}$ m$^2$/s) | $V_g$ (m/s) | $V_\infty$ (m/s) | $\langle V \rangle$ (m/s) | $\langle V \rangle / V_\infty$ | $\mathrm{Re}_\infty$ | $\phi_V$ ($10^{-5}$) |
|---|---|---|---|---|---|---|---|---|---|
| 110 | 2.5 | 2.0 | 3.15 | 0.17 | 0.18 | 0.22 | 1.19 | 120 | 38 |
| 110 | 2.5 | 2.0 | 3.15 | 0.17 | 0.18 | 0.21 | 1.13 | 120 | 20 |
| 170 | 2.5 | 2.0 | 2.05 | 0.17 | 0.25 | 0.31 | 1.25 | 240 | 49 |
| 170 | 2.5 | 2.0 | 2.05 | 0.17 | 0.25 | 0.30 | 1.21 | 240 | 56 |
| 200 | 2.5 | 3.0 | 3.15 | 0.21 | 0.30 | 0.36 | 1.17 | 290 | 79 |
| 200 | 2.5 | 3.0 | 3.15 | 0.21 | 0.30 | 0.38 | 1.23 | 290 | 100 |
| 310 | 2.5 | 3.0 | 2.05 | 0.21 | 0.33 | 0.37 | 1.10 | 490 | 84 |
| 310 | 2.5 | 3.0 | 2.05 | 0.21 | 0.33 | 0.39 | 1.16 | 490 | 79 |
| 310 | 2.5 | 3.0 | 2.05 | 0.21 | 0.33 | 0.39 | 1.17 | 490 | 76 |

## III. RESULTS

The velocity of the particles is inferred from the particle trajectories and is defined as positive in the direction of gravity; see also Fig. 2(a). Visually we already observe the formation of high-speed (orange-red) columns inside the measurement volume. Moreover, during the experiment one can clearly see the column extend way beyond the measurement section. We estimate that the columns are at least 1.5 m long without any sign that they are unstable or that they break up. The probability density function (PDF) of the velocity as a function of Ga can be found in Fig. 3(a). The mean settling velocities of isolated particles are included as colored dashed lines and increases with Ga. We complement our experimental data with numerical simulations [18] with comparable Ga = 178, $\Gamma = 1.5$, and $\Phi_V = 0.00048$; see Fig. 3(a). A large spread of the velocity above its isolated velocity is found, which supports the idea of an enhanced settling velocity in a suspension of particles. Figure 3(b) shows the velocities normalized by their isolated settling velocity. We note that the largest velocity enhancement is seen for Ga = 170. The speed enhancement for Ga = 310 is notably less than for the Ga = 170 and Ga = 200 cases; see also Table I. Several possible reasons might explain this behavior. First, the most probable explanation is that the chaotic wakes of the Ga = 310 particles might prohibit the formation of a stable train of settling particles, which is not the case for intermediate Ga. Second, the volume fraction necessary for "equivalent" clustering might be a

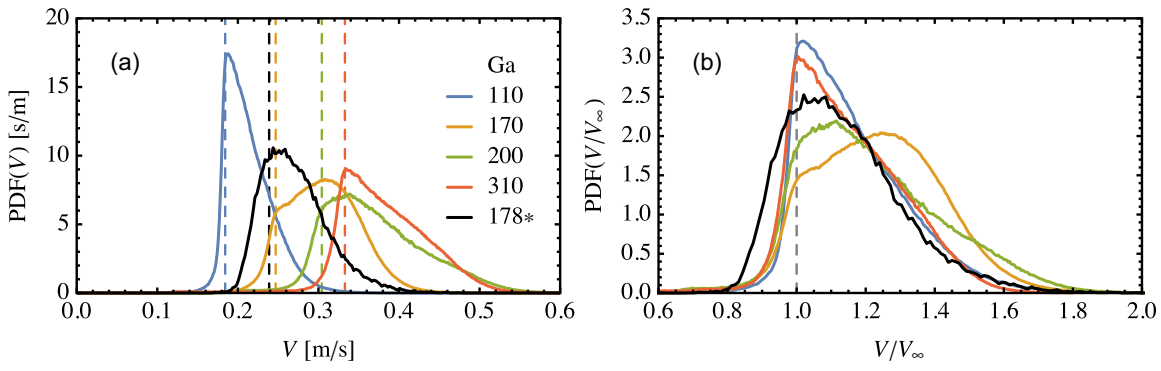


FIG. 3. (a) Velocity probability density function as a function of Ga. Multiple experiments for the same Ga are in agreement and are combined to improve the quality of the statistics. Dashed lines indicate the settling velocity of isolated particles $V_\infty$ for each Ga and are colored analogously. Starred data are from numerical simulations [18]; the data are made dimensional using the diameter and viscosity from the experimental Ga = 170 case. Note that $\Gamma = 1.5$ for the numerical data [9,18], while the experiments have $\Gamma = 2.5$. (b) Vertical velocity normalized by the settling velocity of an isolated particle; see Table I. Same colors as in (a). Average velocities for each experiment can be found in Table I.

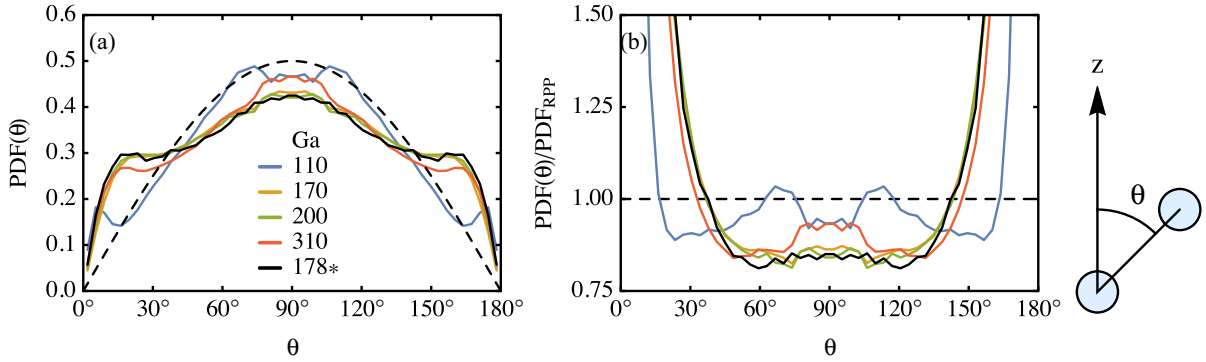


FIG. 4. (a) Angular pair probability density function for various Ga. The angle $\theta$ is defined as the angle between two adjacent particles and the vertical, as seen on the right. The dashed lines indicate the PDF for a set of Poisson particles (RPP), i.e., noninteracting particles that are placed randomly, and is given by $\mathrm{PDF_{RPP}} = \sin(\theta)/2$ and is shown for reference. The graph is, by definition, symmetric around $\theta = 90^\circ$. (b) The data of (a) normalized by $\mathrm{PDF_{RPP}}$. Same colors as in (a). Data bigger than 1 are more likely to occur, while values smaller than 1 are less likely to occur as compared to RPP. Strong enhancement can be seen around $\theta = 0^\circ$ and $\theta = 180^\circ$.

function of Ga. The velocities lower than the mean isolated velocity [below 1 in Fig. 3(b)] are caused by the combined effects of nonmonodispersity, minute density differences, lack of roundness, and the unavoidable adherence of microbubbles. In addition, it is clear that particles drag fluid downwards with them, and, therefore, when fluid is going downward, an equal amount has to go up as per the continuity equation. This upward flow could cause isolated particles (particles in low density regions) to appear to have a lower velocity in the frame of reference of the laboratory. This effect cannot be disentangled by us as we do not have access to the velocity of the fluid. The experiments are performed in the center of a square box and any upward flow can thus go "around" the falling particles *en masse*; however, in the simulation there is no such possibility as the simulation domain is performed in a three-dimensional periodic box. In the simulation we therefore expect more particles with a velocity below $V/V_\infty = 1$. Indeed, this can clearly be seen in Fig. 3(b). The strong enhancement of the velocity can be attributed to particles entering the wake of upstream (leading) particles, similar to what happens with aligned bubbles rising in tandem [21]. We therefore expect that particles tend to align vertically such that a collection of vertically clustered particles can fall faster as they would individually.

To investigate this vertical alignment hypothesis we look at the angle $\theta$ of a particle with other particles in its vicinity and the vertical; see the sketch in Fig. 4. The focus is at close-range interactions, and therefore the distance between two neighboring particles is limited to $8d$. We plot the PDF of the angle $\theta$ as a function of Ga; see Fig. 4(a).

To compare our data we introduce the concept of a random set of Poisson point (RPP) particles. These noninteracting particles are independently and randomly placed inside a volume of choice. We use this as a reference and show that our particles (despite the low Re and relatively low $\Phi_V$) do interact with each other as their statistics strongly differ from that of RPP particles. For such a random set of points the distribution of the angle $\theta$ can be theoretically calculated and follows: $\mathrm{PDF_{RPP}} = \sin(\theta)/2$, where $\theta \in [0,\pi]$, following from the Jacobian of spherical coordinates. Each pair is considered twice and with a different angle $\theta$. The sum of these two angles is, however, 180°, which ensures that the PDF is indeed symmetric around $\theta = 90^\circ$. For the low Ga case of Ga = 110 we see that the PDF [Fig. 4(a)] closely resembles the one that is found if one were to take random particles. We do find a slight increase around $\theta = 0^\circ$ and a slight decrease around $\theta = 90^\circ$ which might be caused by the mild clustering that we see from visual inspection, and which we show later using Voronoï analysis. For the high Ga cases (Ga $\geqslant$ 170), we see a very different behavior; namely, for $45^\circ < \theta < 135^\circ$ we see a clear reduction in the number of neighbors [see also Fig. 4(b), where we present the distribution normalized by the RPP distribution]. So the chance of finding particles

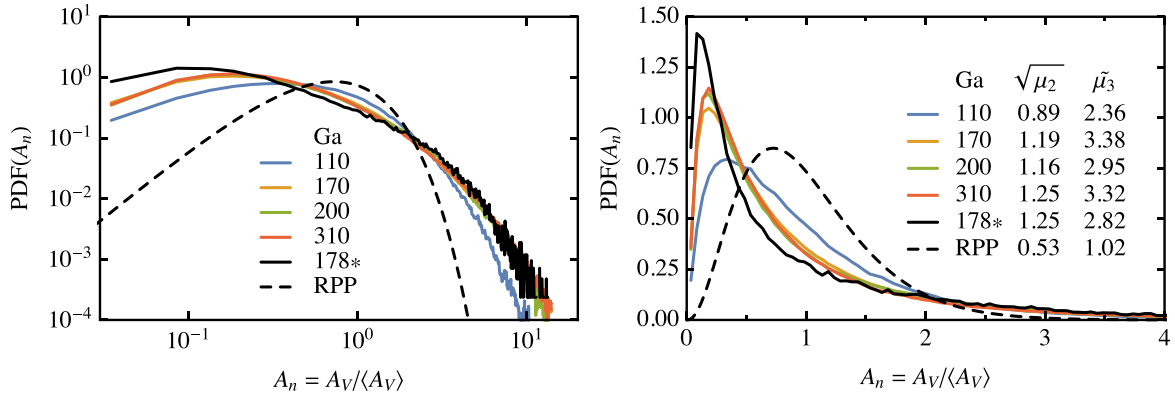


FIG. 5. Probability distribution of the normalized Voronoï areas in the horizontal plane. The corresponding probability density function for randomly distributed points (RPP) is shown as a dashed line. Left: Logarithmic axes. Right: Linear axes; the legend includes the standard deviation ($\sqrt{\mu_2}$) and the skewness ($\tilde{\mu}_3$) of $A_n$.

next to each other is significantly reduced for the high Ga cases. As a consequence, or rather a cause, particles are found to align vertically far more than a random set of Poisson particles; the PDF is found to be much higher for $\theta < 45^\circ$ (or equivalently $\theta > 135^\circ$), which can be more clearly seen in Fig. 4(b). Figure 4 has the inclusion of numerical data [18] with Ga $= 178$, $\Phi_V = 0.00048$, and $\rho_p/\rho_f = 1.5$, which is comparable to our set of parameters. For these data we find that angle-pair distribution is remarkably similar to the experimentally found distributions for Ga $= 170$, despite having a fairly different density ratio $\Gamma = \rho_p/\rho_f$. Indeed a difference in $\Gamma$ can have a profound impact on the stability of the wake as found by Refs. [6,7], though the influence is expected to be relatively small in the range $1.5 < \Gamma < 2.5$ for this value of the Galileo number. Note, however, that the phase spaces presented in Refs. [6,7] are for the case of vanishing $\Phi_V$, and these lines might shift significantly for increasing $\Phi_V$ as neighboring particles can trigger wake instabilities.

A look from the top further corroborates the hypothesis that these particles cluster and thereby form a rapidly settling group (or cluster) of particles; see Fig. 2(b). This top view shows the horizontal position of the particles colored by their velocities. Not only do we observe a set of high-density and low-density regions—far different from a RPP—but also that the settling velocities are higher in high-density regions, which can be attributed to vertical alignment and further corroborates our view of the mechanism of enhanced settling velocity. The observation of relatively low- and high-density regions—different from RPP—can be substantiated by computing the Voronoï tessellation in the horizontal plane. It is indeed the Voronoï tessellation in the horizontal plane that should clearly show a signature of clustering as it is this plane that is perpendicular to gravity. An example of a Voronoï tessellation is included in Fig. 2(b). We take particles over the entire measurement height (roughly 550 mm) so as to have as many samples as possible. Note that the choice of the vertical extent needs to be at least several times the typical vertical distance between descending particles in the same column, such that vertically aligned particles create dense regions once projected on the horizontal plane. We have checked that the PDF of the Voronoï areas is similar if a limited vertical extent (down to 125 mm) is chosen. Each particle is assigned the set of all points (forming a convex polygon called a Voronoï cell) that is closest to itself rather than any other particle. The area of the cell is now inversely proportional to the local density [22]. Mathematically, the Voronoï tessellation is the dual graph of the Delaunay triangulation. We make sure not to include Voronoï cells at the periphery, which create artificially large cells, skewing the statistics.

The Voronoï tessellation is calculated for each frame and the area of the cells ($A_V$) is scaled by the mean area of each frame. The PDF of the normalized area ($A_n = A_V/\langle A_V \rangle$) is calculated for each Ga; see Fig. 5. The figures include the corresponding PDF for random Poisson particles (RPP). For the lowest value of the Galileo number, Ga $= 110$, we already observe an increase in probability density for smaller and larger cells indicating some clustering, as we also observe in the angle-pair distribution in Fig. 4. For large Ga, we find even more increase in the probability

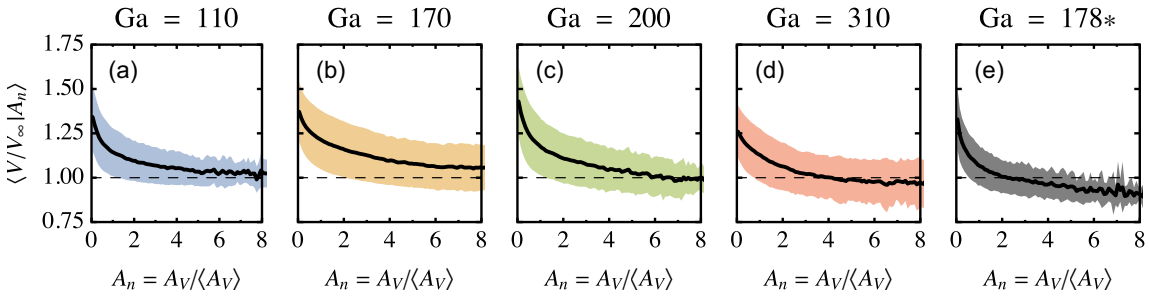


FIG. 6. Velocity of a particle conditioned on its normalized Voronoï area in the horizontal plane. Bands represent $\pm\sigma(v|A_n)_{A_n}$. Velocities are normalized using $V_\infty$, the terminal velocity of an isolated particle settling in a quiescent fluid. (e) Numerical data from Ref. [18]. Note that the "spiky" data for high $A_n$ are caused by a lack of statistics, and that the experiments have more statistics than the very expensive numerical simulations.

density for both small and large Voronoï areas, indicating a more pronounced clustering. Such an important level of clustering could already be observed from a simple visual inspection of Fig. 2(b): more dense and "open" areas than one would expect from randomly placed particles. Broadening of the distribution is also quantified by calculating the standard deviation of the distribution; see Fig. 5. Compared to an RPP ($\sqrt{\mu_2} = 0.53$), we indeed observe an increased standard deviation for Ga $= 110$ ($\sqrt{\mu_2} = 0.89$), indicating clustering, and further increased standard deviations for even higher Ga $\geqslant 170$ (up to $\sqrt{\mu_2} = 1.25$). Increased standard deviation with respect to an RPP is indeed also what one observes in Fig. 2(b). We emphasize that the particles follow an RPP distribution when they exit the injector—very different from the distribution farther downstream.

A visual inspection of Fig. 2(b) also suggests that higher velocities are attained at high-density regions. To substantiate that claim the conditional average of the average settling velocity is calculated; see Fig. 6. The average velocity is conditioned on the normalized Voronoï area $A_n$ which is proportional to the inverse local density. Moreover, along with the mean velocity also the standard deviation is calculated for each $A_n$. The mean velocities and their spread are normalized using the terminal velocity of an isolated particle settling in a quiescent fluid bath. A clear increase in speed of up to 40% can be seen for high-density (low $A_n$) regions for all Ga, and the graphs are very similar, showing the same behavior. As we stated before, the simulations of Refs. [9,18] are performed in a three-dimensional periodic box where upward flow will certainly affect the velocity of some isolated particles. We can now clearly see this in Fig. 6(e); isolated particles ($A_n \gg 1$) have normalized velocities below 1, meaning they settle slower than they would if they were to settle by themselves in an infinite bath. Also here we see that the case of Ga $= 310$ shows slightly less enhanced velocity (for example, at $A_n = 0$) as compared to the Ga $= 170$ and Ga $= 200$ cases.

## IV. CONCLUSION

Starting from the visual observation in Fig. 2(a) that particles look vertically aligned, we find that, indeed, particles are preferentially aligned vertically as per our findings of the PDF of $\theta$ in Fig. 4. In the two-dimensional top view visual inspection suggests low- and high-density regions with low and high velocities, respectively. We confirm this view in Figs. 5 and 6. Altogether, our findings indicate that particles tend to settle in a preferential columnar configuration, with an increased trend to alignment with increasing Galileo number. This columnar alignment then impacts the settling of the particles, as particles that follow in the wake of another particle tend to settle faster. It was found in previous numerical simulations at Ga $= 121$ and Ga $= 178$ (although at a higher seeding density $\Phi_V = 5 \times 10^{-3}$) by Uhlmann and Doychev [9] that only the latter tended to form columns impacting the settling. The different behavior between the low and high Galileo cases is interpreted in terms of the properties of particle wakes. The wakes of the low Ga particles (Ga $\leqslant 155$) have a stable vertical wake (see Fig. 1) and particles fall straight down. Only when two particles are already vertically aligned will the trailing particle fall in the wake of the leading particle. For higher Ga the

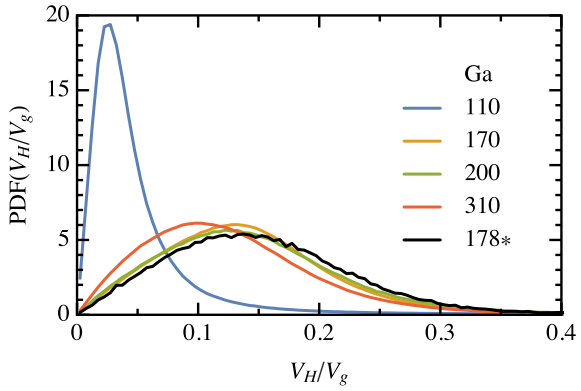


FIG. 7. PDF of the magnitude of the horizontal velocity ($V_H = \sqrt{V_x^2 + V_y^2}$) normalized by the gravitational velocity. Multiple experiments for the same Ga are in agreement and are combined to improve the quality of the statistics. Starred data are from numerical simulations and have $\Gamma = 1.5$ [9,18], while the experiments have $\Gamma = 2.5$.

wakes of the particles are unstable, causing the trajectory of said particles to be either steady oblique (Ga $\geqslant$ 155), oblique oscillating (Ga $\geqslant$ 185), or even chaotic (Ga $\geqslant$ 215). In the aforementioned simulations, the case Ga = 178 was in a steady oblique regime; particles therefore had a horizontal motion with a higher chance of "catching" the slipstream of an upstream particle [9], causing the columnar alignment and the enhanced settling velocity. Our experimental results show that the same behavior (columnar alignment and enhanced settling) prevails for the oblique oscillating (Ga = 200) and chaotic (Ga = 310) situations which all exhibit lateral motion. The strongest impact on overall settling velocity enhancement is observed for particles at intermediate Galileo number (Ga = 170) in the steady oblique situation. The highest Galileo case explored (Ga = 310) was found on the contrary to exhibit less enhanced settling. At first glance this may seem consistent with the slightly reduced alignment observed for the Ga = 310 case from the angular statistics shown in Fig. 4. However, Voronoï statistics in Fig. 5 seem on the other hand to exhibit a slightly enhanced clustering for this same case, which would be on the contrary associated to settling enhancement. A first attempt of interpretation could be related to the chaotic nature of the particle motion at Ga = 310 which could still promote the chance for particles to catch each other's wake and form columns, while disturbing the alignment within the columns. However, the statistics of the horizontal velocity of the particles reveals a more complex situation. The PDF of the amplitude of the horizontal velocity $V_H = \sqrt{V_x^2 + V_y^2}$ of the particles for Ga = 310 is indeed only marginally different as compared to the Ga = 170, Ga = 178, and Ga = 200 cases, but very different from the Ga = 110 case; see Fig. 7. The Ga = 110 case exhibits a low (mean) sideways velocity compared to the other cases, with a narrow distribution, as expected for particles settling mostly in a "steady-straight" regime. The other cases exhibit all very similar PDFs compared to each other, with larger mean sideways velocities and broader distributions (note, though, that the mean sideways horizontal velocity is a little less for the Ga = 310 case as compared to the Ga = 170, Ga = 178, and Ga = 200 cases). Purely oblique trajectories (as expected for individual particles settling at Ga = 170) would exhibit a larger mean sideways motion compared to Ga = 110, but still a narrow PDF (the amplitude of the horizontal velocity being mostly constant). The chaotic case on the contrary is expected to have a wide PDF for the horizontal velocity which undergoes erratic fluctuations. The similarity of the PDFs for the four cases Ga = {170,178,200,310} therefore indicates that, though these particles follow different paths (Fig. 1) when they settle individually, an ensemble of particles eventually shows complex trajectories and chaotic wakes, probably due to particles and the wakes interacting with each other, causing horizontal velocities of the particles to have important and similar fluctuations (see Fig. 7). Furthermore, note that Fig. 7 shows the horizontal velocity of the particles and that the horizontal velocities of the flow in the wake of individual particles can follow a different trend. Overall these

observations show that it is very likely irrelevant to speculate on possible interpretations for the differences in the settling collective behavior for particles at Ga = 170 and at Ga = 310 simply considering the usual "single particle regimes" in Fig. 1, although these regimes certainly play a role in the initial triggering of column formation. Why the Ga = 310 case shows less enhanced velocity, while still having a comparable PDF($\theta$), PDF($A_n$), $\langle V/V_\infty | A_n \rangle$, and PDF($V_H/V_g$) (though in each case it slightly differs from the Ga = 170, Ga = 178, and Ga = 200 cases), is still an open question. Further research, where also the fluid velocity is measured, might help to find an explanation.

An increase or decrease in settling velocity is significant in cases where one wants to predict or prevent settling particles in e.g., chemical reactors with solid reactants or settling of particulate matter in riverbeds, and can probably also affect rainfall (the transition between steady vertical and steady oblique regimes for water droplets in air occurs for droplet diameters of the order of 850 $\mu$m) and ash cloud dynamics.

Finally, a striking observation of the present study is that, contrary to the simulations, we do find in the experiment that particles in the steady vertical regime (Ga = 110) also exhibit mild clustering and column formation, although less pronounced than for particles at larger Galileo number (as shown by Voronoï statistics in Fig. 5 and the angular pair statistics in Fig. 4). A possible reason for the emergence of columns for such a low Galileo number, where no wake instability is expected, can be related to the existence of a large-scale flow caused by an ensemble of settling particles in a closed container such as ours. Such a large-scale flow is absent in the simulations presented in the paper as it has a periodic domain. This large-scale flow might induce some different flow dynamics as particles in low-density regions are less affected by upward flow as compared to those particles for the case of the simulation.

To summarize, we find a coherent set of observations for settling particles that explain the observed features: trajectory properties, vertical alignment, high-density regions, and enhanced settling velocity. Future studies will explore further the role of increasing the seeding density as well as the importance of confinement and boundary conditions. Another important extension of the present study concerns the impact of surrounding turbulence on the column formation and settling enhancement.

## ACKNOWLEDGMENTS

We acknowledge the German-French program PROCOPE (Grant No. 57129319), the French program "TEC2" (Grant No. ANR-12-BS09-0011), and the German Research Foundation (DFG) under Project No. UH242/1-2 for funding this study.

[1] I. Newton, *The Principia: Mathematical Principles of Natural Philosophy* (University of California Press, 1999).

[2] T. A. Johnson and V. C. Patel, Flow past a sphere up to a Reynolds number of 300, J. Fluid Mech. **378**, 19 (1999).

[3] B. Ghidersa and J. Dušek, Breaking of axisymmetry and onset of unsteadiness in the wake of a sphere, J. Fluid Mech. **423**, 33 (2000).

[4] L. Schouveiler and M. Provansal, Self-sustained oscillations in the wake of a sphere, Phys. Fluids **14**, 3846 (2002).

[5] G. Bouchet, M. Mebarek, and J. Dušek, Hydrodynamic forces acting on a rigid fixed sphere in early transitional regimes, Eur. J. Mech. B **25**, 321 (2006).

[6] M. Jenny, J. Dušek, and G. Bouchet, Instabilities and transition of a sphere falling or ascending freely in a Newtonian fluid, J. Fluid Mech. **508**, 201 (2004).

[7] C. H. J. Veldhuis and A. Biesheuvel, An experimental study of the regimes of motion of spheres falling or ascending freely in a Newtonian fluid, Int. J. Multiphase Flow **33**, 1074 (2007).
[8] M. Horowitz and C. H. K. Williamson, The effect of Reynolds number on the dynamics and wakes of freely rising and falling spheres, J. Fluid Mech. **651**, 251 (2010).
[9] M. Uhlmann and T. Doychev, Sedimentation of a dilute suspension of rigid spheres at intermediate Galileo numbers: The effect of clustering upon the particle motion, J. Fluid Mech. **752**, 310 (2014).
[10] P. Ern, F. Risso, D. Fabre, and J. Magnaudet, Wake-induced oscillatory paths of bodies freely rising or falling in fluids, Annu. Rev. Fluid Mech. **44**, 97 (2012).
[11] J. F. Brady and G. Bossis, Stokesian dynamics, Annu. Rev. Fluid Mech. **20**, 111 (1988).
[12] S. Ramaswamy, Issues in the statistical mechanics of steady sedimentation, Adv. Phys. **50**, 297 (2001).
[13] É. Guazzelli and J. F. Morris, *A Physical Introduction to Suspension Dynamics* (Cambridge University Press, Cambridge, UK, 2011).
[14] R. N. Parthasarathy and G. M. Faeth, Turbulence modulation in homogeneous dilute particle-laden flows, J. Fluid Mech. **220**, 485 (1990).
[15] M. Mizukami, R. N. Parthasarathy, and G. M. Faeth, Particle-generated turbulence in homogeneous dilute dispersed flows, Int. J. Multiphase Flow **18**, 397 (1992).
[16] M. Uhlmann, An immersed boundary method with direct forcing for the simulation of particulate flows, J. Comput. Phys. **209**, 448 (2005).
[17] T. Kajishima and S. Takiguchi, Interaction between particle clusters and particle-induced turbulence, Int. J. Heat Fluid Flow **23**, 639 (2002).
[18] T. Doychev, The dynamics of finite-size settling particles, Ph.D. thesis, Karlsruhe Institute of Technology, 2014.
[19] R. Glowinski, T.-W. Pan, T. I. Hesla, and D. D. Joseph, A distributed Lagrange multiplier/fictitious domain method for particulate flows, Int. J. Multiphase Flow **25**, 755 (1999).
[20] N. Machicoane, M. Lopez-Caballero, M. Bourgoin, A. Aliseda, and R. Volk, Improvements on particle tracking velocimetry: Model-free calibration and noiseless measurement of second order statistics of the velocity field, arXiv:1605.03803.
[21] S. G. Huisman, P. Ern, and V. Roig, Interaction and coalescence of large bubbles rising in a thin gap, Phys. Rev. E **85**, 027302 (2012).
[22] R. Monchaux, M. Bourgoin, and A. Cartellier, Preferential concentration of heavy particles: A Voronoi analysis, Phys. Fluids **22**, 103304 (2010).

# Appendix B

# Collaboration 2

T. Barois, P.D. Huck, M.Bourgoin and R. Volk Equilibrium position of a rigid sphere in a turbulent jet: A problem of elastic reconfiguration Phys. Rev. E, **96**, 033105, (2017).

# Equilibrium position of a rigid sphere in a turbulent jet: A problem of elastic reconfiguration

T. Barois,[1] P. D. Huck,[2] M. Bourgoin,[2] and R. Volk[2]
[1]*Univ. Bordeaux, CNRS, LOMA, UMR 5798, F-33405 Talence, France*
[2]*Laboratoire de Physique, École Normale Supérieure de Lyon, Université de Lyon, CNRS, 46 Allée d'Italie, F-69364 Lyon, Cedex 07, France*
(Received 2 March 2017; revised manuscript received 2 June 2017; published 11 September 2017)

The position of floating spheres trapped within an immersed turbulent water jet is investigated. Using the self-similarity properties of the jet velocity profile, the equilibrium problem is formulated in a rescaled space where the sphere is static and deformable. This approach is found to be related to a problem of elastic reconfiguration where elasticity arises here from the geometry of the flow instead of an actual deformation of a body.

DOI: 10.1103/PhysRevE.96.033105

## I. INTRODUCTION

Reconfiguration is a concept that was introduced in botany to describe plants in moving fluids [1]. Because a plant is deformable, its shape may change in a fluid flow. This results in a drag reduction compared to a reference configuration for an equivalent rigid body. The drag reduction is at the core of reconfiguration since the concept is usually associated to a survival strategy in high winds or fast currents [2–5].

The drag exerted on deformable structures has been studied in various contexts such as the study of plants in air [6] or water [7,8] flows and in simplified geometries corresponding to soft rods [9], rolled-up sheets [10], or flexible plates [11]. Contrary to a rigid body, the drag measured for those deformable structures is not proportional to the squared fluid velocity. Nevertheless, the drag $D$ still verifies a simple scaling relation

$$D \sim V^{2+\mathcal{E}}, \tag{1}$$

where $V$ is the fluid velocity and $\mathcal{E}$ a power exponent usually referred as the Vogel exponent.

The existence of a single scaling law (1) is a remarkable and robust result for many different situations. A first argument supporting this result is found by dimensional analysis based on the relevant physical parameters of the fluid-structure interaction problem [12]. A second complementary argument is found in the work of Alben *et al.* [9] in terms of self-similarity of the elastic structure profile. It should be mentioned that scaling laws with Vogel exponents (1) are also reported when the buoyant force [13], or equivalently the weight [14], is involved instead of elastic forces.

In this paper, a fluid-structure problem consisting of a rigid buoyant sphere placed in a self-similar flow is considered. While there is no deformation of the body, the framework of elastic reconfiguration is surprisingly adapted to describe the forces acting on the object. More precisely, it is shown that the fluid-structure interaction problem formulated in a specific rescaled frame is equivalent to a reconfiguration problem involving the isotropic deformation of an elastic body.

For all the practical situations where usual elastic reconfiguration is reported, deformable bodies are slender structures. For nonslender structures, reconfiguration is not likely to be observed as bulk deformations are not expected for a pressure drag ($\sim 10^3$ Pa for a wind of 30 m s$^{-1}$) that remains much smaller than the elastic modulus of usual materials ($\sim 10^9$ Pa) [5]. Beyond the exercise of interpreting a rigid-body problem as a problem of elasticity, the analogy that is proposed here permits the exploration of reconfiguration regimes for nonslender bodies such as spheres.

## II. EXPERIMENTAL SETUP

The experimental setup studied here is depicted in Fig. 1. A turbulent monophasic jet is established in a water tank ($0.3 \times 0.3 \times 0.7$ m$^3$) by the injection of water through a circular nozzle with a diameter $d_N = 6.5$ mm. The flow rate $Q$ in the experiments is between 10 and 50 mL s$^{-1}$, which corresponds to a velocity at the nozzle ranging from 0.3 to 1.5 m s$^{-1}$. The Reynolds numbers at the nozzle, $\mathrm{Re}_N$, then vary between 2000 and 10 000, where $\mathrm{Re}_N = Q/d_N\nu$ with $\nu$ the kinematic viscosity of water. Floating polypropylene spheres (with density $\rho_s = 850$ kg m$^{-3}$ and radius $R$ ranging from 7 to 15 mm) are placed in the vicinity of the jet centerline and reach a stable equilibrium position where the buoyant force and the fluid forces are balanced. This configuration is similar to the levitation of a table-tennis ball over a hair dryer. The latter experiment is a classic teaching demonstration [15,16] exploiting the intriguing aspects of levitation [17].

The trapping stability of the sphere in the plane perpendicular to the jet axis has been discussed in terms of the Coandă effect [18]. If a curved surface is impacted by a jet, the outgoing jet is deflected, which imparts a net force on the curved body because of momentum conservation [19]. The Coandă effect and the associated forces have been investigated for spheres suspended by vertical [20] and tilted jets [21]. The trapping of spheres far from the nozzle is not observed. This is because the confining force in the horizontal plane decreases with the distance to the nozzle [20].

The question addressed here concerns the trapping distance between the sphere and the jet nozzle for a controlled injection flow rate. Despite its apparent simplicity, this problem is not trivial because it requires the computation of the force exerted by an inhomogeneous flow on a sphere. In the case of homogeneous flows, the computation of the drag involves an empirical coefficient known as the drag coefficient. For inhomogeneous flows, a similar empirical coefficient may exist [22] but it has no general formulation and depends on the geometry of the object as well as on the profile of the incoming flow.

The jet profile was determined by three-dimensional (3D) particle tracking velocimetry (PTV). Two cameras are used to record the tracks of submillimeter particles injected from the nozzle. The particles are matched in density with water in

 

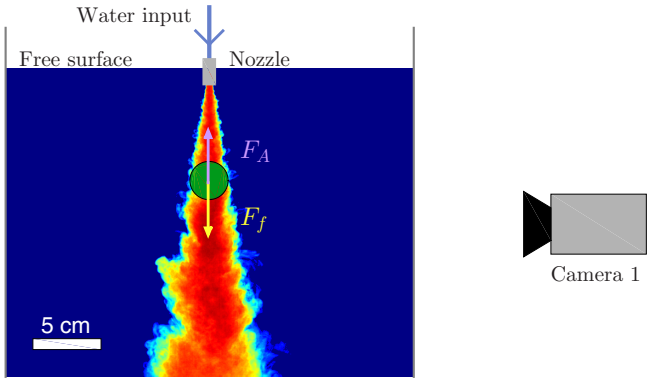


FIG. 1. Schematics of the trapped sphere experiment. Two cameras are positioned at 90° to observe the motion of the sphere in two perpendicular planes. The free jet profile is visualized from camera 2 (not represented) by the injection of dye at the nozzle. A solid circle is inserted to represent the typical trapping of a floating centimeter scale sphere submitted to buoyant forces and fluid forces with magnitudes $F_A$ and $F_f$, respectively.

order to behave as tracers for the large-scale mean flow. The submillimeter particles are small enough to satisfy the uniform sampling condition [23] that occurs when the particles do not exceed 20 times the smallest scales of the turbulent flow. Here the size of the smallest scales is of the order of 0.1 mm. The 3D mean velocity map is obtained from the time averaging of the particle velocity onto a binning grid with submillimeter resolution. The radial profiles are extracted from the map for different distance $z$ to the nozzle. Measurements of the mean profiles are performed for a flow rate of $Q = 27$ mL s$^{-1}$ in the absence of the trapped sphere. Velocity profiles are displayed in Fig. 2 (left). The jet profile is self-similar when it is represented in a specific set of coordinates [24,25] as shown in Fig. 2 (right). The self-similar velocity profile is given by

$$v_z(r,z) = \frac{1}{z}\mathcal{F}\left(\frac{r}{z}\right), \tag{2}$$

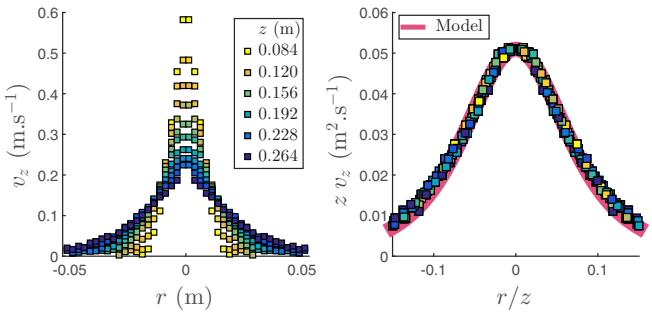


FIG. 2. Left: Axial velocity $v_z$ of the jet as a function of the radial distance $r$. Eleven axial distances to the nozzle are considered for $z$ starting from 84 mm going up to 264 mm with a linear spacing of 18 mm. The flow rate at the nozzle is $Q = 27$ mL s$^{-1}$. Right: Product $zv_z$ (m$^2$ s$^{-1}$) as a function of the normalized radial coordinate $r/z$ for the same data points. The solid line is a fitting function established after the profile $\mathcal{F}(r/z) \propto 1/(1+(r/\tan(\alpha)z)^2)^2$ [24] with $\alpha = 0.12$ rad.

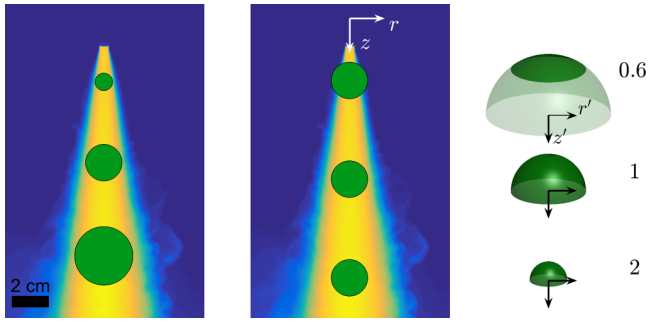


FIG. 3. Illustration of the self-similarity. Left: Three spheres with same drag for the same ratio $z_e/R$, where $z_e$ is the equilibrium distance to the nozzle and $R$ the sphere radius. Center: Three identical spheres at their equilibrium positions for three different flow rates. The cylindrical frame $\{r,z\}$ is represented at the origin of the jet. Right: Profiles in the rescaled frame $\{r' = r/z_e, z' = z/z_e\}$ of the spheres' surfaces impacted by the jet for the three corresponding positions of the central figure. The associated numbers indicate the radial portion of the sphere impacted by the jet in the scaled frame $\alpha z_e/R$, where $\alpha$ is the characteristic opening angle of the jet. This dimensionless number is interpreted as a Cauchy number [see Eq. (5)].

where $r$ is the radial coordinate, $z$ the vertical distance to the origin of the jet, and $\mathcal{F}$ the self-similar profile. The expression $\mathcal{F}(r/z) \propto 1/(1+(r/\tan(\alpha)z)^2)^2$ [24] is used for the fitting function in Fig. 2 (right). The parameter $\alpha$ relates to the opening half-angle of the jet with $\alpha = 0.12$ rad.

## III. SELF-SIMILARITY

The stationary trapping of a sphere by a vertical jet occurs if the fluid forces and the buoyant forces are balanced (see Fig. 1). In this case, the magnitudes of these forces verify

$$F_A = F_f, \tag{3}$$

where $F_f$ are the net fluid forces exerted on the sphere and $F_A$ the buoyant forces given by the Archimedes principle $F_A = (4\pi/3)\Delta\rho R^3 g$, where $R$ is the sphere radius, $g$ the gravity field, and $\Delta\rho = \rho_w - \rho_s$ the apparent density with $\rho_w$ the density of water and $\rho_s$ the density of the sphere.

As mentioned before the expression $F_f$ for the drag exerted on a spherical body in an inhomogeneous flow is a delicate problem. In this experiment, the sphere is only trapped close to the nozzle where the jet typical width does not exceed the sphere diameter. This means that the flow profile is strongly inhomogeneous over the sphere's surface and the presence of the sphere strongly modifies the flow profile. As a consequence, direct computation of the net fluid force acting on the sphere is challenging.

The strategy adopted here is to use geometric considerations related to the jet profile in order to reinterpret the vertical equilibrium position of a sphere. Because the jet profile is self-similar, the fluid forces acting on a sphere at a given position should be the same as the forces acting on a smaller sphere at a proportionally smaller distance to the origin of the jet. This geometrical property is sketched in Fig. 3 (left). If

self-similarity is verified, the fluid force may be written as

$$F_f = \mathcal{G}\left(\frac{R}{z_e}\right), \tag{4}$$

where $z_e$ is the distance between the nozzle and the equilibrium position of the sphere. The function $\mathcal{G}$ depends on the jet profile (2) modified by the presence of the sphere.

The fluid force acting on a sphere in a jet [Eq. (4)] depends on the dimensionless radius $R/z_e$ only. This means that a variation of the sphere position along the jet centerline $z_e$ is equivalent to a decrease of the sphere radius $R$ by the same factor (see Fig. 3).

The approach of this work is to consider the problem of the sphere trapped in the jet after the rescaling of the space coordinates $\{r,z\}$ by the factor $z_e$. In the dimensionless space $\{r',z'\}$, the sphere does not move as it lies at a distance unity ${z_e}' = 1$ from the nozzle. The sphere is effectively deformable with a radius $R' = R/z_e$. In the rescaled frame, the deformable sphere obeys a mechanical equilibrium with a stationary flow (Fig. 2, right).

## IV. EFFECTIVE RECONFIGURATION

The study of drag reduction in reconfiguration problems uses two dimensionless parameters: the Cauchy number $C_Y$ and the reconfiguration number $\mathcal{R}$.

The Cauchy number quantifies the deformation induced by the fluid flow by comparing the fluid dynamic pressure $\sigma_f$ and the elastic stress $\sigma_E$ for a typical deformation. For usual reconfiguration problems, i.e., with an actual elastic deformable body, the typical elastic stress is the elastic Young modulus $E$, and the Cauchy number is given by $C_Y = \sigma_f/E$. For the problem addressed here, there is *a priori* no expression for an elastic modulus. However, a Cauchy number can be proposed by considering a generic elastic relation $\sigma_f = E\epsilon$ that the deformable sphere would verify in the rescaled frame, where $\sigma_f$ is the external stress due to the fluid and $\epsilon$ is the resulting deformation ratio. In this case, the Cauchy number is simply given by $C_Y = \epsilon$. In the rescaled frame, the deformation of the sphere corresponds to an isotropic deformation for which the strain in the linear regime is $\epsilon \sim \delta R/R$. As the variation of $R$ and $z_e$ is equivalent, the strain parameter may scale as $\epsilon \sim z_e/R$. In the following, the Cauchy number is defined by

$$C_Y = \alpha\frac{z_e}{R}, \tag{5}$$

where the opening angle of the jet, $\alpha$, has been introduced.

The reconfiguration number $\mathcal{R}$ quantifies the efficiency of the drag reduction by comparing the drag exerted on the deformable body and the drag that would be exerted on the equivalent rigid body. As mentioned before, the drag exerted on the sphere equals the buoyancy. The drag on the equivalent rigid body corresponds to the drag in the limit $\epsilon = 0$. In this limit, the sphere is asymptotically close to the jet nozzle and impacted on its top surface which is perpendicular to the flow. Consequently one can write the reconfiguration number as

$$\mathcal{R} = \frac{(4\pi/3)\Delta\rho R^3 g}{(1/2)c_P\rho_w(Q^2/S_N)}, \tag{6}$$

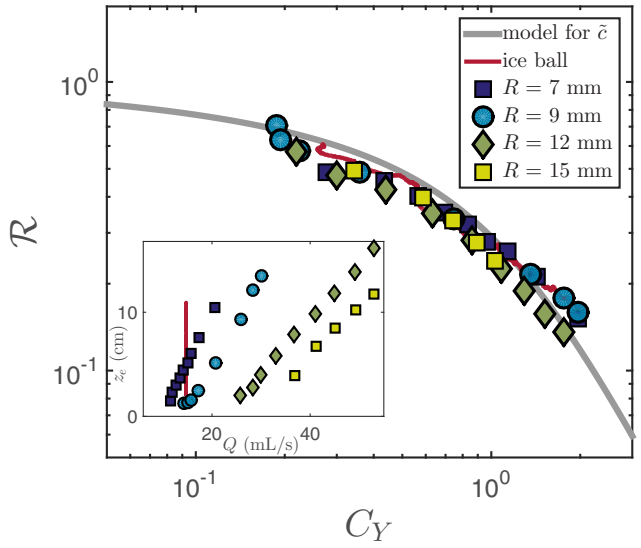


FIG. 4. Reconfiguration number [Eq. (6)] as a function of the Cauchy number [Eq. (5)] for polypropylene spheres and a melting ice ball. The solid line corresponds to the equilibrium problem (3) with an empirical expression for the drag coefficient, $\tilde{c}(r/R) = 1 - (r/R)^\eta$, with $\eta = 0.5$. The inset plot shows the equilibrium distance to the nozzle,$z_e$, as a function of the flow rate $Q$ for the same data points.

where $c_P = 2.1$ is the drag coefficient of a plate for the jet profile and $S_N = (\pi/4){d_N}^2$ the cross-sectional area of the nozzle.

The equilibrium positions of spheres for varying flow rates of the jet have been measured for a set of four floating spheres and a melting spherical ice ball. The ice ball was obtained by crystallization of dyed water in a specific mold previously designed [26]. The relative density is 0.85 for the polypropylene spheres and 0.92 for the ice ball. The average positions of the spheres are obtained from acquisitions of 45 s, corresponding to an order of $10^2$ oscillations of the sphere in the confining potential with a typical amplitude $\sim R$. The resulting data are plotted in Fig. 4 using the dimensionless numbers $C_Y$ and $\mathcal{R}$ defined in Eqs. (5) and (6). For comparison, the equilibrium distance with respect to the flow rate has been also represented in usual coordinates in the inset plot in the same figure.

The experimental data collapse on a master curve when represented with the dimensionless numbers $C_Y$ and $\mathcal{R}$. This master curve shows a quantitative agreement with reconfiguration of actual deformable bodies in a flow (see [5] for example).

The limit $C_Y \ll 1$ relates to a low drag limit where the deformable body in the rescaled space is weakly deformed. This implies that the drag is that of an equivalent rigid body ($\mathcal{R} \sim 1$). In physical space, this limit corresponds to a sphere impacted by the jet at its very center where the sphere is locally a surface perpendicular to the flow. According to its definition, the reconfiguration number is expected to approach unity in the low drag limit where deformation is asymptotically small. This is the case here, notably because the parameter $c_P$ has been introduced to account for the drag of the sphere when it is close to the jet nozzle.

For $C_Y \sim 1$, the body is moderately deformed. The reconfiguration and drag reduction are dominated by the streamlining of the body rather than the area reduction [11]. In physical space, this regime corresponds to the jet impacting the sphere on its typical size. This justifies the introduction of the opening angle $\alpha = 0.12$ rad in the expression of the Cauchy number since this transition is expected for $C_Y \sim 1$.

For higher Cauchy numbers, the whole sphere is impacted by the jet and the drag reduction may be attributed to the area reduction in the rescaled frame. In physical space, the sphere is far from the nozzle, $z_e > R/\alpha$, and in a spatially homogeneous flow corresponding to the axial velocity on the jet centerline [27]. In this regime of uniform flow, the drag is $1/2 c_s \rho_w \pi R^2 {v_e}^2$, where $c_s$ is the drag coefficient for a sphere and $v_e$ the equilibrium velocity needed to balance buoyancy. The asymptotic regime $C_Y \gg 1$ is not observed for trapped spheres since the confinement is not possible without velocity gradients. The stationary trapping is experimentally lost around $C_Y \sim 2$. If stability was possible for $C_Y \gg 1$, one should expect a scaling regime for the reconfiguration number where $\mathcal{R} \sim {C_Y}^{-2}$ (or a Vogel exponent $\mathcal{E} = -2$) after the definition of $\mathcal{R}$ and the expression for the equilibrium velocity on the centerline, $v_e = v(r = 0, z_e) \propto (1/z_e) Q/S_N$. This regime could be explored by a force measurement while maintaining the sphere in the jet.

The relation between $\mathcal{R}$ and $C_Y$ has also been explored for a given flow rate $Q = 18$ mL s$^{-1}$ with a melting ice ball as plotted in Fig. 4. Contrary to an attached body [28], the melting is isotropic because the ice ball is free to rotate when it is suspended in the jet. This experiment allows for a continuous variation of $\mathcal{R}$ and $C_Y$ as the ball progressively melts and reduces in size. As for the rigid spheres, the equilibrium is lost when $C_Y$ approaches 2.

The collapse of the data in Fig. 4 implies that, in the rescaled frame, the sphere behaves as a deformable body with a stress-to-strain relation similar to Hooke's law. The analogy with reconfiguration allows for the introduction of an effective elastic coefficient for the sphere. For an elastic body, the Cauchy number is given by $C_Y = \rho U^2/E$, where $\rho$ is the density of the fluid, $U$ the flow velocity, and $E$ the elastic modulus. With this relation considered for $C_Y = 1$, one obtains an effective elastic modulus $\tilde{E} = \rho_w (Q/S_N)^2$.

In Sec. III, the self-similarity of the fluid force [Eq. (3)] has been assumed as it is suggested by the self-similar properties of the jet flow. The net force [Eq. (4)] can be explicitly obtained from the jet profile [Eq. (2)] by integrating a simplified model for local drag over the sphere cross section,

$$dF_f(r,z) = (1/2)\rho_w \tilde{c}(r/R) v_z(r,z)^2 \, dS, \tag{7}$$

where $\tilde{c}$ is a dimensionless local drag coefficient. This approach is usual for slender structures where the local drag description is valid. Here, the flow around a sphere is highly nonlocal which means that inconsistencies are expected. The empirical expression $\tilde{c}(r/R) = c_P(1 - (r/R)^\eta)$ is used in a local drag approach [Eq. (7)], where $c_P = 2.1$ is the drag coefficient for a perpendicular plate and the exponent $\eta = 0.5$ is the only free parameter used to obtain a satisfactory fit of the rescaled data in Fig. 4. However, the local drag approach and the expression of $\tilde{c}$ are limited to this experiment as they are not valid, for instance, for a sphere in a uniform flow: $v_z(r, z_e) = v_0$.

## V. CONCLUSION AND PERSPECTIVES

In this paper, we have proposed an original approach to account for the equilibrium position of a sphere trapped by a turbulent jet. It was shown that the existence of self-similar forces establishes a connection with a problem of elasticity based on a geometric interpretation of self-similarity. In this interpretation, the space may be rescaled which means that the sphere is static but deformable.

A relation similar to linear elasticity was proposed to account for the mechanical equilibrium of the sphere in the rescaled coordinates. The representation of reconfiguration based on the dimensionless numbers $\mathcal{R}$ and $C_Y$ shows remarkable similarities with classical reconfiguration studies involving the actual deformation of a truly elastic body. With this analogy, it is possible to define an effective elastic modulus for the deformable sphere in the rescaled frame.

The asymptotic regime of high deformation, $C_Y \gg 1$, or equivalently $z_e \gg R/\alpha$, is not accessible for a trapped sphere. This is because the confining associated with the velocity gradients of the jet profile is too weak to overcome the forces induced by the velocity fluctuations of the fluid. However, reconfiguration in this regime is predictable because the velocity is homogeneous on the scale of the sphere with a simple scaling on the centerline, $v(r = 0, z) \propto z^{-1}$. The asymptotic regime $C_Y \gg 1$, where $\mathcal{R} \propto {C_Y}^{-2}$ would be observed by maintaining the sphere in the jet centerline where the vertical forces vanish.

Future work following this contribution may consider a usual reconfiguration experiment with spheres truly capable of deformation. The center of the soft sphere should be maintained in a fixed position in the similar jet flow. A technical difficulty would be to manufacture an elastic spherical body for which the deformations are purely isotropic. A promising approach would be to use a class of soft mechanical metamaterials [29–31] close to the limit of dilational elasticity [32]. The dilational regime corresponds to the pure extensional deformations, which means with a Poisson ratio that is equal to $-1$. In this limit, the only deformation modes allowed are the ones that change the size of the object but not its shape. In these conditions, some unconventional regime of reconfiguration could be observed for a nonslender metamaterial body, such as regimes of drag independent of the flow velocity, that was only reported in a previous work [14] for slender structures.

[1] S. Vogel, Amer. Zool. **24**, 37 (1984).
[2] A. R. Ennos, J. Exp. Bio. **202**, 3281 (1999).
[3] K. J. Niklas, New Phytol. **143**, 19 (1999).
[4] L. H. Harder, O. Speck, C. L. Hurd, and T. Speck, J. Plant Growth Regul. **23**, 98 (2004).
[5] E. de Langre, Annu. Rev. Fluid Mech. **40**, 141 (2008).

[6] S. Vogel, J. Exp. Bot. **40**, 941 (1989).
[7] K. Sand-Jensen, Freshwater Biol. **48**, 271 (2003).
[8] H. M. Nepf, J. Hydraul. Res. **50**, 262 (2012).
[9] S. Alben, M. Shelley, and J. Zhang, Nature (London) **420**, 479 (2002).
[10] L. Schouveiler and A. Boudaoud, J. Fluid Mech. **563**, 71 (2006).
[11] F. Gosselin, E. de Langre, and B. A. Machado-Almeida, J. Fluid Mech. **650**, 319 (2010).
[12] E. de Langre, A. Gutierrez, and J. Cossé, C. R. Mec. **340**, 35 (2011).
[13] M. Luhar and H. M. Nepf, Limnol. Oceanogr. **56**, 2003 (2011).
[14] T. Barois and E. de Langre, J. Fluid Mech. **735** (2013).
[15] J. Güémez, C. Fiolhais, and M. Fiolhais, Phys. Educ. **44**, 53 (2009).
[16] T. López-Arias, Eur. J. Phys. **33**, 253 (2012).
[17] E. H. Brandt, Science **243**, 349 (1989).
[18] R. Wille and A. Fernholz, J. Fluid Mech. **23**, 801 (1965).
[19] T. A. Vil'gel'mi, J. Appl. Mech. Tech. Phys. **10**, 754 (1969).
[20] T. López-Arias, L. M. Gratton, G. Zendri, and S. Oss, Phys. Educ. **46**, 146 (2011).
[21] J. Feng and D. D. Joseph, J. Fluid Mech. **315**, 367 (1996).
[22] S. Davoust and L. Jacquin, in *Sixth International Symposium on Turbulence and Shear Flow Phenomena* (Begell House, Danbury, CT, 2009), pp. 1237–1242.
[23] N. Machicoane, R. Zimmermann, L. Fiabane, M. Bourgoin, J.-F. Pinton, and R. Volk, New J. Phys. **16**, 013053 (2014).
[24] S. B. Pope, *Turbulent Flows* (Cambridge University Press, Cambridge, UK, 2000).
[25] I. Wygnanski and H. Fiedler, J. Fluid Mech. **38**, 577 (1969).
[26] N. Machicoane, J. Bonaventure, and R. Volk, Phys. Fluids **25**, 125101 (2013).
[27] K. T. McDonald, Am. J. Phys. **68**, 388 (2000).
[28] L. Ristroph, M. N. J. Moore, S. Childress, M. J. Shelley, and J. Zhang, Proc. Natl. Acad. Sci. USA **109**, 19606 (2012).
[29] J. Shim, C. Perdigou, E. R. Chen, K. Bertoldi, and P. M. Reis, Proc. Natl. Acad. Sci. USA **109**, 5978 (2012).
[30] S. Babaee, J. Shim, J. C. Weaver, E. R. Chen, N. Patel, and K. Bertoldi, Adv. Mater. **25**, 5044 (2013).
[31] C. Coulais, Int. J. Solids Struct. **97**, 226 (2016).
[32] T. Bückmann, R. Schittny, M. Thiel, M. Kadic, G. W. Milton, and M. Wegener, New J. Phys. **16**, 033032 (2014).

# Appendix C

# On the origin of the relationship: $C_0 = B_0\pi$

The acceleration spectrum can be shown to be related to the second order velocity structure function. The latter statistic is briefly discussed. The second order velocity structure function is defined as:

$$D_2^L(\tau) = \langle (v'(t+\tau) - v'(t))^2 \rangle, \tag{C.1}$$

Application of Kolmogorov similarity scaling to Lagrangian statistics in the inertial range gives:

$$D_2^L(\tau) \simeq C_0 \varepsilon \tau. \tag{C.2}$$

when $\tau_\eta \ll \tau \ll T_L$ and $C_0$ is a universal, "Kolmogorov" constant [180]. Equation (C.1) is calculated for each Reynolds number and (C.2) is plotted in figure C.1 indicating that the value of $C_{0,i}$ follows the hierarchy in the velocity variance (ch. 3, fig. 3.5b). The restricted Reynolds number range explains the slow variation in each component. The absence of plateau as predicted by Kolmogorov similarity is due to the low Reynolds numbers in the experiments. There is evidence in the literature that estimation of $C_0$ from the second order structure functions require Reynolds numbers of order $\mathcal{O}(10^4)$ to converge to an asymptotic value. On the other hand the relationship linking $D_2^L(\tau)$ to the acceleration spectrum is thought to provide a better an estimation of $C_0$ from the acceleration structure functions has been seen to converge as early as $\mathrm{Re}_\lambda \sim 10^2$ and may explain the high values of $\beta_0\pi$ measured in figure 5.11 with respect to $C_0$ in the figure C.1 [132].

Equation (C.1) is related to the acceleration covariance by a kinematic relation written as:

$$d^2 D_2^L(\tau)/d\tau^2 = 2\langle a(t)a(t+\tau)\rangle. \tag{C.3}$$

Using the relationship between the velocity autocorrelation function ($R_{vv}(\tau)$) function and the second order structure function( $D_2^L(\tau)$): $R_{vv}(\tau) = 1 - D_2^L(\tau)/(2\langle v^2\rangle)$, and equation 5.14, one may show [180] that in the inertial range the acceleration spectrum has the following form:

$$\pi\phi_a(\omega) \sim C_0\varepsilon, \tag{C.4}$$

when ${\tau_L}^{-1} \ll \omega \ll \tau_\eta^{-1}$).

The stationarity of the acceleration measurement in order to assume the equivalence: $\phi_{_A}(\omega) = \omega^2\phi_V(\omega)$, where the right hand side is used to derive $C_0 = B_0\pi$. Figure 5.10(a,inset) depicts the ratio of the two estimations of the acceleration spectra

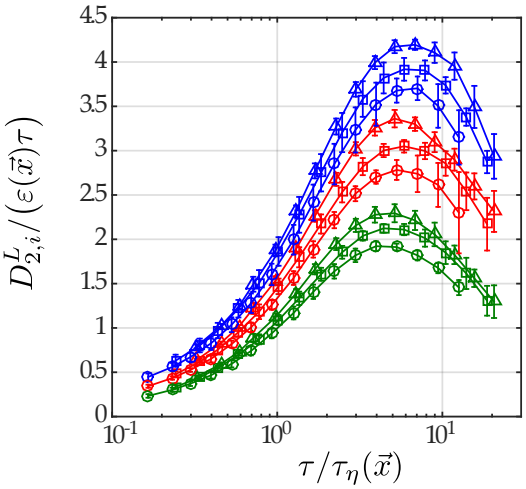


Figure C.1: Second order Lagrangian structure functions measured at $\mathrm{Re}_\lambda = 155$: ○, $\mathrm{Re}_\lambda = 190$: □, $\mathrm{Re}_\lambda = 225$: △. Components are given by colors: $x$ : blue, $y$ : red, $z$ : green. Each curve represents the average of 5 structure functions taken at different positions along the converging direction of the stagnation point that were normalized by the local dissipation rate: $\langle\varepsilon(\vec{x})\rangle = -\langle v' \cdot a'\rangle$ from which the local Kolmogorov time scale is estimated. The small error bars show that the collapse of the 5 positions is good. The collapse indicates that a local dissipation rate is sufficient to determine increments over a significant range of scales.

for the four different particle classes. This is assumed to be a measure of stationarity with values larger than one indicative of non-stationarity. The value of $B_0\pi$ may be overestimated by about 20% but are still in agreement with the references given above. Of note is the increasingly non-stationary nature of the inertial particles. This may have consequences for the evolution of $\tilde{\tau}$ calculated in chapter 4.

# Bibliography


[1] L. da Vinci. Heavy particle concentration in turbulence at dissipative and inertial scales. Codex Atlanticus (ca 1500). 7

[2] E.L. Paul, Atiemo-Obeng V.A., and Kresta S.M., editors. Handbook of Industrial Mixing: Science and Practice. John Wiley and Sons, Inc., 2004. 8, 13

[3] G.T. Csanady. Turbulent diffusion in the environment. D. Reidel Publishing Company, Dordrecht, Holland, 1973. 8, 19

[4] S. A. Thorpe. The Turbulent Ocean. Cambridge University Press, 2005. 8, 12

[5] C. Lester, A. Dettmer, and J. Street. Report on the fukushima dai-ichi nuclear disaster and radioactivity along the california coast. California Coastal Commission, 2014. 8

[6] P. E. Dimotakis, R. C. Miake-Lye, and D. A. Papantoniou. Structure and dynamics of round turbulent jets. Phys. Fluids, 26:3185–3192, 1983. 8

[7] A. Venaille and F. Bouchet. Oceanic rings and jets as statistical equilibrium states. Journal of Physical Oceanography, 41(10):1860–1873, 2011. 8

[8] W. Sullivan. If the shoe floats, follow it. The New York TImes, September 22, 1992. 9

[9] G. A. Voth, A. LaPorta, A. M. Crawford, J. Alexander, and E. Bodenschatz. Measurement of particle accelerations in fully developed turbulence. Journal of Fluid Mechanics, 469:121–160, 2002. 9, 45, 46, 48, 53, 62, 63, 89, 90

[10] N. Mordant, P. Metz, O. Michel, and J.-F. Pinton. Measurement of Lagrangian velocity in fully developed turbulence. Physical Review Letters, 87(21):214501, November 2001. 9, 103, 104

[11] J. Bec, L. Biferale, G. Boffetta, A. Celani, M. Cencini, A. Lanotte, S. Musacchio, and F. Toschi. Acceleration statistics of heavy particles in turbulence. Journal of Fluid Mechanics, 550:349–358, 2006. 9, 19, 88, 93, 108

[12] S.G. Huisman, T. Barois, M. Bourgoin, A. Chouippe, T. Doychev, P. Huck, C.E. Morales, Bello, M. Uhlmann, and R. Volk. Columnar structure formation of a dilute suspension of settling spherical particles in a quiescent fluid. Phys. Rev. Fluids, 074204:1–8, 2016. 9, 112

[13] S. Balachandar and J.K. Eaton. Turbulent dispersed multiphase flow. Annual Review of Fluid Mechanics, 42(1):111–133, 2010. 9

[14] O. Reynolds. An experimental investigation of the circumstances which determine whether the motion of water shall be direct or sinuous, and of the law of resistance in parallel channels. Phil. Trans. R. Soc. Lond., 174:935–9825, 1883. 10, 13

[15] L. F. Richardson. Weather prediction by numerical process. 1922. 10

[16] A. N. Kolmogorov. Turbulent pair dispersion of inertial particles. Dokl. Akad. Nauk SSSR, 30:299–393, 1941. 11

[17] F. S. Godeferd and F. Moisy. Structure and Dynamics of Rotating Turbulence: A Review of Recent Experimental and Numerical Results. Appl. Mech. Rev, 6(3), 2002. 12

[18] G. K. Batchelor. Small-scale variation of convected quantities like temperature in turbulent fluid part 1. general discussion and the case of small conductivity. Journal of Fluid Mechanics, 5(1):113–133, 1959. 12

[19] Harper's New Monthly Magazine, 231, 1869. 13

[20] L. Marié. Transport de moment cinétique et de champ magnétique par un écoulement tourbillonnaire turbulent : influence de la rotation. PhD thesis, l'Université Paris 7 - Denis Diderot, 2014. 13

[21] B. Rousset, P. Bonnay, P. Diribarne, A. Girard, J. M. Poncet, E. Herbert, J. Salort, C. Baudet, B. Castaing, L. Chevillard, F. Daviaud, B. Dubrulle, Y. Gagne, M. Gibert, B. Hébral, Th. Lehner, P.-E. Roche, B. Saint-Michel, and M. Bon Mardion. Superfluid high reynolds von kÃąrmÃąn experiment. Review of Scientific Instruments, 85(10):103908, 2014. 13

[22] J. P. Joule. On the mechanical equivalen of heat. Phil. Trans. R. Soc. Lond., 140(1):196–212, 1850. 12

[23] P. J. Zandbergen and D. Dijkstra. Von kármán swirling flows. Annual Review of Fluid Mechanics, 19(1):465–491, 1987. 14

[24] T. von Kármán. Über laminare und turbulent reibung. Zeitschrift für Angewandte Mathematik und Mechanik, 1:233–252, 1921. 14

[25] G. K. Batchelor. Note on a class of solutions of the navier-stokes equations representing steady rotationally-symmetric flow. The Quarterly Journal of Mechanics and Applied Mathematics, 4(1):29–41, 1951. 14

[26] B. Saint-Michel, E. Herbert, J. Salort, C. Baudet, M. Bon Mardion, P. Bonnay, M. Bourgoin, B. Castaing, L. Chevillard, F. Daviaud, P. Diribarne, B. Dubrulle, Y. Gagne, M. Gibert, A. Girard, B. Hébral, Th. Lehner, and B. Rousset. Probing quantum and classical turbulence analogy in von kármán liquid helium, nitrogen, and water experiments. Physics of Fluids, 26(12):125109, 2014. 14

[27] W. S. Saric. Görtler vortices. Annual Review of Fluid Mechanics, 26(1):379–409, 1994. 15

[28] H. Göruler. Dreidimensionales zur stabilitätstheorie laminarer grenzschichten. Journal of Applied Mathematics and Mechanics, 35:362–363, 1987. 15

[29] F. Ravelet, L. Marié, A. Chiffaudel, and F. Daviaud. Multistability and memory effect in a highly turbulent flow: Experimental evidence for a global bifurcation. Phys. Rev. Lett., 93:164501, Oct 2004. 15, 48, 63

[30] N. T. Ouellette, H. Xu, M. Bourgoin, and E. Bodenschatz. Small-scale anisotropy in Lagrangian turbulence. New Journal of Physics, 8, 2006. 15, 45, 46, 89, 106, 107

[31] P. P. Cortet, P. Diribarne, R. Monchaux, A. Chiffaudel, F. Daviaud, and B. Dubrulle. Normalized kinetic energy as a hydrodynamical global quantity for inhomogeneous anisotropic turbulence. Physics of Fluids, 21(2):025104, 2009. 15

[32] P. Sagaut and C. Cambon. Homogeneous turbulence dynamics. Cambridge University Press, 2008. 15

[33] G.A.Voth, A La Porta, A.M.Crawford, J.Alexander, and E.Bodenschatz. Measurement of particle accelerations in fully developed turbulence. J. Fluid Mech., 469:121–160, 2002. 15, 28, 41, 43, 97

[34] G. I. Taylor. Statistical Theory of Turbulence. Proc. Roy. Soc. A, 151(873):421–478, 1937. 15, 30, 100

[35] T. Von Kármán. The Fundamentals of the Statistical Theory of Turbulence. Journal of the Aeronautical Science, 4(4), 1937. 15, 100

[36] W. T. Ashurst, A. R. Kerstein, R. M. Kerr, and C. H. Gibson. Alignment of vorticity and scalar gradient with strain rate in simulated navier-stokes turbulence. The Physics of Fluids, 30(8):2343–2353, 1987. 15, 100

[37] C.-M. Lee, À. Gylfason, P. Perlekar, and F. Toschi. Inertial particle acceleration in strained turbulence. Journal of Fluid Mechanics, 785:31–53, 2015. 15, 90, 91, 100

[38] Clay M. P. and Yeung P. K. A numerical study of turbulence under temporally evolving axisymmetric contraction and subsequent relaxation. Journal of Fluid Mechanics, 805:460–493, 2016. 15, 61, 62, 100

[39] N. Mordant, J.-F. Pinton, and O. Michel. Time-resolved tracking of a sound scatterer in a complex flow: Nonstationary signal analysis and applications. The Journal of the Acoustical Society of America, 112(1):108–118, 2002. 15

[40] N. T. Ouellette, Haitao Xu, and Eberhard Bodenschatz. A quantitative study of three-dimensional lagrangian particle tracking algorithms. Experiments in Fluids, 40(2):301–313, 2006. 15, 28, 29

[41] M. Bourgoin, J.-F. Pinton, and R. Volk. Lagrangian Methods in Experimental Fluid Mechanics, pages 277–296. John Wiley and Sons Inc, 2014. 15

[42] H. Xu, A. Pumir, G. Falkovich, E. Bodenschatz, M. Shats, H. Xia, N. Francois, and H. Boffetta. Flight-crash events in turbulence. Proceedings of the National Academy of Sciences, 111(21):7558–7563, 2014. 16

[43] L. Chevillard, B. Castaing, A. Arneodo, E. Lévêque, J.-F. Pinton, and S. G. Roux. A phenomenological theory of eulerian and lagrangian velocity fluctuations in turbulent flows. Comptes Rendus Physique, 13(9):899 – 928, 2012. Structures and statistics of fluid turbulence/Structures et statistiques de la turbulence des fluides. 17

[44] H. Kahalerras, Y. Malécot, Y. Gagne, and B. Castaing. Intermittency and reynolds number. Physics of Fluids, 10(4):910–921, 1998. 17

[45] A. B. Basset. A treatise on hydrodynamics. Deighton, Bell and Co., 1888. 17

[46] J. Boussinesq. Théorie analytique de la chaleur: mise en harmonie avec la thermondynamique et avec la thé mécanique de la lumière. Almqvist & Wiksell, 1911. 17

[47] Maxey M. R. and Riley J.J. Equation of motion for a small rigid sphere in a nonuniform flow. Phys. Fluids, 1983. 17, 93

[48] R. Gatignol. The Faxen formulae for a rigid particle in an unsteady nonuniform Stokes flow. Journal de Mécanique Théorique et Appliquée, 1983. 17

[49] E. Calzavarini, R. Volk, M. Bourgoin, E. Leveque, J.-F. Pinton, and F. Toschi. Acceleration statistics of finite-sized particles in turbulent flow: the role of Faxen forces. Journal of Fluid Mechanics, 630:179–189, 2009. 17, 89

[50] H. Homann and J. Bec. Finite-size effects in the dynamics of neutrally buoyant particles in turbulent flow. Journal of Fluid Mechanics, 651:81–91, 2010. 17

[51] E. Calzavarini, R. Volk, E. Lévêque, J.-F. Pinton, and F. Toschi. Impact of trailing wake drag on the statistical properties and dynamics of finite-sized particle in turbulence. Physica D, 241(3):237–244, 2012. 18

[52] P. Nielsen. Turbulence effects of the settling of suspended particles. J. Sed. Petrology, 63(5):835–838, 1993. 18

[53] S. Sumbekova. Clustering of inertial sub-Kolmogorov particles : Structure of clusters and their dynamics. PhD thesis, Université de Grenoble Joseph Fourier, 2016. 18, 112, 123

[54] G. H. Good, P. J. Ireland, G. P. Bewley, E. Bodenschatz, L. R. Collins, and Z. Warhaft. Settling regimes of inertial particles in isotropic turbulence. J Fluid Mech., 759:R3, 2014. 18, 112

[55] V. Mathai, E. Calzavarini, J. Brons, C. Sun, and D. Lohse. Microbubbles and microparticles are not faithful tracers of turbulent acceleration. Phys. Rev. Lett., 117:024501, Jul 2016. 18

[56] I. M. Mazzitelli, D. Lohse, and F. Toschi. On the relevance of the lift force in bubbly turbulence. Journal of Fluid Mechanics, 488:283–313, 2003. 18

[57] I. M. Mazzitelli, D. Lohse, and F. Toschi. The effect of microbubbles on developed turbulence. Physics of Fluids, 15(1):L5–L8, 2003. 18

[58] O. Cadot, S. Douady, and Y. Couder. Characterization of the low pressure filaments in a three-dimensional turbulent shear flow. Physics of Fluids, 7(3):630–646, 1995. 18

[59] R. Volk, E. Calzavarini, G. Verhille, D. Lohse, N. Mordant, J. F. Pinton, and F. Toschi. Acceleration of heavy and light particles in turbulence: Comparison between experiments and direct numerical simulations. Physica D, 237(14-17):2084–2089, 2008. 18, 36, 95

[60] R. Volk, N. Mordant, G. Verhille, and J.-F. Pinton. Laser Doppler measurement of inertial particle and bubble accelerations in turbulence. European Physics Letters, 81:34002, 2008. 18, 28, 41, 48, 53, 97

[61] P. J. Ireland, A. D. Bragg, and L.R. Collins. The effect of reynolds number on inertial particle dynamics in isotropic turbulence. part 1. simulations without gravitational effects. Journal of Fluid Mechanics, 796:617–658, 2016. 19, 108

[62] G. Falkovich and A. Pumir. Intermittent distribution of heavy particles in a turbulent flow. Physics of Fluids, 16:L47–L51, 2004. 19

[63] B. Rosa, H. Parishani, O. Ayala, and L.-P. Wang. Settling velocity of small inertial particles in homogeneous isotropic turbulence from high-resolution DNS. Int. J. Multiph. Flow, 83:217–231, 2016. 19, 108, 112

[64] C.-M. Tchen. Mean value and correlation problems connected with the motion of small particles suspended in a turbulent fluid. PhD thesis, TUDelft, 1947. 19

[65] J. Hinze. Turbulence. McGraw-Hill, 1959. 19, 106

[66] W. J. Cocke. Turbulent hydrodynamic line stretching: Consequences of isotropy. The Physics of Fluids, 12(12):2488–2492, 1969. 19

[67] G.K. Batchelor. The effect of homogeneous turbulence on material lines and surfaces. Proc. R. Soc. A, 213(1114):349–366, 1952. 19

[68] G. T. Csanady. Turbulent diffusion of heavy particles in the atmosphere. Journal of the Atmospheric Sciences, 20(3):201–208, 1963. 19

[69] M.I. Yudine. Physical Considerations on Heavy-Particle Diffusion. Advances in Geophysics, 6:185–191, 1959. 19

[70] E. Calzavarini, M. Kerscher, D. Lohse, and F. Toschi. Dimensionality and morphology of particle and bubble clusters in turbulent flow. J. Fluid Mech., 607:13–24, 2008. 20, 88, 93

[71] E. Balkovsky, G. Falkovich, and A. Fouxon. Intermittent distribution of inertial particles in turbulent flows. Physical Review Letters, 86(13):2790–2793, March 2001. 20

[72] J.R. Fessler, J.D. Kulick, and J.K. Eaton. Preferential concentration of heavy-particles in a turbulent channel flow. Physics of Fluids, 6(11):3742–3749, 1994. 21

[73] A. Aliseda, Cartellier A., F. Hainaux, and J.C. Lasheras. Effect of preferential concentration on the settling velocity of heavy particles in homogeneous isotropic turbulence. J. Fluid Mech., 468:77–105, 2002. 21, 111, 112, 119, 121

[74] L.-P. Wang and M. R. Maxey. Settling velocity and concentration distribution of heavy particles in homogeneous isotropic turbulence. J. Fluid Mech., 256:27–68, 1993. 21

[75] R. Monchaux, M. Bourgoin, and A. Cartellier. Preferential concentration of heavy particles: A Voronoi analysis. Physics of Fluids, 22(10):103304, 2010. 21

[76] J. Bec, L. Biferale, M. Cencini, A. Lanotte, S. Musacchio, and F. Toschi. Heavy particle concentration in turbulence at dissipative and inertial scales. Phys. Rev. Lett., 98:084502, Feb 2007. 21

[77] W.H. Snyder and J.L. Lumley. Some measurements of particle velocity autocorrelation functions in a turbulent flow. J. Fluid Mech., 48:41–71, 1971. 21

[78] G.K. Batchelor. The Theory of Homogeneous Turbulence. Cambridge University Press, 1959. 21, 114

[79] G. I. Taylor. Diffusion by continuous movements. Proc. Lond. Math. Soc., 20:196–212, 1920. 22, 66, 71, 130

[80] C. Tong and Z. Warhaft. Passive scalar dispersion and mixing in a turbulent jet. Journal of Fluid Mechanics, 292:1–38, 1995. 23

[81] Z. Warhaft. The interference of thermal fields from line sources in grid turbulence. Journal of Fluid Mechanics, 144:363–387, 1984. 23

[82] H. Stapountzis, B. L. Sawford, J. C. R. Hunt, and R. E. Britter. Structure of the temperature field downwind of a line source in grid turbulence. Journal of Fluid Mechanics, 165:401–424, 1986. 23

[83] S. B. Pope. Simple models of turbulent flows. Physics of Fluids, 23(1):011301, 2011. 23

[84] M. S. Anand and S. B. Pope. Diffusion Behind a Line Source in Grid Turbulence, pages 46–61. Springer Berlin Heidelberg, Berlin, Heidelberg, 1985. 23

[85] P.D. Huck, N. Machicoane, and R. Volk. A Cost-efficient Shadow Particle Tracking Velocimetry Setup Suitable for Tracking Small Objects in a Large Volume. Procedia IUTAM, 20:175–182, 2017. 25, 46

[86] N. Machicoane. Particules matérielles en écoulement turbulent. Transport, dynamique aux temps longs et transfert thermique. PhD thesis, École Normale Supérieure de Lyon, 2014. 25, 30, 34

[87] R. Zimmermann. How large spheres spin and move in Turbulent Flows. PhD thesis, Université de Lyon, 2013. 25

[88] F. Ravelet, A. Chiffaudel, and F. Daviaud. Supercritical transition to turbulence in an inertially driven von karman closed flow. Journal of Fluid Mechanics, 601:339–364, 2008. 25, 30, 72

[89] N. Machicoane, J. Bonaventure, and R. Volk. Melting dynamics of large ice balls in a turbulent swirling flow. Physics of Fluids, 25:125101, 2013. 25, 26, 46

[90] P. K. Yeung and S. B. Pope. Lagrangian statistics from direct numerical simulations of isotropic turbulence. Journal of Fluid Mechanics, 207:531–586, 1989. 28, 31, 48, 53, 95

[91] N.T. Ouellette. Probing the statistical structure of turbulence with measurements of tracer particle tracks. PhD thesis, Cornell University, 2006. 28

[92] H. Xu. Tracking Lagrangian trajectories in position-velocity space. Measurements Science and Technologie, 19(7):075105, 2008. 28

[93] W. Heisenberg. Zur statistischen theorie der kernreaktionen. Zeitschrift fur Physik, 171:379–402, 1948. 30

[94] A.M. Yaglom. On acceleration fields in a turbulent flow. Dokl. Akad.Nauk. SSSR, 69:531, 1949. 30

[95] R. Volk, E. Calzavarini, E. Leveque, and J.-F. Pinton. Dynamics of inertial range particles in a turbulent flow. Journal of Fluid Mechanics, 668:223–235, 2011. 30, 31, 41, 42, 43

[96] U. Frisch. The Legacy of A. N. Kolmogorov. Cambridge University Press, 1996. 31, 45

[97] R. Monchaux, F. Ravelet, B. Dubrulle, A. Chiffaudel, and F. Daviaud. Properties of steady states in turbulent axisymmetric flows. Physical Review Letters, 96:124502, 2006. 33

[98] D. Faranda, F.M.E. Pons, B. Dubrulle, F. Daviaud, B. Saint-Michel, É. Herbert, and P.-P. Cortet. Modelling and analysis of turbulent datasets using auto regressive moving average processes. Physics of Fluids (1994-present), 26(10):105101, 2014. 34

[99] N. Machicoane, P. D. Huck, and R. Volk. Estimating two-point statistics from derivatives of a signal containing noise: Application to auto-correlation functions of turbulent lagrangian tracks. Review of Scientific Instruments, 88(6):065113, 2017. 34

[100] E. Calzavarini, M. Kerscher, D. Lohse, and F. Toschi. Dimensionality and morphology of particle and bubble clusters in turbulent flow. Journal of Fluid Mechanics, 607:13–24, 2008. 36

[101] N. Machicoane and R. Volk. Lagrangian velocity and acceleration correlations of large inertial particles in a closed turbulent flow. Physics of Fluids, 28(3):035113, 2016. 39, 40, 41, 105

[102] N. Machicoane, R. Zimmermann, L. Fiabane, M. Bourgoin, J.-F. Pinton, and R. Volk. Large sphere motion in a turbulent swirling flow. New Journal of Physics, 16:013053, 2014. 39

[103] Nicolas Mordant, Jean-François Pinton, and Olivier Michel. Time-resolved tracking of a sound scatterer in a complex flow: Nonstationary signal analysis and applications. Journal of the Acoustical Society of America, 112(1):108–118, 2002. 41

[104] N. Machicoane, M. López-Caballero, L. Fiabane, J.-F. Pinton, M. Bourgoin, J. Burguete, and R. Volk. Stochastic dynamics of particles trapped in turbulent flows. Phys. Rev. E, 93:023118, Feb 2016. 43, 63

[105] A. de la Torre and J. Burguete. Slow Dynamics in a Turbulent von Kármán Swirling Flow. Physical Review Letters, 99(5):3–6, August 2007. 43, 47, 48, 63

[106] B. L. Sawford. Reynolds number effects in Lagrangian stochastic models of turbulent dispersion. Physics of Fluids A, 3(6):1577–1586, 1991. 44, 103

[107] P. D. Huck, N. Machicoane, and R. Volk. Production and dissipation of turbulent fluctuations close to a stagnation point. Phys. Rev. Fluids, 2:084601, Aug 2017. 45

[108] H. Tennekes and J.L. Lumley. A First Course in Turbulence. The MIT Press, 2000. 45, 51, 53, 71, 114

[109] S.B. Pope. Turbulent Flows. Cambridge University Press, 2010. 45, 53, 55, 59, 103, 105

[110] A. J. Reynolds and H. J. Tucker. The distortion of turbulence by general uniform irrotational strain. Journal of Fluid Mechanics, 68(4):673–693, 1975. 45, 52

[111] J.-N. Gence. Linear and non linear models of anisotropic turbulence. Annual Review of Fluid Mechanics, 15:201–222, 1983. 45

[112] K. Nishino, M. Samada, K. Kasuya, and K. Torii. Turbulence statistics in the stagnation region of an axisymmetric impinging jet flow. International Journal of Heat and Fluid Flow, 17(3):193–201, 6 1996. 45

[113] L. Marié and F. Daviaud. Experimental measurement of the scale-by-scale momentum transport budget in a turbulent shear flow. Physics of Fluids, 16(2):457–461, 2004. 45, 46

[114] G. Zocchi, P. Tabeling, J. Maurer, and H. Willaime. Measurement of the scaling of dissipation at high Reynolds numbers. Phys. Rev. E, 50(5), 1994. 46, 91

[115] D. Kuzzay, D. Faranda, and B. Dubrulle. Global vs local energy dissipation: The energy cycle of the turbulent von kármán flow. Physics of Fluids, 27(7):075105, 2015. 46, 55

[116] M. López-Caballero and J. Burguete. Inverse cascades sustained by the transfer rate of angular momentum in a 3d turbulent flow. Phys. Rev. Lett., 110:124501, Mar 2013. 48, 63

[117] J. C. R. Hunt and D. J. Carruthers. Rapid distortion theory and the problems of turbulence. Journal of Fluid Mechanics, 212:497–532, 1990. 52

[118] C. Cambon, , and J. F. Scott. Linear and nonlinear models of anisotropic turbulence. Annual Review of Fluid Mechanics, 31(1):1–53, 1999. 52

[119] M. M. Rogers and R. D. Moser. Direct simulation of a self-similar turbulent mixing layer. Physics of Fluids, 6(2):903–923, 1994. 55

[120] W. K. George and H. J. Hussein. Locally axisymmetric turbulence. Journal of Fluid Mechanics, 233:1–23, 1991. 59, 60

[121] P. R. Spalart. Direct simulation of a turbulent boundary layer up to re= 1410. Journal of Fluid Mechanics, 187:61–98, 1988. 59, 60

[122] J. Kim, P. Moin, and R. Moser. Turbulence statistics in fully developed channel flow at low reynolds number. Journal of Fluid Mechanics, 177:133–166, 1987. 59

[123] W. K. George. Lectures in Turbulence for the 2st Century. 2013. 59

[124] S. Ayyalasomayajula, A. Gylfason, L. R. Collins, E. Bodenschatz, and Z. Warhaft. Lagrangian measurements of inertial particle accelerations in grid generated wind tunnel turbulence. Phys. Rev. Lett., 97(14), 2006. 61, 62, 111

[125] R. J. Hill. Opportunities for use of exact statistical equations. Journal of Turbulence, 7:N43, 2006. 62

[126] N. T. Ouellette, H. Xu, M. Bourgoin, and E. Bodenschatz. An experimental study of turbulent relative dispersion models. New Journal of Physics, 8(6):109, 2006. 62

[127] O. Liot and J. Burguete. Bifurcation induced by the aspect ratio in a turbulent von kármán swirling flow. Phys. Rev. E, 95:013101, Jan 2017. 63

[128] G. Rigas, A. S. Morgans, R. D. Brackston, and J. F. Morrison. Diffusive dynamics and stochastic models of turbulent axisymmetric wakes. Journal of Fluid Mechanics, 778, 2015. 63

[129] J.-F. Pinton and B. L. Sawford. A Lagrangian View of Turbulent Dispersion and Mixing. Cambridge University Press, 2012. 72, 78, 82, 90, 91, 96, 108

[130] A. M. Reynolds. Third-order lagrangian stochastic modeling. Physics of Fluids, 15(9):2773–2777, 2003. 76, 77, 104

[131] A. M. Reynolds, K. Yeo, and C. Lee. Anisotropy of acceleration in turbulent flows. Phys. Rev. E, 70:017302, Jul 2004. 76, 77

[132] R. C. Lien and E. A. D'Asaro. The Kolmogorov constant for the Lagrangian velocity spectrum and structure function. Physics Of Fluids, 14(12):4456–4459, 2002. 78, 149

[133] B. L. Sawford and P. K. Yeung. Kolmogorov similarity scaling for one-particle lagrangian statistics. Physics of Fluids, 23(9):091704, 2011. 78

[134] W. Feller. An introduction to probability theory and its applications. Wiley, 1971. 78

[135] N. Wiener. Generalized harmonic analysis. Acta Mathematica, 55:117–258, 1930. 78

[136] A. Khintchine. Korrelationstheorie der stationaren stochastischen prozesse. Mathematische Annalen, 109(1):604–615, 1934. 78

[137] M.S. Uberoi and S. Corrsin. Diffusion of heat from a line source in isotropic turbulence. N.A.C.P Report, 1142, 1953. 80

[138] S. Wetchagarun and J. J. Riley. Dispersion and temperature statistics of inertial particles in isotropic turbulence. Physics of Fluids, 22(6):063301, 2010. 93

[139] J. Bec, L. Biferale, A Lanotte, A. Scagliarini, and F. Toschi. Turbulent pair dispersion of inertial particles. Journal of Fluid Mechanics, 645:497–528, 2010. 92

[140] R. Volk, E. Calzavarini, E. Leveque, and J.-F. Pinton. Dynamics of inertial particles in a turbulent von Karman flow. Journal of Fluid Mechanics, 668:223–235, 2011. 95, 97, 98, 104

[141] R. Volk, D. Chareyron, and J.-F. Pinton. Mesures d'accélération lagrangienne dans un écoulement anisotrope par vélocimétrie laser Doppler étendue. Proceeding du 20ième Congrès Français de Mécanique, pages 1–6, 2011. 97

[142] S. Vajedi, K. Gustavsson, B. Mehlig, and L. Biferale. Inertial-particle accelerations in turbulence: a lagrangian closure. Journal of Fluid Mechanics, 798:187–200, 2016. 100

[143] P. Langevin. Sur la théorie du mouvement brownien. Comptes-rendus de l'Académie des sciences, 645:497–528, 1908. 102

[144] N. Stelzenmuller, J.-I. Polanco, L. Vignal, I. Vinkovic, and N. Mordant. Lagrangian acceleration statistics in a turbulent channel flow. Phys. Rev. Fluids, 2:054602, May 2017. 103

[145] S. R. Hanna. Lagrangian and Eulerian time-scale relations in the daytime boundary-layer. Journal Of Applied Meteorology, 20(3):242–249, 1981. 104

[146] R.-C. Lien, E. A. D'Asaro, and G. T. Dairiki. Lagrangian frequency spectra of vertical velocity and vorticity in high-Reynolds-number oceanic turbulence. Journal of Fluid Mechanics, 362:177, 1998. 104

[147] W. W. Grabowksi and L.-W. Wang. Growth of Cloud Droplets in a Turbulent Environment. Annu. Rev. Fluid Mech., 45:293–324, 2013. 111

[148] R. A. Shaw. Particle-Turbulence Interactions in Atmospheric Clouds. Annu. Rev. Fluid Mech., 37(1):473–491, 2003. 111

[149] H. Siebert, S. Gerashchenko, A. Gylfason, K. Lehmann, L. R. Collins, R. A. Shaw, and Z. Warhaft. Towards understanding the role of turbulence on droplets in clouds: In situ and laboratory measurements. Atmos. Res., 97(4):426–437, 2010. 112

[150] G. C. Elghobashi, S. & Trusdell. On the two-way interaction between homogeneous turbulence and dispersed solid particles. I. Turbulence modification. Phys. Fluids A: Fluid, 5(7):1790–1801, 1993. 112, 121

[151] S. Maxey, M. R. & Corrsin. Gravitational Settling of Aerosol Particles in Randomly Oriented Cellular Flow Fields. 43(11):1112, 1986. 112

[152] M. R. Maxey. The gravitational settling of aerosol particles in homogeneous turbulence and random flow fields. J. Fluid Mech., 174(1):441, 1987. 112

[153] L.-P. Wang, O. Ayala, and W. W. Grabowski. Effects of aerodynamic interactions on the motion of heavy particles in a bidisperse suspension. J. Turbul., 8(25):N25, 2007. 112

[154] S. Sundaram and L. R. Collins. Collision statistics in an isotropic particle-laden turbulent suspension. Part 1. Direct numerical simulations. J. Fluid Mech., 335:75–109, 1997. 112, 126

[155] C.P. Bateson and A. Aliseda. Wind tunnel measurements of the preferential concentration of inertial droplets in homogeneous isotropic turbulence. Exp. Fluids, 52(6):1373–1387, 2012. 112, 114

[156] Bourgoin M. & Cartellier A. Monchaux, R. Analyzing preferential concentration and clustering of inertial particles in turbulence. Int. J. Multiphase Flow, 40:1–18, 2012. 112

[157] R. Monchaux, M. Bourgoin, and A. Cartellier. Preferential concentration of heavy particles: A Voronöi analysis. Phys. Fluids, 22(10):1–10, 2010. 112, 115, 117

[158] S. Sumbekova, A. Cartellier, A. Aliseda, and M. Bourgoin. Preferential concentration of inertial sub-Kolmogorov particles: The roles of mass loading of particles, Stokes numbers, and Reynolds numbers. Phys. Rev. Fluids, 2(2), 2017. 112

[159] M. Obligado, T. Teitelbaum, A. Cartellier, P. Mininni, and M. Bourgoin. Preferential concentration of heavy particles in turbulence. J. Turbul., 15(APRIL 2014):293–310, 2014. 112

[160] R. Jackson. The Dynamics of Fluidized Particles. Cambridge University Press, 2000. 112, 119, 120, 121, 130

[161] C. Bateson. Experimental Study of Inertial Particles in Turbulence: Preferential Concentration, Relative Velocity and Droplet Collisions. PhD thesis, University of Washington, 2016. 112, 114

[162] M. R. Wells and D. E. Stock. The effects of crossing trajectories on the dispersion of particles in a turbulent flow. J . Fluid Mech, 136(1983):31–62, 1983. 114

[163] N.T. Ouellette, H. Xu, and E. Bodenschatz. A quantitative study of three-dimensional Lagrangian particle tracking algorithms. Exp. Fluids, 40(2):301–313, 2006. 114

[164] M. Obligado, A. Cartellier, and M. Bourgoin. Experimental detection of superclusters of water droplets in homogeneous isotropic turbulence. EPL, 112(5), 2015. 117

[165] T. Le Borgne, M. Dentz, and E. Villermaux. Stretching, coalescence, and mixing in porous media. Phys. Rev. Lett., 110:204501, May 2013. 117

[166] J. Duplat, C. Innocenti, and E. Villermaux. A nonsequential turbulent mixing process. Physics of Fluids, 22(3):035104, 2010. 117

[167] J.-S. Ferenc and N. Zoltan. On the size distribution of poisson voronoi cells. Physica A, 385(2):518–526, 2007. 116

[168] T. Bosse, L. Kleiser, and E. Meiburg. Small particles in homogeneous turbulence: Settling velocity enhancement by two-way coupling. Physics of Fluids, 18(2):027102, 2006. 117, 120, 121

[169] É Guazzelli and J. Hinch. Fluctuations and instability in sedimentation. Annual Review of Fluid Mechanics, 43(1):97–116, 2011. 119

[170] J. Hinch. Sedimentation of small particles. In Nadal J-P Guyan, E and Y Pomeau, editors, Disorder and Mixing: Convection, Diffusion and Reaction in Random Materials and Processes, chapter 9, pages 153–162. Kluwer Academic Publishers, Dordrecht, 1988. 119

[171] T. B. Anderson and R. Jackson. Fluid mechanical description of fluidized beds. equations of motion. Industrial & Engineering Chemistry Fundamentals, 6(4):527–539, 1967. 119

[172] É. Guazzelli and J. Morris. A Physical Introduction to Suspension Dynamics. Cambridge University Press, 2012. 119, 120, 121

[173] R Nott, P, É Guazzelli, and O Pouliquen. The suspension balance model revisited. Physics of Fluids, 23(4):043304, 2011. 121

[174] R. Monchaux and A. Dejoan. Settling velocity and preferential concentration of heavy particles under two-way coupling effects in homogeneous turbulence. Phys. Rev. Fluids, 2:104302, Oct 2017. 121

[175] A. M. Wood, W. Hwang, and J. K. Eaton. Preferential concentration of particles in homogeneous and isotropic turbulence. International Journal of Multiphase Flow, 31:1220–1230, 2005. 121

[176] R. Monchaux. Measuring concentration with voronoï diagrams: the study of possible biases. New Journal of Physics, 14(9):095013, 2012. 122

[177] H.R. Pruppacher and J.D. Klett. Microphysics of Clouds and Precipitation. Kluwer Academic Publishers, 2004. 126, 127

[178] Pumir, A. and Wilkinson, M. Collisional Aggregation Due to Turbulence. Annu. Rev. Condens. Matter Phys., 67(January):1–26, 2016. 127

[179] G. A. Voth and A. Soldati. Anisotropic particles in turbulence. Annual Review of Fluid Mechanics, 49(1):249–276, 2017. 130

[180] A. S. Monin and A. M. Yaglom. Statistical fluid mechanics, volume II. MIT press, 1975. 149

# Table des matières

**Résumé:** La turbulence est connue pour sa capacité à disperser efficacement de la matière, que ce soit des polluantes dans les océans ou du carburant dans les moteurs à combustion. Deux considérations essentielles s'imposent lorsqu'on considère de telles situations. Primo, l'écoulement sous-jacente pourrait avoir une influence non-négligeable sur le comportement des particules. Secundo, la concentration locale de la matière pourrait empêcher le transport ou l'augmenter. Pour répondre à ces deux problématiques distinctes, deux dispositifs expérimentaux ont été étudiés au cours de cette thèse.

Un premier dispositif a été mis en place pour étudier l'écoulement de von Kàrmàn, qui consiste en une enceinte fermé avec de l'eau forcé par deux disques en contra-rotation. Cette écoulement est connu pour être très turbulent, inhomogène, et anisotrope. Deux caméras rapides ont facilité le suivi Lagrangien des particules isodenses avec l'eau et petites par rapport aux échelles de la turbulence. Ceci a permis une étude du bilan d'énergie cinétique turbulente qui est directement relié aux propriétés de transport. Des particules plus lourdes que l'eau ont aussi été étudiées et montrent le rôle de l'anisotropie de l'écoulement dans la dispersion des particules inertielles.

Un deuxième dispositif, un écoulement de soufflerie ensemencé avec des gouttelettes d'eau micrométriques a permis une étude de l'effet de la concentration locale de l'eau sur la vitesse de chute des gouttelettes grâce à une montage préexistant. Un modèle basé sur des méthodes théorique d'écoulements multiphasiques a été élaboré enfin de prendre en compte les effets collectifs de ces particules sedimentant dans un écoulement turbulent. Les résultats théoriques et expérimentaux mettent en évidence le rôle de la polydispersité et du couplage entre les deux phases dans l'augmentation de la sédimentation des gouttelettes.

### Mots-clés

Turbulence, Particules inertielles, Effets collectives, Particle Tracking Velocimetry (PTV), Statistiques Lagrangiennes.

**Abstract:** Turbulence is well known for its ability to efficiently disperse matter, whether it be atmospheric pollutants or gasoline in combustion motors. Two considerations are fundamental when considering such situations. First, the underlying flow may have a strong influence of the behavior of the dispersed particles. Second, the local concentration of particles may enhance or impede the transport properties of turbulence. This dissertation addresses these points separately through the experimental study of two different turbulent flows.

The first experimental device used is the so-called von Kármán flow which consists of an enclosed vessel filled with water that is forced by two counter rotating disks creating a strongly inhomogeneous and anisotropic turbulence. Two high-speed cameras permitted the creation a trajectory data base particles that were both isodense and heavier than water but were smaller than the smallest turbulent scales. The trajectories of this data base permitted a study of the turbulent kinetic energy budget which was shown to directly related to the transport properties of the turbulent flow. The heavy particles illustrate the role of flow anisotropy in the dispersive dynamics of particles dominated by effects related to their inertia.

The second flow studied was a wind tunnel seeded with micrometer sized water droplets which was used to study the effects of local concentration of the settling velocities of these particles. A model based on theoretical multi-phase methods was developed in order to take into account the role of collective effects on sedimentation in a turbulent flow. The theoretical results emphasize the role of coupling between the underlying flow and the dispersed phase.

### Keywords

Turbulence, Inertial particles, Collective effects, Particle Tracking Velocimetry (PTV), Lagrangian statistics.